Titania Nanotopography for Control of Cell Response to Bioactive Calcium Phosphate Coatings

Shannon Wilson BSc

Faculty of Computing, Engineering and the Built Environment

Ulster University

Thesis submitted for the degree of Doctor of Philosophy

September 2020

I confirm that the word count of this thesis is less than 100,000 words

Table of Contents

Acknowledgments

To my supervisor Professor Brian Meenan, my sincerest thanks for giving me this opportunity and for your valued support and guidance over the years throughout this thesis.

Also, many thanks to Dr Adrian Boyd for the continued support, coffee, and pints over the years to ensure everything was going smoothly and giving me a place to run by any queries or concerns.

To Dr Mary Josephine Morton, thank you for being an incredible teacher. Your knowledge and patience were detrimental to the cell work in this thesis and I couldn't have done it without you. You've given me skills I can carry forwards and given me confidence in my own ability.

To Dr Mark Tweedy, thank you very much for your knowledge and training in piranha etching.

Dr. Jonathon Acheson, thank you for the wonderful ToFSIMS data, as well as giving me a place where I could discuss ideas.

To the staff and students of NIBEC, especially my fellow lab colleagues, thank you! Thank you for the early mornings and late nights and everything in between. Thank you for the tea and crosswords, nights out and quizzes. Thank for ensuring we always had a supply of snacks, and for cake every birthday. You all helped to ensure this experience was as positive as possible and the encouragement was crucial in the finishing of this thesis.

I would like to acknowledge and thank Rowan Drilling Inc for the opportunities they have provided me through their scholarship and their funding, allowing me to complete my studies.

To my parents Steven and Vivienne, a huge thank you for everything you've ever done for me and for being a constant support in anything I do. Without you both this PhD wouldn't have been possible. Your unwavering love and pride in me helped me achieve my goals. To my brother and sister, Dean and Taylor, thanks for putting up with me and always encouraging me. To the other members of my family, extended family and close friends, thank you for your continued love, support and pick me ups.

Laura, the Lola to my Hannah. Thank you for being there no matter what and knowing how to put a smile back on my face. 16 years and counting!

Ross, thank you for listening to me rant and rave when things got stressful and turning it all around into positives and motivation. Your continuous love, support and encouragement gave me the confidence I needed to see it through.

And last but certainly not least, I would like to thank my Nanny Garrett. Thank you for making me the person I am today and for always believing in me. I hope I've made you proud. See you later alligator, after a while crocodile.

Abstract

Titanium and its alloys are used extensively in the field of orthopaedic implants and are commonly coated with calcium phosphate (CaP) materials, normally hydroxyapatite (HA), to improve their bioactivity and osseointegration. In general, these coatings are designed to be stable *in vivo* thereby promoting an osteoconductive response. Radio frequency (RF) magnetron sputtering offers the opportunity to deposit CaP coatings with a range of chemical properties using HA and substituted HA materials at relatively low processing temperatures, compared to those for commercially applied plasma spraying. In the as-deposited (sputtered) state, these CaP coatings are amorphous and highly soluble, dissolving rapidly in aqueous solution. Control of this inherent solubility can lead to enhanced bioactivity in the surrounding environment which offers the means to engender an osteoinductive effect. Roughened titanium surfaces have been shown to offer a means to control the dissolution of CaP coatings thereon, thereby avoiding the need for thermal annealing in this regard. However, most of the processing techniques employed to date are expensive and time consuming. In this work, chemical etching of titanium surfaces to create a roughened pitted morphology capable of controlling as-deposited CaP is investigated. The resulting topography offers control of dissolution of as-deposited sputtered CaP thin films created from HA and strontium substituted hydroxyapatite (SrHA) targets, which has been determined and compared with that of a pristine titanium control and sputter deposited polycrystalline titanium layer. Detailed surface characterisation using XPS, ToFSIMS and XRD indicated that conformal thin films are produced on each substrate surface, which although removed in part are still present as a continuous layer after 7-days in aqueous culture media. *In vitro* studies of HA coated etched titanium showed increased cell adhesion and proliferation as seen from MTT and PicoGreen™ assay data from cells on the chemically etched surfaces compared to those on the control and comparator system. Cells on the etched surfaces were found to present with a higher coverage and had morphology indicative of pronounced surface interaction when imaged using SEM. Although still chemically intact at 7-days exposure to media, the cell culture studies for SrHA coated surfaces showed the presence of much fewer cells compared to both the HA coated and uncoated substrates. It is proposed that this is due to the higher solubility of the SrHA which causes a high degree of instability on these surfaces leading to cells being unable to adhere. A 28-day culture study confirms that morphology, with and without a HA coating, supports U-2 OS differentiation as measured by ALP and BCA assay measurements, and Alizarin red staining of excreted calcium.

Abbreviations

A	Amps
Å	Angstroms
ACaP	Amorphous Calcium Phosphate
AFM	Atomic Force Microscopy
AKU	Alkaptonuria
ALP	Alkaline Phosphatase
amu	Atomic Mass Units
ANOVA	One-Way Analysis of Variance
BCA	Biocinchonic Acid Assay
BE	Binding Energy
Bi	Bismuth
Bi^{+}	Bismuth Ion
BMP2	Bone Morphogenic Protein
BSA	Bovine Serum Albumin
BTE	Bone Tissue Engineering
C	Carbon
Ca	Calcium
Ca^{2+}	Calcium Ion
CaP	Calcium Phosphate
Ca/P	Calcium to Phosphate Ratio
Cl^{-}	Chloride Ion
cm	Centimetres
cm^2	Centimetres Squared
CO_2	Carbon Dioxide

CO_3	Carbonate
CO_3^{2-}	Carbonate Ion
cps	Counts per Second
Cu	Copper
Cu^{2+}	Copper Ion
Cu Kα	Copper K alpha
˚C	Degrees in Celsius
˚	Degrees
2D	Two Dimensional
3D	Three Dimensional
DAPI	4’,6-diamidino-2-phenylindole dihydrochloride
DC	Direct Current
dH_2O	Deionised Water
DMSO	Dimethylsulfoxide
ds	Double Stranded
ECA	Electrochemical Anodisation
ECM	Extracellular Matrix
EDTA	Ethylenediaminetetraacetic Acid
EG	Ethylene Glycol
ESCs	Embryonic Stem Cells
hESCs	Human Embryonic Stem Cells
eV	Electron Volts
F	Fluorine
F^-	Fluoride ion
FA	Fluorapatite

FBR	Foreign Body Response
FE	Field Emission
FN	Fibronectin
FTIR	Fourier Transform Infrared
g	Grams
HA	Hydroxyapatite
HCL	Hydrochloric Acid
HGD	Homogentisate 1,2, - Dioxygenase
HF	Hydrofluoric Acid
HMDS	Hexamethyldisiloxane
HNO_3	Nitric Acid
H_2O_2	Hydrogen Peroxide
hr	Hour
hrs	Hours
H_2SO_4	Sulfuric Acid
Hz	Hertz
ICDD	International Centre for Diffraction Data
IPA	Iso propan-2-ol
K	Potassium
K^+	Potassium Ion
Kα	K-alpha
keV	Kiloelectron Volts
kN	Kilo Newtons
kN/min	Kilo Newtons per Minute
kV	Kilovolts

Li	Lithium
Li^+	Lithium Ion
M	Molar
mA	Milliamps
mbar	Millibar
mg	Milligrams
mg/ml	Milligram per Millilitre
MG-63	Osteosarcoma Cells Derived from 14-Year-Old Male
Mg	Magnesium
Mg^{2+}	Magnesium Ion
MgTCP	Magnesium Substituted Tricalcium Phosphate
mins	Minutes
mm	Millimetre
mM	Millimolar
µM	Micromolar
µg/ml	Microgram per Millilitre
ml	Millilitres
µA	Microamps
µl	Microlitre
µm	Micrometre
MSCs	Mesenchymal Stem Cells
hMSCs	Human Mesenchymal Stem Cells
MTT	(3-(4,5-Dimethylthiazol-2-Y1)-2,5-Diphenyltetrazolium Bromide)
Na	Sodium

Na^+	Sodium ion
NF-κB	Nuclear Factor κB
ng	Nanograms
ng/ml	Nanograms per Millilitre
NH_4F	Ammonium Fluoride
nm	Nanometres
O	Oxygen
OCN	Osteocalcin
OPG	Osteoprotegerin
OPN	Osteopontin
P	Phosphorus
Pa	Pascals
PBS	Phosphate Buffered Saline
hv	Photon Energy
PCL	Polycaprolactone
PFA	Paraformaldehyde
PGA	Polyglycolic Acid
PG	Pico Green
PLA	Polylactic Acid
pNPP	Para-Nitrophenylphosphate
PO_4^{3-}	Phosphate Group
PolyTi	Polycrystalline Titanium
PolyTi250	Polycrystalline Titanium Sputtered at 250 Watts
PolyTi400	Polycrystalline Titanium Sputtered at 400 Watts
PolyTi250HA	Polycrystalline Titanium Sputtered at 250 Watts with Hydroxyapatite Thin Film Coating

PS	Polystyrene
PTH	Parathyroid Hormone
PVD	Physical Vapour Deposition
Ra	Arithmetic Mean Roughness
RCF	Relative Centrifugal Force
RF	Radio Frequency
RPM	Revolutions Per Minute
Rq	Root Mean Square Roughness
Saos-2	Osteosarcoma Cells Derived from 11-Year-Old Female
SBF	Simulated Body Fluid
SDS	Sodium Dodecylsulfate
Secs	Seconds
SEM	Scanning Electron Microscopy
Sr	Strontium
Sr^{2+}	Strontium ion
SrHA	Strontium Substituted Hydroxyapatite
13SrHA	13% Strontium Substituted Hydroxyapatite
aTi	Annealed Ti
aPolyTi250	Annealed 250W Polycrystalline Titanium
aPolyTi400	Annealed 400W Polycrystalline Titanium
2θ	2-Theta
TCP	Tri-Calcium Phosphate
TE	Triple Express
TERM	Tissue Engineering and Regenerative Medicine
eTi	Piranha Etched Titanium

3eTi	Piranha Etched Titanium for 3 Hours
24eTi	Piranha Etched Titanium for 24 Hours
Ti	Titanium
TiHA	Titanium with Hydroxyapatite Thin Film Coating
TiNT	Titanium Nanotubes
TiO_2	Titanium Dioxide
Ti	Unannealed Titanium
TNAP	Tissue-nonspecific Alkaline Phosphatase
U-2 OS	Osteosarcoma Cells Derived from15-Year-Old Female
V	Volts
v/v	Volume for Volume
λ	Wavelength
W	Watts
wc	Working Concentration
WESS	Wide Energy Survey Scans
W/min	Watts per minute
WR	Working Reagent
%wt	Percentage Weight
XPS	X-ray Photoelectron Spectroscopy
XRD	X-ray Diffraction
Zn	Zinc
Zn^{2+}	Zinc Ion
ZnHA	Zinc Substituted Hydroxyapatite

Declaration

I hereby declare that with effect from the date on which the thesis is deposited in the Library of the Ulster University, I permit

1. The Librarian of the University to allow the thesis to be copied in whole or in part without reference to me on the understanding that such authority applies to the provision of single copies made for study purposes or for inclusion within the stock of another library

2. The thesis to be made available through the Ulster Institutional Repository and/or EThOS under the terms of the Ulster eTheses Deposit Agreement which I have signed

IT IS A CONDITION OF USE OF THIS THESIS THAT ANYONE WHO CONSULTS IT MUST RECOGNISE THAT THE COPYRIGHT RESTS WITH THE AUTHOR AND THAT NO QUOTATION FROM THE THESIS AND NO INFORMATION DERIVED FROM IT MAY BE PUBLISHED UNLESS THE SOURCE IS PROPERLY ACKNOWLEDGED

Chapter 1: Introduction

1.1 Overview

Biomaterials are central to the provision of both established and evolving medical interventions that bring direct benefit to individual patients and to society more generally[1–3]. The functional properties that are required from such systems are continuously changing and evolving as our understanding of how the body works improves. In this regard, even those biomaterials that have a substantial history of usage for the fabrication of successful implant devices are subject to a process of continual improvement. With an ever-increasing aging population, there is a necessity to have clinical treatments which address degenerative diseases, particularly those associated with the musculoskeletal system. In this regard, there is much interest in developing implants that can work in tandem with bone in a manner that takes account of the non-optimal biological environment concerned such as the presence of osteoarthritis or related conditions. Hence, there is a need for the biomaterials from which these devices are fabricated to work in tandem with the body and the natural processes that occur due to relevant bone diseases. A key aspect of how such implants engage with bodily tissues relates to the attendant cell-surface interactions and so, control of the biomaterial surface chemistry and/or microstructure.

Titanium and its alloys have been used in the medical implant industry for many decades and are especially relevant to the fabrication of orthopaedic devices including hip replacements[4,5], knee replacements[6–8], dental implants[9–11], surgical pins[12,13] and spinal fusion[14–16]. The use of titanium has been the basis of various research and projects, with generally positive results obtained due to its biocompatibility and strength. However, titanium itself is not bioactive and so the success of the osseointegration of the titanium implant is usually dependant on the addition of a bioactive element to the implant material and/or modification of its surface microstructure. Changing the surface properties of titanium presents the opportunity to control cell response thereon and can be realised through various methods that allow for specific attributes to be added, dependant on the desired application. The surface chemistry of titanium has been modified by many processing methods including sand blasting[17,18], chemical etching[19,20], electrochemical anodisation[21,22], physical vapour deposition (PVD)[23,24] and thermal treatment[25,26]. Dalby et al.[27] discussed how an offset topography on the titanium surface can influence superior differentiation of human mesenchymal stem cells compared to that of ordered topography or smooth surfaces.

Previous work at Ulster has investigated how a combination of chemical and microstructural characteristics can influence the cell response of titanium without affecting its bulk properties. In particular, McCafferty *et al.*[28] combined titanium substrates with a sputtered calcium phosphate thin film. These combination surfaces were found to increase cellular attachment, proliferation and differentiation of mesenchymal stem cells when compared to control surfaces. McLister[29] found that titanium nanotubes slowed the dissolution of calcium phosphate materials, whilst encouraging mesenchymal stem cells attachment and proliferation.

Based on the findings to date, a major consideration for their practical application is the accessibility of the modification process employed, particularly when there are multiple steps in the processing that all require expensive technology and/or time to deliver the attendant benefits. The subsequent addition of a bioactive element, commonly in the form of calcium phosphate (CaP) coatings, to directly influence *in vitro* cellular response[22,29–31] has been shown too.

Chemical etching of titanium is a simple method that has been observed previously to produce pronounced changes in surface microstructure depending, in the main, on the etchant solution used and length of time that the material is exposed, with other factors such temperature and pressure also important. Although, this form of processing requires high levels of good health & safety practice to be observed, it does not need the specialist equipment associated with many of the other approaches. Hence, its ability to work in combination with a suitable bioactive system is of interest here in the context of providing a means to control cell response.

Calcium phosphates are a well-known family of ceramic biomaterials[32,33] some of whom occur naturally mainly in mineral component of bone. Many CaP biomaterials are bioactive, i.e. they can directly produce a response from a biological system *in vivo*. However, these ceramics do not possess the mechanical (tensile) strength required for load bearing orthopaedic implant applications and so are generally used as coatings in such demanding environments. Hydroxyapatite (HA) is the most commonly used CaP bioactive coating for such applications, typically plasma sprayed onto implants surfaces[25,34,35]. There has also been recent interest in the addition of various ions into the HA lattice to provide certain properties, dependent on the chosen application. For example, the addition of zinc has been found to provide antimicrobial properties[36] whilst the addition of strontium has been found to promote osteoblast activity[37,38].

The work undertaken here combines chemical modification of a titanium surface with a CaP thin film coating in a manner that seeks to use both as attributes to promote

cell response thereon. As such, an optimum titanium morphology (generated by chemical etching) that is capable of allowing a degree of control over dissolution of RF sputter deposited CaP thin films thereon, as well as providing an underlying topography that cells will respond positively to *in vitro.* Pristine titanium has been used as a control surface representative of the native morphology. A comparative sample has also been used comprising polycrystalline titanium created by sputter deposition from a pure titanium target which has been shown previously to have surface properties that can work effectively with a CaP layer thereon. Calcium phosphate (CaP) coatings sputter deposited from both hydroxyapatite (HA) and strontium substituted hydroxyapatite (SrHA) targets have been investigated on each of the titanium microstructures concerned. Surface analysis and associated imaging techniques have been used to determine the nature of the native substrates and the CaP (HA and SrHA) coated surfaces before and after exposure to culture media. *In vitro* cell culture studies of both coated and uncoated samples have been performed to measure the effects of residual CaP in the presence of each titanium surface microstructure.

1.2 Aims and Objectives

The overall aim of this project is to evaluate the ability of a chemically etched titanium surface to provide control of the dissolution of as-deposited sputtered CaP coatings (HA and SrHA) thereon in a manner that delivers a residual bioactive response.

This aim was then achieved through the following objectives:

- Generation of chemically etched titanium surface from two chosen time points using piranha solution;
- Identification of the characteristics of a pristine control sample by comparing properties of unannealed and annealed titanium;
- Provision of a comparator titanium morphology from previously investigated systems - titania nanotubes or sputtered deposited polycrystalline titanium;
- Radio frequency (RF) magnetron sputter coating of thin films from hydroxyapatite (HA) or strontium substituted hydroxyapatite (SrHA) targets onto chemically etched, control and comparator titanium surfaces;
- Detailed surface characterisation of CaP thin film coating (HA or SrHA) on chemically etched, control and comparator titanium surfaces over a 7-day period in cell culture media;

- Evaluation of *in vitro* study of uncoated surfaces to analyse U-2 OS cell viability and adhesion over a 7-day study;
- Initial *in vitro* U-2 OS cell viability and adhesion on CaP coated surfaces at day 3;
- 28-day *in vitro* study of uncoated these CaP coated surfaces to analyse U-2 OS differentiation via alkaline phosphatase (ALP) and whole protein biocinchonic acid (BCA) assays; and
- Overall comparison of cell response to CaP (HA) coated, and substituted CaP (SrHA) on chemically etched, control and comparator titanium substrates to establish the relative effects of residual CaP chemistry and microstructure.

1.3 Structure of Thesis

The structure of the thesis as presented here is as follows;

- Chapter 1 presents an introduction to the thesis, including the aim and objectives
- Chapter 2 provides a detailed literature review covering past, present and ongoing; research relating to the core topics of relevance, as well as including background information to bone biology and rationale behind certain biomaterial choices;
- Chapter 3 explains the methods and materials used in experimentation and characterisation (physiochemical analysis and *in vitro* cell studies) employed throughout the thesis;
- Chapter 4 details the full characterisation of the surface chemistry and morphology of the chemically etched, control and comparator titanium surfaces
- Chapter 5 presents a detailed appraisal of the chemistry of RF magnetron sputter deposited CaP thin film (HA and SrHA) coatings – before and after exposure to cell culture media for 7-days;
- Chapter 6 describes a series of three interrelated *in vitro* U-2 OS cell culture evaluations, namely: uncoated surfaces at day 7, HA and SrHA coated substrates at day 3 and HA and SrHA coated substrates over a 28-day period; and
- Chapter 7 provides the overall conclusions that can be drawn from the data and suggestions for future work

Chapter 2: Literature Review

2.1 Introduction

Topography can be defined as '*the morphology or configuration of a surface'*[39], and in combination with chemistry, is key in creating a medical implant substrate surface that can influence cellular function up to and including the differentiation necessary for tissue formation. Cells are very sensitive to their surrounding environment, receiving various cues from chemical and mechanical stimuli. However, too much of a certain stimulus can have negative effects upon the cells and the surrounding tissue. Therefore, control of such stimuli allows for manipulation of how cells interact with a substrate surface, as well as minimising the risk of an adverse immunoregulatory response when it is implanted *in vivo.* Mechanotransduction is '*the process by which external mechanical stimuli are transmitted into the nucleus, resulting in adaptive gene and protein level changes'* [40] and also plays an important role in this regard, especially in the maturation of osteoblast cells to create or repair bone tissue. Hence, a combination of the correct surface features, chemistry and mechanical stimuli can produce direct effects on maturation of cells that do not require the use of additional biological factors. As indicated earlier, the work undertaken in this thesis concerns the effects that a chemically etched titanium surface with a soluble calcium phosphate coating has on bone cell response as a means to develop an implant system that can work with a mechanotransduction environment.

There have been several studies focusing on coating of titanium substrates with calcium phosphate (CaP)[21,41–45] and substituted calcium phosphates[37,46–48], namely those systems based on hydroxyapatite (HA) and tri-calcium phosphate (TCP), as highlighted in Table 2.1. In general, these studies have shown that surface topography can significantly influence the function of several cell types, including osteoblast attachment, proliferation and differentiation. The majority of these studies involve the creation of crystalline CaP thin films, which generally result in little or no dissolution in physiological conditions. By contrast, this study concerns the use of amorphous coatings of calcium phosphate and strontium substituted calcium phosphate systems. Naturally occurring bioapatite present in bone tissue includes a range of trace impurity ions including strontium (Sr), zinc (Zn), magnesium (Mg) and fluoride (F). These trace ions can heavily influence how cells behave depending on the concentrations of the various ions present. Synthetic forms of crystalline apatite coatings can be obtained through thermal annealing of hydroxyapatite (HA) or ion substituted hydroxyapatite (SrHA). Any substituted ion that becomes properly incorporated into the crystalline lattice of the HA

alters its material properties with respect to crystal structure and stoichiometry. However, if substituent materials are not bound into the HA lattice, the resulting systems are referred to as 'doped' instead of 'substituted', as the ions have not been incorporated into the lattice to replace any other ions (e.g. strontium ions (Sr^{2+}) replacing calcium ion (Ca^{2+})). Whether a HA material is doped or substituted, if amorphous, it can still undergo dissolution in physiological conditions and release its ions into the surrounding body fluid. In the case where such HA and SrHA materials are used to create coatings, either in their amorphous or crystalline forms, their stability is also dependant on the coating technique and any subsequent processing post-deposition. The effects that the deliberate dissolution of amorphous CaP thin films has on bone cell response has not been addressed in great detail in the literature as most coatings are annealed to a crystalline phase to engender a more stable biological response *in vivo*, as is the case for HA coatings on orthopaedic implant devices by way of delivering cementless fixation. The use of highly soluble amorphous CaP coatings that dissolve rapidly has limited applicability to engender bone creation and hence in this work, surface topography (rather than annealing) is used to influence the CaP degrades and thereby prolong their bioactive behaviour *in vivo*.

Table 2.1 Chemical names and formula for CaP and substituted CaP systems

Chemical Name and Abbreviation	Chemical Formula	Ca/P Ratio
Tri-Calcium Phosphate (TCP)	$Ca_3(PO_4)_2$	1.67
Amorphous Calcium Phosphate (ACaP)	$Ca_9(PO_4)_6$	1.50
Dicalcium Phosphate Anhydrous (DCPA)	$CaHPO_4$	1.00
Monocalcium Phosphate Anhydrous (MCPA)	$Ca(H_2PO_4)_2$	0.50
Amorphous Calcium Phosphate (ACaP)	$Ca_x(PO_4)_y.nH_2O$	1.20-2.20
Hydroxyapatite (HA)	$Ca_{10}(PO_4)_6(OH)_2$	1.67
Strontium Substituted Hydroxyapatite (SrHA)	$Ca_{10x}Sr_x(PO_4)_6(OH)_2$	1.67
Fluorapatite (FHA)	$Ca_{10}(PO_4)_6(F)_2$	1.67

2.2 Bone Biology

The skeletal system not only provides structural and load bearing support for the body, whilst providing protection for vital organs, but is also the major site for calcium homeostasis[49]. Bone is a natural composite composed of approximately 30 % organic matrix material and approximately 70 % inorganic nanosized minerals[50]. The main components of bone are natural hydroxyapatite (also referred to as bioapatite), collagen (types I, III and VI) and water. The amount of the mineral components present varies depending on the type and location of the bone tissue. Bone (Figure 2.1) is composed of two types of tissue: compact and cancellous. Compact, also known as cortical bone tissue, is the hard-outer layer commonly found on long bones, which is strong and dense. The inner cancellous tissue, also referred to as trabecular bone, is spongy, lighter and much less dense. Bone tissue acts as a storage area for a number of minerals (as mineral salts), as well as providing an environment where blood cells are regenerated. Moreover, as indicated in Figure 2.2, it contains cells including osteoblasts and osteoclasts as well as non-collagen proteins (osteoids)[51,52].

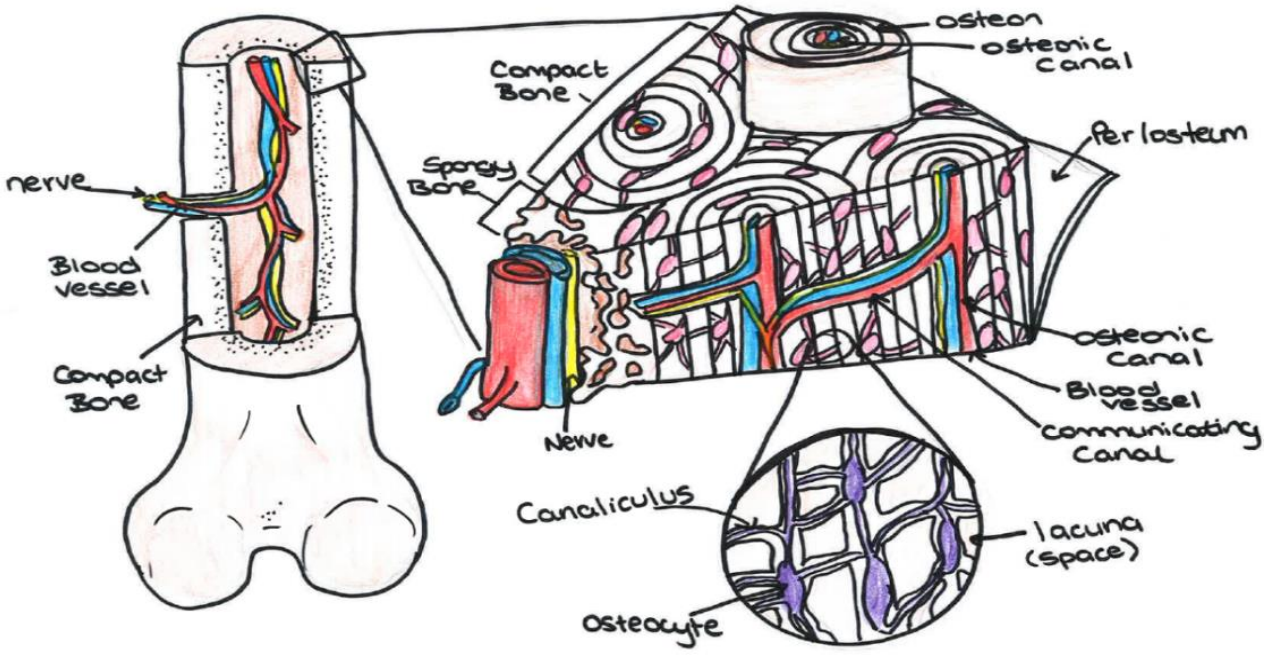

Figure 2.1 Schematic diagram of bone structure

Bone tissue formation occurs via a flexible, semi-solid cartilaginous matrix produced by chondroblasts and consists of hyaluronic acid, chondroitin sulfate, collagen fibres and water. Osteoblasts within the matrix excrete uncalcified matrix (osteoid) containing

minerals including bioapatite to form osteocytes which when isolated within the growing structure become osteons. In the case of compact bone, a network of blood capillaries is created within the growing tissue to supply nutrients to the cells, whereas in cancellous bone this occurs by diffusion through the spongy, porous structure. Bone remodelling is the separate but continuous process in which mature tissue is removed through bone resorption and new bone formed by ossification which maintains bone mass[53]. Excessive bone resorption is the basis of many bone diseases, including osteoporosis[54].

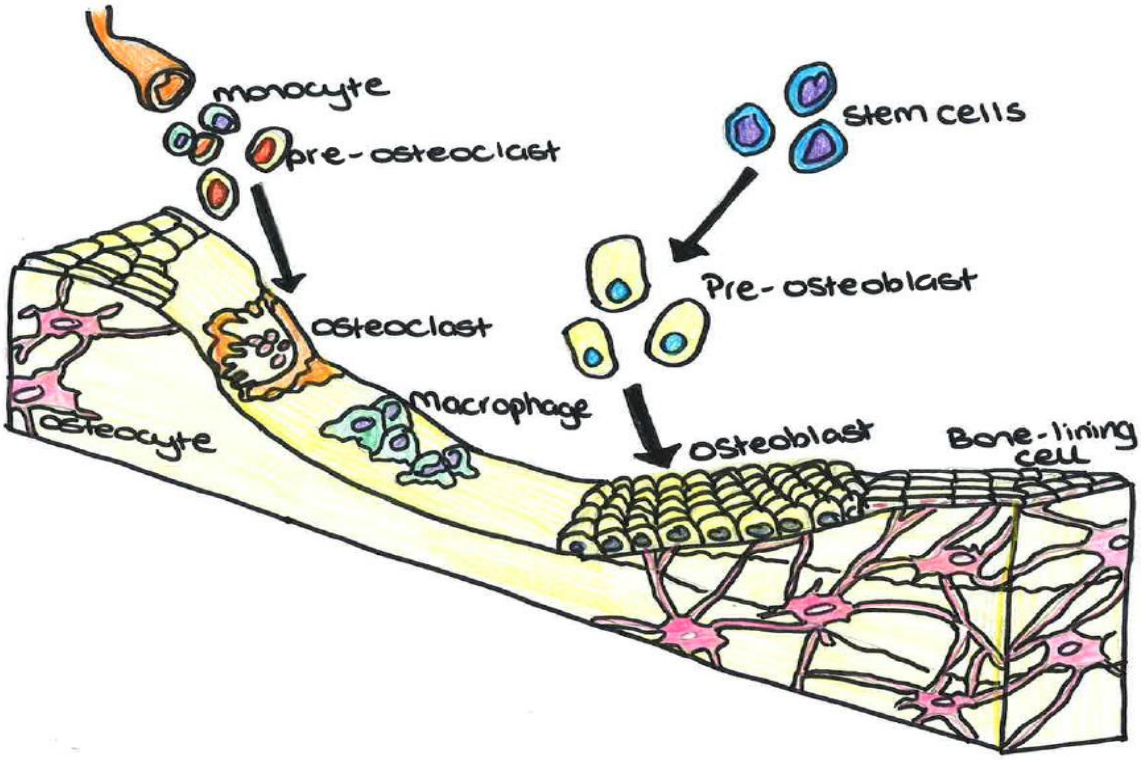

Figure 2.2 Schematic diagram showing osteoblasts, osteocytes and osteoclasts in the bone

2.2.1 Bone cell types and their markers

Osteoprogenitor cells are referred to as potential bone cells and have the capability to differentiate into osteoblasts. Osteoblasts, also known as bone-forming cells, and as described above, produce bone matrix through the synthesis and secretion of bone matrix proteins, both collagenous and non-collagenous[55]. After the formation of the organic bone matrix, some osteoblast cells become 'buried' within this matrix and form osteocytes. Osteocyte cells are mature osteoblasts that maintain the bone tissue through regulation of bone metabolism and remodeling[53]. These cells are usually found in lacunae within the bone. Osteoclasts are large multinucleated cells of hemopoietic origin and are responsible for the resorption of mineralised tissue and can be found on the bone surface at active

resorption sites. Osteogenesis is the term commonly given to the development of new bone tissue[56,57]. This can occur through two main routes:

- Intramembranous ossification – involves replacement of connective tissue membranes and is responsible for the formation of flat bones, such as in the skull. Here mesenchymal progenitor cells differentiate straight to osteoblasts.
- Endochondral ossification – involves replacement of cartilaginous matrix with bone tissue, such as in the femur. In this process, mesenchymal progenitor cells go through a sequence of differentiation before final mineralisation.

There are three main periods of osteoblast phenotype development, as follows:

1. Proliferation
2. Extra cellular matrix (ECM) development and maturation
3. Mineralisation

These processes are accompanied by the production of various biomarkers as osteoblast maturation to bone progresses. Alkaline phosphatase (ALP), also referred to as tissue non-specific alkaline phosphatase (TNAP), is a protein enzyme that is expressed in the early stages of bone development, along with other growth factors, and promotes the differentiation of pre-osteoblasts into mature osteoblasts[58]. Therefore, measurement of ALP activity can be used as an early indicator of osteogenic differentiation and evidence that the cell activities connected to the formation of ECM are present, as these matrix vesicles present in the ECM are the site at which the mineralisation begins[59].

Osteocalcin (OCN), a vitamin K dependent protein, is commonly used as a marker to determine if there are mature osteoblasts present and is linked to the mineralisation phase and nodule formation[60]. Osteopontin (OPN) has been shown to bind to fibronectin (FN), as well as collagen types I-V, which then act as a bridge between the extracellular matrix (ECM) and the surface of the cell.

2.2.2 Bone Loss and Disease

Significant bone loss can occur due to several conditions such as traumatic non-union fracture, calcium deficiency, disease such as osteoporosis, and tumour resection. Loss of bone mass occurs in both men and women and increases with age, but significant bone loss is more common in postmenopausal women[61,62]. Substantial bone loss is due to high osteoclast activity, meaning that bone is being resorbed faster than osteoblast activity can form new tissue. This leads to bones that are a lot weaker and are therefore more prone

to damage and fracture. Osteoporosis has been recognised as a major health concern worldwide that affects approximately 27.5 million men and women and this number is expected to rise to 33.9 million by 2025[63]. Johnell *et al* state that more than 8.9 million fractures occur worldwide due to osteoporosis[54]. The end goal in the treatment of osteoporosis is the prevention of fractures, so as to allow the patient to live as close to a normal life as possible.

Current methods of treating and alleviating the symptoms of osteoporosis and related conditions include the use of bisphosphonates, which are a class of drugs that inhibit osteoclast activity, thus slowing bone resorption. Injection of parathyroid hormone (PTH) is a treatment to stimulate bone formation and thus reduce fracture risk. It has been found to increase bone mineral density in postmenopausal women[62]. Another treatment that has been used for osteoporosis is the ingestion of strontium in the form of strontium ranelate (commercially known as Protelos). Delannoy *et al.*[64] used this drug in a study with mice observed over 2 years and found that there was increased trabecular bone volume, reduced osteoclast activity and increased mineralised bone volume. Even when given at the highest dose, there was no osteoid thickness change, indicating that this drug would not have any toxic influence on bone mineralisation. However, despite the worldwide use of this drug and the many research papers focusing on the positive outcomes of this drug for the treatment of osteoporosis, strontium ranelate was discontinued in 2017. The reason for this discontinuation by the company was mainly due in part to the limited users taking the medication. This fall in patients being prescribed strontium ranelate was due to several factors, with one being an increase of cardiovascular risks associated with the long-term use of this drug.

2.3 Biomaterials

A biomaterial can be defined as '*A material intended to interface with biological systems to evaluate, treat, augment or replace any tissue, organ or function of the body'* [65]. Moreover, a consensus at a 2018 conference defined a biomaterial as '*A material designed to take a form that can direct, through interactions with living systems, the course of any therapeutic or diagnostic procedure'* [66]. Hence, they are used to fabricate an implant or graft to act as a biomimetic support system to encourage the regeneration of new tissue. These materials can be natural, such as silk, collagen and fibrin, or synthetic including metals, polymers, glasses, composites and ceramics (as summarised in Table 2.2).

Metals and metal alloys are commonly used for the production of load bearing bone and dental implants[67,68]. They are frequently combined with other materials such as ceramics and/or polymers in order to improve upon the biocompatibility and bioactivity of the implant. In contrast, polymers are, in general, organic based compounds consisting of a basic monomer unit which repeats to form large polymeric structures, usually through addition or condensation polymerisation. Polymers are ductile and malleable, which allows them to be made into complex shapes. These materials tend to be biologically inert and so are applied readily to biomaterial applications commonly as porous scaffolds or as a drug delivery system[69]. Ceramic are compounds formed between metallic and non-metallic elements containing ionic or covalent bonding. This bonding gives strength to ceramics; however, they can be very brittle and prone to fracture. Ceramics tend to have excellent bioactivity and so are readily used as coatings on other implants to enhance the bioactivity and subsequent biocompatibility of the material[32,70].

Table 2.2 Biomaterials and their common applications

Material	**Natural/Synthetic**	**Principal Applications**
Metal and Metal Alloys		
• Titanium	Synthetic	Bone and Joint Replacement,
• Stainless steel	Synthetic	Fracture Fixation,
• Cobalt Chromium	Synthetic	Dental Implants
Polymers		
• Collagen	Natural	Skin and Cartilage
• Alginate	Natural	Replacement, Ocular
• Chitosan	Natural	Implants, Drug Delivery,
• Polylactic Acid (PLA)	Synthetic	Scaffolds
• Polycaprolactone (PCL)	Synthetic	
• Polyglycolic Acid (PGA)	Synthetic	
Ceramics		
• Calcium Carbonate	Natural	Heart Valves, Dental
• Calcium Silicate	Natural	Implants, Implant Coatings,
• Bioactive Glass	Synthetic	Bone Replacement
• Hydroxyapatite (HA)	Synthetic	
• Biphasic Calcium Phosphate (BCaP)	Synthetic	

The success of a biomaterial (as a device) when implanted into the body (*in vivo)* depends on various factors including chemistry, topography, wettability and biocompatibility. In the context of bone, these properties all play a role in the regulation of cellular response to a particular biomaterial to encourage osseointegration of the implant[71,72]. Other influential factors include device design, surgical techniques, health of the patient and post-surgery activity. Another important consideration to be made when deciding on which biomaterial is suitable for the desired application is the nature and rate of any degradation or breakdown that are associated with that material when placed in aqueous solution (*in vivo*). The by-products of biomaterial degradation, even those that are naturally found in the body, in large quantities can invoke an immune response leading to inflammation and possibly rejection of the implant. Hence, the properties of degradation products should be non-toxic and easily removed from the body to avoid any inflammation and subsequent host response[73]. Deliberate degradation of a material, particularly in orthopaedic applications, can release products that can benefit *in vivo*. In regard to this thesis, deliberate degradation of a CaP coating can release particular ions into the surrounding cell environment which in turn can engender new tissue (bone) growth[74–76].

2.3.1 Bone Repair

Healthy bone tissue can repair small cracks or fractures naturally. However, larger defects caused by severe injury, non-union fractures, infection, age or disease cannot heal effectively without intervention[10]. Therefore, bone tissue has the highest demand for regeneration, reconstruction or replacement due to the aging world population. This is usually achieved clinically through autografts, allografts or xenografts. Autogenous bone grafts are known as the 'gold standard' of bone replacement/repair, as they involve tissue taken from the same patient and so possess good biological properties as well as having significant mechanical strength. The bone is typically harvested from the iliac crest, fibula or rib, with in some instances small amounts of bone being removed from the mandible chin[77,78]. Autografts are the current 'go to' method as there is no risk of rejection or transfection. However, this type of graft requires two surgery sites. This can be expensive and lead to donor site injury or morbidity at two separate sites. This increases the patients risk of haemorrhage, infection, damage to surrounding nerves, inflammation and increased scarring[79]. These complications have led to the need for alternative methods when repairing bone defects.

Allografts are harvested from a donor and implanted into a recipient. The donor

tissue is often taken from a cadaver or harvested during an orthopaedic procedure and is screened, processed and preserved for implantation into the recipient patient. The processing of these grafts generally involves washing to remove any of the donor's cells rendering it cell free, and gamma irradiation sterilisation. This type of graft eliminates the risks that come with a second surgery site, but as this is from another donor, there is a risk of an immune response from the new host, despite the heavy processing carried out before implantation.

Xenografts are tissues taken from non-human species, typically porcine or bovine. The grafts are heavily processed to remove any native animal cells and steps are taken to ensure their sterility. However, as this tissue is harvested from a non-human species, there is a risk of disease transmission, and despite the heavy processing to reduce this risk it is never fully eliminated. The main issue with these types of grafts though is the ethical issue of using bone from a different species, which greatly reduces their clinical applications.

In circumstances where natural grafts are not available or are unsuitable for the patient, a biomaterial system can be used. In the context of a load bearing bone environment, both ceramics and metal/ metal alloys have been used to promote and support repair and regeneration. These implants are commonly coated with a surface finish to improve the biocompatibility and encourage rapid bone growth so as to enhance bone affixation with the implant. For example, Brånemark found that during a blood flow study using titanium chambers in rabbits, that the metal implant, (titanium in this instance), underwent osseointegration, i.e. was completely integrated into the surrounding bone[80]. Most bone implants require osteoconduction, wherein osteoblasts are adhered to the biomaterial surface, to initiate a response leading to osteogenesis[81]. Effective osteoconduction of implants/grafts depends on two main factors; the chemical structure of the material, and the physical properties, upon which osseointegration induces osteogenesis through the stimulation of immature cells to preosteoblasts[82]. This stimulation will then lead to bone healing and thus proper anchorage of the implant itself with the native tissue. Implants made from low biocompatibility materials show little to no osteoconduction, which means there is no bone growth over the implant and can lead to loosening of the material. Implant failure can occur due to loosening of the device, soft tissue encapsulation or an immune response by the host. Hence, in order to reduce and eventually eliminate implant failure, it is necessary to improve osteointegration and minimise the host immune response[83].

2.4 Osteoblast-like Cells for Cell Models

Throughout the extensive research that has been carried out relating to biomaterial surfaces that can repair and/or regenerate bone tissue, several forms of osteoblast-like cells have been utilised for *in vitro* cell culture evaluation[84]. Based on an understanding of human osteoblast biology and their interactions at implant sites, cell models that can mimic these environments have been generated over time in order to allow for accurate as possible assessment of surfaces and materials intended for use. The cells used vary from animal derived cells, such as mice and rat bone cells[85,86], to human derived cells, such as primary human mesenchymal stem cells (hMSCs). However, their application requires ethical approval and specialised culture media. As an alternative, immortalised osteosarcoma cell lines are commercially available in large quantities with no need for ethical approval. Commonly used human osteosarcoma cell lines for biomedical related research include MG-63 (osteosarcoma cells derived from a 14-year-old male), Saos-2 (osteosarcoma cells derived from an 11-year-old female) and U-2 OS cells (osteosarcoma cells derived from a 15-year-old female)[87–89]. It is noted that these cells are sourced from tumorous cancer cell lines and so certain cell interactions may be elevated or suppressed compared to those of primary human osteoblasts. However, working with these immortalised cell lines gives a reliable indication of what can be expected in terms of primary interactions with the material/surface in question.

Osteoblasts used for culture studies require the use of aqueous media to promote the required cell responses. In the case of stem cells, an osteogenic media that contains the standard DMEM basal media supplemented with foetal bovine serum (FBS), β-glicerophosphate, ascorbic acid and dexamethasone is used to promote a bone cell lineage. Many studies, including this thesis, aim to reduce or even eliminate the need for supplemented media by replacing the media with specific topography and/or bioactive thin film coatings thereon that directly promote these cells to an osteoblastic lineage.

2.5 Manipulation of Titanium Surface Topography

As indicated previously, titanium and its alloys have a long history as biomaterials for the fabrication of orthopaedic implants due to their desirable mechanical properties including a low density, mechanical loading strength, resistance to corrosion and the natural surface oxide layer is biocompatible. In order to enhance biological response in a manner that is vital for osteoconductivity[90,91], their surface topography has been manipulated at the micron, sub-micron and nanoscale scales. As the molecular building blocks (proteins, lipids, carbohydrates and nucleic acids) operate at the nanoscale, interactions at these

dimensions mediate how bone cells adhere, proliferate and differentiate[92,93].

Surface topography can be modified by a number of techniques, depending on the desired application; to either promote cell adhesion or if required, to reduce it. The features created can lead to changes in the focal adhesions to which cells adhere. The provision of sub-micron to nanoscale topography has been the focus of many research studies over the last decade, specifically studies involving the ability of roughened surfaces to direct the lineage of MSCs[90,94–96] towards that of an osteoblast phenotype. It has been found that, in particular, nanoscale surfaces play a crucial role in the regulation of cell survival, proliferation and differentiation[97]. Titanium surface roughness has been acknowledged as a significant parameter for influencing osteointegration [26,27,98–103]. Cell response to nanotopographical cues has been investigated in a range of cell types including osteoblasts, osteoclasts, fibroblasts, endothelial and epithelial cells[83,104–106]. It is recognised that titanium topography can influence the differentiation of osteoblast cells through several mechanisms, including the modulation of growth factor pathways[107,108]. Dalby *et al.*[27] showed that a nanoscale disordered titanium topography could stimulate hMSCs to produce bone mineral *in vitro* without the addition of osteogenic supplements to the culture media. It was found that highly ordered nanotopographies generated minor cellular adhesions and osteoblastic differentiation whereas cells on more offset orientated nanotopographies showed a morphology more consistent to that of osteoblasts. Further investigations found that nanovibrational stimulation (nanokicking) of the cells on these offset topographies in culture provided for an elevated cell response[90]. Boyan *et al.*[109] described how titanium surface roughness leads to increased surface area which in turn can affect cell morphology. This increased surface area due to roughening has also been found to increase osteoblast differentiation. Gittens *et al.*[110] sandblasted and acid etched titanium surfaces to create a roughened surface onto which they cultured MG-63 cells. These surfaces were found to illicit a positive cell response and increased ALP expression. Research also suggests that porous and roughened titanium surfaces offer beneficial properties for implant fixation and subsequent long term stability[111,112].

Minagar *et al.*[113], also indicate that a high surface area with spacing between the nanofeatures, such as nanotubes, offers beneficial conditions for cells to interact with. Titania nanotubes have been synthesised in several ways, each with conflicting opinions on the best diameter size onto which cells best respond to[114–117]. For example, McLister[29] looked at various processing times and voltages for creating TiNT and found that the optimal nanotube diameter size was in the range of 30 nm to 50 nm for the desired cellular response. This range allowed for the best cell focal adhesions during *in vitro* testing.

Mutreja *et al.*[31] synthesised nanotubes with pore sizes of 30 ± 7.5 nm and found this to be not only sufficient in slowing and controlling the release of a CaP thin film, but also exhibiting positive influence when tested *in vitro*. However, Oh *et al.*[118] found that titanium nanotubes with a diameter of 70 nm provided the best stimulation for MC3T3-E1 adhesion and proliferation. Skoog *et al.*[119] discuss how both chemical etching and electrochemical methods affect the thickness of the natural oxide layer on the titanium surface, which can lead to improved surface roughness and chemistry.

Although titanium topography can induce an enhanced cell respond, the material still has poor bioactive properties, and so is combined with other biomaterials, such as calcium phosphate ceramics, most commonly in the form of hydroxyapatite (HA) coatings, to improve the bioactivity and further promote osseointegration of the implant[108,120].

2.6 Calcium Phosphate Coatings

Calcium phosphate (CaP) materials are a family of bioceramics that are known to exhibit both biocompatibility and in some cases bioactivity, that include osteoconductive and osseointegrative properties[33]. However, many bioceramics have poor bulk mechanical properties and so although they can be strong, they can also be brittle in nature. To overcome their poor load bearing capability, CaPs have been used as a thin film coating on stronger material substrates and implants (Table 2.2).

Amorphous calcium phosphates (ACaPs) are typically the first solid phase that occurs after the mixing of calcium (Ca^{2+}) and phosphate (PO_4^{3-}) ions. These materials are generally thermodynamically unstable and can transform to a crystalline form of CaP, commonly referred to as apatite, if no stabilisers or dry storage conditions are used in the reaction[121]. Tao *et al.*[122] found that ACaPs seem to play an important part in bone formation and have a role in the assembly of HA particles into collagen to provide an ordered structure. However, there is a lack of data to substantially back up their function in this regard, as well as uncertainty around the true nature of the ACaP phases that occur in new mineralised bone tissue. What is clear, is that the increased dissolution of ACaPs and their subsequent resorption leads to enhanced bioactivity[123]. Kilpadi *et al.*[124] predicted that hydroxyapatite, a major form of CaP, would bind to proteins more efficiently when compared to that of titanium. Their studies went on to show that fibronectin, vitronectin and osteoblast precursor cells were all integrated in higher amounts in the presence of hydroxyapatite than compared to that on the uncoated metal. This supports the knowledge that metal implants, when coated with a bioceramic layer,

have improved integration within the implant site and associated reduced loosening *in vivo*.

The sintering of CaP layers is common in order to slow degradation and this has been found to be the case in a number of projects that report little resorption of sintered CaP coatings *in vivo*[125]. Various means to control the rate of dissolution of CaP have been explored[126,127]. Diez-Escudero e*t al.*[128] found that the incorporation of carbonate ions into calcium phosphate material decreased the rate of coating degradation rather than increasing it as might be expected. Yokota *et al.*[129] investigated the dissolution of as-deposited sputtered CaP coatings on titanium screws *in vivo*. They found that after 1-week *in vivo* the thin film was still present on the surface. However, it was found to be absent at the 2- and 4-week evaluation time points. Overall, the published data suggests that sputtered ACaP thin films can have a decreased solubility than expected when placed *in vivo* depending on the conditions employed. Factors which can influence the dissolution of CaP thin films include the crystallinity of the coating (i.e.amorphous), the chemical composition of the CaP, porosity of the surface and the surface area present[130,131].

2.6.1 Hydroxyapatite

Calcium phosphates are commonly applied to a range of orthopaedic applications in the form of synthetic hydroxyapatite (HA) due to its inherent bioactivity being able to induce bone repair and regeneration[35,132–135]. Hydroxyapatite has the chemical formula of $Ca_{10}(PO_4)_3(OH)_2$ and is structurally and chemically similar to that of the main bioapatite component found in native bone tissue. Biological apatite (bioapatite) is non-stoichiometric and nanocrystalline, with rod-like shaped crystals containing several CaP phases as well as other ions[47]. By contrast, chemically pure synthesised HA has a stoichiometric calcium to phosphate (Ca/P) molar ratio of 1.67 and has been found to be osteoconductive. Due to these desirable properties, HA is used in its bulk for orthopaedic applications such as bone grafts and fillers. However, as indicated previously, bioceramics such as HA have limited mechanical strength, particularly under tensile loading and so are not used as load bearing implants. Hence, it has been developed for use as a bioactive/osteoconductive coating on stronger metal/metal alloy implant materials. Whereas, HA can have a low rate of dissolution in the bulk form, an amorphous coating it is much more soluble which has a significant influence on the attendant *in vivo* biological response. Ohgushi *et al.*[136] showed that bone marrow cells embedded in porous HA ceramic materials could induce bone nodule formation just three weeks after

implantation. This research also showed the vast potential for the use of HA materials in the application of bone regeneration. A subsequent study where the HA substrates were subcutaneously implanted into rats, with or without marrow cells present on the substrate indicated that after 4 weeks, bone formation was present in the substrates were marrow cells were present and there was no bone formed on any of the substrates were marrow cells were absent [137].

As mentioned previously, biological apatite has a variable stoichiometry compared to that of chemically synthesised apatites, which is due in the main to ionic substitutions and a reduction in the number of Ca^{2+} ions in the natural lattice. Even though the Ca/P ratio in natural bone is 1.54, i.e. calcium deficient, the desirable Ca/P ratio in synthetic HA is typically 1.67. However, this can decrease to around 1.3 without disrupting the crystallographic symmetry of the lattice. The ionic substitutions of trace elements into the natural apatite lattice include, but are not limited to, sodium (Na^{+}), magnesium (Mg^{2+}), strontium (Sr^{2+}), zinc (Zn^{2+}), fluorine (F^{-}) and carbonate (CO_3^{2-}). Handschin and Stern determined the ion concentrations in human bone and found a variance in ion levels[138]. They concluded that ions such as Na^{+} and CO_3^{2-} increase in concentration with increasing age, whereas potassium (K^{+}), chlorine (Cl^{-}) and magnesium (Mg^{2+}) concentrations decrease. Figure 2.3 depicts the hexagonal HA unit cell arranged along the *c*-axis. The *a* and *b* planes are positively charged and therefore can attract negatively charged ions, whilst the *c* plane is negative, thus attracting positively charge ions[139]. In the pure form, synthetic HA has only Ca^{2+} ions present, however, some of these can undergo ionic substitution such that various analogues of HA can be prepared that have properties closer to that of the natural apatite in bone.

2.6.2 Substituted Apatites

Ionic substitutions into the HA lattice can be used to alter and manipulate core properties such as solubility, hardness, thermal and optical stability[140]. Moreover, such modifications of these properties can cause major changes in the biological response and performance of the substituted hydroxyapatites. By substituting ions into the HA, it is intended that the complex chemistry of organic human bone tissue can be somewhat mimicked, thereby improving the biological function of the material[23]. The relative ease of ionic substitution during the solid stage reactions used for their preparation provides an opportunity for use in a wide range of biomedical applications, including drug delivery systems, 3D scaffolds, bioactive coatings or as filler for biocomposites. The three common types of bonds observed in any atomic structure are: ionic bonding, covalent

bonding or metallic. In the case of ionic substitutions on HA, ionic bonding is the most important. As mentioned in the previous section, the *a* and *b* planes of pure HA attract negatively charge molecules and so it is here that anionic substitutions most readily occur, with a negatively charged ion usually replacing a hydroxyl (OH^-) group. The negatively charged *c* planes attract positively charged ions, such as Sr^{2+}, Mg^{2+}, Zn^{2+} etc. which replace Ca^{2+} ions in the lattice. The general formula of the resulting substituted CaP systems is $M_{10}(XO_4)_6Y_2$ where M is commonly a bivalent cation (Ca^{2+}) and as such is substituted by another bivalent cation (Sr^{2+}, Mg^{2+}, Zn^{2+}). However, monovalent cations can also substitute here including Na^+, as well as trivalent cations such as Al^{3+}. The XO_4, usually PO_4^{3-} in the case of HA, can be substituted by anionic compounds including VO_4^{3-} , SiO_4^{3-} or CO_3^{2-}. Y is typically a monovalent anion such as F^-, OH^- or Cl^-[141,142].

2.6.3 Cationic Substitutions

Bivalent cationic ions are most commonly used for substitutions in the synthetic HA lattice as they cause no charge imbalance[46]. Magnesium ions (Mg^{2+}) play a vital role in the metabolism of bone and have the ability to influence activity of both osteoblasts and osteoclasts[143]. Mg^{2+} ion substitutions, at approximately 10 mol%, occur in cartilage and bone tissue at the early stages of osteogenesis, but decrease in concentration with increasing tissue maturity[144]. A shortage of Mg^{2+} in the body can have adverse effects on skeletal metabolism, which can stop bone growth, decrease bone formation as well as bone resorption and this can lead to bone fragility. When substituted into the HA lattice, the parameters of the crystalline structure decrease with increasing Mg^{2+} concentration, due to the smaller ionic radius of Mg^{2+} compared to that of Ca^{2+}. Landi *et al.*[145] synthesised a MgHA apatite with 5.7 mol% Mg and found that it was similar to bioapatite in terms of morphology and crystallinity. The synthesised apatite showed no cytotoxicity, carcinogenicity or genotoxicity when *in vivo* tests were carried out.

Strontium (Sr) can be found in native bone tissue and is mainly concentrated in areas of a high metabolic turnover. Even at low concentrations, Sr^{2+} can influence both osteoblast and osteoclast proliferation. Strontium has been used to treat osteoporosis and to decrease the incidence of fractures in osteoporotic patients. The clinical drug, commonly known as ‘strontium ranelate’, has been found to inhibit osteoclast activity whilst stimulating the differentiation of osteoblastic cells[64,146]. This dual effect has shown to reduce fragility and frequency of fractures in patients suffering from osteoporosis. When introduced to the HA lattice, as illustrated in Figure 2.3, it can improve the bioactivity of the material by suppressing the tricalcium phosphate (TCP)

formation [147-149]. It has been shown to promote significant osteoblast activity, including differentiation at relatively low concentrations (3-7 %)[37]. However, the Sr^{2+} ion is larger than Ca^{2+} and so can cause disruption in the lattice, leading to an increase in the solubility of the apatite. Zinc (Zn) is present in all biological tissue but is most concentrated in bone. Like the other bivalent cations, Zn^{2+} can inhibit osteoclast differentiation while still promoting the activity of osteoblasts, leading to an increase in bone formation, thereby limiting the bone resorption process. In addition, Zn^{2+} has been shown to have antimicrobial properties[150] as well as improving the wound healing process post-surgery. Guo *et al.*[36] used a process of phosphate chemical conversion to incorporate Zn into a calcium phosphate material. Their results suggest that the Zn^{2+} present has the capability to inhibit bacterial growth, with both gram negative and gram positive being affected. A deficiency of Zn^{2+} in the body can lead to reduced bone density which then leads to an increased risk of fracture. In a similar way to Mg^{2+}, Zn^{2+} has a smaller ionic radius than Ca^{2+} [151].

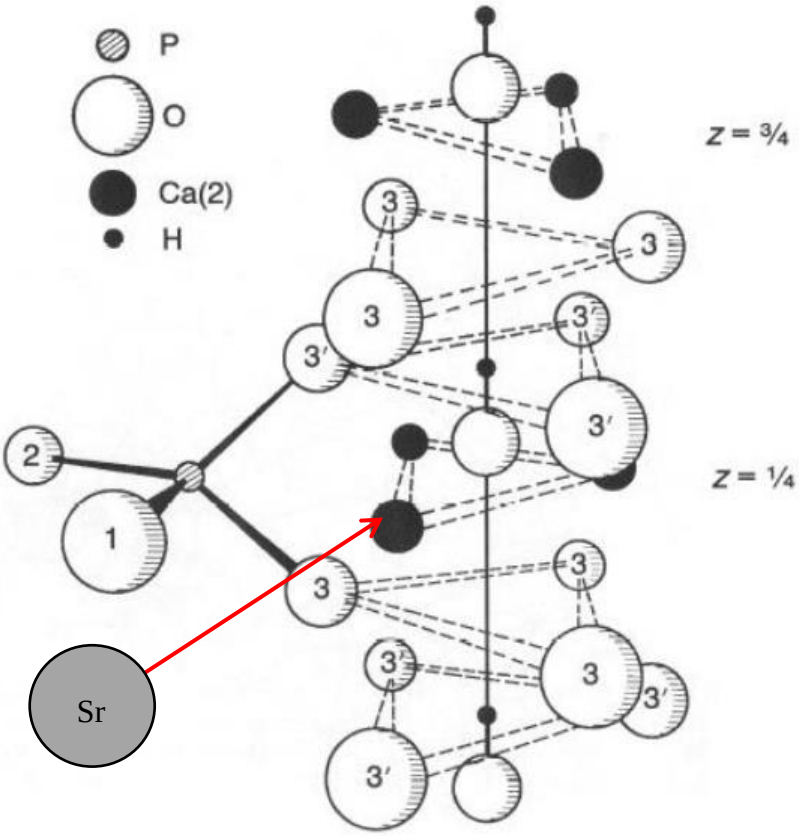

Figure 2.3 Ionic arrangement of atoms in the HA lattice around the c axis demonstrating the substitution of a larger strontium ion for the smaller calcium ion

2.6.4 Anionic Substitutions

Monovalent anionic substitutions usually occur in the Y site ($M_{10}(XO_4)_6Y_2$) as previously discussed[152,153]. Fluoride ions (F^-) can replace OH^- in the HA lattice with the resulting fluoroapatite showing significant corrosion resistance when in contact with bodily fluids and is also a remedial agent used in the treatment of osteoporosis. Several studies have investigated how various F^- concentrations affect cell culture with a high F^- concentration producing a low surface potential, which is known to favour cell attachment. Kim *et al.*[154] explored the effects of fluoride ion substitutions into the HA lattice of a hydroxyapatite/alumina composite. Their study focused on changes to the HA/alumina composite mechanical properties and the inhibition of phase decomposition. They found that the substitution of fluoride ions (F^-) for the hydroxyl group (OH^-) caused a suppression in the decomposition of the HA. It has also been found that co-substitution of Mg^{2+} and F^- into HA produced a material with a greater ability to supress decomposition as compared to that of a Ca^{2+} and F^- system, as well as it having improved bulk mechanical properties compared to that of a pure hydroxyapatite/alumina composite. The addition of F^- to the HA lattice has shown in other studies to decrease the solubility of the apatite, as well as increasing the thermal stability[155–157].

2.6.5 Co-Substituted Apatites

Bivalent or trivalent co-substitutions occur at the XO_4 site ($M_{10}(XO_4)_6Y_2$)[152,153] and can be either cationic-cationic, anionic-anionic or cationic-anionic. This range allows for the manufacture of many various apatites with specific tailored properties, depending on the experimental procedure employed. Many co-substitutions are an attempt to balance the lattice charge due to the introduction of ions with less charge whilst others are done on the basis of trying to incorporate desirable bioactive and/or antibacterial properties. Studies carried out by Robinson *et al.*[47] have investigated the combination of Sr^{2+} and Zn^{2+} into co-substituted HA coatings. Here titanium coupons were sputter deposited with a thin film coating created from separate Sr^{2+} and Zn^{2+} substituted HA targets (10 %wt SrHA and 10 %wt ZnHA), before being thermally annealed at 500 ˚C for 2 hours. It was found that the sputtering process produced co-doped Sr^{2+} and Zn^{2+} CaP coatings. Lowry *et al.*[158,159] synthesised a co-substituted nanophase apatite with both Sr^{2+} and Zn^{2+} through the wet precipitation method. In this case, both ions were substituted into the HA lattice at the same time. These co-substituted materials were created with varying ionic concentrations to allow for comparison into any changes apparent in the crystal structure,

as well as mechanical properties. The synthesis was found to be successful and a preliminary *in vitro* evaluation confirmed the material to be biocompatible.

2.7 Cell Responses to Titanium and CaP Surfaces

As highlighted earlier, cellular responses to biomaterials have been found to be highly influenced by both the chemical and mechanical properties of the surface[119]. Titanium and CaP materials have been widely used separately and in combination for orthopaedic applications where the interactions with cells is critical. In general, although biocompatible, titanium and its alloys have generally poor bioactive properties and so, as mentioned previously, bioactivity can be added to the substrate/implant in the form of a CaP coating, typically HA. The addition of HA to Ti implants has shown to improve the fixation of the implant to bone[44]. For example, McCafferty[160] found that the combination of titanium with a sputtered Ca-P thin film coating showed increased levels of cellular attachment, proliferation and differentiation of MSCs when compared to control surfaces without the coatings. In such applications, the effect of CaP coating solubility on cell response is a significant consideration and a number of methods have been used to control its dissolution *in vitro* and *in vivo*. Whereas, post-deposition processing provides a means to control CaP coating solubility by changing its phase composition, alternative methods for the as-deposited CaP are more limited. A significant body of work has addressed the role of substrate topography in this regard wherein the CaP is partially dissolved with residual amount of the material remaining due to physical keying to surface features. For example, titanium nanotubes have been found to allow more control over the dissolution rate of amorphous CaP, as the nanoscale topography retains some of the CaP, allowing for a slower release rate. Cell responses to these surfaces have shown positive results towards stimulation and differentiation. McLister[29] found that hMSCs responded to both of the stimuli provided in combination by the titanium nanotubes and the amorphous CaP coating. The hMSCs that had been cultured in osteogenic media (OM) showed higher levels of late stage osteogenic markers compared to those hMSCs that were cultured in normal media.

In this regard, Mingar *et al.*[161] state that the response of bone cells is dependant not only on the topography of a surface, but the physiochemistry, mechanics and electronics of the surface as a whole. In another study, anodisation of the titanium can lead the surface to become negatively charged due to the adsorption of anions from the electrolyte used. Mutreja *et al.*[31] created titanium nanotubes for the aim of slowing CaP thin film dissolution. Here, it was found that the titania nanotubes prolonged the

dissolution of the thin film over a long-term study, whilst the thin film on the smooth titanium surface had dissolved after 48 hrs. It was concluded that the pore size and length of these nanotubes affected not only the rate of CaP dissolution, but the subsequent attendant cell behaviour. The various studies addressing the role of surface roughness and attendant topography build on Dalby's work[27,162], as well as subsequent studies[90,102,163,164], that have shown that the underlying morphology of a biomaterial surface or implant is significantly influential to cells. In this regard, the morphology of a titanium surface before the deposition of any form of CaP thin film coating is important to ensure that both the chemical and topographical properties work together in order to give a positive influence on the cells when placed in cell culture.

2.*7.1 Dissolution Behaviour of CaP Coatings*

The use of CaP materials in orthopaedic and dental applications has been widely attributed to the chemical properties of the CaP materials that can evoke a similar biological response to that of natural bioapatite which would be generated for bone remodelling in the body. They have been shown to enhance the stimulation of new bone formation, as well as encourage bone resorption. These interactions with the surface and the surrounding environment at the cellular level are important to influence interactions including ionic exchanges and cellular activity.

Dissolution studies allow an insight into how the material, and the subsequent thin film coating, will behave when placed in aqueous solution during future *in vitro* and/or *in vivo* screening. Literature has shown how the dissolution of CaP coatings on surfaces is dependent on several factors, including the roughness of the surface, the surface chemistry and surface charge. Typically, CaP coatings will dissolve almost instantly on flat surfaces (i.e. glass substrates) when placed in aqueous solution. However, there are several other factors which have an influence on how CaP coatings will behave when placed in aqueous solution. These factors include but are not limited to solution composition, pH and temperature. Dissolution studies of CaP coatings have been carried out in varying forms of aqueous media, with the type of solution dependant on the desired application of the CaP coating. Commonly used aqueous solutions include simulated body fluid, phosphate buffered saline or cell media.

Formation of an electric bilayer commonly occurs in dissolution of CaP based materials[165,166]. When the biomaterial is placed in aqueous solution, a salt electric double layer can form on the surface of the biomaterial when partially dissolved ions form two parallel layers of charge (Figure 2.4). This typically occurs when there is a high salt

concentration which leads to a high excess of charged ions. The first layer is adsorbed onto the sample surface due to ongoing chemical interactions in the surrounding environment with the sample. This layer then attracts oppositely charged ions, thus creating the double layer of charge. This bilayer can form a film across the surface of the sample which can prevent further dissolution of a coating on the surface of the biomaterial.

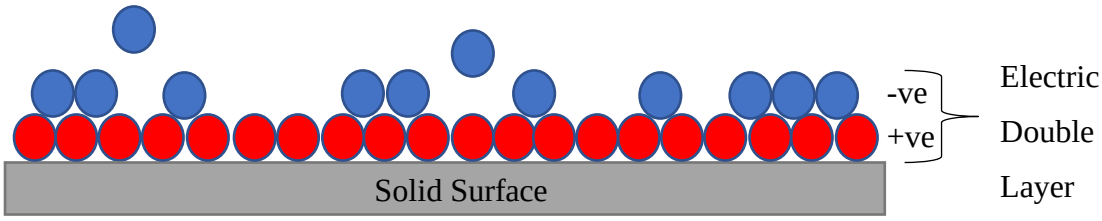

Figure 2.4 Schematic of electric double layer formation on a solid surface when placed in aqueous solution

Protein adsorption commonly occurs in aqueous solutions that have been designed to mimic the *in vivo* conditions of the human body, such as cell culture media which commonly contains foetal bovine serum (FBS). High salt concentrations in the environment can further promote the precipitation of proteins. Surface energy, polarity charge and morphology also have an influence the adsorption of proteins onto the sample surface. Particular ions can promote protein precipitation and are referred to as kosmotropes (SO_4^{2-}, Mg^{2+} and Ca^{2+}) whilst ions that have been seen to slow the precipitation of proteins are known as chaotropes (ClO_4^-, SCN^- and NH_4^+). Notably here, calcium ions are kosmotropes, and so actively promote protein adsorption. This incorporation of proteins into the CaP can affect the dissolution kinetics depending on the protein charge and concentration[167,168]. As mentioned previously, cell interactions with biomaterials are generally influenced by the biomaterials surface topography, chemistry and physics, as well as the rate of protein adhesion to the surface. The rate of dissolution of the CaP can have an effect on the cellular proliferation and maturation[169–171]. Cell migration and adhesion are typically mediated through integrins (transmembrane proteins), including fibronectin, which ensure that the cytoskeleton of the cell is attached to the ECM[172,173]. Therefore, adhesion of proteins to the surface is important in the mediation of cellular attachment. As mentioned in 2.6.1, HA coatings have been found to

increase this integration of integrins, including fibronectin, vitronectin and osteoblast precursors[124,174].

2.8 Titanium Surface Modification and CaP Coating Techniques

As indicated above, it is common practice in the use of biomaterials intended for load bearing orthopaedic implants to combine materials with high strength with those with chemical and physical characteristics that can direct bone cell response to achieve optimum qualities for the desired application. This can be through the creation of surface micro- and nanoscale topographies, and/or the addition of thin film coatings. There are an abundant number of means to augment surface topography and chemistry, with some processes being favoured over others. These include, but are not limited to, physical vapour deposition (PVD)[24,48,175], plasma spraying[25,34,176], laser etching[177–179], electrochemical anodisation[29,115,180,181], radio frequency (RF) magnetron sputtering[30,45,47,182], sol-gel deposition[41,183] and chemical etching[19,20,184].

This thesis will address a number of methods for augmenting both the underlying titanium substrate and subsequent CaP coating. Chemically etched titanium (eTi) surfaces will be produced alongside sputtered polycrystalline titanium (PolyTi) using radio frequency (RF) magnetron sputtering, as well as titanium nanotubes (TiNT) through electrochemical anodisation (ECA). Sputter deposition of CaP thin film coatings will utilise RF magnetron sputtering to coat the titanium substrates with CaP thin film coatings.

2.8.1 Chemical Etching

Chemical etching is a relatively cheap and simple processing method by which varying topographies can be added to a substrate to increase the roughness of the surface. In many ways, it is similar to ECA; however, no current is applied in this instance. Corrosive chemicals, including strong acids, are used to etch the surface oxide, thus creating pitting and other topographies across the surface of the material. Aggressive chemical etching can be used to completely remove the outer oxide layer and clean the material surface before the controlled growth of a new oxide or the addition of a secondary material as a coating[111,130,185–187]. However, by careful use of properties of the etchant solution and time, a pronounced microstructure can be created on the surface of many metallic biomaterials, including titanium. For example, Carradò *et al.*[85] etched titanium disks, as well as commercial dental implants, in Kroll solution, a mixture of nitric acid (HNO_3) and hydrogen fluoride (HF) in water. This removed the oxide layers, after which, a sodium titanate layer was added on the surface through submersion in sodium hydroxide

(NaOH). They found that the etched surfaces showed improved osteoconduction and osteointegration than that of the control samples. This mixture of HF and HNO_3 is also referred to as 'pickling' of the titanium surface. Schneiker *et al.*[188] have reviewed the factors that influence the rate of 'pickling' (etching) including acid concentration, temperature and concentration of free HF in the solution. They suggest that the use of hydrogen peroxide (H_2O_2) to etch the surface of metal produces a high surface area 'sponge-like' pitting topography[101]. Freitas *et al.*[189] discuss how etching using hydrochloric acid (HCL), H_2SO_4 and phosphoric acid (H_3PO_4) can modify the titanium surface and create pitting topography across the surface. Further discussion considers how chemical etching provides a feasible and relatively straight forward method of achieving a reproducible morphology, which increases the surface area and roughness and exhibits a low contaminant rate. This process is also known to thicken the natural biocompatible titanium oxide (TiO_2) layer.

For any form of chemical etching the submersion time is also extremely important in determining the degree to which the surface will undergo etching to create a specific surface morphology. It is important to ensure no volatile chemicals become bonded to the surfaces in any concentration that could have detrimental effects on cellular response when placed in culture. To the authors knowledge, the chemical etching of titanium using piranha solution at the chosen timepoints employed in this thesis have not been investigated previously. Therefore, surface and chemical characterisation of these substrates will provide an understanding of the physical and chemical attributes that this particular chemical etching imparts onto the titanium surface.

2.8.2 Radio Frequency Magnetron Sputtering

Radio frequency (RF) magnetron sputtering is a well-established thin film coating deposition method that produces a uniform thin film coating, with a controllable deposition rate[30,190]. Although not used commercially for HA coating of orthopaedic implants due to the dominance of plasma spraying, it does offer a unique opportunity in other clinical areas where control of coating dissolution has significant benefits. It accommodates co-deposition of multiple target materials with an enhanced interfacial adhesion between the substrate and the coating[45,47,182]. In essence, a target material is bombarded by high energy gaseous ions (typically argon) that are created in a high vacuum plasma. These ions are directed to the target and cause atoms from the material to be ejected and sputtered upwards onto the chosen substrate, forming a thin film coating. The use of a radio frequency (RF) power supply to create the plasma avoids a build-up of

electrical charge on the source and target assembly, which if present can cause inefficient sputtering and damage to the target. The RF frequency most commonly employed in sputter deposition is 13.56 MHz[129]. As presented in Figure 2.5, a magnetron source is preferred in RF sputtering as the magnetic field lines confine the electrons in helical paths within the plasma such that there are more collisions with the gaseous (argon) atoms leading to an increased flux of ions that subsequently cause more sputtered particles. RF magnetron sputtering can be used for metals, semiconductors and insulators[191]. This sputtering process is carried out under vacuum conditions, as this pressure enhances the ionisation rate of the argon gas, leading to an increased deposition rate.

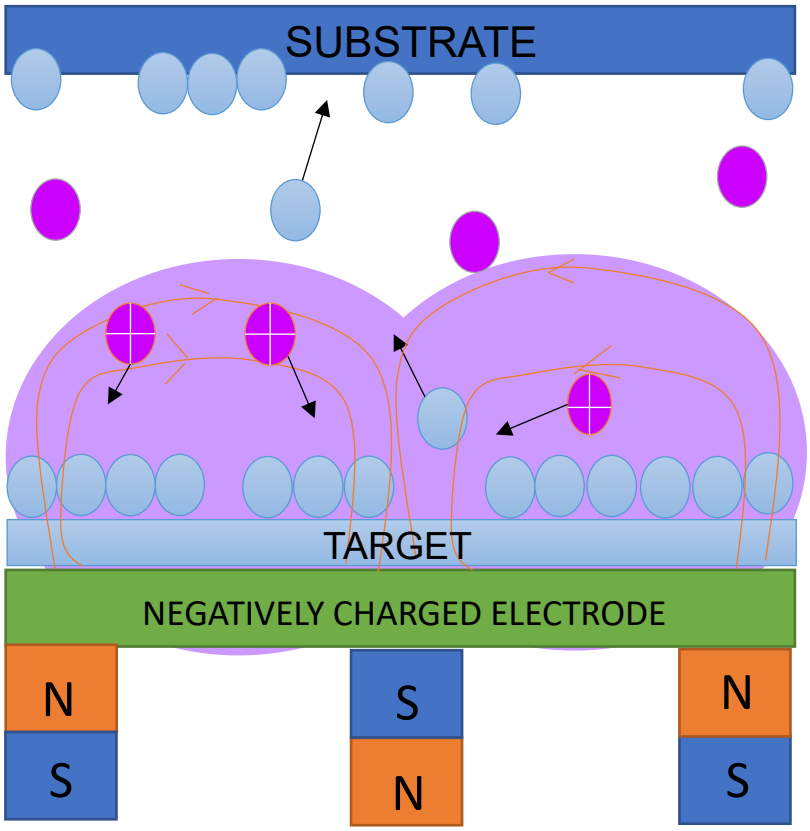

Figure 2.5 Diagram showing the basic components of a RF magnetron sputtering system, with the target particles being sputtered from the target and moving in line of sight to the substrate where they form a coating. The role of the magnetic field in ensuring more collisions take place leading to formation of incident ions and enhanced sputter rates is also illustrated

2.8.3 Electrochemical Anodisation

Electrochemical anodisation (ECA) is an electrolytic passivation process which is commonly used to increase the thickness of a natural oxide layer present on metal surfaces. Anodising increases resistance to corrosion and wear, and is a familiar processing method used in industry to enhance the properties and service lifetime of metals[192–194]. This surface processing technique has also been utilised for orthopaedic biomaterials, in the presence of fluoride, to produce a porous surface composed of self-organised nanotubes (section 2.5). Anodising changes the microscopic texture of the surface, as well as altering the crystal structure of the metal lattice near the surface. An electrolyte is the electrical conducting solution into which the metal surface to be anodised is submerged while the metal to be processed acts as the anode, which is then connected in an electrochemical circuit to a cathode, typically platinum. The electrochemical anodisation of titanium, can create a nanotubular surface topography with features ranging from 20 nm to 100 nm in size, dependent on processing time and voltage charge[195]. These varying sizes have shown to be important in directing cellular response *in vitro*. In this regard, fluoride ions are commonly used in the ECA process for self-organisation, usually in the form of ammonium fluoride (NH_4F) or hydrogen fluoride (HF)[21,22,196,197]. These solutions can be diluted with an organic solution, including but not limited to, ethylene glycol (EG), or in acid such as phosphoric acid (H_3PO_4). This use of fluoride in the anodisation process does mean that fluoride ions can bond to the sample surface during the passivation process and their presence when processing biomaterials needs to be monitored as fluoride at low concentrations can be beneficial to cells[153,198], however, at a higher concentrations it can become cytotoxic[199].

Chapter 3: Materials and Methods

This chapter describes the processes and techniques employed to prepare the pristine titanium control substrates, chemically etched titanium surface morphology and the comparator radio frequency (RF) magnetron sputtered polycrystalline titanium samples. The methodology for RF magnetron sputter deposition of thin film calcium phosphate (CaP) coatings (hydroxyapatite (HA) or strontium substituted hydroxyapatite (SrHA)) onto these various surfaces is also described. Characterisation of the various substrates has been carried out before and after CaP thin film coating (HA or SrHA) using a range of surface analysis and imaging techniques as described herein. The effects that exposure to cell culture media at 37 °C has on the as-deposited CaP (HA and SrHA) coatings has also been determined using specific surface analysis and imaging techniques. An *in vitro* evaluation of U-2 OS cell response to the uncoated and coated surfaces has been undertaken using biomarker assays, nuclei staining, adhered cell imaging and staining of mineralised cells.

3.1 Substrate Preparation and Processing

Titanium coupons, 15 mm x 15 mm, were cut from a medical grade titanium foil sheet (99.7 % trace metal purity, 0.25 mm, Sigma Aldrich, UK). One side of these coupons were abraded with silicon carbide paper, starting with p800, p1200 as an intermediate step and p4000 to finish. Coupons were sonicated twice in isopropan-2-ol (IPA) for 15 minutes (mins) with the solvent changed between the two cycles, before being sonicated for a further 15 mins in deionised water (dH_2O). All coupons were then dried using a lint free cloth and stored in a desiccator at room temperature until use.

3.1.1 Piranha Chemical Etching

Chemical etching of titanium coupons was achieved by exposure to piranha solution, a mixture of sulfuric acid (H_2SO_4) and hydrogen peroxide (H_2O_2), in a ratio of 3:1, respectively. The previously cleaned titanium were sprayed with a nitrogen gun to remove any residual debris before being submerged in piranha solution for either 3 hrs or 24 hrs. Immediately after exposure, the coupons were triple rinsed in dH_2O before being dried in air and stored in a glass petri dish and placed within a desiccator at room temperature until required.

3.1.2 Radio Frequency Sputtering from Titanium Targets

RF magnetron sputtering from pure titanium targets was utilised to produce a polycrystalline titanium layer (PolyTi) on the cleaned titanium. Sputtering was carried out using a custom built Lesker system (Kurt. J. Lesker Ltd, UK) which has been described in detail in several publications[29–31,45,47,182,200]. The system comprises a high vacuum chamber equipped with an array of three 76 mm Torus™ sputtering sources fixed to a stainless-steel base plate. Substrates to be coated were attached to a rotatable holder that is situated above the sputtering sources, with the distance between the sources and samples changeable by raising the base plate carrying the sources via a manual vacuum compatible drive assemble. Titanium targets (99.995 % pure, Kurt J. Lesker Ltd, UK) of dimensions 76 mm wide and 9.5 mm thick were placed in two of the three Torus™ sources with the third left blank. To obtain the polycrystalline titanium surface, clean titanium coupons were placed onto the rotating substrate holder above the plate holding the sources equipped with the titanium targets and the so-called 'throw distance' between them set to 100 mm. The system was then pumped down via a dedicated rotary vane and turbo pump assembly to a base pressure of 5×10^{-6} mbar as measured via a filamentary pressure gauge in the vacuum chamber. Dry argon (99.98 %, BOC, UK) was then introduced into the processing chamber via a high precision flow valve, to attain a reduced pressure of 5×10^{-3} mbar. The RF power supplies to sources 1 and 2 were now engaged to create a plasma above each of these sources. A computer-controlled air capacitor matching network that is attached to each source power supply was used to minimise any reflected power from the target surface and thereby optimise sputter rate. The main parameters for titanium sputtering are detailed in Table 3.1 with two different power settings used (250 W and 400 W) to create the polycrystalline titanium coatings on the titanium coupons with all of the other settings kept at the values indicated. During each sputtering run, the power supply was ramped up to the required value starting at a value of 70 W and increasing it by 10 W per minute to 250 W or 400 W, respectively. Substrates were exposed for 2 hrs.

Table 3.1 Sputtering parameters for deposition of polycrystalline titanium thin films

Target Type	Starting Wattage (W)	Final Wattage (W)	Ramp (W/min)	Chamber Pressure (mbar)	Sputter time (hrs)
Titanium	70	250	10	5×10^{-5}	2
Titanium	70	400	10	5×10^{-5}	2

3.1.3 High Temperature Annealing

Thermal processing of pristine titanium coupons and sputter deposited polycrystalline titanium films on these coupons was performed to allow for a comparison between the surface properties of annealed and unannealed samples. In this way, an investigation of any significant differences in the sample surfaces, both chemically and physically, was undertaken to determine if an extra annealing step in the substrate processing was warranted. Samples of titanium and polycrystalline titanium were annealed using a Lenton 3216 furnace (AWF 12/5) (Lenton, UK). A starting temperature of 65 ˚C was used and the temperature then ramped up at 5 ˚C per minute, to reach a maximum temperature of 500 ˚C. Samples were then exposed to a dwell time of 3 hours (hrs) (180 mins) at 500 ˚C before ramping down to 65 ˚C at 5 ˚C per min. Samples were then allowed to reach room temperature before being removed from the furnace and stored in a desiccator at room temperature until required.

3.1.4 Electrochemical Anodisation

Electrochemical anodisation was utilised to create titania nanotubes on the cleaned titanium coupon surface. A purpose-built perspex cell (Figure 3.1) was used for this processing method, using parameters previously employed by McLister[29]. The chamber holds 100 ml of the electrolyte solution with a cover plate that provides for a 0.78 cm^2 contact areas for the solution on the titanium coupon surface. The electrolyte used here comprised 0.3 % weight (%wt) ammonium fluoride (NH_4F) (Sigma Aldrich, UK) in ethylene glycol (EG) which was then made up to a 3 %wt dH_2O solution[29,31,115].

A platinum disk (99.95 %, Goodfellow, UK) was used as the cathode with the titanium coupon acting as the anode. Both electrodes were attached to copper backing plates within the cell which were then connected to a power supply. To anodise the exposed titanium coupon surface, a current of 30 volts (V) was applied for 2 hrs, after which, samples were rinsed twice in dH_2O and stored in a desiccator at room temperature until required.

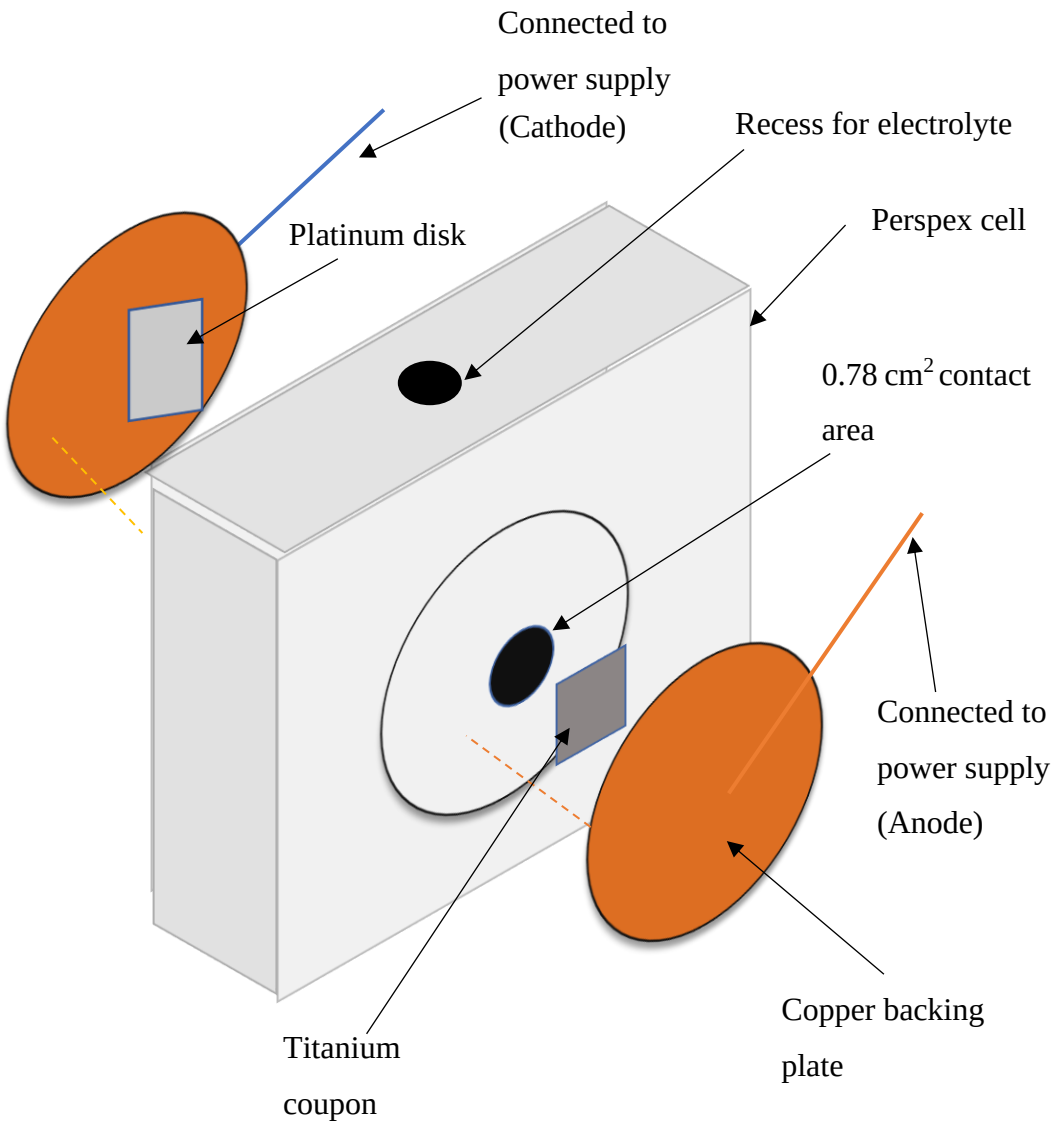

Figure 3.1 Schematic diagram of purpose-built perspex cell for titanium electrochemical anodisation

3.2 RF Magnetron Sputtering of Calcium Phosphate Thin Films onto Titanium Substrates

Radio frequency (RF) magnetron sputtering was utilised here for several reasons. CaP material targets (HA or SrHA) are naturally electrically insulating and so direct current (DC) sputtering cannot be used due to build-up of charge at the target surface, distorting the process[42,191,201]. RF magnetron sputtering eliminates this build-up of charge across the target material, whilst the magnetic field ensures that more successful collisions occur by guiding electrons back into the central region of the plasma where they create ions. In the case of sputtering from HA and SrHA targets, this leads to a conformal thin film with some chemical bonding and mechanical interlocking occurring when the target material is deposited onto the substrate surface at high energy[30,45,182]. Hence, it was hypothesised herein that RF magnetron sputtering would allow for homogeneous CaP thin films with HA or SrHA characteristics to be deposited onto the various substrate surfaces in a way that yields a Ca/P ratio similar to that of the target material (1.67)[202].

Commercially sourced HA (Captol R, Plasma Biotal Ltd, UK) and 13 % SrHA (HIMED, NY, USA) were used to create sputter targets via a dry pressing method. Each target was made from 12 g of powder by placing it into the recessed area of a copper trough backing plate, as shown in (Figure 3.2 (a)). A stainless-steel die barrel (Figure 3.2 (b)) was then placed on top and dry pressed in a uniaxial direction using a manual hydraulic press (Specac, UK) operating with a load of 3 tonnes for 1 min. The resulting 76 mm diameter x 4 mm deep targets were stored in a dry oven at 80 °C until use.

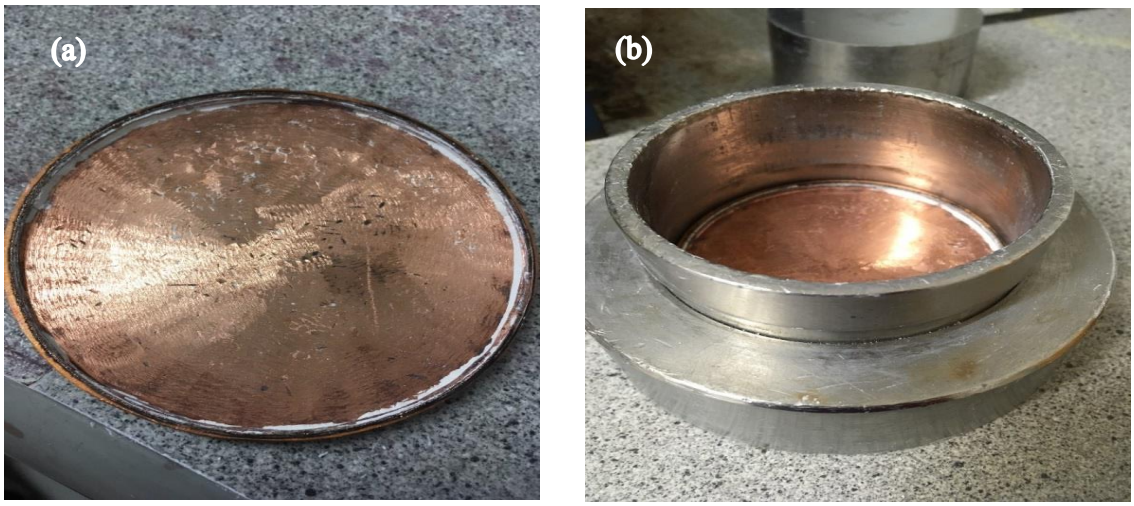

Figure 3.2 (a) Copper backing plate for apatite powder targets and (b) the copper backing plate placed into the stainless-steel barrel die

The dry pressed HA or SrHA targets and recessed backing plates were placed into two of the three Torus™ sources (Kurt J. Lesker Ltd, UK) in the high vacuum chamber with the third left blank. Batches of the various substrates to be coated were placed on the rotating substrate holder located above the sources and the throw distance set to 100 mm. The system was then pumped down via the dedicated rotary vane and turbo pump assembly to a base pressure of 5 $x10^{-6}$ mbar as measured via a filamentary pressure gauge in the vacuum chamber. Dry argon (99.98 %, BOC, UK) was then introduced into the processing chamber via a high precision flow valve to attain a reduced pressure of 5 $x10^{-3}$ mbar. The RF power supplies to sources 1 and 2 were then operated to create a plasma above each of the sources. The computer-controlled air capacitor matching network for each source power supply was used to minimise any reflected power from the target surface and thereby optimise sputter rate. The main parameters from both HA and SrHA targets are detailed in Table 3.2. A power setting of 150 W was used in all cases to create coatings on the various substrates with all of the other settings, as indicated. During each sputtering run, the power supply was ramped up to the required value starting at a value of 50 W and increasing it by 5 W per minute to 150 W. Substrates were exposed for 5 hrs.

Table 3.2 Sputtering parameters for the deposition of hydroxyapatite (HA) and strontium substituted hydroxyapatite (SrHA) thin films

Target Type	Starting Wattage (W)	Final Wattage (W)	Ramp (W/min)	Chamber Pressure (mbar)	Sputter time (hrs)
Hydroxyapatite	50	150	5	5 $x10^{-5}$	5
Strontium Substituted Hydroxyapatite	50	150	5	5 $x10^{-5}$	5

3.3 Physical and Chemical Characterisation

All samples were characterised, before and after apatite coating with CaP thin films (HA and SrHA), using a range of surface analytical techniques to determine their respective surface chemistry and topography

3.3.1 X-ray Photon Spectroscopy

X-ray photoelectron spectroscopy (XPS) provides details of the chemical and elemental composition of a materials uppermost surface (<10 nm) at specific points on the sample. XPS analysis was obtained here with a Kratos Axis Ultra spectrometer with Delay Line Detector (Kratos, UK) equipped with a monochromated Alkα x-ray source (photon energy (hv)= 1486.6 electron volts (eV)). The x-ray source was operated with an emission current of 10 milliamps (mA) and an emission voltage of 15 kilovolts (kV). A low energy electron charge neutralisation system (Kratos, UK) was applied to all samples, utilising a filament current of 1.95 amps (A) with the charge balance plate set at a value between 3.3 V and 3.6 V. Wide energy survey scans (WESS) were acquired at 3 sites on each sample, at a pass energy of 160 eV and plotted as binding energy (BE) versus photoelectron intensity in counts per second (cps) in accordance with Equation 3.1 provided below. High resolution spectra were recorded at a pass energy of 40 eV on all samples for titanium (Ti 2p), oxygen (O 1s), calcium (Ca 2p), carbon (C 1s) and phosphorus (P 2p), with the incorporation of the strontium (Sr 3p) and fluorine (F 1s) peaks, as required.

$$\mathbf{BE = KE - hv - \varphi} \qquad \textit{Equation 3.1}$$

Where,

BE is the binding energy of the photoelectron

KE is the kinetic energy of the photoelectron

hv is the x-ray energy

φ is the work function of the instrument, which is measured as a constant

Effects of residual sample charging were addressed by calibrating the calculated binding energy (BE) value for the lowest BE contribution in the C 1s spectral envelope to 284.8 eV[203,204], the accepted value for adventitious carbon on non-polymeric samples.

Based on this numerical correction, the BE position of all other peaks was then corrected accordingly. In order to obtain quantitative data, a linear background was subtracted from each spectral scan and the residual area under the curve calculated. The most intense spectral peaks for each element detected were used to determine their relevant percentage atomic concentration (At. Conc %). Casa XPS software (CasaXPS, UK) was used to carry out peak fitting of the high resolution spectral envelopes using a mixed Gaussian-Lorentzian (GL (30))[203]. The At. Conc. % for each deconvoluted component was then calculated after linear background subtraction, using the area under the curve.

All samples were analysed at n = 3, with three spots analysed per sample, giving n = 9 per sample type. Typical WESS and high-resolution spectra for the particular sample types are presented in the following results chapters, and the averaged At. Conc % (n = 9) with the standard deviation tabled.

3.3.2 X-ray Diffraction

X-ray diffraction (XRD) was performed on the various samples using a Bruker D8 Diffractometer equipped with a Gobel mirror to provide for better focus of the incident x-ray beam. Diffractograms were attained with a copper K-alpha (Cu Kα) x-ray radiation source, at a wavelength (λ) of 1.540 Angstroms (Å). The tube voltage and tube current were 40 kV and 40 mA, respectively. All scans were recorded as 2-theta (2θ) versus intensity (cps) values in the range 20 - 60˚, with the precision Goniometer stepped in increments of 0.05˚ and a detection dwell time of 90 seconds (secs) at each point. Given that these analyses are addressing substrate surfaces and thin film CaP coatings thereon, in order to investigate the present or otherwise crystalline phases, a grazing incidence technique was utilised. Peaks present in the diffractograms collected here have been labelled with the corresponding Miller Index assignments (hkl), according to the database at the International Centre for Diffraction Data (ICDD)[205]. All samples here were tested in n = 3 per sample type.

3.3.3 Scanning Electron Microscopy

Scanning Electron Microscopy (SEM) is widely used to generate high resolution images of the surface topography of a material. Electrons generated by a suitable filamentary or field emission source are focused and accelerated onto the sample surface by an array of apertures, electrical charge plates and/or magnetic field. The kinetic energy of the majority of these electrons is absorbed by the material and cause interactions at an atomic level that generate secondary electrons which level the surface and are detected by a suitable photomultiplier array adjacent to the sample. The intensity of these secondary

electrons is then represented as a grey scale image of the surface microstructure. As required, backscattered electrons can also be detected using a separate detector and given the nature of their interaction with the sample, the images produced can show compositional differences determined by the atomic masses that have caused the backscattering. In this work, SEM was used to examine the surface morphology of various titanium substrates with and without CaP coatings (HA and SrHA) before and after exposure to cell culture media at 37 °C. SEM imaging allowed an insight into the surface topography, giving an indication to whether the topography is offset rather than ordered. In addition, SEM images were also obtained for U-2 OS bone cells adhered on selected surfaces. The SEM images were obtained on a Hitachi SU5000 field emission scanning electron microscope (FE-SEM) (Hitachi, UK). Images were collected at 10 kV with varying magnification using both planar and 80° tilt views. Images of adhered U-2 OS cells adhered to certain substrates were acquired at 5 kV. The magnification and scale bars are detailed in all images presented. Given the poor conductivity of the CaP coated (HA and SrHA) samples, an ultra-thin gold coating was deposited on their surfaces using an Emitech K500X sputtering system (Quorum Technologies, UK) operating at 25 mA for 150 secs. Based on these conditions, a coating with an appropriate thickness of 18 nm (180 Å) is produced. All samples imaged using SEM were carried out in n = 3 per sample type.

3.3.4 Atomic Force Microscopy

Atomic force microscopy (AFM), allows for the measurement and spatial mapping of surface topography at the sub-nanometre scale with high resolution that allows for the imaging of conducting and insulating surfaces with atomic resolution[206–208]. AFM has been applied to applications to obtain high-resolution imaging of biomolecules, polymers, patterned silicon surfaces and other biomaterial surfaces[209,210]. All measurements here were performed using the Veeco Digital Instrumentation Dimension 3100 system (Bruker Axs, UK). The amplitude modulation atomic force microscopy (AM-AFM), or tapping mode as it is also known, whereby the silicon tip is oscillated at a frequency at, or close to, the resonant frequency of the cantilever to which it is attached, was utilised for these analyses at a scan rate of 0.96 Hertz (Hz). AFM was utilised here to give an indication of the roughness of the different surfaces. Whilst it can be difficult to accurately measure the roughness and randomness of a topography, AFM has been employed here to give an estimation of the roughness and degree of randomness if the surface topography. As discussed in Chapter 2, surface roughness plays an important role in slowing dissolution

of a CaP film, as well as promoting cellular adhesion and proliferation. Scans of 20 µm x 20 µm square regions on each sample were collected at three different points across the sample surfaces (n = 3). These data were presented as images using the NanoScope Analysis software (v1.5, Bruker Axs, UK). Data were further processed using first order flattening to account for sample tilt and/or piezoelectric nonlinearity, to generate pseudo-colour 3D images of the features present. Average (n = 6) Rq (root mean square) and Ra (arithmetic mean) surface roughness measurements were made from 3 µm x 3 µm regions within each 20 µm x 20 µm scanned area, giving n = 18 for Rq and Ra measurements per sample type. Image surface area difference percentages were also measured in n = 3, to give another indication of the overall roughness of the surfaces.

3.3.5 Time of Flight Secondary Ion Mass Spectrometry

Time-of-flight secondary ion mass spectrometry (ToFSIMS) is a sensitive analysis technique that allows for determination of elemental information from a material interface through the analysation of secondary ions[211–213]. It can also be utilised to depth profile thin films in order to calculate the coating thickness, as well as allowing for chemical mapping of the titanium substrates with CaP coatings (HA and SrHA). ToFSIMS was carried out using a ToFSIMS V instrument (ION-TOFF, GmbH, Germany) operating with bismuth (Bi) primary ion source ions created from a liquid metal ion gun operating at 25 kiloelectron volts (keV) and an emission current of 1 microamps (µA) with a pulsed source current of 14 nanoamps (nA). An analysis chamber base pressure of 5 $x10^{-2}$ mbar was maintained throughout analysis via the associated rotary and turbo pump assembly. An electron flood gun operating at a filament current of 2.35 A was used during acquisition to shower the sample with electrons to prevent charge build-up. Data were collected using the Bi^{+} primary ion gun operating in the positive polarities. Ion intensity images were acquired using a random raster in spectroscopy mode over an area of 500 µm x 500 µm on the substrate surface. The resulting positive ion scans were recorded as ion mass, in atomic mass units (amu) versus intensity in c/s. False colour ion maps for selected positive ion masses detected were produced using Surface Lab 6 software routines (ION-TOFF, GmbH, Germany). Samples were analysed as n = 3 per sample type.

Thickness of the HA and SrHA coatings was approximated through depth profiling of a 100-hr sputtered TiHA sample. The time taken to sputter through the HA layer to the underlying Ti gave an equation which gave an approximate coating thickness, dependent on the sputtering time. Using this equation, the HA and SrHA coated samples, which were coated for 5 hrs each, gave an approximate thickness of 111 nm.

3.4 Dissolution Studies

Initial dissolution studies were carried out on CaP coated (HA and SrHA) titanium substrates by exposing them to cell culture medium at 37 ˚C with 5 % CO_2 over a 7-day period. The culture media was prepared using McCoy's 5A medium (Sigma-Aldrich, UK) supplemented with 10 % (v/v) foetal bovine serum (FBS) (Gibco, UK) and 1 % (v/v) penicillin (5 units/ml) / streptomycin (5 µg/ml) (Gibco, UK). Using a pipettor, 2 ml of culture medium was placed in each well of a clear 12-well plate along with the sample. At days 1 and 7, the solution was aspirated from the well, samples were removed and drip dried and placed in a desiccator at room temperature until required. Samples were chemically analysed using XPS and ToFSIMS, with the morphology investigated using SEM.

3.5 *In Vitro* Cell Culture and Associated Analysis

3.5.1 U-2 OS Cell Culture

U-2 OS (ATCC® HTB-96™, USA) human osteosarcoma cells were cultured in T-75 tissue culture flasks in McCoy's 5A medium modified with L-glutamine and sodium bicarbonate (Sigma-Aldrich, UK) and supplemented with 10 % (v/v) foetal bovine serum (FBS) (Sigma-Aldrich, UK) and 1 % (v/v) antibiotic mix (5,000 units penicillin and 5 mg streptomycin/ml (Sigma-Aldrich,UK). The flasks were placed in an incubator in 5 % CO_2, 95 % humidified air at 37 ˚C. Cells were passaged weekly using 0.05 % Trypsin with 0.02 % ethylenediaminetetraacetic acid (EDTA) to remove them from the flask surface. These cells were chosen as the culture model system as they have characteristics close to those of human primary osteoblasts, and in addition have been found to mineralise in the presence of appropriate stimuli[88,214].

Three related culture studies were designed and undertaken to determine the cell response to the various titanium substrates with and without CaP coatings (HA and SrHA), as follows:

Cell Study A – 7 days in culture with U-2 OS cells, analysing MTT, PicoGreen™, DAPI nuclei staining and SEM of adhered cells for the following samples:

- Titanium (Ti)
- 24hr piranha etched titanium (24eTi)
- Polycrystalline titanium sputtered at 250 W (PolyTi250)

Cell Study B – 3 days in culture with U-2 OS cells, analysing MTT, PicoGreen™, DAPI nuclei staining and SEM of adhered cells for the following samples:

- Titanium with hydroxyapatite thin film (TiHA)
- 24 hr piranha etched titanium with hydroxyapatite thin film (24eTiHA)
- Polycrystalline titanium sputtered at 250 W with hydroxyapatite thin film (PolyTi250HA)
- Titanium with strontium substituted hydroxyapatite thin film (TiSrHA)
- 24 hr piranha etched titanium with strontium substituted hydroxyapatite thin film (24eTiSrHA)
- Polycrystalline titanium sputtered at 250 W with strontium substituted hydroxyapatite thin film (PolyTi250SrHA)

Cell Study C – 28 days in culture with U-2 OS cells, analysing ALP and BCA for the following samples:

- Titanium with hydroxyapatite thin film (TiHA)
- 24 hr piranha etched titanium with hydroxyapatite thin film (24eTiHA)
- Polycrystalline titanium sputtered at 250 W with hydroxyapatite thin film (PolyTi250HA)
- Titanium with strontium substituted hydroxyapatite thin film (TiSrHA)
- 24 hr piranha etched titanium with strontium substituted hydroxyapatite thin film (24eTiSrHA)
- Polycrystalline titanium sputtered at 250 W with strontium substituted hydroxyapatite thin film (PolyTi250SrHA)

Prior to the culture studies, all substrates were wrapped in aluminium foil, sealed with autoclave tape and subjected to sterilisation using dry heat at 160 ˚C in a Lenton 3216 furnace (AWF 12/5) (Lenton, UK) for 4 hrs. Substrates were then placed in sterile clear 12-well tissue culture plastic plates (Sigma-Aldrich, UK) and maintained in a sterile environment. A verified cell concentration of the U-2 OS cells was obtained using a Biorad TC20 Automated Cell Counter (Biorad, UK) using the Trypan Blue exclusion assay[215]. Cell suspensions were normalised to 1.5 $x10^5$ and a 100 µl aliquot (15,000 cells) pipetted onto each substrate surface. The populated well plates were then incubated at 37 ˚C in 5 % CO_2 for 2 hrs to allow for initial attachment before 1.9 ml of cell growth media was added to each well, ensuring the final well volume was 2 ml. The seeded

substrates were returned to the incubator until the test time points, as indicated. Cell growth media was replenished every week.

3.5.2 Determination of Cellular Metabolic Activity

3-(4,5-dimethylthiazol-2-Y1)-2,5-diphenyltetrazolium bromide (MTT) is a colorimetric assay utilised for measuring cellular metabolic activity. It relies on the ability of NADH-dependant cellular oxidoreductase enzymes to reduce the tetrazolium dye (MTT) to an insoluble purple formazan salt. This reduction is used to reflect the number of viable cells present as it measures only live and actively metabolic cells[216,217]. Cellular metabolic activity was examined at specific timepoints using an MTT assay (Sigma-Aldrich, UK). The MTT reagent was prepared at a working concentration of 5 mg/ml in PBS which itself was generated at a 1X concentration by using a PBS tablet (Sigma-Aldrich, UK) dissolved in 200 ml of dH_2O to give a concentration of 0.01 molar (M) phosphate buffer, 0.0027 M potassium chloride (KCl) and 0.137 M sodium chloride (NaCl), with a pH of 7.4. The PBS was then autoclaved and kept in a sterile environment until required. The final stock reagent was filter sterilised (0.22 µm filter), wrapped in aluminium foil due to light sensitivity, and stored at 2 - 8 ˚C until used. The MTT assay was carried out on cells at day 1,3 and 7 for the uncoated substrates, and at day 3 for both the HA and SrHA coated substrates. At each timepoint substrates and their media were moved to a new clear 12-well plate to ensure only cells present on the substrate surface were measured and not cells that may have migrated to the tissue culture plastic. After which, 200 µl of stock MTT reagent (10 % of the total well volume) was added to each well. These plates were wrapped in aluminium foil and agitated for 2 - 3 mins at 40 revolutions per minute (RPM) followed by incubation at 37 ˚C in 5 % CO_2 for 3 hrs. The solution in the wells was then aspirated and 500 µl of a 10 % sodium dodecylsulfate (SDS) (Sigma-Aldrich, UK)/0.01 M hydrochloric acid (HCL) (Sigma-Aldrich, UK) solution added, after which the plates were again wrapped in aluminium foil and incubated at room temperature overnight. Wells were thoroughly mixed and 100 µl of resting solution transferred to a clear 96-well plate in triplicate, giving each substrate a repeat of n = 9. A positive control (tissue culture plastic with cells present but no substrate) and a negative control (tissue culture plastic with no cells present and no substrate) were also performed at each timepoint to add to the validity to the experiment. The controls were also tested as described above for each set of samples. The absorbance value for the solution taken from the sample and control wells was measured using a TECAN Sunrise microtiter plate

spectrophotometer (TECAN, Switzerland), at λ = 562 nm. Results are plotted as relative absorbance at λ = 562 nm (arbitrary units) at each time point.

3.5.3 DNA Quantification

Double stranded (ds) DNA contains the genetic code for organisms. Measurement of dsDNA can be used as an indicator of cell adhesion, viability and proliferation. The addition of an ultra-sensitive fluorescent nucleic acid stain allows for measurement of small quantities of DNA present[218]. Here, dsDNA was measured using a Quant-iT™ PicoGreen™ dsDNA assay kit (Thermo Fisher Scientific, USA) which uses a sensitive fluorescent nucleic acid stain to bind to healthy viable dsDNA in cells. The assay kit contained the following stock reagents;

- Component A – 200X PicoGreen™ fluorescent probe Dimethylsulfoxide (DMSO) (light sensitive)
- Component B – 20X TrypLE Express (TE) buffer (200 millimolar (mM) Tris-HCL, 20 mM EDTA, pH 7.5)
- Component C – Lambda DNA standard (100 µg/ml) in 1X TE buffer

The TE buffer stock 20X was diluted to 1X using nucleic acid-free molecular grade water (Thermo Fisher Scientific, USA). The 200X PG fluorescent probe solution was diluted to 1X using this TE buffer and wrapped in foil due to light sensitivity until use. A serial dilution of the DNA standard stock solution gave seven standards of 0, 3.1, 6.25, 12.5, 25, 50 and 100 ng/ml, which were used to generate a 7-point standard curve from which to calculate the unknown DNA concentration for each sample.

Substrates were plated as previously described in section 3.8.1. At each timepoint, samples were moved to a new well plate, and the media aspirated. Substrates were then washed x2 with PBS (Chapter 3.5.2) and cells released from the substrates on incubation with TE /1 % Triton X-100 (Sigma-Aldrich, UK) at 37 ˚C in 5 % CO_2 for 30 mins. The solution in the wells were thoroughly mixed to maximise cell recovery and suspensions transferred to sterile microtubes which were then frozen and thawed twice to maximise the breakdown of cell membranes and the associate release of DNA. The microtubes containing the standards and samples were again thoroughly mixed and then further mixed with the PicoGreen™ fluorescent probe 1X in a 1:1 ratio. These solutions were incubated at room temperature for 5 mins in the dark to protect the fluorescent probe from exposure to light. Subsequently, they were mixed again and aliquoted into a black 96-well plate in triplicate at a volume of 200 µl per well per standard/sample (n = 3 for standards

and n = 9 for samples). The fluorescence from the various solutions was measured using the Tecan Genios fluorescent plate reader (TECAN, Switzerland) at an excitation λ = 480 nm and an emission λ = 540 nm, and these values were converted to DNA concentration (ng/ml) using the straight-line equation for the DNA standard curve shown in Figure 3.3.

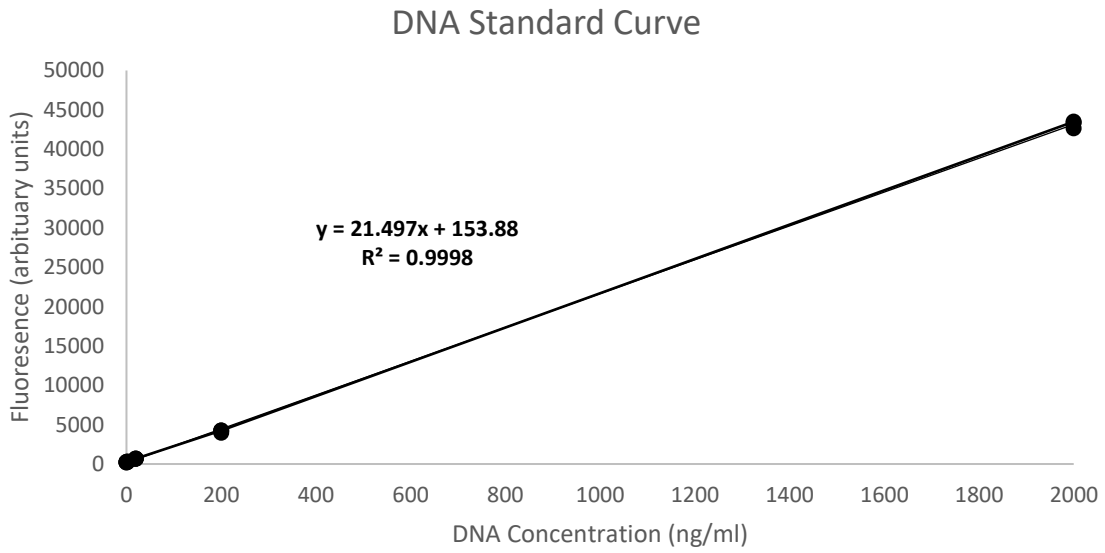

Figure 3.3 A DNA standard curve generated from fluorescence measurements from standards of 0, 3.1, 6.25, 12.5, 25, 50 and 100 ng/ml used to find unknown DNA concentrations for samples. Error bars are present on the graph but are too small to be seen. The straight-line equation used for the DNA concentration calculations from samples is y = 42.994x + 153.88, with an R^2 value of 0.9998

3.5.4 Cell counts using DAPI staining techniques

Visualisation and quantification of actual cell attachment on substrates was investigated using U-2 OS cells fluorescently stained with the 4',6-diamidino-2-phenylindole dihydrochloride (DAPI) dye. This dye is generally cell impermeable and so, cells normally need to be permeabilised or fixed/dead to become stained. However, live cells can be stained if DAPI is used at a higher concentration in which case it binds to the minor grooves of the nucleobases, adenine and thymine, within dsDNA, forming strong blue coloured fluorescent DNA-DAPI complexes with high specificity.

At each time point, media was aspirated from the plate wells and the wells washed x2 with PBS (Chapter 3.5.2). Substrates were chemically fixed using 4 %

paraformaldehyde (PFA) for 8 minutes at room temperature, and then washed again x2 with PBS. DAPI solution, 300 nanomolar (nM) in PBS, was added to each well for 10 mins at room temperature to directly bind to the nuclei of the U-2 OS cells on the various substrate surfaces. The wells were once again washed x2 with PBS, to remove any traces of residual DAPI staining solution. Samples were wrapped in aluminium foil and stored at 2 – 8 °C until needed. Substrates with stained cells were placed on a glass slide and viewed using a fluorescence microscope using a x10 objective lens. Images were taken at 6 random areas across the substrate. In each case, Image J (Image J 1.50i, National Institute of Health, USA) was used to obtain an average cell count across these 6 images. Images were counted and averaged using two techniques. The first method involved counting of pixels using ImageJ generated histograms to generate cell numbers. However, this method was not found to be as accurate at further timepoints were cell clumping occurred. The second method involved using the cell counter plugin of ImageJ. Cell numbers generated were compared and contrasted.

3.5.5 Scanning Electron Microscopy Imaging of Cells

SEM analysis was carried out on fixed U-2 OS cells on various substrates at day 1, 3 and 7 for the uncoated substrates, and at day 3 for the CaP coated (HA and SrHA) substrates, at n = 3. In order to fix the cells on the substrates, well plates were removed from the incubator and washed x2 with PBS (Chapter 3.5.2). The adhered cells were fixed with 2.5 % glutaraldehyde (Sigma-Aldrich, UK) in dH_2O for 45 mins. The glutaraldehyde was aspirated, and substrates were washed x2 with PBS. The adhered cells on the substrates were then gradually dehydrated using increasing concentration of ethanol (Sigma-Aldrich, UK) as follows:

- 25 % ethanol for 10 mins
- 50 % ethanol for 10 mins
- 75 % ethanol for 10 mins
- 90 % ethanol for 10 mins
- 100 % ethanol for 10 mins (x2)
- 50/50 ethanol/hexamethyldisiloxane (HMDS) (Sigma-Aldrich, UK) for 10 mins

Substrates were then further chemically dried overnight at room temperature using 2-3 drops of 100 % HMDS per well. Before SEM analysis, each substrate was gold coated using an Emitech K500X sputtering system (Quorum Technologies, UK) at 25 mA for 150 secs. As described in Chapter 3.3.3, the fixed cells on the substrates were imaged in

planar view at varying magnification using a Hitachi SU5000 Field emission SEM (Hitachi, UK) at an electron voltage of 5 kV. Magnification details and scale bars are detailed in all images presented.

3.5.6 Alkaline Phosphatase Activity

As indicated earlier, alkaline phosphatase (ALP) is a protein enzyme expressed in the early stages of bone development and is an indicator of osteogenic activity. Measurement of ALP concentration has been used extensively as an indication of bone and bone-like cell differentiation[29,95,160,219,220]. In this work, CaP coatings (HA and SrHA) on various titanium substrates were subjected to ALP analysis at 7-, 14-, 21- and 28-day time points. Substrates were plated as described for previous assays and an ALP kit, Sensolyte para-Nitrophenyl phosphate (pNPP) (AS-72146) (Anaspec, UK)[221], was used to evaluate the amount expressed from cells on each sample type. This kit contains five components, A-E, as follows;

- Component A – pNPP colorimetric ALP substrate (light sensitive)
- Component B – 10X Assay Buffer
- Component C – Stop Solution
- Component D – Trition-X-100
- Component E – ALP Standard Stock (Calf Intestine, 10 µg/ml)

ALP buffer 10X was diluted to 1X with nucleic acid free molecular grade water (Thermo Fisher Scientific, USA). ALP standard solutions to generate a standard curve were prepared by serially diluting the ALP standard stock (10 µg/ml) with the 1X assay buffer to give concentrations of 200, 100, 50, 12.5, 6.25, 3.1 and 0 ng/ml. At each specified time point, the media was aspirated and substrates (with adhered cells) were moved to a new 12-well plate. Substrates were washed x2 with PBS (Chapter 3.5.2) and cells released from the substrate surface by incubation with TE /1 % Triton X-100 (Sigma-Aldrich, UK) at 37 ˚C in 5 % CO_2 for 30 mins. Maximisation of cell collection was insured by pipetting up and down each well volume 10 times. The cells were then collected using a pipette and transferred to a sterile microtube. The microtubes were subjected to a freeze thaw method, were they were frozen and thawed twice to maximise the breakdown of cell membranes and the associated release of ALP. After the microtubes were thawed, they were thoroughly mixed and microcentrifuged at 14,000 RPM (20817 RCF) for 10 mins at 4 ˚C. The supernatant was collected (~ 600 µl) and transferred to a new sterile microtube. The cell pellet was stored at -25 ˚C for further analysis, as required.

Standard solutions (n = 2) and those acquired from cells removed from substrate surfaces (n = 3) were aliquoted into a clear 96-well plate, at a volume of 50 µl per well, to which 50 µl of pNPP was added. The plates were then wrapped in foil and placed on a plate shaker for 5 mins at 40 RPM followed by an incubation of 60 mins in 5 % CO_2 at 37 ˚C. The stop solution (50 µl) was now added to each well before the plate was rewrapped and mixed on a plate shaker for 5 mins at 40 RPM and left to cool to room temperature for 30 mins. Absorbance was measured using a Tecan Sunrise plate spectrometer (TECAN, Switzerland) at λ = 405 nm. ALP concentration (ng/ml) for the solutions derived for each substrate type were determined using the 7-point standard curve as presented in Figure 3.4. The curve was fitted using a 4-parmeter polynomial equation.

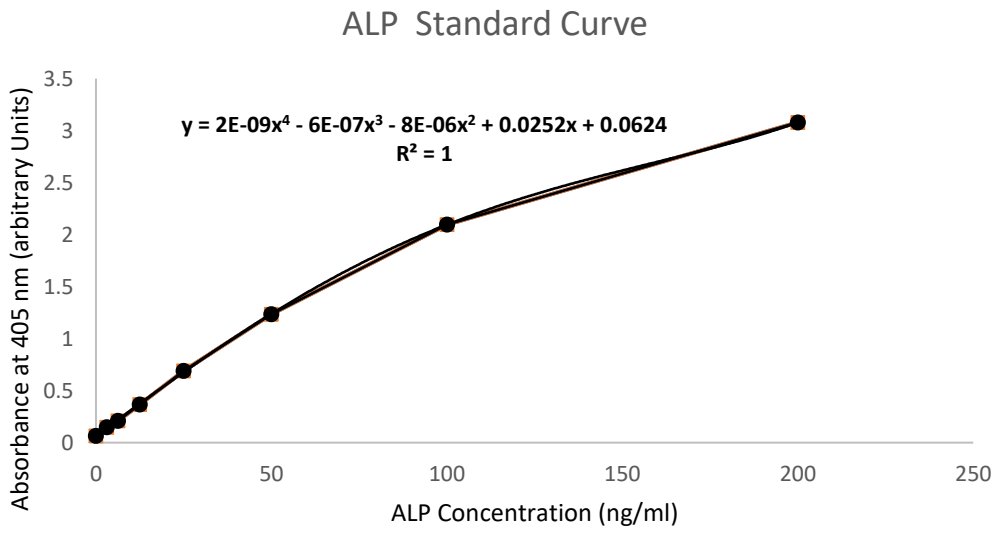

Figure 3.4 Standard curve generated to calculate ALP concentrations for cells removed from various substrate types. Error bars are included but are too small to be seen. The curve was fitted using a 4-parameter polynomial equation $y = 2E\text{-}9x^4 – 6E\text{-}07x^3 – 8E – 06x^2 + 0.0252x + 0.0624$, *with an* R^2 *value of 1*

3.5.7 BCA Protein Quantification

The biocinchonic acid assay (BCA) allows for quantitative measurements of the total protein content that has been expressed by cells. The BCA assay relies on the reduction of copper ions (Cu^{2+}) to copper (Cu) by the proteins present in the sample, in the presence of an alkaline medium. This subsequent binding of copper ions to bicinchonic molecules produces a purple coloured ion compound ($Cu(BCA)_2^{3-}$) which gives a strong absorbance at $\lambda = 562$ nm and has been shown to be proportional to protein concentration[222]. A BCA protein assay kit (Thermo Fisher Scientific, USA) was utilised for this assay. The kit contained;

- BCA reagent A (sodium carbonate, sodium bicarbonate, bicinchoninic acid and sodium tartrate in 0.1 M sodium hydroxide)
- BCA reagent B (4 % cupric sulfate)
- Albumin standard (bovine serum albumin (BSA) 2 mg/ml in 0.9 % saline and 0.05 % sodium azide)

The BCA working reagent was prepared by combining BCA reagent A with BCA reagent B at a ratio of 50:1. The BCA standards were generated by serially diluting the albumin stock (2 mg/ml) with TE/1 % Triton X-100 to create 2000, 1500, 100, 750, 500, 250, 125, 25 and 0 µg/ml to create a 9-point standard curve. Titanium substrates with CaP coatings (HA and SrHA), were subjected to a 28-day cell culture study and analysed for total protein concentration at days 7, 14, 21 and 28. At each timepoint the media was aspirated, and substrates moved to a new plate. Substrate wells were washed x2 with PBS (Chapter 3.5.2) and cells released from their surface on incubation with TE /1 % Triton X-100 (Sigma-Aldrich, UK) at 37 ˚C in 5 % CO_2 for 30 mins. The solutions in the wells were thoroughly mixed to maximise cell recovery and suspensions transferred to sterile microtubes which were frozen and thawed twice to maximise the breakdown of cell membranes and release of all the proteins. Maximisation of cell collection was insured by pipetting up and down each well 10 times before transferring to the sterile microtubes. The microtubes were then subjected to a second freeze-thaw method cycle. The microtubes were then thawed, thoroughly mixed and microcentrifuged at 14,000 RPM (20817 RCF) for 10 mins at 4 ˚C. The supernatant was collected (~600 µl) and transferred to a new sterile microtube. The cell pellet was stored at -25 ˚C for further analysis, as required. The standard solutions (n = 2) and those isolated from the samples (n = 3) were aliquoted into a clear 96-well plate at 10 µl per well. To these wells, 200 µl of BCA working reagent was added, before the plate was covered with aluminium foil and placed

on a plate shaker at 40 RPM for 5 mins, followed by an incubation at 37 ˚C in 5 % CO_2 for 30 mins followed by a cooling period of 30 mins to room temperature. Absorbance was recorded at λ = 562 nm using a Tecan Sunrise plate reader (TECAN, Switzerland). The BCA concentrations (µg/ml) of the various samples were calculated using the 9-point standard curve, as presented in Figure 3.5, using a 4-parameter polynomial equation.

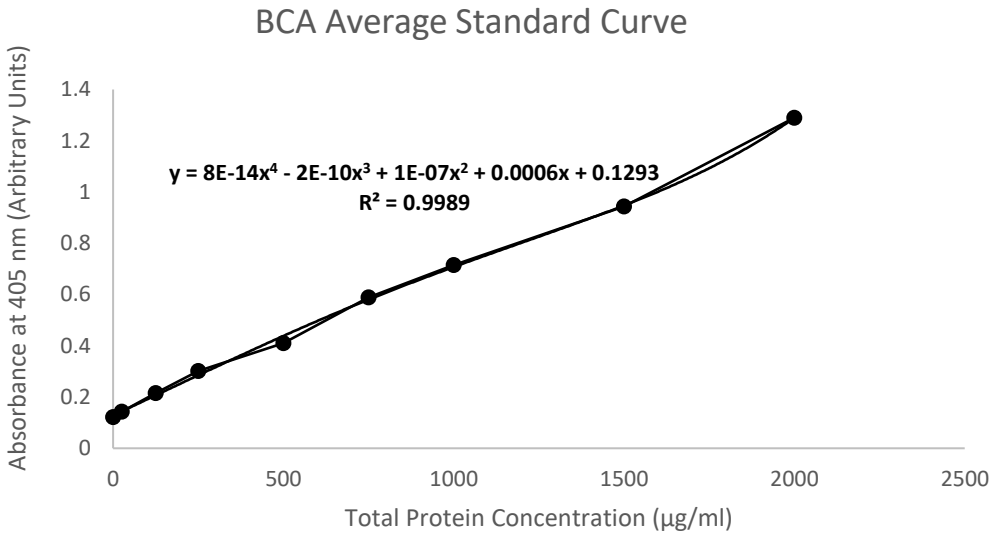

Figure 3.5 BCA standard curve generated to calculate total protein concentrations from cells cultured on CaP coated (HA and SrHA) coated titanium substrates. Error bars are presented, as shown. The curve was fitted using a 4-parameter polynomial equation $y = 8E\text{-}14x^4 – 2E\text{-}10x^3 + 1E–07x^2 + 0.0006x + 0.1293$*, with an* R^2 *value of 0.9989*

3.5.8 Alizarin Red Staining

Alizarin red stain is a water-soluble sodium salt that has been used in cell culture studies for the staining of calcium in cells that is indicative of mineralisation having occurred. When Alizarin red reacts with calcium bone cells, areas of a reddish-brown colouration occur. In this work, U-2 OS cells cultured on various substrate surfaces for 28 days where exposed to Alazarin red stain. Samples were cultured as described previously in Chapter 3.5.1, and at the required time were washed x2 with PBS (Chapter 3.5.2), after which 1 ml of Alizarin red (Sigma-Aldrich, UK) solution was added to each sample well, and plates incubated at room temperature for 25 mins. Wells were washed with sterile dH_2O until the run-off from the washings was colour-free. Samples were dried at 37 ˚C overnight after which they were imaged using an optical microscope using a x10 objective lens. A qualitative analysis was obtained from these images; the absence of red colour indicated no mineralisation and the presence of red colour indicated mineralisation.

3.5.9 Statistical Analysis

Statistical analyse of MTT, PicoGreen™, ALP and BCA assays were performed using Graph Pad Prism version 8 software package (GraphPad, USA). One-way analysis of variance (ANOVA) was used to compare mean values in order to determine equivalence of variance between samples for the MTT and DNA quantification data. Two-way analysis of variance (ANOVA) was used to compare mean values of ALP and BCA over the 28-day study. Samples were tested in at least n = 3, with statistical significance between sample groups determined using the Tukey's multiple comparison test. A value of $P < 0.05$ = * was taken as statistically significant.

Chapter 4: Control of Substrate Chemistry and Morphology

4.1 Introduction

As indicated previously, titanium and its alloys have been used for many decades for the fabrication of medical and dental implants[67,101,178,184] due, in the main, to their low density, high mechanical loading strength and the extensive corrosion resistance that is offered by the naturally occurring oxide layer. In particular, their use for the provision of a range of load bearing orthopaedic devices is well established for applications in joint replacement, spinal stabilisation and fracture fixation. Although these materials are deemed to be biocompatible, they do not normally have inherent bioactive properties and so are commonly combined with other materials, including calcium phosphate (CaP) bioceramic coatings such as hydroxyapatite (HA), as a means of providing for direct (cementless) fixation and/or the promotion of tissue integration *in vivo*. Whereas, plasma spraying is the normal commercial method of choice for such implant coating applications[25,35,183], it has limitations in regard to the control of the interface that develops between the coated device and native bone. In addition, it is difficult to create surface microstructural features that can help to promote rapid integration of the device. Radio frequency (RF) magnetron sputtering offers an alternative means to coat a range of biomaterials with HA in the context of implant fixation[45,190,191,201], but generally requires a post-deposition thermal sintering step in order to avoid the rapid dissolution of the film. Notwithstanding the benefits that this coating method offers, such as the creation of a novel surface chemistry and/or microstructure, these limitations have tended to restrict its commercial attraction. When deposited by RF magnetron sputtering from targets pressed from pure commercial HA powder, the resulting thin films tend to be HA-like[130], i.e. their stoichiometry is not identical to that of the target HA powder[30,45] and so for the purposes of this work are referred to as calcium phosphate (CaP) coatings that are HA-like.

One way to reduce, and also potentially control, the normally rapid dissolution of as-deposited RF magnetron sputtered CaP coatings, is to create a substrate surface morphology that provides for physical entrapment and/or interlocking of the continuous thin film. In this regard, stock titanium (and its alloys), are usually employed as medical grade materials in the form of sheets, wires, billets etc, that predominantly have flat uniform surface features, although some may have pronounced lines and grooves attributed to their processing, i.e. cold/hot working, rolling etc. This native surface morphology can then be altered by a number of methods ranging from simple physical abrasion to the complex masking and etching processes used in the semiconductor

industry. There are pros and cons to each of these surface processing techniques, with some methods being favoured over others. As such, choice of processing techniques is commonly based on individual experience and resource availability. Importantly, the principal application for which the substrate will be used influences the surface engineering methodology employed significantly, in order that the characteristics that are needed in order for the substrate to function effectively are delivered.

Chemical etching of titanium is well established method for surface modification which does not need complicated or time-consuming processing technologies but has not been studied in detail for as a means to create morphology that can influence the dissolution of sputter deposited coatings[19,20,223]. Hence the work reported here is related to determining how chemical etching can be used to deliver surface roughness conditions that control the dissolution of CaP thin films in a manner that provides both chemical and topographical features that cells tend to favour[22,27,40].

Therefore, this chapter provides a detailed analysis of the chemistry and topography generated on titanium surfaces by direct chemical etching in piranha solution. The properties produced are compared with titania surfaces created by sputter deposition from titanium targets and titania nanotubes produced via electrochemical anodisation of titanium coupons. Both of these comparator surfaces have shown previously to offer a level of control for the dissolution of sputter deposited CaP thin film coatings thereon[29,31,115,160]. In advance of the chemical etching, sputter deposition and anodisation of titanium, thermal annealing of the titanium coupons has also been carried out to investigate how simply enhancing the native oxide affects the associated surface chemistry and topography. In all cases, comprehensive surface analysis has been undertaken using x-ray photoelectron spectroscopy (XPS), x-ray diffraction (XRD), scanning electron microscopy (SEM) and atomic force microscopy (AFM). Numerous samples, at least n = 3 unless otherwise stated, were taken from different sample set batches to be analysed and compared sample-to-sample to ensure reproducibility of samples of each type.

Unless otherwise stated, the abbreviations for each of the processed sample types used throughout this and subsequent chapters of the thesis are as follows:

- Thermally Treated Titanium
    - Ti - Unannealed titanium
    - aTi – 500 ˚C thermally annealed titanium
- Chemically Etched Titanium

- 3eTi – 3 hr piranha etched titanium
- 24eTi – 24 hr piranha etched titanium

- RF Magnetron Sputtered Deposited Titanium Thin Films on Titanium
  - PolyTi250 - 2hr sputtered at 250 W titanium
  - PolyTi400 - 2hr sputtered at 400 W titanium
- Anodised Titanium
  - TiNT - Titanium nanotubes

4.2 Thermally Treated Titanium

When comparing surface processing methods to deliver key chemical and topographical properties, it is important to have suitable control sample surfaces. Whereas, many studies have used the as-received native titanium as a control, others have opted to use annealed titanium. Hence, an understanding of both of these surfaces is valuable in the context of their inherent ability to control the subsequent dissolution of CaP thin films thereon. To this end, as-received titanium was cleaned and annealed at 500 ˚C in a Lenton furnace, as described in section 3.1.3. Samples were then characterised before and after annealing by XPS, XRD, SEM and AFM to provide baseline data for comparison with the surface features created on chemically etched, sputter deposited and anodised titanium.

4.2.1 XPS Analysis

XPS was used to determine changes in the elemental composition of the surface region of the titanium substrate before and after thermal annealing at 500 ˚C. Figure 4.1 (a) shows the wide energy survey spectra (WESS) collected for the pristine (unannealed) titanium (Ti) with the peaks present indicating the expected chemistry of a typical titanium metal sample, as well as the corresponding C 1s, O 1s and Ti 2p high resolution spectra for this Ti control surface. The lowest binding energy (BE) component (C-C, C-H) in the C 1s envelope (Fig 4.1 (b)) was assigned to adventitious carbon and set at a BE of 284.8 eV in order to calibrate the peak positions for surface charging effects. The remaining three contributions to the C 1s region are assigned to C-O, C=O and O-C=O at 286.3 eV, 287.8 eV and 288.9 eV, respectively. The corresponding O 1s plot (Figure 4.1 (c)) comprises two partially resolved peaks with that at 530.1 eV attributed to the lattice oxide (from TiO_2) and the peak at 531.5 eV assigned to hydroxide bonding (OH^-). As expected, there is a significant metal (Ti (0)) contribution to the Ti 2p high resolution plot (Figure 4.1 (d)), as well as a smaller component from TiO_2 (Ti (IV)), as indicated by the two overlapping doublets observed. The titanium metal (Ti (0)) doublet Ti $2p_{3/2}$ present at 453.8eV and Ti $2p_{1/2}$ at 460.1eV, whilst the TiO_2 (Ti (IV)) doublet is

present as Ti $2p_{3/2}$ at 458.5eV and Ti $2p_{1/2}$ at 464.3eV. Table 4.1 provides the XPS quantitative data for this unannealed titanium (Ti) sample which indicates that the chemistry of the uppermost surface is dominated by adventitious carbon (284.8 eV). The oxygen from the lattice oxide peak at 530.1 eV (from TiO_2) and the hydroxide peak at 531.5 eV are the next most prevalent contributions, with the corresponding titanium Ti 2p doublets for titanium metal (453.8 eV and 460.1 eV) and titanium oxide (458.5 eV and 464.3 eV) making up the balance, such that the titanium to oxygen ratio (Ti/O) is 0.31.

The WESS for the 500 ˚C thermally annealed titanium (aTi) is provided in Figure 4.2 (a) and initially shows no apparent differences to that for the native Ti (Figure 4.1 (a)). However, the high-resolution spectra provided in Figure 4.2 (b) - (d), indicate that thermal annealing not only reduces the amount of surface adventitious carbon present, but also eliminates the previously present Ti metal (Ti (0)) doublet resulting in an increased titanium oxide content, as indicated by a Ti/O of 0.38. Whereas, the high-resolution spectra plots collected for C1s and O1s in aTi are similar to those seen for Ti, the Ti 2p region for aTi shows only one doublet, which corresponds to presence of TiO_2 (Ti (IV)). This confirms the growth of the expected outer oxide layer to a depth of at least 100 nm (the XPS analysis depth), thereby eliminating the detection of the underlying Ti metal (Ti (0)). The amount of oxygen present on the surface has almost doubled compared to that for Ti.

Table 4.1 XPS quantification data (n = 9) for Ti and aTi samples with standard deviation included

	Ti			aTi		
Element	**Binding Energy (eV)**	**Atomic Concentration %**	**Total Atomic Concentration %**	**Binding Energy (eV)**	**Atomic Concentration %**	**Total Atomic Concentration %**
C 1s	284.8	31.70 ± 7.78	50.07 ± 2.67	284.8	20.73 ± 0.97	25.40 ± 1.26
	286.3	11.02 ± 5.83		286.3	2.56 ± 0.17	
	287.8	5.57 ± 2.31		287.8	0.55 ± 0.33	
	288.8	1.95 ± 1.48		288.8	1.63 ± 0.32	
O 1s	530.1	19.30 ± 1.97	36.68 ± 2.18	530.2	39.71 ± 0.44	54.05 ± 1.13
	531.5	19.20 ± 2.78		531.6	14.99 ± 0.91	
Ti 2p	453.8	2.48 ± 0.26	11.25 ± 1.27	-	-	20.55 ± 0.17
	460.1	1.24 ± 0.13		-	-	
	458.5	5.22 ± 0.77		458.9	13.22 ± 0.16	
	464.3	2.33 ± 0.85		464.6	6.61 ± 0.08	

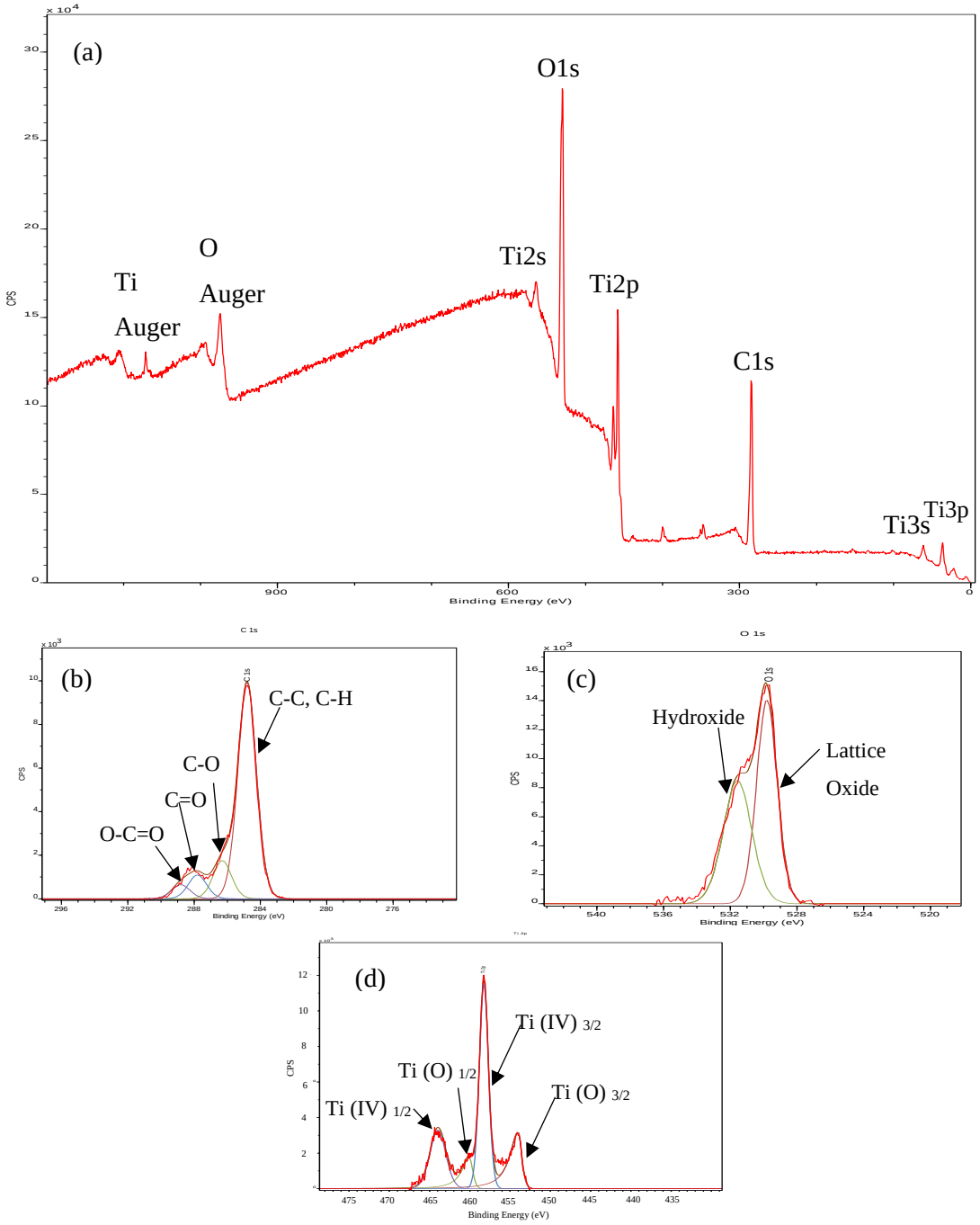

Figure 4.1 XPS spectra for Ti showing (a) WESS and high-resolution spectra for (b) C 1s, (c) O 1s and (d) Ti 2p regions

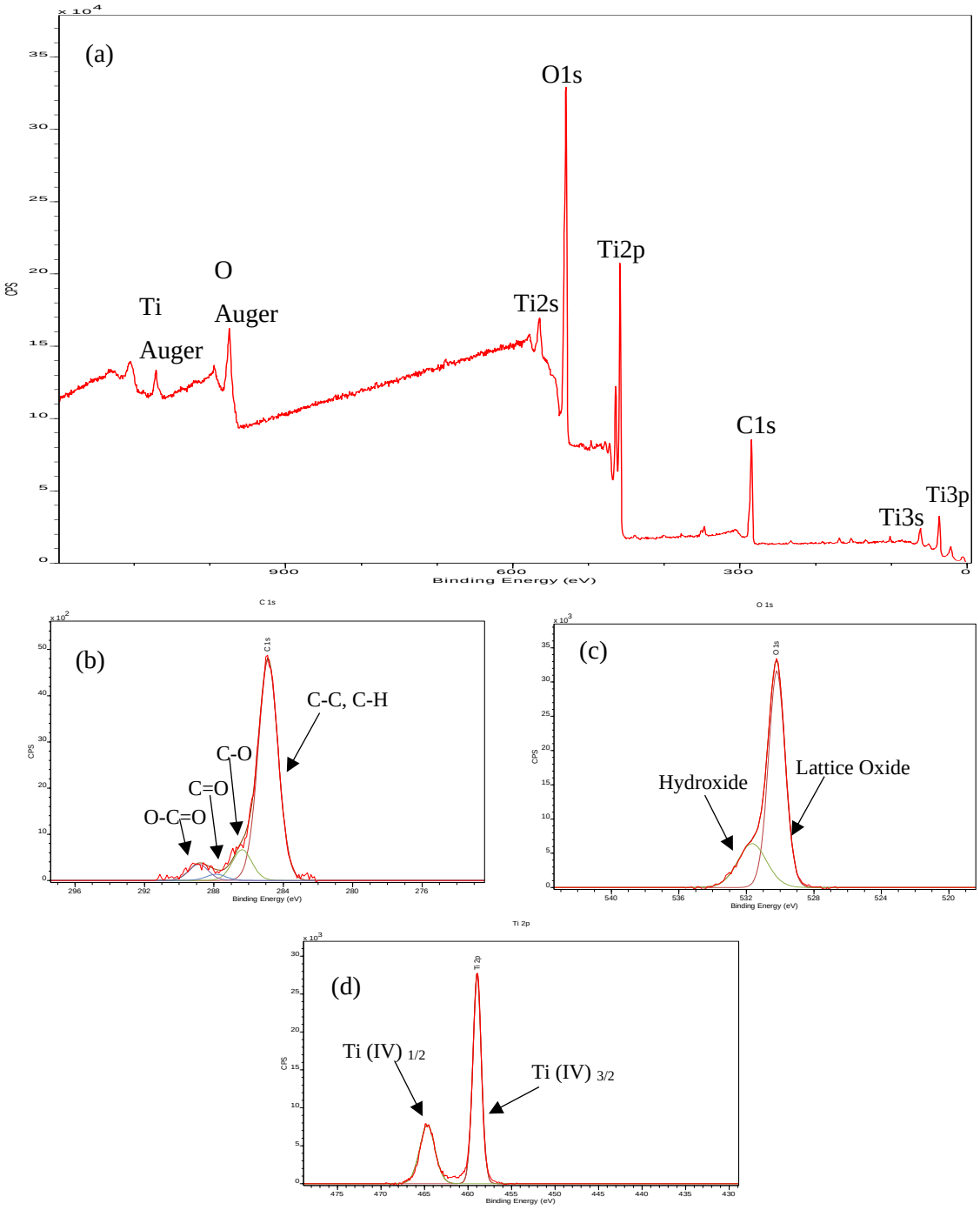

Figure 4.2 XPS spectra for aTi showing (a) WESS and high-resolution spectra for (b) C 1s, (c) O 1s and (d) Ti 2p regions

4.2.2 XRD Analysis

XRD analysis of titanium substrates before (Ti) and after thermal annealing (aTi), was carried out to investigate any changes in crystallinity. Figure 4.3 (a) shows an x-ray diffractogram for Ti with the most intense peaks observed at 2θ = 35˚, 38.3˚, 40.1˚ and 53.1˚ corresponding to Miller indices (hkl) in the 100, 002, 101 and 102 planes, respectively. There is a minor peak observed at 2θ = 36.4˚ which corresponds to the 004 plane, indicative of titanium dioxide (TiO_2). This is expected as unannealed Ti has a natural oxide layer present. These features are indicative of the as expected semi-crystalline metallic titanium structure when compared to the ICDD file 00-044-1294 for titanium[205].

As can be seen in Figure 4.3 (b), the main peaks for aTi are at 2θ = 35˚, 36.4˚, 38.3˚, 40.1˚ and 53.1˚ representative of Miller indices (hkl) in the 100, 004, 002, 101 and 102 planes, respectively. Overall, this x-ray diffractogram shows similar peaks as those present for Ti samples, with the main difference being that the most intense peak is in the 101 plane rather than the 002 plane. There is also an increase in the 004 plane for aTi which is indicative of the increased oxide layer that has formed. Hence, despite the 500 ˚C thermal annealing that the titanium has undergone, it still retains a semi-crystalline phase that is similar to that of the unannealed titanium.

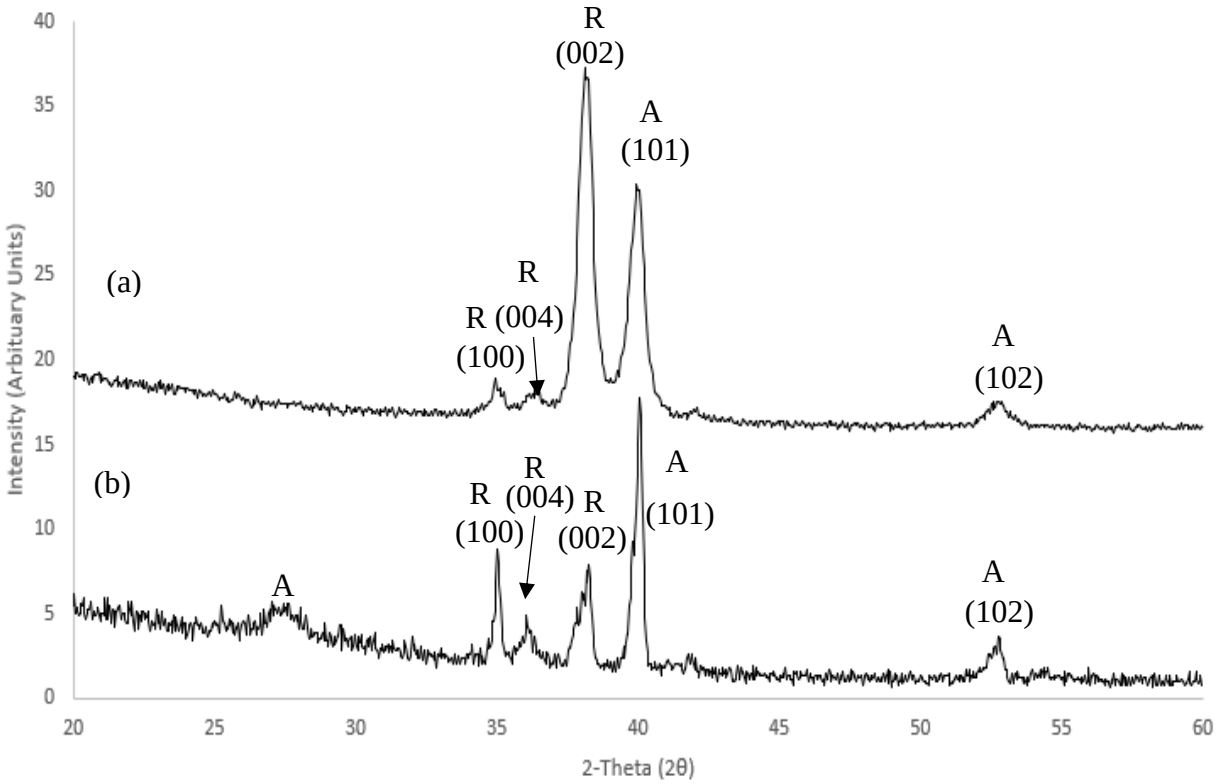

Figure 4.3 X-ray diffractograms for (a) Ti and (b) aTi with Miller index assignments labelled according to ICDD file 00-044-1294. Anatase (A) and rutile (R) phases also labelled

4.2.3 SEM Analysis

SEM was utilised to examine changes in surface morphology of titanium before and after thermal annealing at 500 ˚C. Images were taken both in normal planar view and at an 80˚ side angle view, to better visualize the topographical surface features. Figure 4.4 (a) - (d) shows the normal planar images for the Ti surfaces, as well as an 80˚ side angle view of Ti seen in Figure 4.4 (e) - (h). Lines and grooves can be seen at all magnifications which are in the main attributed to commercial processing augmented with the standard cleaning protocol utilised here. The surface is not completely flat, as seen in the images presented here. The corresponding images collected for the aTi surfaces are provided in Figure 4.5 (a) - (h) and show similar features to those for Ti. However, there is clear evidence of ‘smoothing’ of the surface in the aTi samples, which is expected due to the thermally induced growth of the oxide layer.

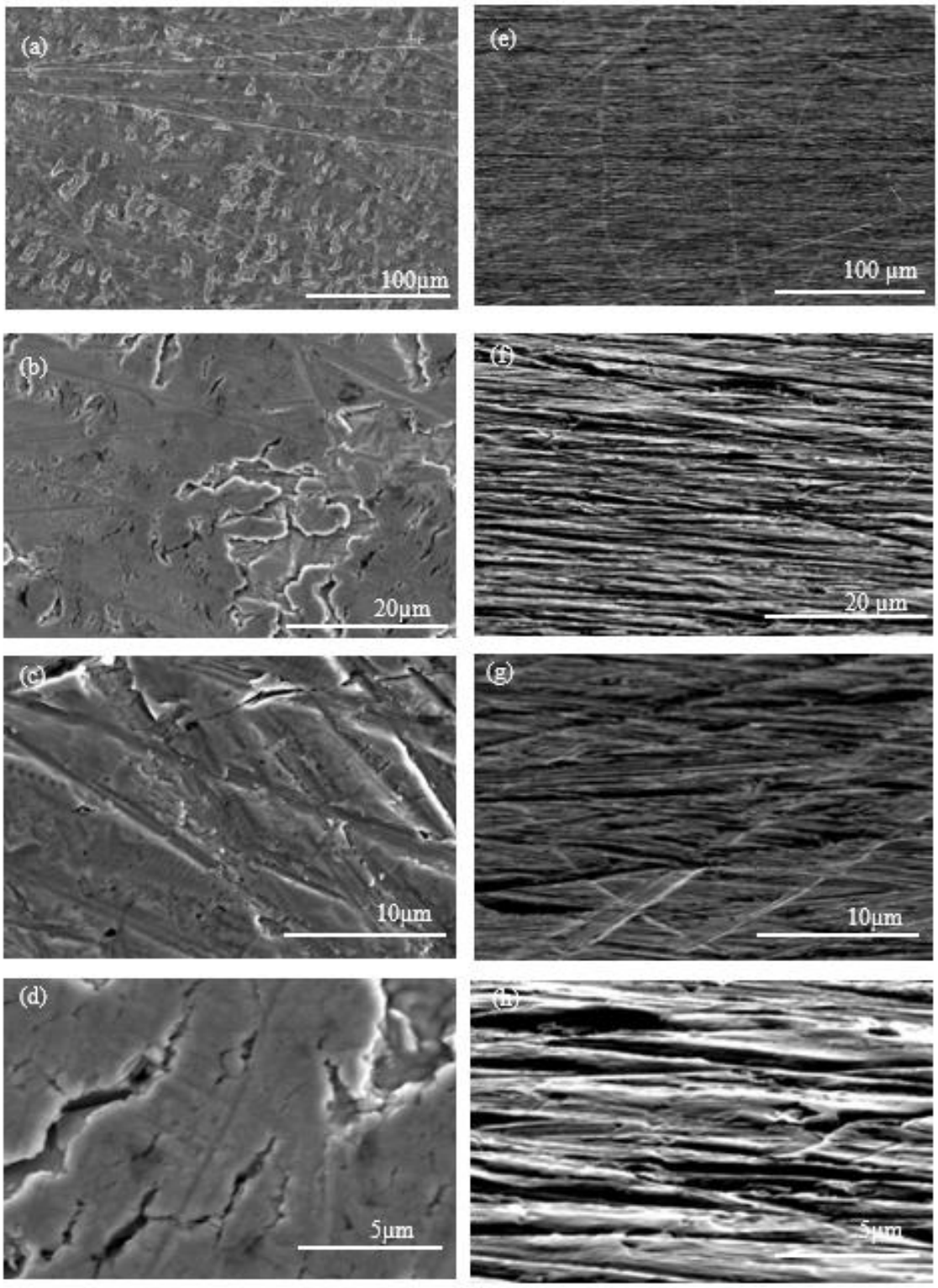

Figure 4.4 SEM images for Ti showing normal planar views (a) - (d) and 80˚ tilt side angle views (e) - (h) at magnifications of (a) x400, (b) x2.5k, (c) x4.5k (d) x8k, (e) x400, (f) x2.5k, (g) x4.5k and (h) x8k

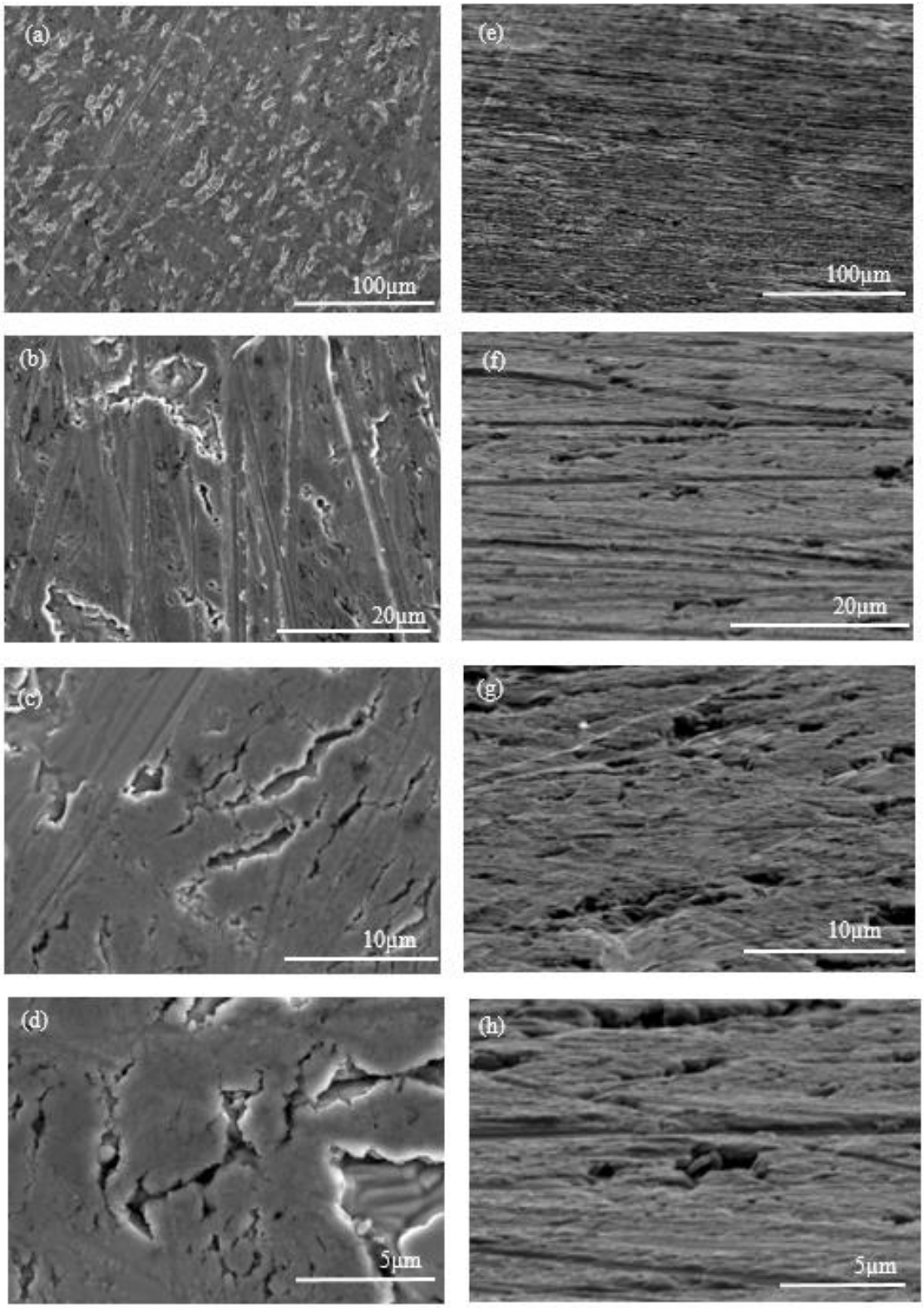

Figure 4.5 SEM images for aTi showing normal planar views (a) - (d) and 80˚ tilt side angle views (e) - (h) at magnifications of (a) x400, (b) x2.5k, (c) x4.5k (d) x8k, (e) x400, (f) x2.5k, (g) x4.5k, and (h) x8k

4.2.4 AFM Analysis

AFM was used to map the features on the Ti and aTi samples at sub-micron resolution and to determine the Rq and Ra surface roughness values. It should be noted that the 20µm x 20µm resolution used here does not directly correspond to the dimensions presented in the SEM images in the previous section. The Ra and Rq values were averaged across 3 samples from each of the Ti and aTi sample sets with then Ra and Rq measurements taken from 3µm x 3µm square regions across the individual scan collected and presented in Table 4.2.

The 2D and 3D AFM images for Ti are shown in Figure 4.6 and indicate regions of roughness associated with the lines and grooves present from the processing and standard cleaning protocol. The average Ra and Rq values, calculated for Ti are 25.96 ± 2.08 nm and 30.69 ± 4.03 nm, respectively indicating that there is a relatively smooth topography between the larger lines.

The corresponding 2D and 3D AFM images for aTi are provided in Figure 4.7 and suggest the presence of a generally smoother surface which is consistent with what was seen in the SEM images (Figure 4.5). The average Ra and Rq values here are 26.83 ± 3.78 nm and 33.85 ± 3.82 nm, respectively which suggest that the annealing process applied to the titanium substrate here causes smoothing of the larger surface features but does not significantly affect the roughness in areas between these features.

Table 4.2 Average Ra and Rq values (n = 18) and image surface area difference in % (n =3) for Ti and aTi surfaces calculated from AFM images (n = 3) with standard deviation included

Sample Type	Ra (nm) ± Standard Deviation	Rq (nm) ± Standard Deviation	Image Surface Area Difference % ± Standard Deviation
Ti	25.96 ± 2.08	30.69 ± 4.03	4.56 ± 2.56
aTi	26.83 ± 3.78	33.85 ± 3.82	9.33 ± 7.09

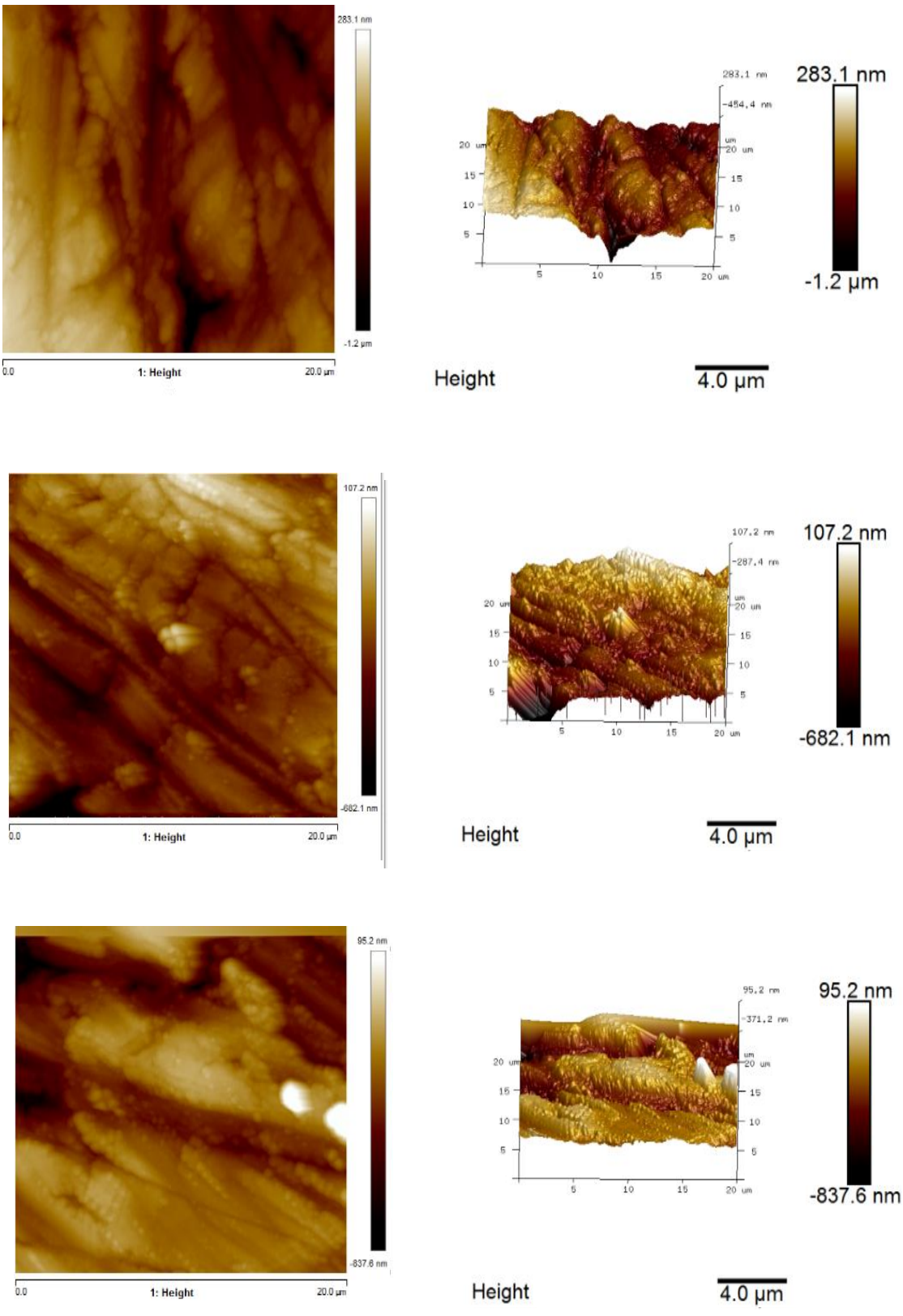

Figure 4.6 Pseudo- colour 20 µm x 20 µm 2D AFM images and corresponding 3D plots for Ti

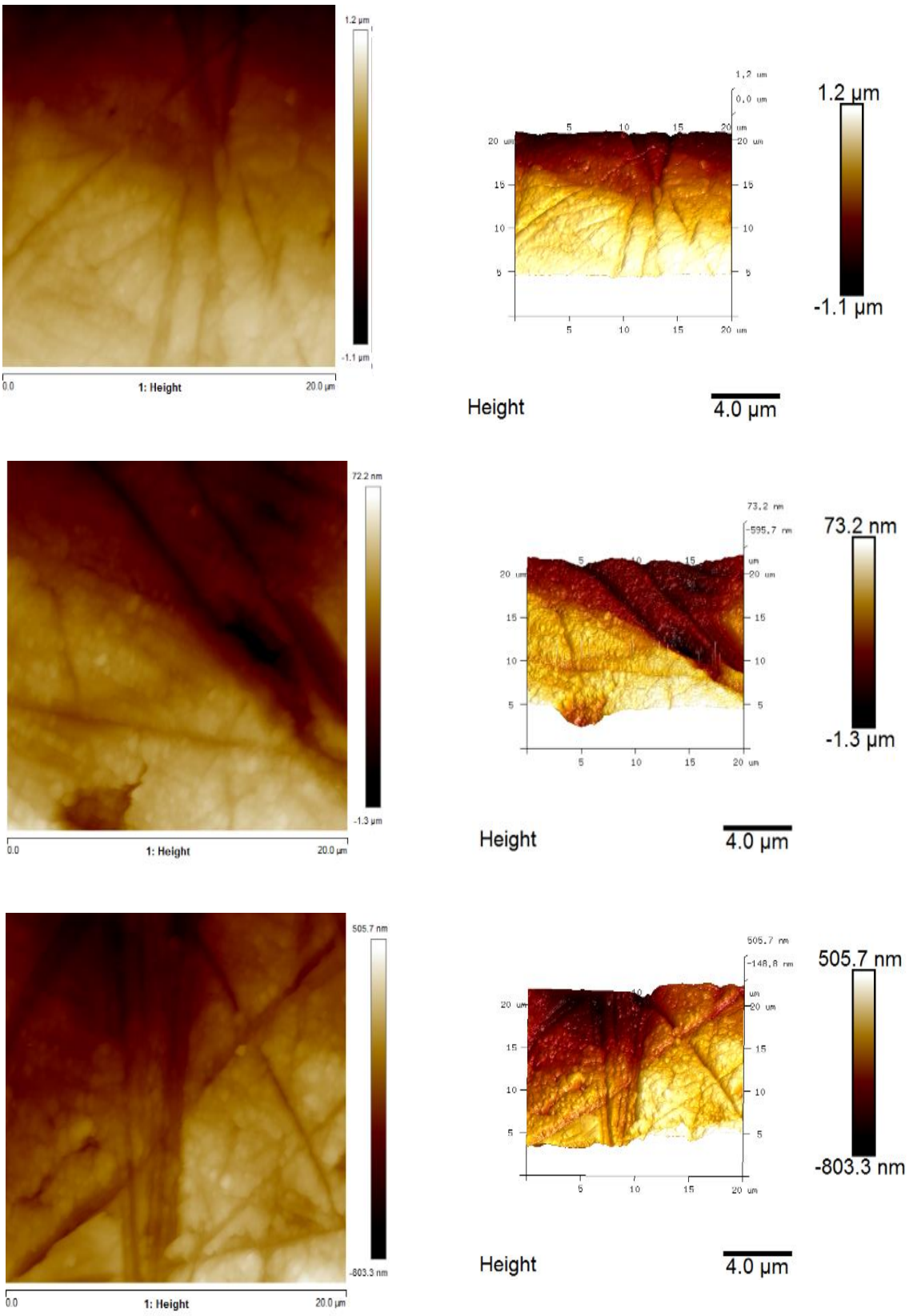

Figure 4.7 Pseudo- colour 20 µm x 20 µm 2D AFM images and corresponding 3D plots for aTi

4.3 Chemically Etched Titanium

As previously described, the piranha etching method, which involves controlled exposure to a mixture of sulfuric acid (H_2SO_4) and hydrogen peroxide (H_2O_2) at a ratio of 3:1 respectively, has been applied to the Ti samples to effect direct chemical etching. Etch duration timepoints of 3 hr and 24 hr were chosen to further investigate the evolution of the morphology created on the titanium coupons. As well as investigating the resulting chemical and microstructural properties, the analyses were also used to ensure that no cytotoxic by-products are formed on the surface.

4.3.1 XPS Analysis

Figure 4.8 (a) shows an XPS WESS collected for a 3hr etched (3eTi) sample the features of which are very similar to those observed for Ti (Figure 4.1 (a)). The corresponding spectrum for 24hr etched titanium (24eTi) is provided in Figure 4.9 (a) and is again similar to that of the native Ti sample. However, from closer examination of the high-resolution C 1s, O1s and Ti 2p spectra plots, shown in Figure 4.8 (b) - (d) for 3eTi and Figure 4.9 (b) - (d) for 24eTi, it is clear that there are several elemental differences between the samples resulting from the two timepoints. Whereas, the C 1s regions for both 3eTi (Figure 4.8 (b)) and 24eTi (Figure 4.9 (b)) have the four peaks seen previously for Ti and aTi, with the most intense peak at 284.8 eV attributed to adventitious carbon, there is now a fifth peak present in this 3 hr etched sample at 281.8 eV. This additional peak is attributed to a carbide contribution[203]. The O 1s region for the samples generated at both timepoints (Figure 4.8 (c) and Figure 4.9 (c)) comprise of two resolved peaks with the expected peak for the lattice oxide at 530.1 eV and hydroxide bonding at 531.5 eV, which are similar to those seen previously for Ti and aTi. The Ti 2p high-resolution spectra plot (Figure 4.8 (d)) has two overlapping doublets, the first of which is attributed to Ti metal (Ti (0)) doublets of Ti $2p_{3/2}$ at 454.1 eV and Ti $2p_{1/2}$ at 460.1 eV. The second doublet is due to TiO_2 (Ti (IV)) seen for Ti $2p_{3/2}$ at 458.7 eV and Ti $2p_{1/2}$ at 464.4 eV. As any carbide in the Ti 2p will show up at the same binding energy position as the Ti metal (Ti (0)) doublet peaks, it is not possible to confirm its presence from these data. However, as seen in Table 4.3, the relative Ti metal (Ti (0)) contribution for 3eTi is greater than that observed for Ti, which may be due to the contribution being made by the titanium carbide. Although the XPS results for 24eTi show similarities to those for the Ti, aTi and 3eTi samples, the Ti 2p plot here shows only a single doublet, as seen previously for aTi. The quantification data are shown in Table 4.3 and indicate a reduction in the amount of C 1s present on 24eTi compared to that detected on 3eTi. The C/O ratio for 3eTi is 1.07 which

decreases to 0.83 in the 24eTi samples, confirming an increase in the amount of O 1s present on 24eTi samples. The Ti/O ratio for 3eTi is 0.48 which decreases to 0.35 in the 24eTi samples, corresponding to a reduction in Ti metal peaks and an associated increase in the oxide presence. Overall, the XPS quantification of the 24eTi surface shows elemental composition similar to that of aTi. Importantly, there are no other by-products detected in either of the etched samples, suggesting that despite the highly corrosive chemicals used, no detrimental reactions have occurred that may have subsequent negative effects on cells.

Table 4.3 XPS quantification data (n = 9) for 3eTi and 24eTi samples with standard deviation included

	3eTi			24eTi		
Element	**Binding Energy (eV)**	**Atomic Concentration %**	**Total Atomic Concentration %**	**Binding Energy (eV)**	**Atomic Concentration %**	**Total Atomic Concentration %**
C 1s	281.1	6.41 ± 1.03	41.96 ± 0.79	-	-	37.42 ± 2.76
	284.8	28.14 ± 1.64		284.8	26.25 ± 4.90	
	286.3	4.35 ± 0.06		286.3	8.46 ± 4.78	
	287.8	0.54 ± 0.13		287.8	2.06 ± 1.50	
	288.8	2.58 ± 0.36		288.8	3.08 ± 0.61	
O 1s	530.1	23.75 ± 1.66	39.13 ± 0.16	530.5	27.86 ± 2.57	45.13 ± 1.44
	531.7	15.06 ± 1.82		531.9	18.41 ± 4.53	
Ti 2p	454.1	4.81 ± 0.57	18.93 ± 0.61	-	-	15.97 ± 1.02
	460.1	2.40 ± 0.28		-	-	
	458.7	8.22 ± 0.22		459.1	10.43 ± 0.50	
	464.4	3.73 ± 0.22		464.8	5.32 ± 0.25	

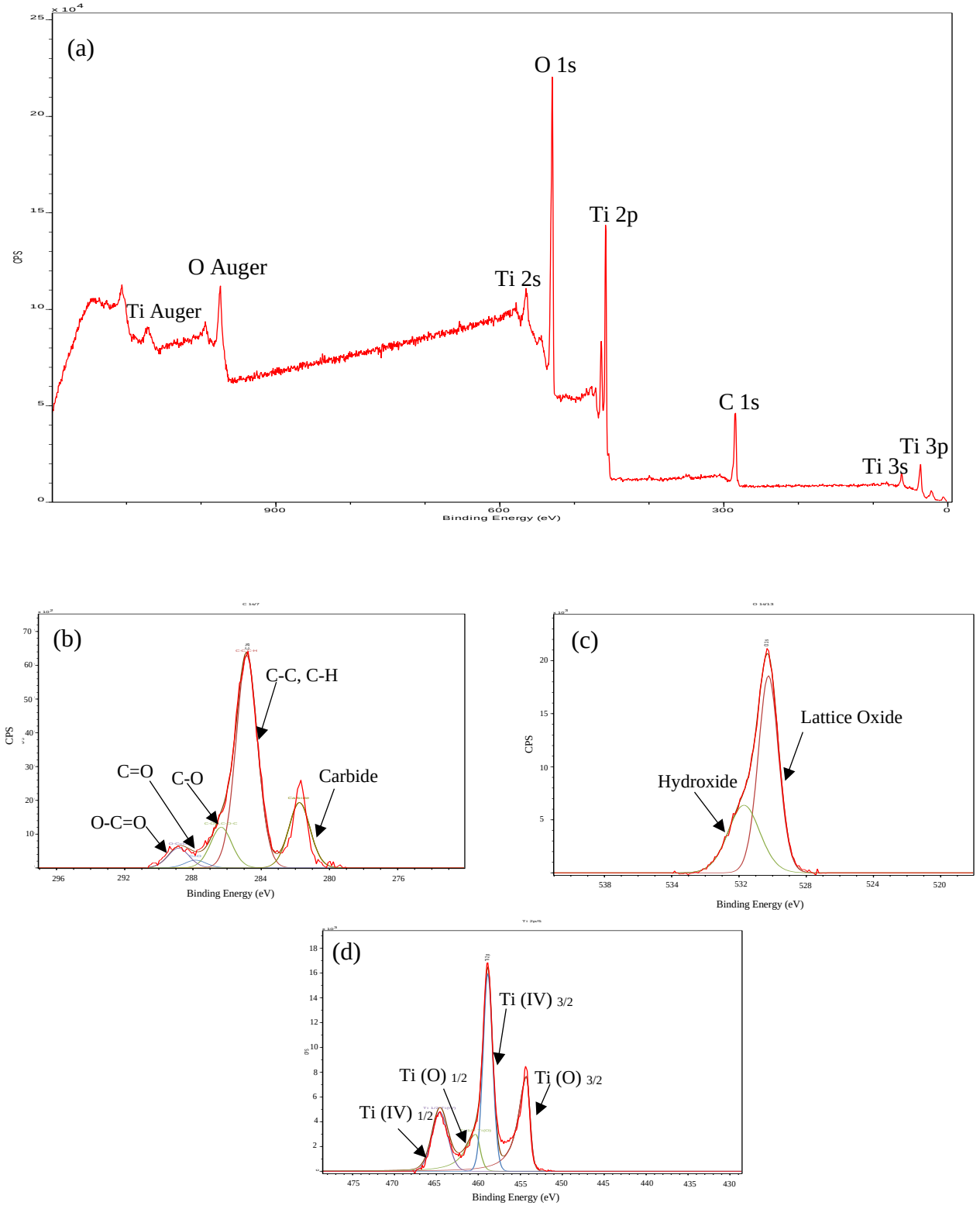

Figure 4.8 XPS spectra for 3eTi showing (a) WESS, and high-resolution spectra for (b) C 1s, (c) O 1s and (d) Ti 2p regions

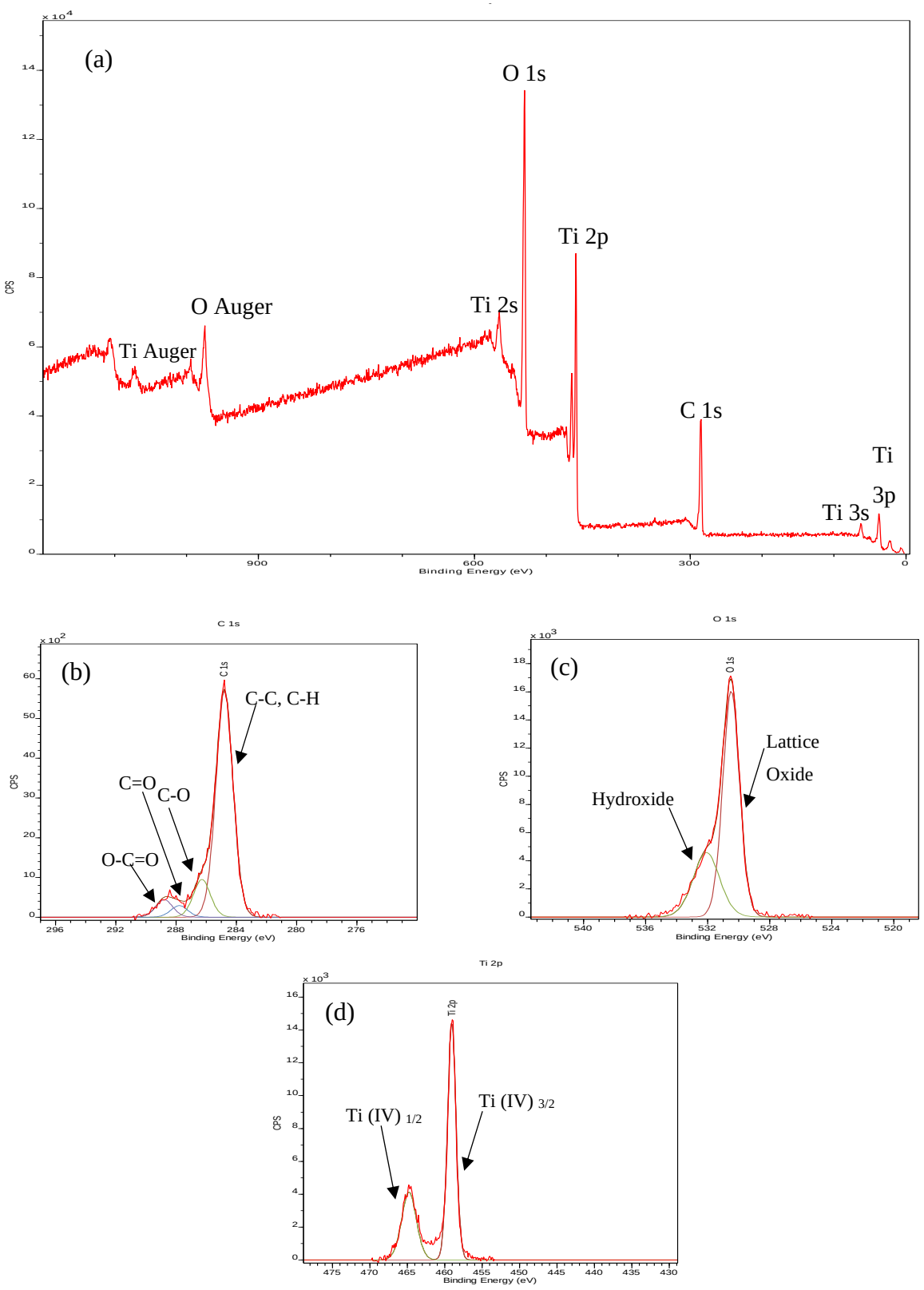

Figure 4.9 XPS spectra for 24eTi showing (a) WESS, and high-resolution spectra for (b) C 1s, (c) O 1s and (d) Ti 2p regions

4.3.2 XRD Analysis

An XRD plot for 3eTi is provided in Figure 4.10 (a) with peaks observed for at 2θ = 35˚, 36.4˚, 38.3˚, 40.1˚ and 53.1˚ corresponding to Miller indices (hkl) showing orientation in the 100, 004, 002, 101 and 102 planes, respectively, matching those for semi-crystalline titanium as indicated by ICDD file 00-044-1294[205].

Figure 4.10 (b) shows the x-ray diffractogram for the 24eTi samples with peaks present at 2θ = 35˚,38.3˚, 40.1˚ and 53.1˚ corresponding to the Miller indices (hkl) showing orientation in the 100, 002, 101 and 102 planes, respectively, which are again indicative of a semi-crystalline titanium substrate, according to ICDD file 00-044-1294[205]. Most notable here is the absence of the 004 plane which suggests that etching for the longer period of time reduces the occurrence of the natural oxide layer. However, these x-ray diffractograms support the assumption that this type of modification, for both timepoints, only influences surface morphology and does not have an impact on the crystallinity of the sample as a whole.

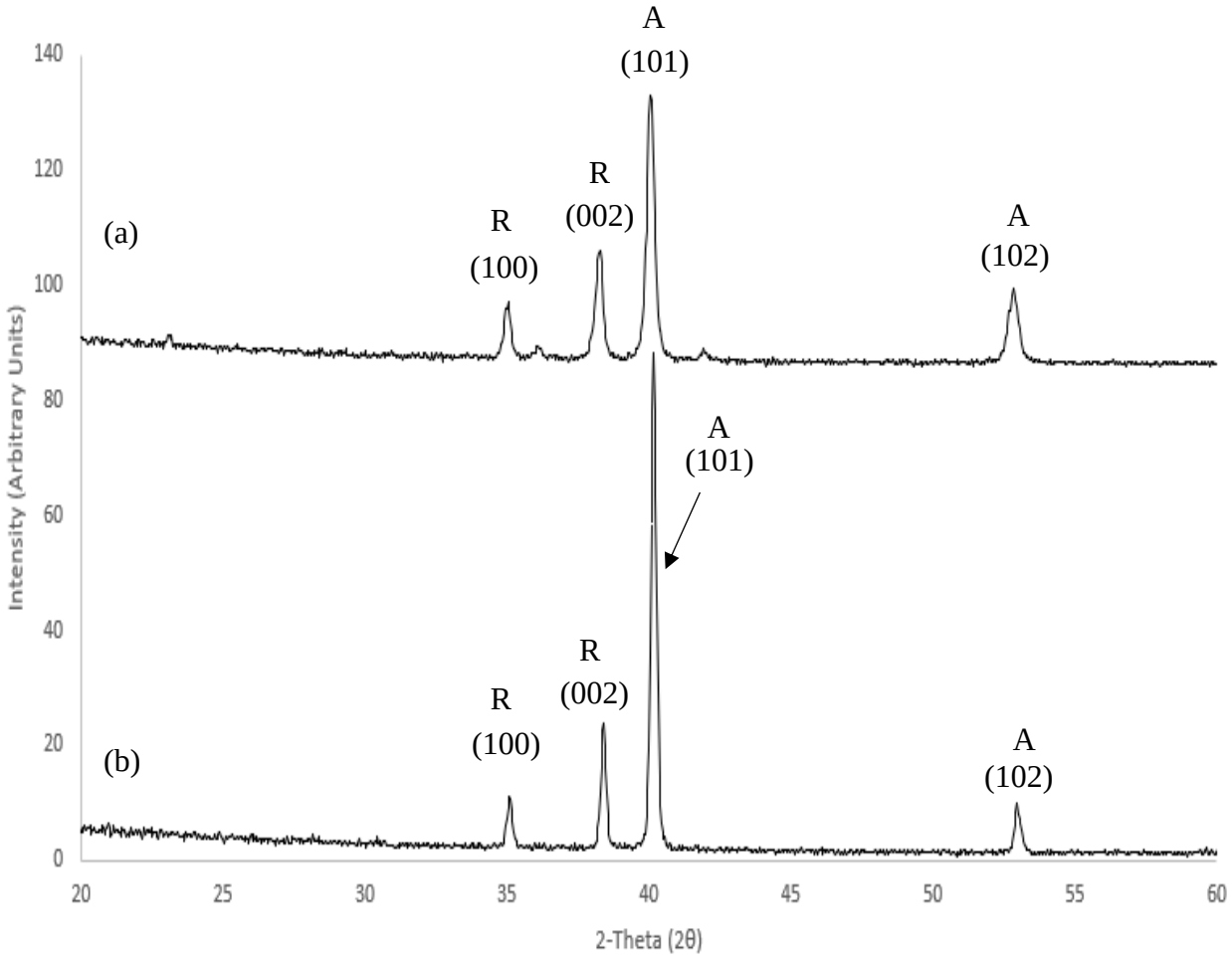

Figure 4.10 X-ray diffractograms for (a) 3eTi and (b) 24eTi with Miller index assignments labelled according to ICDD file 00-044-1394. Anatase (A) and rutile (R) phases also labelled

4.3.3 SEM Analysis

SEM images for the chemically etched samples were obtained at the same magnification as those for the Ti and the aTi samples. Figure 4.11 (a) – (d) shows the planar view images for 3eTi, with the corresponding 80˚ tilted images shown in Figure 4.11 (e) - (h). The x400 in planar view shows the lines and grooves that are also present in the Ti sample, in combination with what looks to be pitting on the surface. Higher magnification images indicate that this produces a randomly orientated morphology with nucleated material present around some of the pits.

SEM images of the 24eTi surface morphology are provided in Figure 4.12 (a) - (h), with both planar view ((a) - (d)) and 80˚ tilted views ((e) - (h)). In this case, there is a much more pronounced ‘honeycomb’ pitting across the substrate surface but no build-up of nucleated material around the pits is observed. Overall, the pitting seems to be homogenous across the samples leading to an offset but somewhat repeatable topography having been generated.

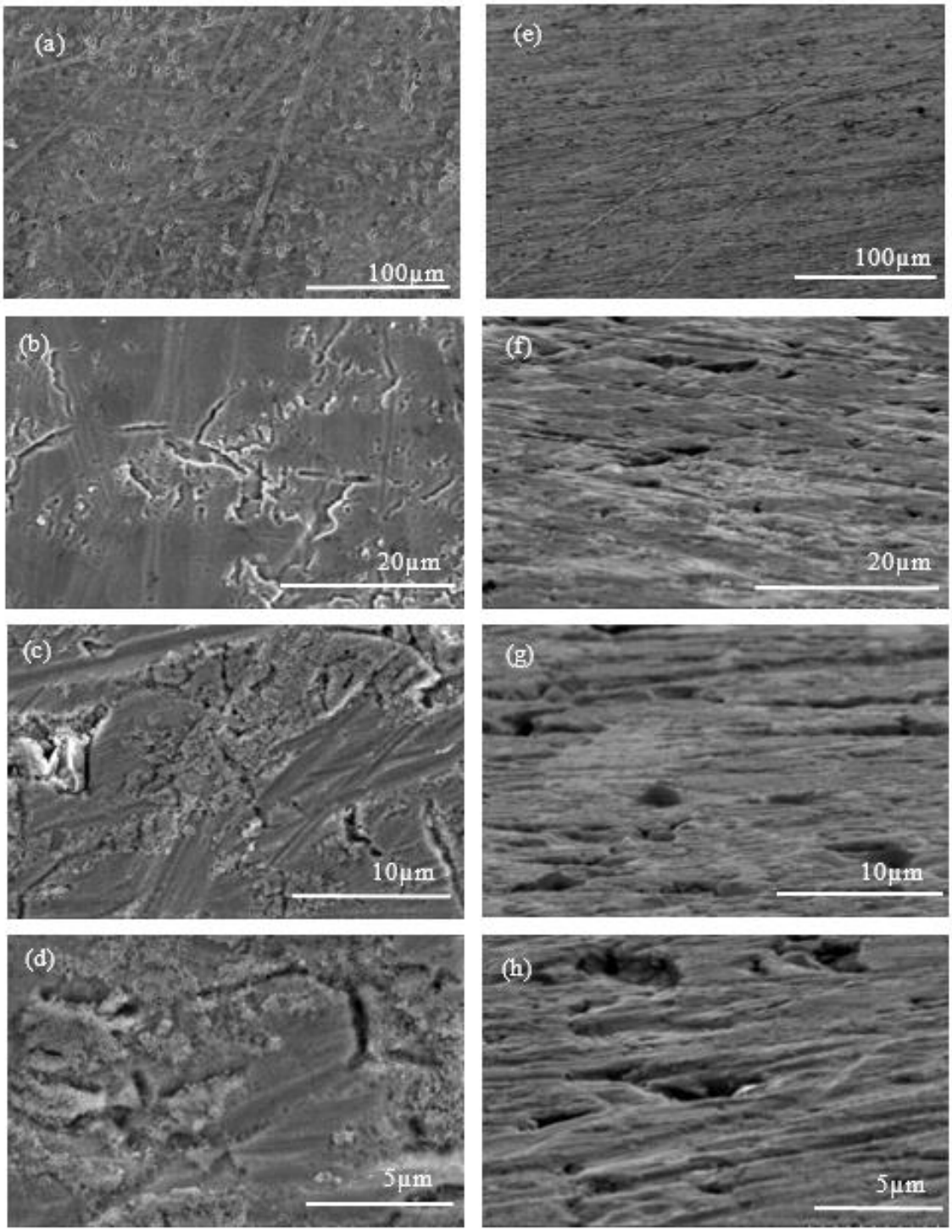

Figure 4.11 SEM images for 3eTi showing normal planar views (a) - (d) and 80˚ tilt side angle views (e)-(h) at magnifications of (a) x400, (b) x2.5k, (c) x4.5k (d) x8k, (e) x400, (f) x2.5k, (g) x4.5k, and (h) x8k

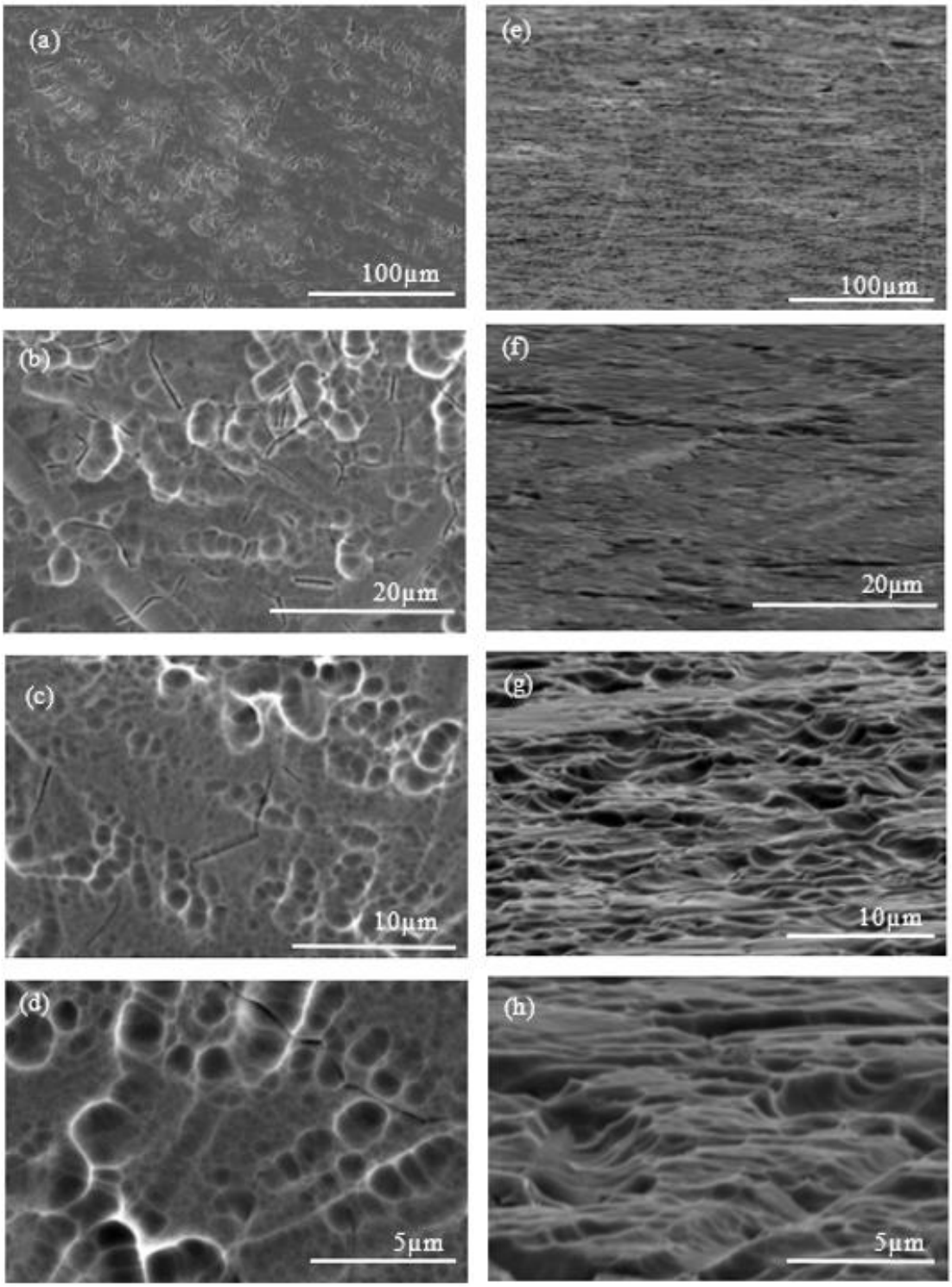

Figure 4.12 SEM images for 24eTi showing normal planar views (a)-(d) and 80˚ tilt side angle views (e) - (h) at magnifications of (a) x400, (b) x2.5k, (c) x4.5k (d) x8k, (e) x400, (f) x2.5k, (g) x4.5k, and (h) x8k

4.3.4 AFM Analysis

The 2D and 3D pseudo-colour AFM images for 3eTi samples are provided in Figure 4.13. In general, these surfaces look to be a lot rougher than those of the Ti and aTi samples (Figure 4.6 and Figure 4.7, respectively). The build-up of material around pitted areas, as noted in the SEM analysis, is also clearly evident in these AFM scans, as are the lines and grooves, characteristic of the pristine Ti surface. The Ra and Rq surface roughness data calculated are provided in Table 4.4 and indicate that the average Ra value is 44.04 ± 8.76 nm and the average Rq is 52.27 ± 11.44 nm. These values are significantly higher than those reported for the Ti and aTi samples, as is perhaps to be expected due to the piranha etching process. The standard deviation values are also higher here, suggesting that there is variation in surface roughness across the sample set.

Figure 4.14 shows the corresponding 2D and 3D pseudo-colour AFM images for the 24eTi samples and confirm an offset orientated but repeatable morphology across the substrate surface, as observed previously in the SEM images. The average Ra and Rq values (Table 4.4) for 24eTi are 49.30 ± 3.13 nm and 62.23 ± 2.88 nm, respectively and again reflect a greater overall surface roughness compared to the Ti, aTi and 3eTi samples. The lower standard deviation values for the 24eTi suggests that the surface roughness here is more consistent across the etched titanium surface.

Table 4.4 Average Ra and Rq values (n = 18) and image surface area difference in % (n =3) for 3eTi and 24eTi surfaces calculated from AFM images (n = 3) with standard deviation included

Sample Type	Ra (nm) ± Standard Deviation	Rq (nm) ± Standard Deviation	Image Surface Area Difference % ± Standard Deviation
3eTi	44.04 ± 8.76	52.27 ± 11.44	13.73 ± 2.37
24eTi	49.30 ± 3.13	62.23 ± 2.88	19.30 ± 3.47

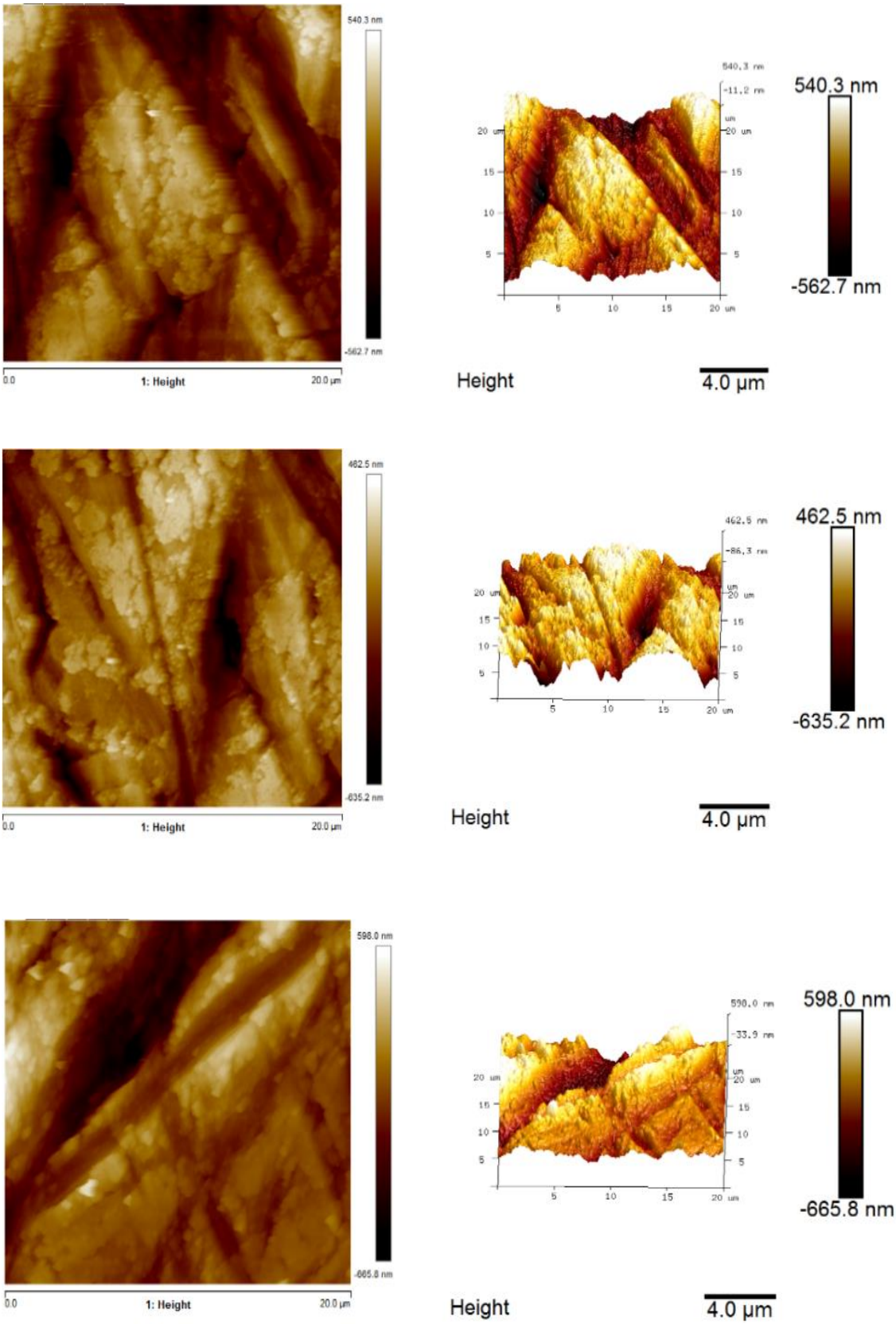

Figure 4.13 Pseudo- colour 20 µm x 20 µm 2D AFM images and corresponding 3D plots for 3eTi

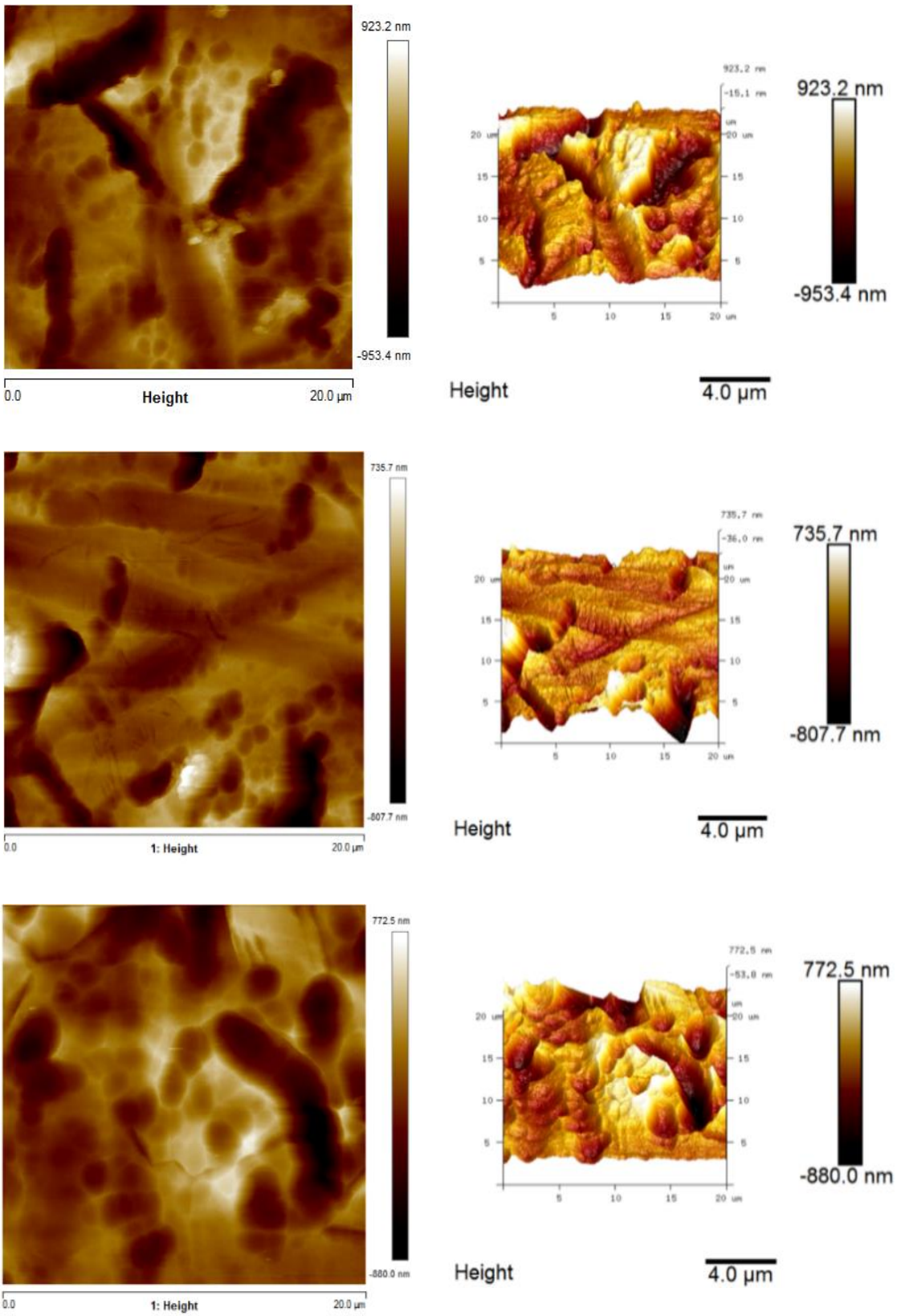

Figure 4.14 Pseudo- colour 20 µm x 20 µm 2D AFM images and corresponding 3D plots for 24eTi

4.4 Sputter Deposited Titanium Thin Films on Titanium

RF magnetron sputtering from pure titanium targets was used to create a polycrystalline (PolyTi) surface on Ti coupons at plasma power settings of 250 watts (W) and 400 W and compared to the chemically etched samples described in the previous section. The polycrystalline description used here refers to offset orientated areas of ordered microstructure that have been previously reported[29]. Both types of PolyTi samples generated here were subsequently thermally annealed at 500 ˚C (aPolyTi) in the same manner that was used to create the aTi surfaces reported in the previous section.

4.4.1 XPS Analysis

Figure 4.15 (a) shows the XPS WESS plot for polycrystalline titanium sputter deposited at 250 W (PolyTi250) with the peaks detected being very similar to those for Ti, aTi, 3eTi and 24eTi. The WESS spectrum for this sample after annealing at 500 ˚C (aPolyTi250) is provided in Figure 4.16 (a). The corresponding XPS WESS plots for polycrystalline surface sputtered at 400 W, before (PolyTi400) and after annealing at 500 ˚C (aPolyTi400) are given in Figure 4.17 (a) and Figure 4.18 (a), respectively.

The high-resolution spectra plots for the C 1s, O 1s and Ti 2p XPS regions for PolyTi250 and aPolyTi250 can be seen in Figures 4.15 (b) - (d) and 4.16 (b) - (d), respectively. The C 1s envelope shown in Figure 4.15 (b) details four peaks, as seen previously in Ti, aTi, 3eTi and 24eTi samples, with the largest peak attributed to adventitious carbon at 284.8 eV. The O 1s region (Figure 4.15 (c)) shows two peaks, with the larger of the two indicative of the lattice oxide at 530.1 eV, with the hydroxide peak at 531.5 eV. Figure 4.15 (d) shows that there are two doublets present in the Ti 2p region. The first doublet, seen for Ti $2p_{3/2}$ at 453.8 eV and Ti $2p_{1/2}$ at 460.1 eV, is indicative of the presence of Ti metal, which is as expected in the unannealed Ti samples. The second doublet is attributed to TiO_2, notable for Ti $2p_{3/2}$ at 458.5 eV and Ti $2p_{1/2}$ at 464.3 eV. The quantification data of these surfaces are provided in Table 4.5.

Figure 4.16 (b) shows the C 1s region for aPolyTi250. As seen in the previous samples, there are again four carbon peaks present with the most intense of the peaks attributed to adventitious carbon on the surface. There is a notable decrease in overall carbon content in aPolyTi250, as reflected by a decrease in C/O from 0.98 for PolyTi250 to 0.75 for aPolyTi250. The O 1s region (Figure 4.16 (c)) shows two peaks; a larger peak at 530.2 eV indicative of the lattice oxide, and a smaller hydroxide peak at 531.6 eV. As expected, the aPolyTi250 sample in Figure 4.16 (d) shows a single doublet for Ti 2p, indicative of an increase of the amount of surface oxide compared to the PolyTi250

sample (Figure 4.15 (d)). This is further supported by the data in Table 4.5 which shows a slight increase in the Ti/O of 0.39 for PolyTi250 compared to 0.34 for aPolyTi250 samples.

Table 4.5 XPS quantification data (n = 9) for PolyTi250 and aPolyTi250 samples with standard deviation included

	PolyTi250			aPolyTi250		
Element	**Binding Energy (eV)**	**Atomic Concentration %**	**Total Atomic Concentration %**	**Binding Energy (eV)**	**Atomic Concentration %**	**Total Atomic Concentration %**
C 1s	284.8	33.38 ± 5.39	41.29 ± 6.37	284.8	30.38 ± 3.91	35.83 ± 5.18
	286.3	4.43 ± 1.86		286.3	2.22 ± 0.47	
	287.8	1.51 ± 0.23		287.8	1.23 ± 0.65	
	288.8	2.24 ± 0.51		288.8	1.99 ± 0.79	
O 1s	530.1	25.52 ± 5.29	42.24 ± 3.55	530.2	34.36 ± 2.60	47.81 ± 3.16
	531.5	16.41 ± 1.47		531.6	13.57 ± 1.80	
Ti 2p	453.8	2.59 ± 0.30	16.47 ± 2.95	-	-	16.36 ± 2.02
	460.1	1.22 ± 0.20		-	-	
	458.5	8.64 ± 1.69		458.9	10.83 ± 1.09	
	464.3	4.06 ± 0.91		464.6	5.41 ± 0.55	

Table 4.6 XPS quantification data (n = 9) for PolyTi400 and aPolyTi400 samples with standard deviation included

	PolyTi400			aPolyTi400		
Element	**Binding Energy (eV)**	**Atomic Concentration %**	**Total Atomic Concentration %**	**Binding Energy (eV)**	**Atomic Concentration %**	**Total Atomic Concentration %**
C 1s	284.8	20.76 ± 1.10	27.69 ± 2.20	284.8	25.80 ± 2.07	31.33 ± 3.62
	286.3	3.49 ± 0.46		286.4	2.40 ± 0.56	
	287.9	1.15 ± 0.32		287.9	1.14 ± 0.19	
	288.8	2.24 ± 0.35		288.9	2.28 ± 0.77	
O 1s	530.1	31.52 ± 2.94	50.96 ± 1.49	529.9	37.83 ± 3.62	49.86 ± 1.52
	531.5	19.08 ± 2.50		531.5	12.42 ± 2.02	
Ti 2p	453.8	3.20 ± 0.24	21.35 ± 0.78	-	-	18.88 ± 2.04
	460.1	1.60 ± 0.12		-	-	
	458.5	11.44 ± 0.64		458.6	12.09 ± 1.26	
	464.3	5.51 ± 0.25		464.3	6.02 ± 0.65	

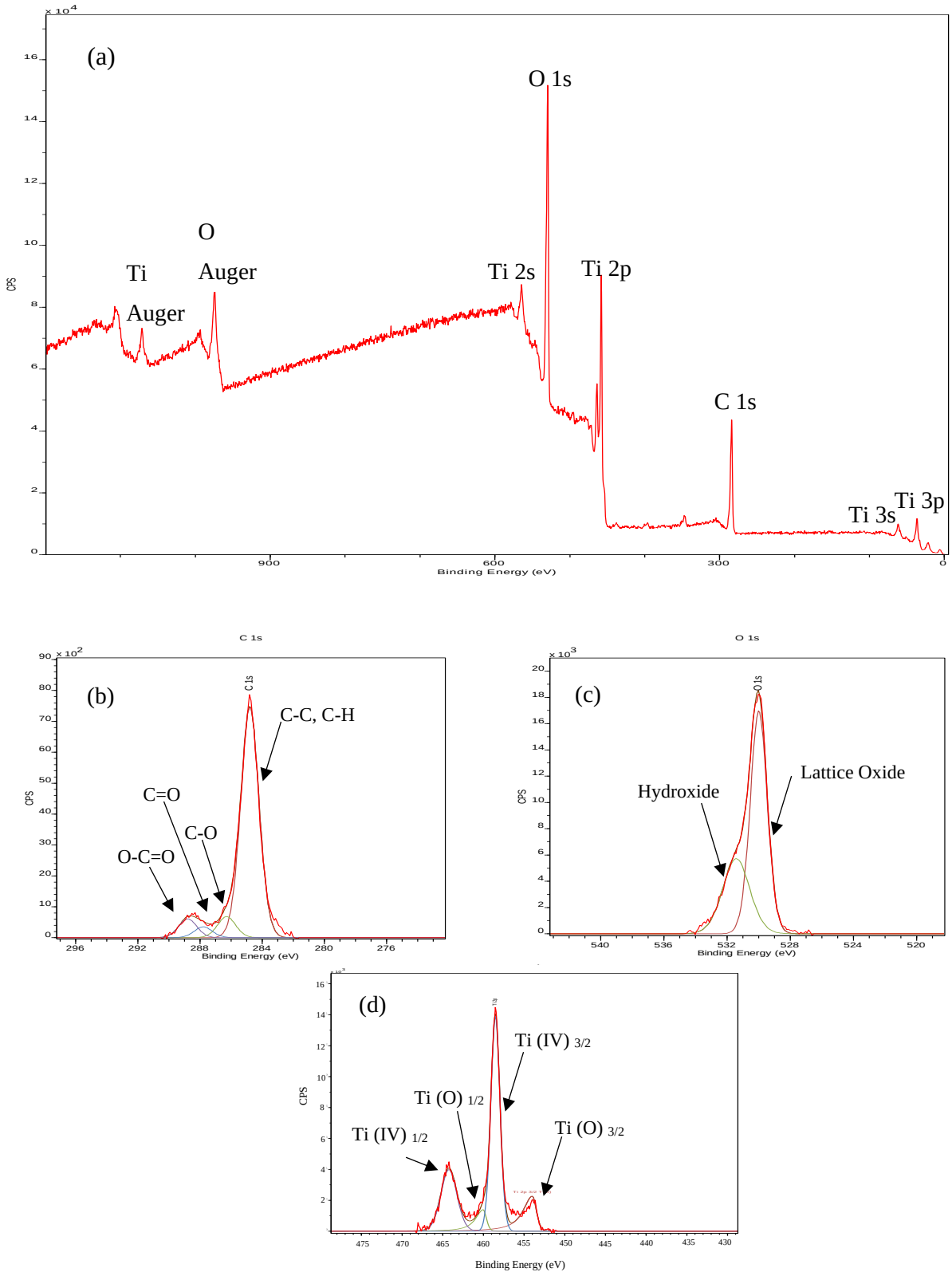

Figure 4.15 XPS spectra for PolyTi250 showing (a) WESS, and high-resolution spectra for (b) C 1s, (c) O 1s and (d) Ti 2p regions

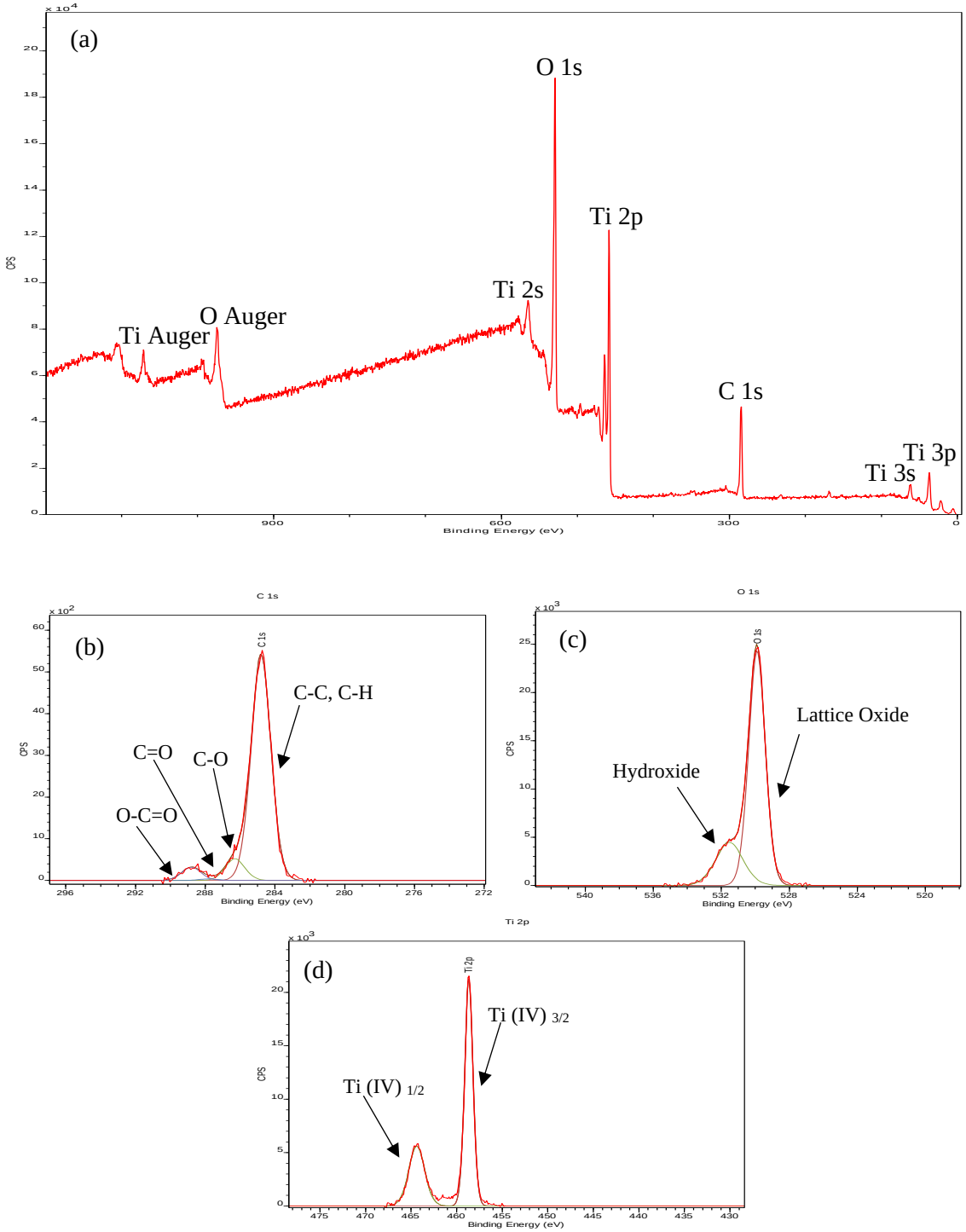

Figure 4.16 XPS spectra for aPolyTi250 showing (a) WESS, and high-resolution spectra for (b) C 1s, (c) O 1s and (d) Ti 2p regions

The XPS WESS plots for PolyTi400 and aPolyTi400 are provided in Figure 4.17 (a) and Figure 4.18 (a), respectively, with the corresponding high-resolution C 1s, O 1s and Ti 2p spectra presented in Figure 4.17 (b) - (d) and Figure 4.18 (b) - (d), respectively. The C 1s region for the PolyTi400 sample (Figure 4.17 (b)) shows the expected four carbon peaks, as seen in Ti, aTi, 3eTi, 24eTi, PolyTi250 and aPolyTi250 samples. The O 1s region (Figure 4.17 (c)) shows two peaks with the hydroxide peak at 531.5 eV being similar in intensity to that of the aPolyTi250 and a more intense lattice oxide peak at 530.1 eV. The Ti 2p region presented (Figure 4.17 (d)) shows two doublets, of which are attributed to Ti metal and TiO_2. The quantitative data are provided in Table 4.6 and indicate that the amount of TiO_2 present on the PolyTi400 sample, is similar to that for aPolyTi250.

Figure 4.18 (b) shows the C 1s region for aPolyTi400 and has the four expected peaks which are similar to those seen for the previous samples. The dominant peak in the O 1s region (Figure 4.18 (c)) at 529.9 eV is that of the lattice oxide, with a hydroxide peak of decreased intensity seen at 531.5 eV. There is an expected increase in the relative amount of the lattice oxide peak due to an increased surface oxide layer that occurs after annealing. This is confirmed in the Ti 2p region (Figure 4.18 (d)) where there is only a single doublet present for Ti $2p_{3/2}$ at 458.6 eV and Ti $2p_{1/2}$ at 464.3 eV, attributed to Ti (IV), indicative of TiO_2. However, the increase in oxide here is lower than that for the PolyTi400 samples (Table 4.6). The calculated Ti/O for PolyTi400 is 0.42 which decreases to 0.38 in aPolyTi400. The C/O increases from 0.54 in PolyTi400 to 0.63 for aPolyTi400, thereby showing that an increase in the carbon content occurs after annealing which is different to the decrease reported for all of the previous annealed samples.

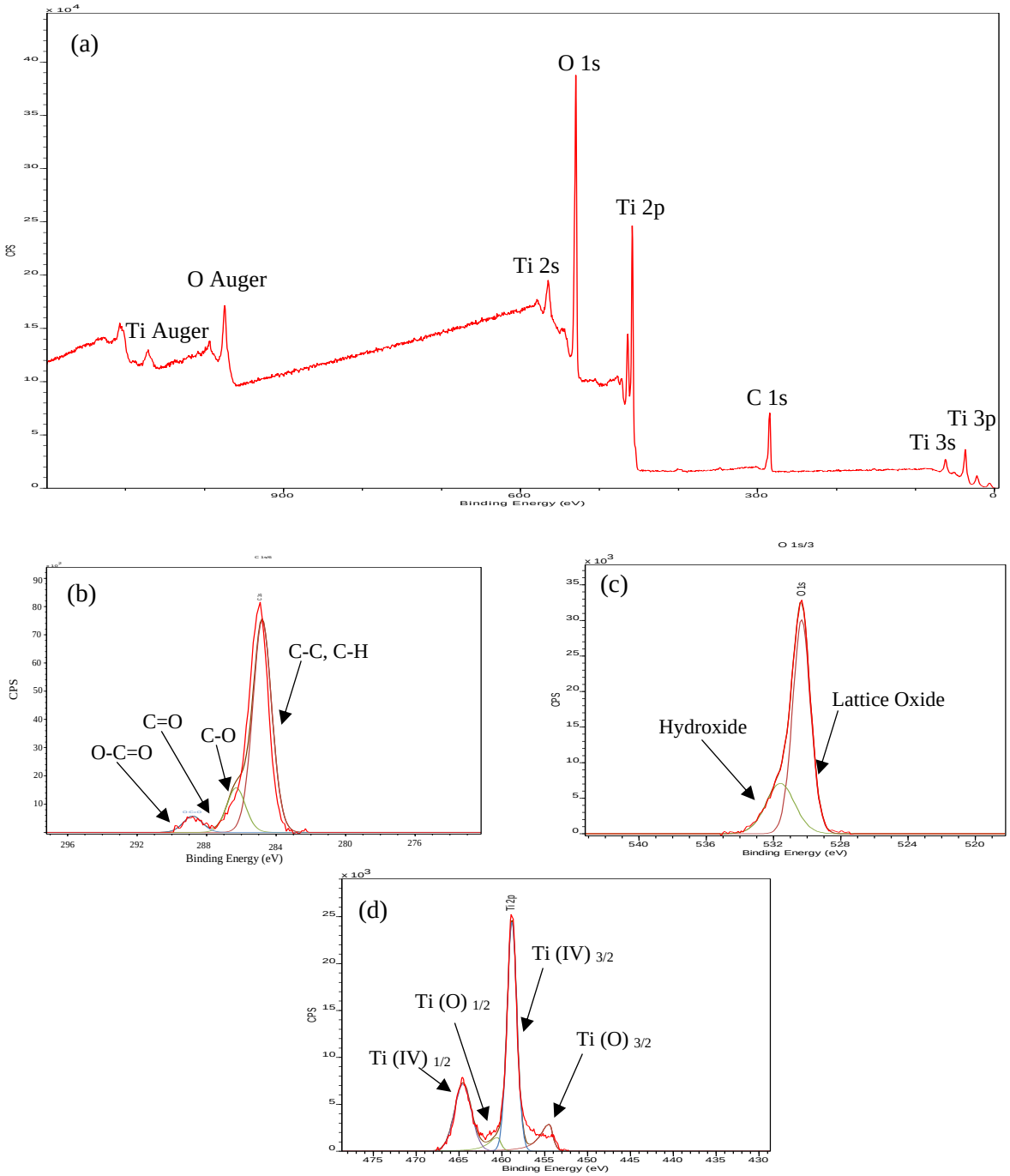

Figure 4.17 XPS spectra for PolyTi400 showing (a) WESS, and high-resolution spectra for (b) C 1s, (c) O 1s and (d) Ti 2p regions

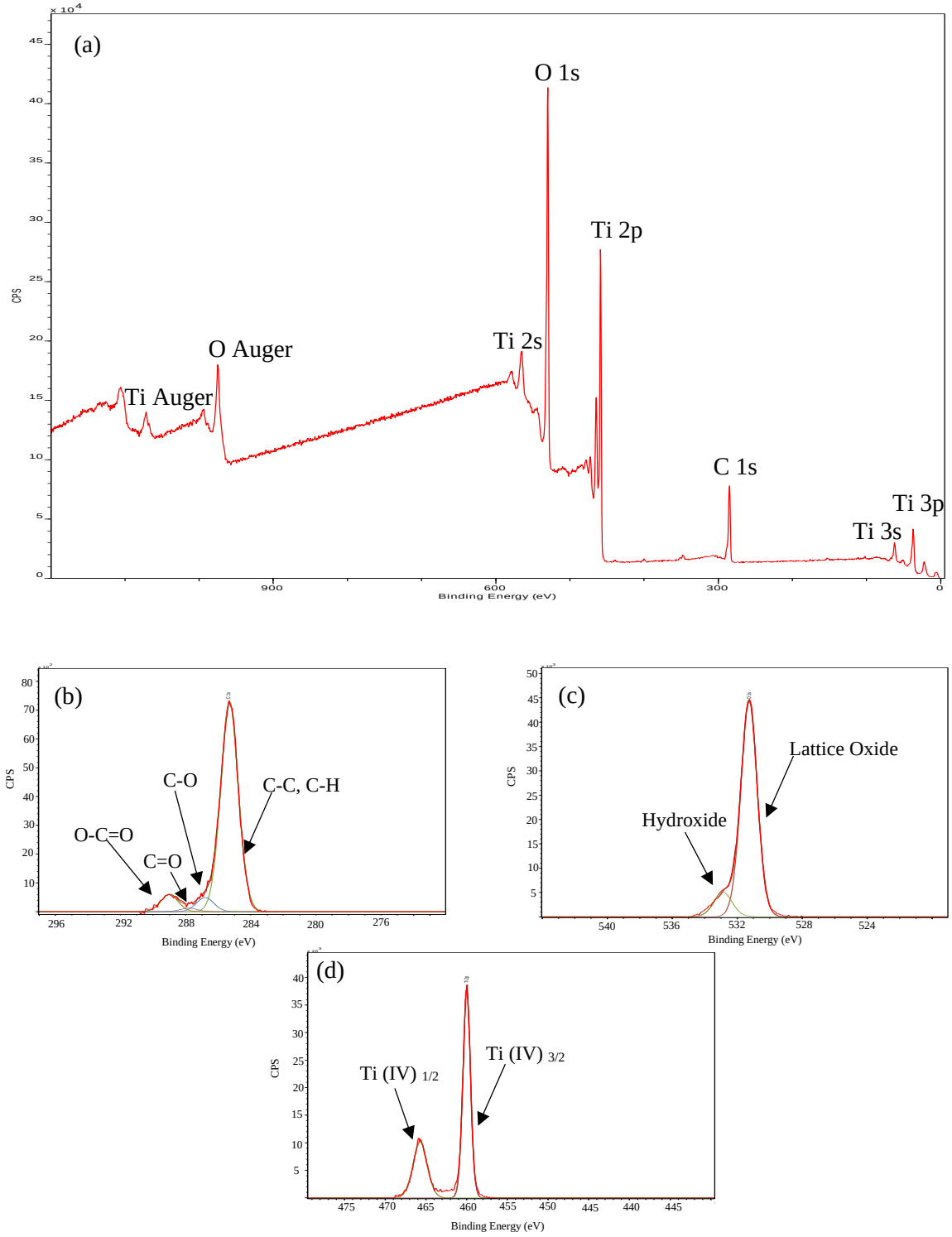

Figure 4.18 XPS spectra for aPolyTi400 showing (a) WESS, and high-resolution spectra for (b) C 1s, (c) O 1s and (d) Ti 2p regions

4.4.2 XRD Analysis

The x-ray diffractograms for PolyTi250, aPolyTi250, PolyTi400 and aPolyTi400 are provided in Figure 4.19 (a) - (d), respectively. The peaks detected are found to be similar to those observed for Ti, aTi, 3eTi and 24eTi. The only significant difference here is seen for the 2θ = 36.2˚ peak associated with Miller index (hkl) orientation in the 004 plane, which is significantly more intense for the PolyTi250 and aPolyTi250 samples (Figure 4.19 (a) - (b), respectively). In the case of the PolyTi400 (Figure 4.19 (c)), only one peak is present at 2θ = 36.4˚, which corresponds to the Miller index (hkl) orientation in the 004 plane, indicative of TiO_2. When PolyTi400 is thermally annealed to create aPolyTi400 (Figure 4.19 (d)), the diffractogram reverts to being similar to that seen for previous samples, i.e. representing the expected semi-crystalline state of titanium. This suggests that the higher sputtering power causes thickening of the natural oxide layer on the polycrystalline titanium surface.

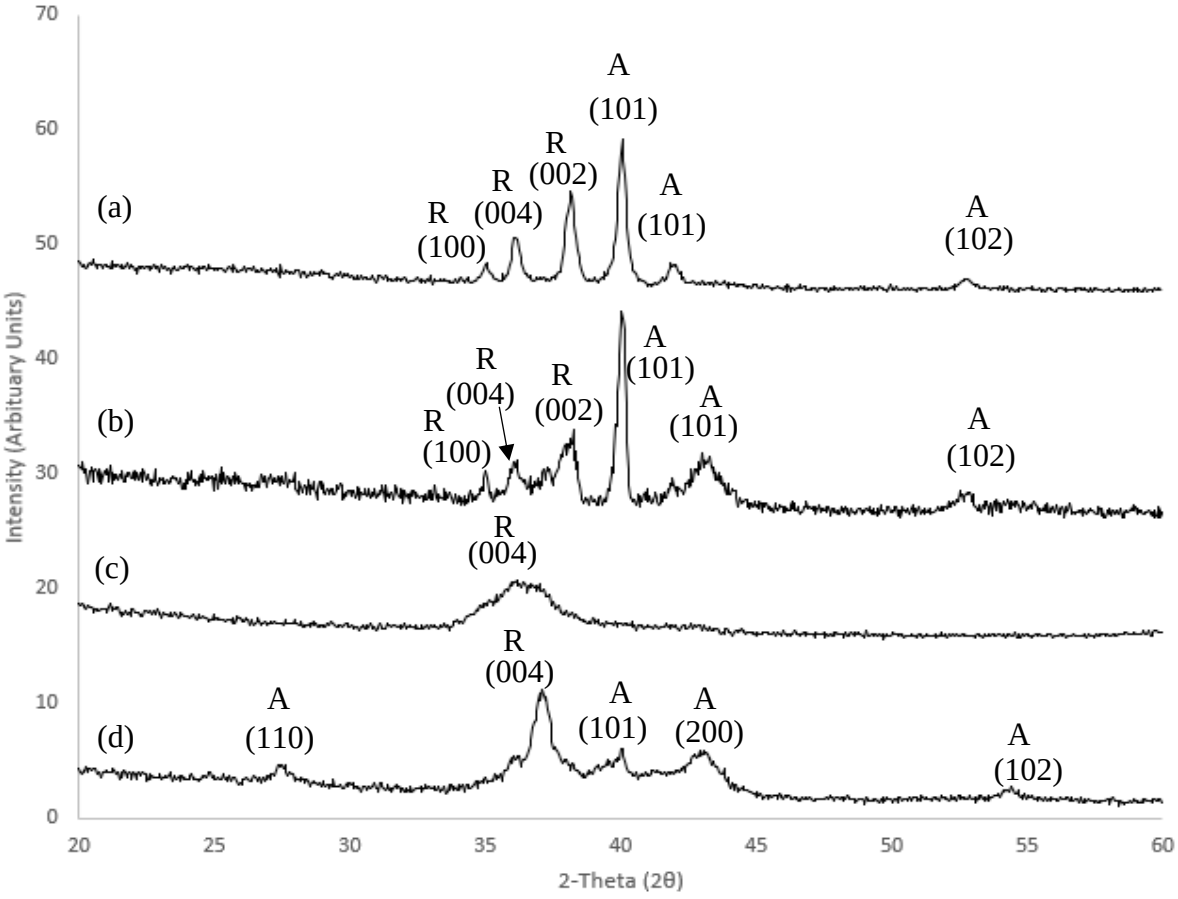

Figure 4.19 X-ray diffractograms for (a) PolyTi250, (b) aPolyTi250, (c) PolyTi400 and (d) aPolyTi400, with Miller index assignments labelled according to ICDD file 00-044-1294. Anatase (A) and rutile phases (R) also labelled

4.4.3 SEM Analysis

Images gathered and presented for the polycrystalline samples were taken at the same magnifications as the samples presented in this chapter previously, so as to allow for comparison. The SEM images for PolyTi250, aPolyTi250, PolyTi400 and aPolyTi400 are shown in Figure 4.20 (a) - (h), Figure 4.21 (a) - (h), Figure 4.22 (a) - (h) and Figure 4.23 (a) - (h), respectively. Images collected for PolyTi250 (Figure 4.20 (a) – (h)) suggest a surface morphology similar to that of the pristine Ti (Figure 4.4). However, there are some areas of nucleation of the sputtered Ti material, predominantly present along the lines and grooves on surface. Although, the aPolyTi250 images (Figure 4.21 (a) – (h)) do present a surface morphology similar to that of the PolyTi250, but with less nucleation of material present across the surface.

The PolyTi400 and aPolyTi400 (Figure 4.20 (a) - (h) and Figure 4.21 (a) - (h), respectively) exhibit a similar morphology to the PolyTi250 samples, both annealed and unannealed, but upon higher magnification display areas of nucleation. The aPolyTi400 samples show a higher amount of nucleated material on the surface, predominantly along the lines and grooves across the surface.

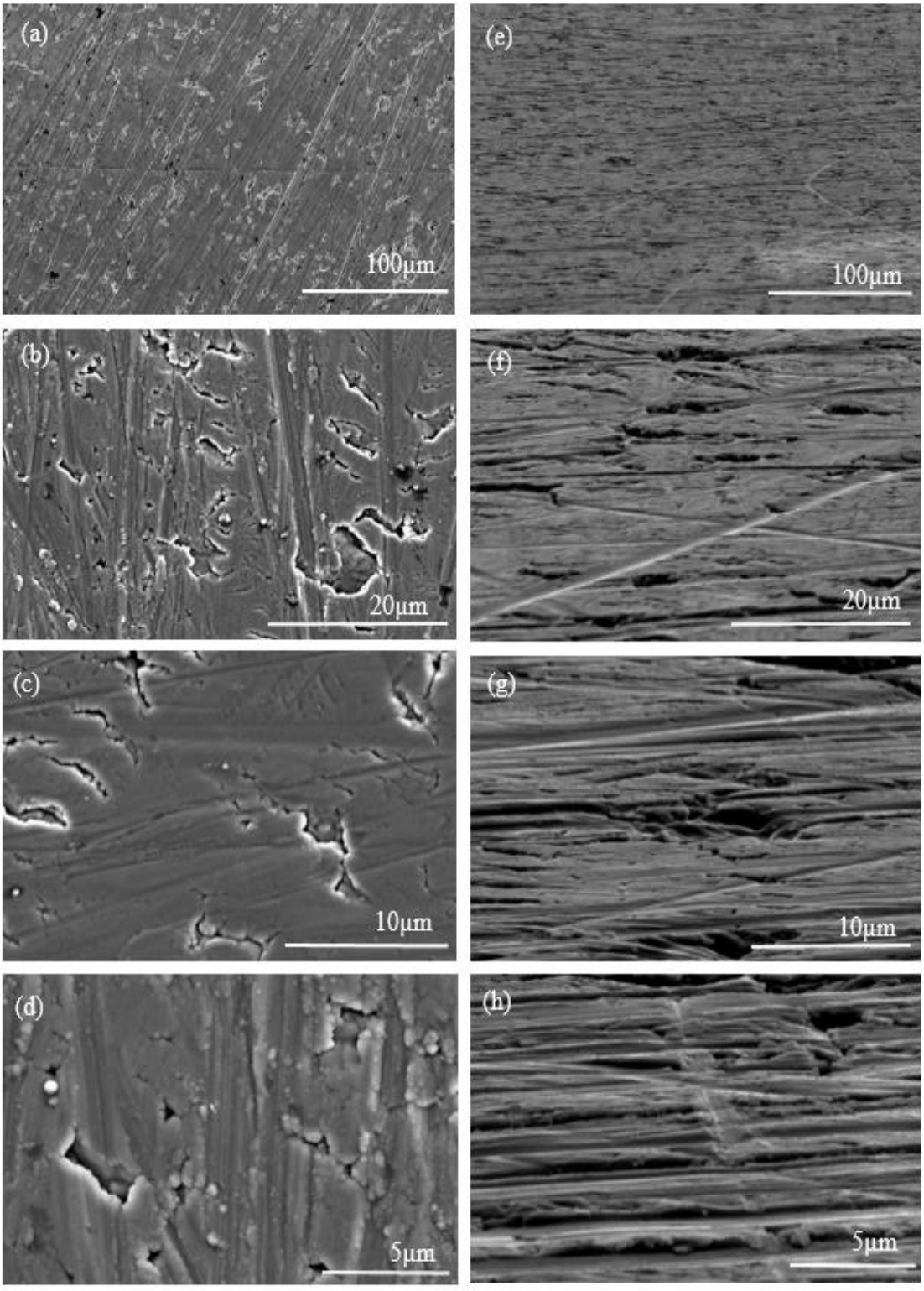

Figure 4.20 SEM images for PolyTi250 showing normal planar views (a)-(d) and 80˚ tilt side angle views (e)-(h) at magnifications of (a) x400, (b) x2.5k, (c) x4.5k (d) x8k, (e) x400, (f) x2.5k, (g) x4.5k, and (h) x8k

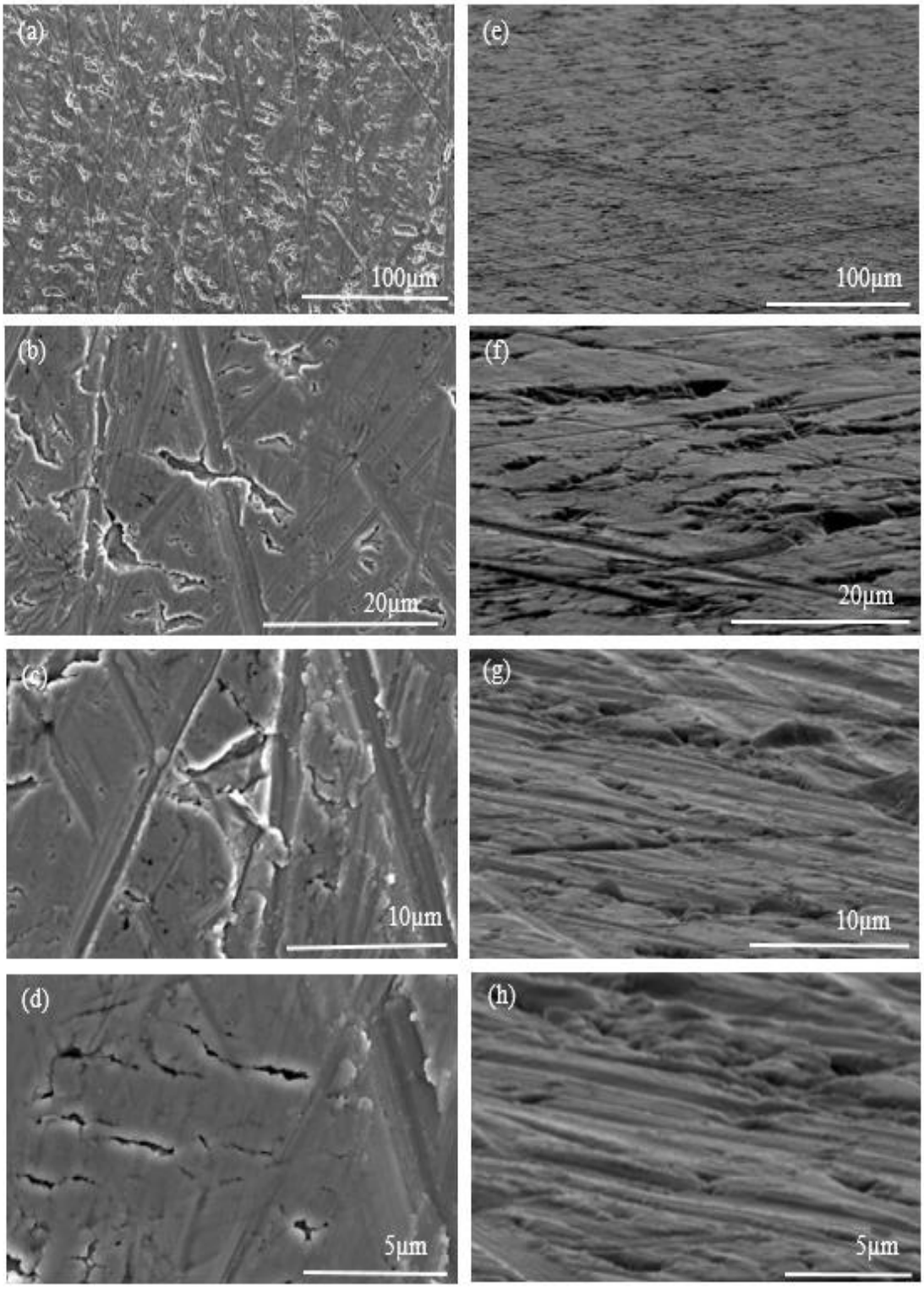

Figure 4.21 SEM images for aPolyTi250 showing normal planar views (a)-(d) and 80˚ tilt side angle views (e)-(h) at magnifications of (a) x400, (b) x2.5k, (c) x4.5k (d) x8k, (e) x400, (f) x2.5k, (g) x4.5k, and (h) x8k

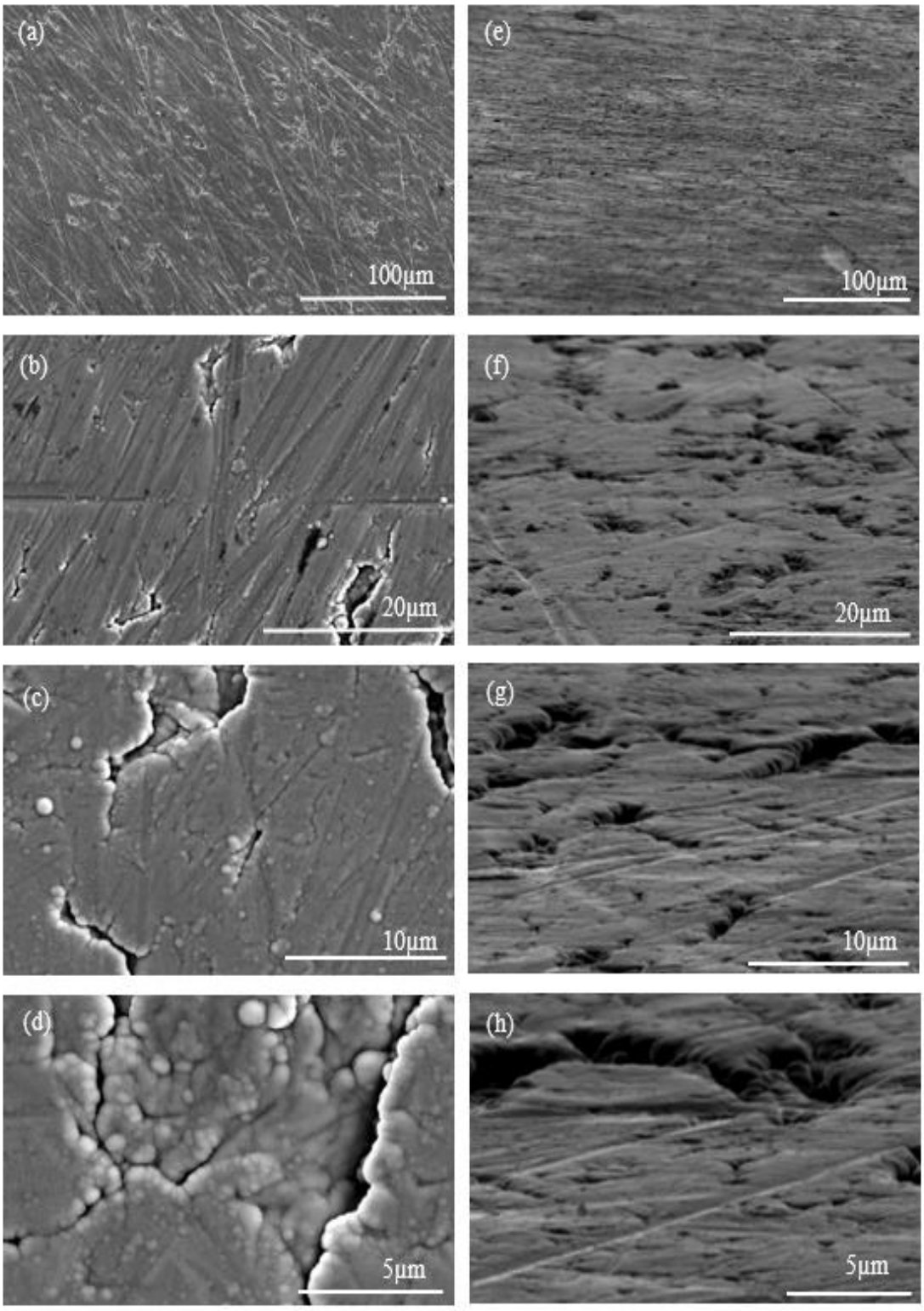

Figure 4.22 SEM images for PolyTi400 showing normal planar views (a)-(d) and 80˚ tilt side angle views (e)-(h) at magnifications of (a) x400, (b) x2.5k, (c) x4.5k (d) x8k, (e) x400, (f) x2.5k, (g) x4.5k, and (h) x8k

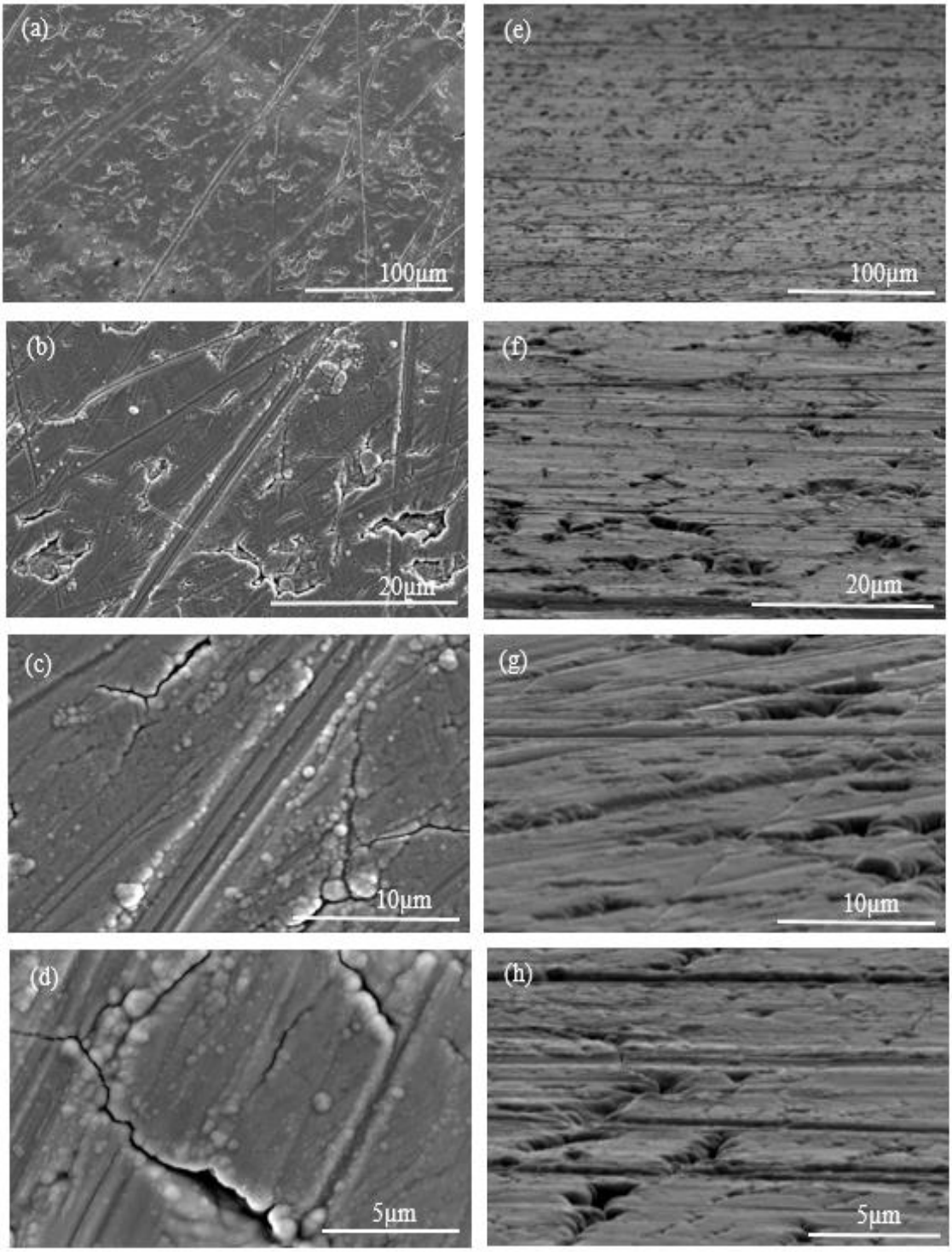

Figure 4.23 SEM images for aPolyTi400 showing normal planar views (a)-(d) and 80˚ tilt side angle views (e)-(h) at magnifications of (a) x400, (b) x2.5k, (c) x4.5k (d) x8k, (e) x400, (f) x2.5k, (g) x4.5k, and (h) x8k

4.4.4 AFM Analysis

Figure 4.24 shows the 2D and 3D AFM images generated for PolyTi250. The lines and grooves present due to processing and cleaning of the pristine Ti are still evident, as the SEM images confirmed. There are also areas of nucleation, predominantly seen along these lines and grooves. The average Ra and Rq values calculated for PolyTi250 are 33.14 ± 8.87 nm and 41.09 ± 10.37 nm each respectively as provided in Table 4.7.

Figure 4.25 provides the corresponding 2D and 3D AFM images for aPolyTi250. As observed in the SEM images, obvious surface smoothing has occurred here, indicating the growth of surface titanium dioxide (TiO_2) due to thermal annealing. The average Ra and Rq values (Table 4.7) confirm a significant drop in surface roughness. Although there are still areas of nucleation present overall, these surface appears to much smoother than that of PolyTi250.

Table 4.7 Average Ra and Rq values (n = 18) and image surface area difference in % (n =3) for PolyTi250 and aPolyTi250 surfaces calculated from AFM images (n = 3) with standard deviation included

Sample Type	**Ra (nm) ± Standard Deviation**	**Rq (nm) ± Standard ± Standard Deviation**	**Image Surface Area Difference % ± Standard Deviation**
PolyTi250	33.14 ± 8.87	41.09 ± 10.37	2.76 ± 0.07
aPolyTi250	17.45 ± 2.55	21.68 ± 3.17	2.11 ± 0.84

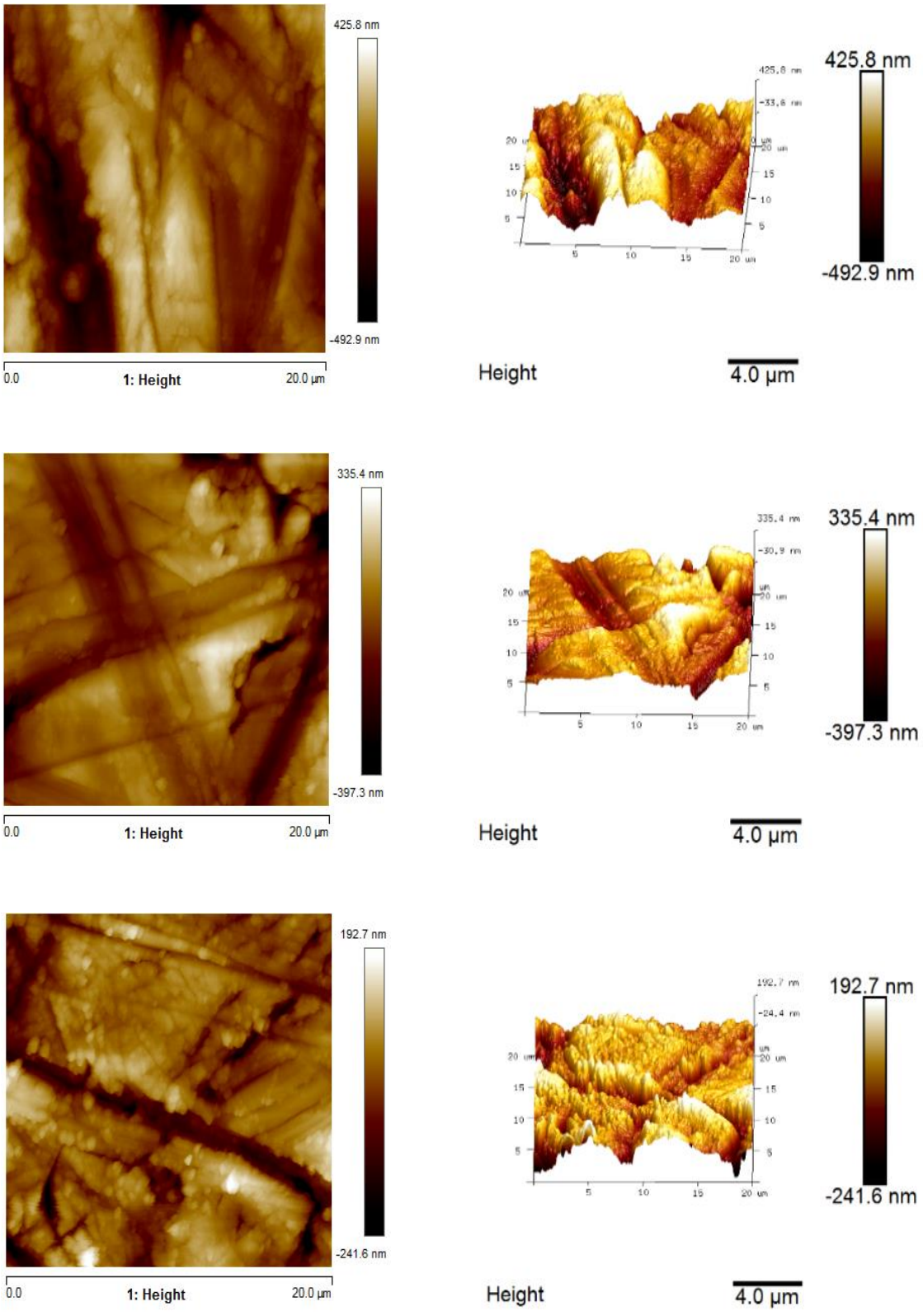

Figure 4.24 Pseudo- colour 20 µm x 20 µm 2D AFM images and corresponding 3D plots for PolyTi250

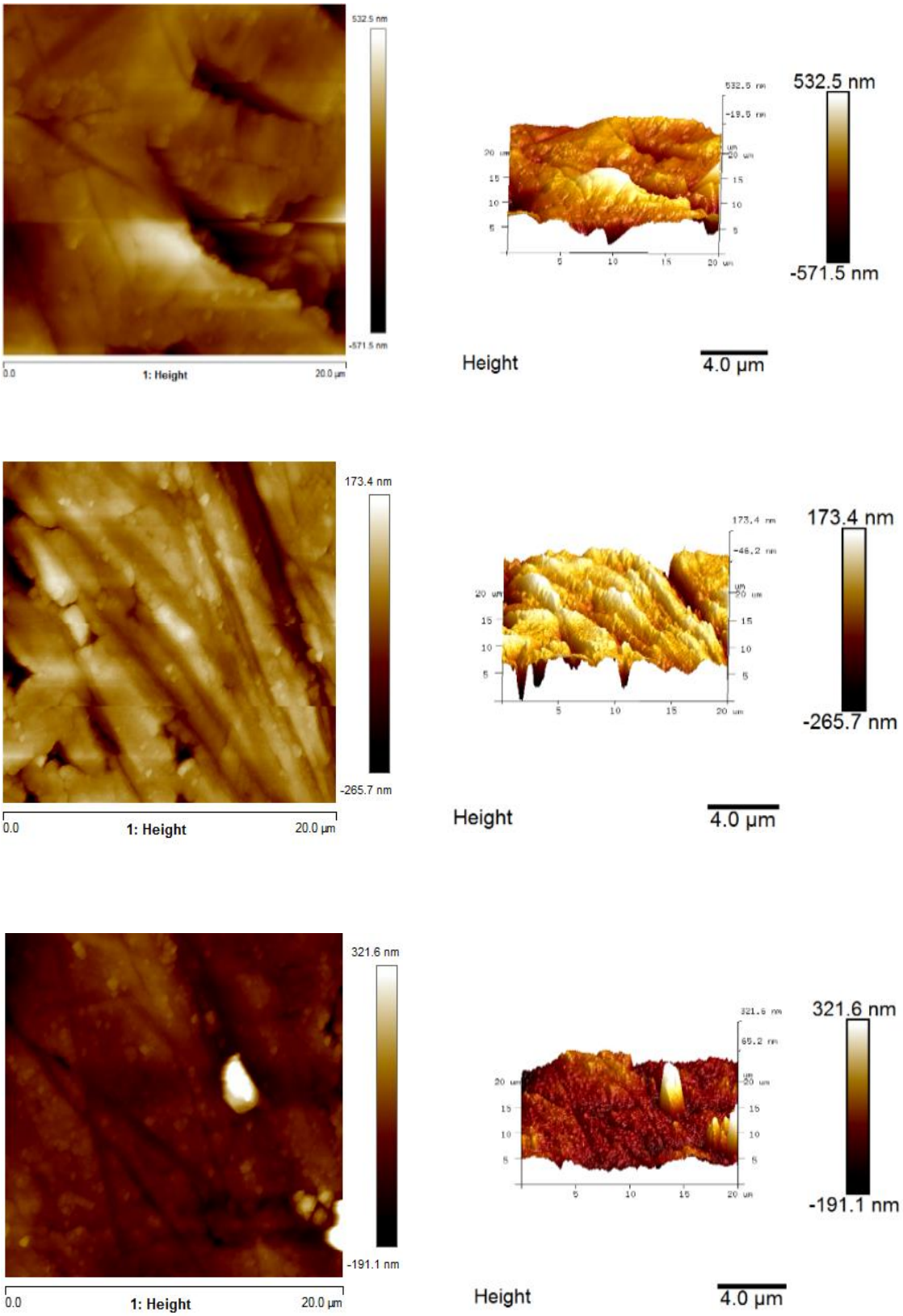

Figure 4.25 Pseudo- colour 20 µm x 20 µm 2D AFM images and corresponding 3D plots for aPolyTi250

The equivalent AFM images for PolyTi400 are provided in Figure 4.26 and those for aPolyTi400 in Figure 4.27 and show that the annealed surface appears to be rougher than that of the unannealed sample.

The Ra and Rq values calculated from the AFM data for PolyTi400 and aPolyTi400 are provided in Table 4.8. PolyTi400 has an average Ra of 22.80 ± 1.56 nm and a Rq value of 29.77 ± 1.60 nm, indicating a lower roughness than that of native Ti. This smoothing is consistent with the XPS and XRD data findings. For aPolyTi400 the Ra is 25.36 ± 9.24 nm and Rq is 31.88 ± 11.27. The standard deviation is larger here than for PolyTi400 but similar to the values recorded for Ti and aTi.

Table 4.8 Average Ra and Rq values (n = 18) and image surface area difference in % (n =3) for PolyTi400 and aPolyTi400 surfaces calculated from AFM images (n = 3) with standard deviation included

Sample Type	**Ra (nm) ± Standard Deviation**	**Rq (nm) ± Standard Deviation**	**Image Surface Area Difference % ± Standard Deviation**
PolyTi400	22.80 ± 1.56	29.77 ± 1.60	1.77 ± 0.40
aPolyTi400	25.36 ± 9.24	31.88 ±11.27	22.39 ± 15.93

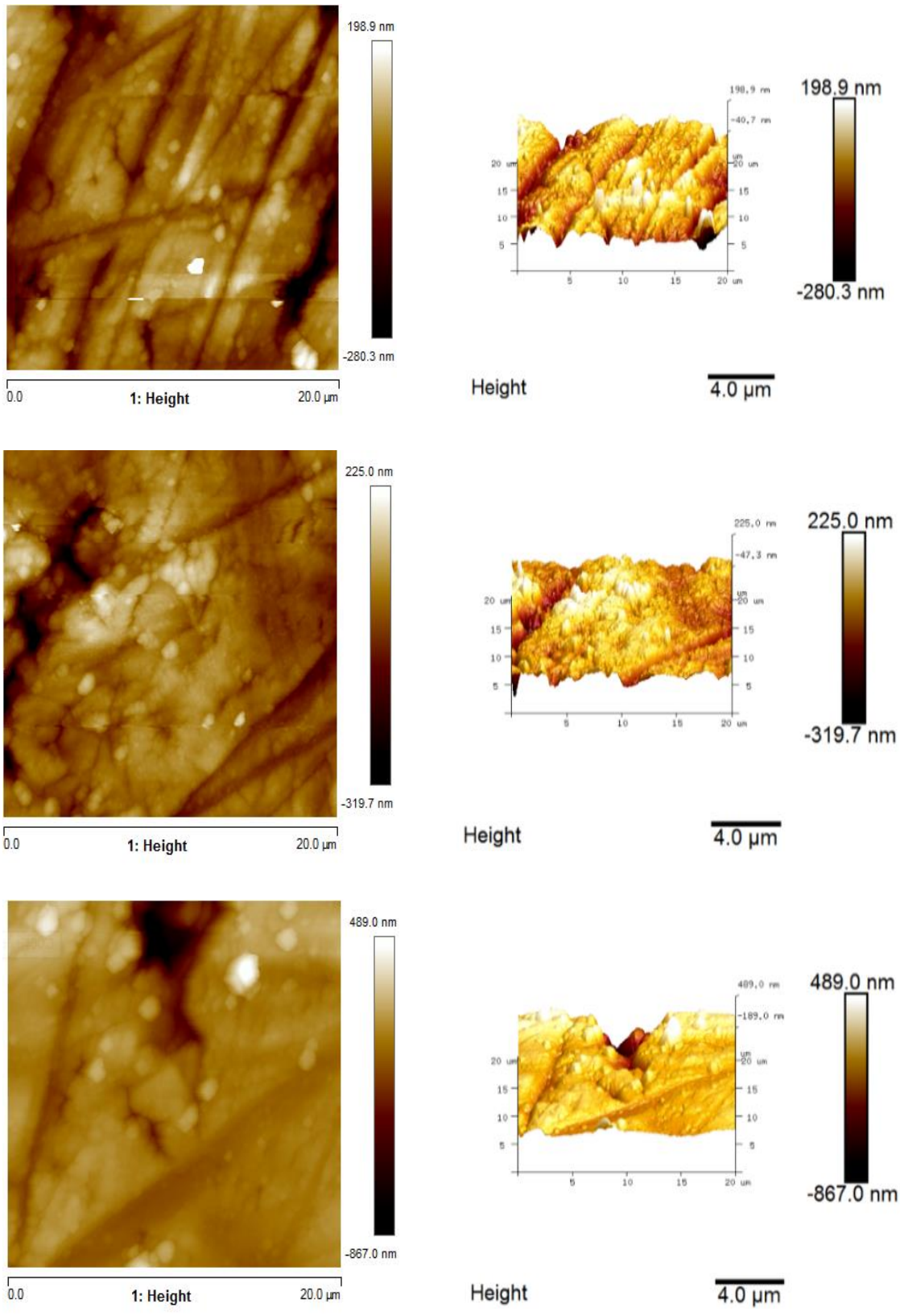

Figure 4.26 Pseudo- colour 20 µm x 20 µm 2D AFM images and corresponding 3D plots for PolyTi400

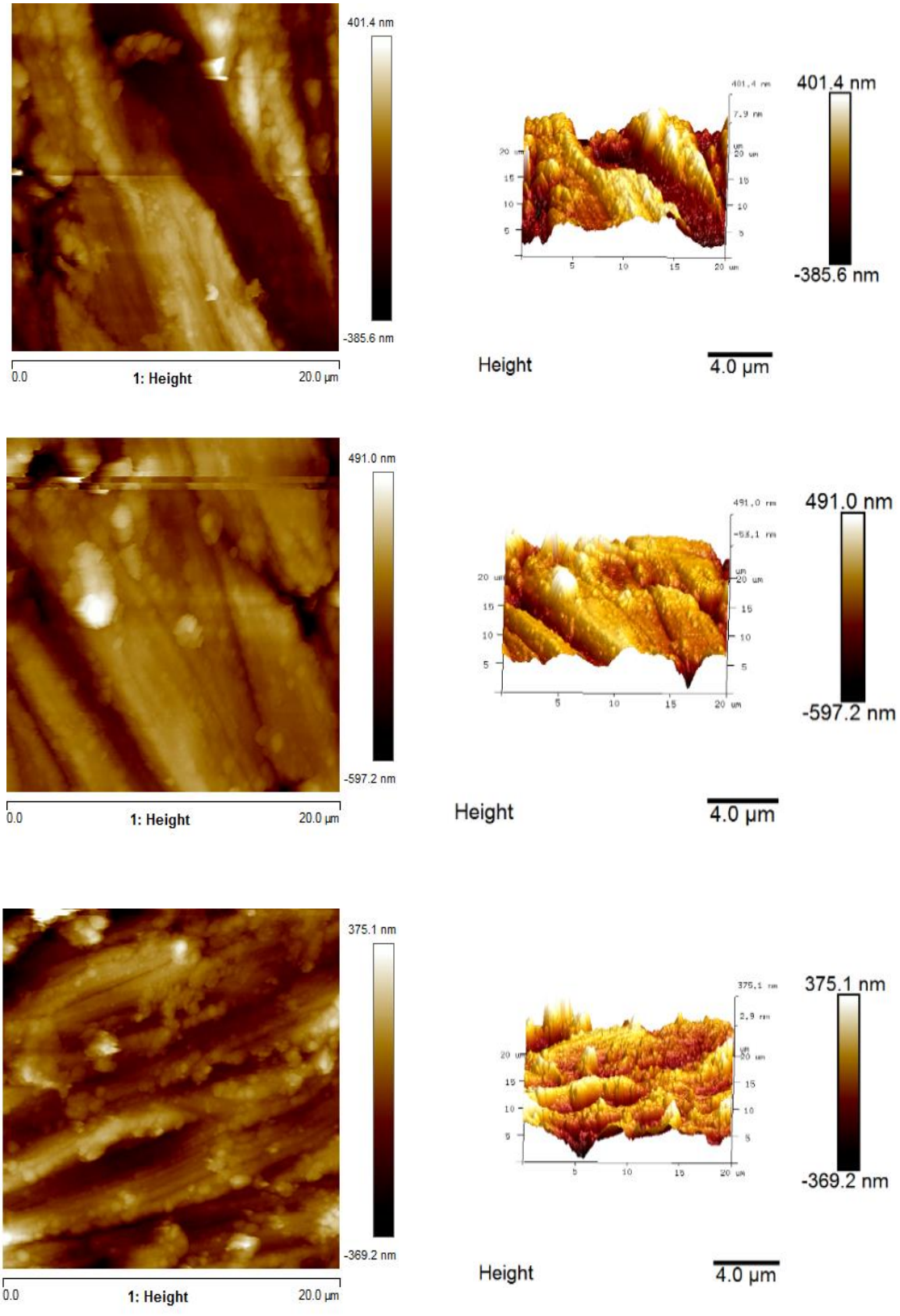

Figure 4.27 Pseudo- colour 20 µm x 20 µm 2D AFM images and corresponding 3D plots for aPolyTi400

4.5 Anodised Titanium

Chemical anodising of titanium has been shown to create various forms of titanium nanotubes (TiNT) and nanoscale topography, the properties of which depend on the electrochemical conditions applied. In order to create the surface conditions that can influence the dissolution of as-deposited CaP coatings, a protocol was used here that has been shown previously to create a nanotube topography[29,31,115].

4.5.1 XPS Analysis

XPS was again carried out to determine the surface chemistry of the titanium after anodisation. The WESS for TiNT is provided in Figure 4.28 (a) and shows many similarities to those of the samples presented in previous sections, with the exception that a fluorine (F 1s) signal is detected, the high-resolution spectra of which is presented in Figure 4.28 (e). Trace amounts of the ion are common after anodisation using a fluorine-based solvent. At small levels this fluorine is non-toxic to cells, but it was important to ensure that levels are as expected, and no other trace elements have become attached to the surface. The high-resolution spectra plots for all the major peaks (C 1s, O 1s, Ti 2p and F 1s) are shown in Figure 4.28 (b) - (e), respectively. Quantification data for these samples are given in Table 4.9 and confirm that the fluorine present is at levels below those that would lead to concern. Of particular note here is the large standard deviations for the C 1s, O 1s and Ti 2p contributions. The calculated Ti/O ratio of 0.26 here is much lower than for all previous samples. Conversely, the C/O ratio of 1.55 is higher than in previous cases, indicating that a high concentration of carbon is present on the surface of the TiNT samples.

Table 4.9 XPS quantification (n = 9) for TiNT samples with standard deviation included

	TiNT		
Element	**Binding Energy (eV)**	**Atomic Concentration %**	**Total Atomic Concentration %**
C 1s	284.8	41.13 ± 15.49	54.61 ± 18.89
	286.3	6.51 ± 2.76	
	287.8	2.89 ± 0.81	
	288.8	3.98 ± 0.18	
O 1s	530.2	17.39 ± 11.10	35.31 ± 12.11
	531.6	18.40 ± 6.29	
Ti 2p	458.9	5.93 ± 4.40	9.33 ± 6.71
	464.6	3.00 ± 2.11	
F 1s	684.1	0.78 ± 0.95	0.78 ± 0.95

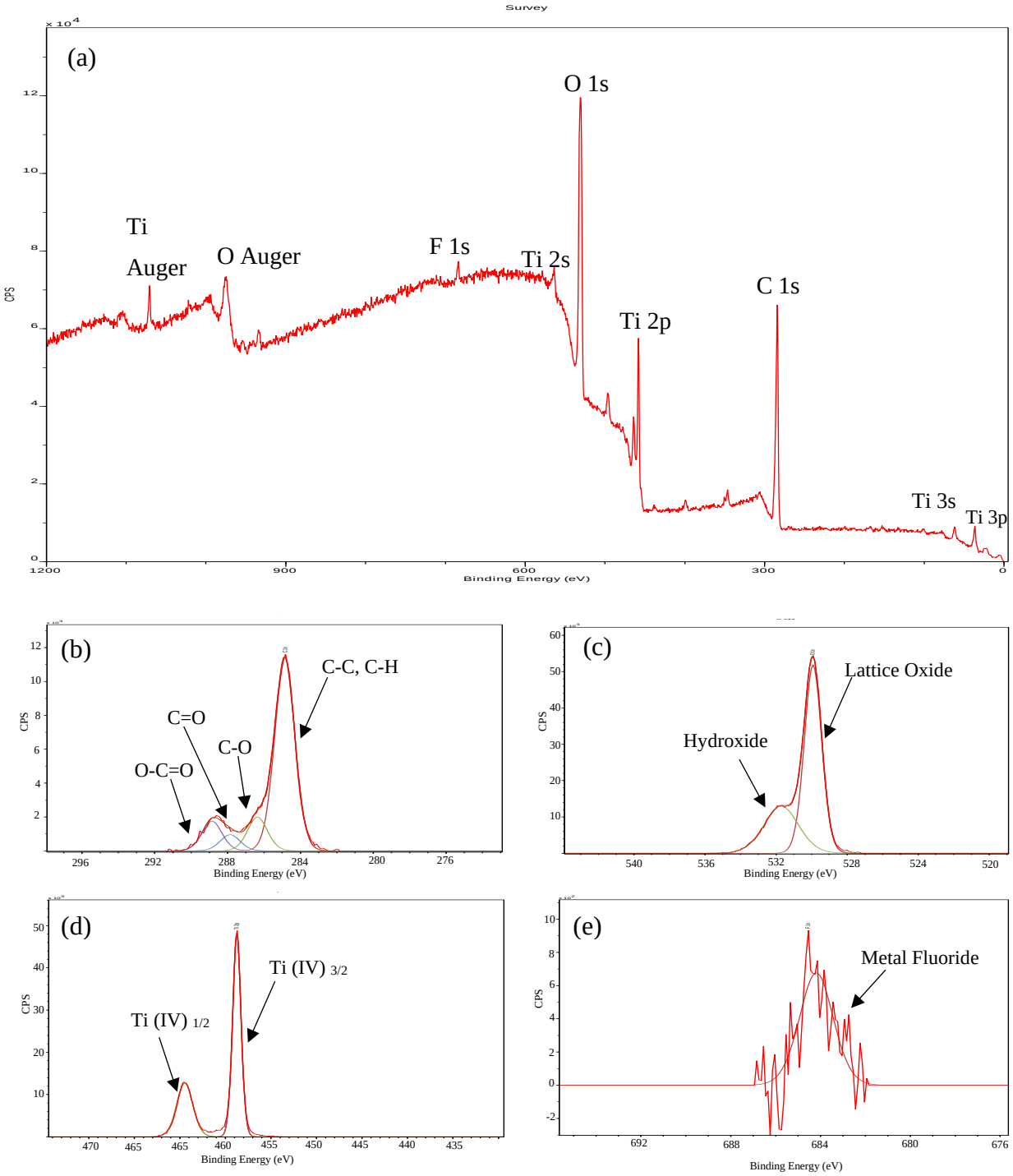

Figure 4.28 XPS spectra for TiNT showing (a) WESS, and high-resolution spectra for (b) C 1s, (c) O 1s, (d) Ti 2p and (e) F 1s regions

4.5.2 XRD Analysis

Figure 4.29 shows the x-ray diffractogram generated for the TiNT samples. Peaks were found to be present at 2θ = 25.3˚, 35.1˚, 36.3˚, 38.3˚, 40.1˚, 43.1˚, 48.2˚, 52.9˚ and 54.5˚ which are attributed to the Miller indices (hkl) for crystallographic planes 101, 100, 004, 002, 101, 200, 102, 105 and 211, respectively. These planes correspond to a combination of ICDD file 00-044-1294 for semi-crystalline titanium and ICDD file 01-078-2486 for the anatase phase of titanium dioxide (TiO_2) thereby confirming that this substrate comprises a surface chemistry comprising semi-crystalline titanium and titanium dioxide. The nature of the TiO_2 peaks suggest that a substantial oxide layer is present, which is to be expected as a result of the anodisation process.

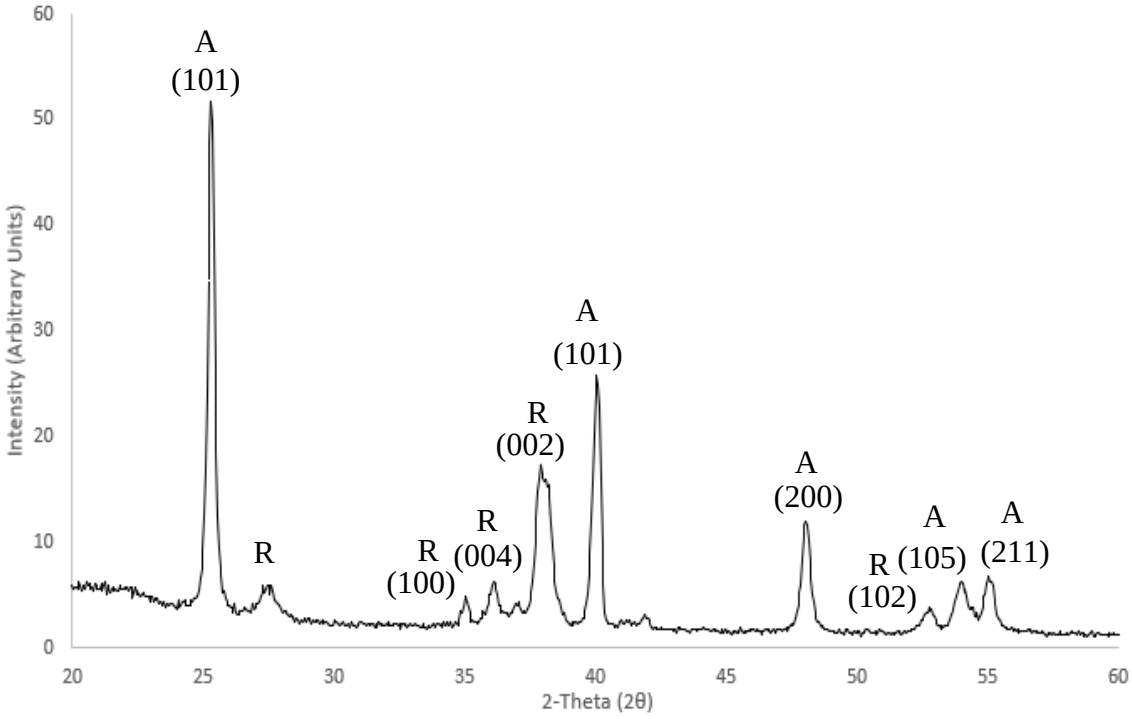

Figure 4.29 X-ray diffractogram for TiNT with Miller index assignments labelled according to ICDD files 00-044-1294 and 01-078-2486. Anatase (A) and rutile (R) phases also labelled

4.5.3 SEM Analysis

SEM images for TiNT are provided in Figure 4.30 and indicate that the expected nanotubular morphology cannot be seen below a magnification of x4.5k. Hence, a higher magnification (x22k) was chosen for SEM imaging here, which is in general, greater than that used for previous samples. The titania nanotubes identified here (Figure 4.30 (d)) show a high level of homogeneity in regard to their tubular circumference. When imaging the samples at a tilt (Figure 4.30 (e) - (h), it was difficult to maintain resolution at magnifications matching those used for planar view and so lower magnifications were used to maintain visual quality. These images do suggest that there are varying heights of nanotubular features across the sample surface.

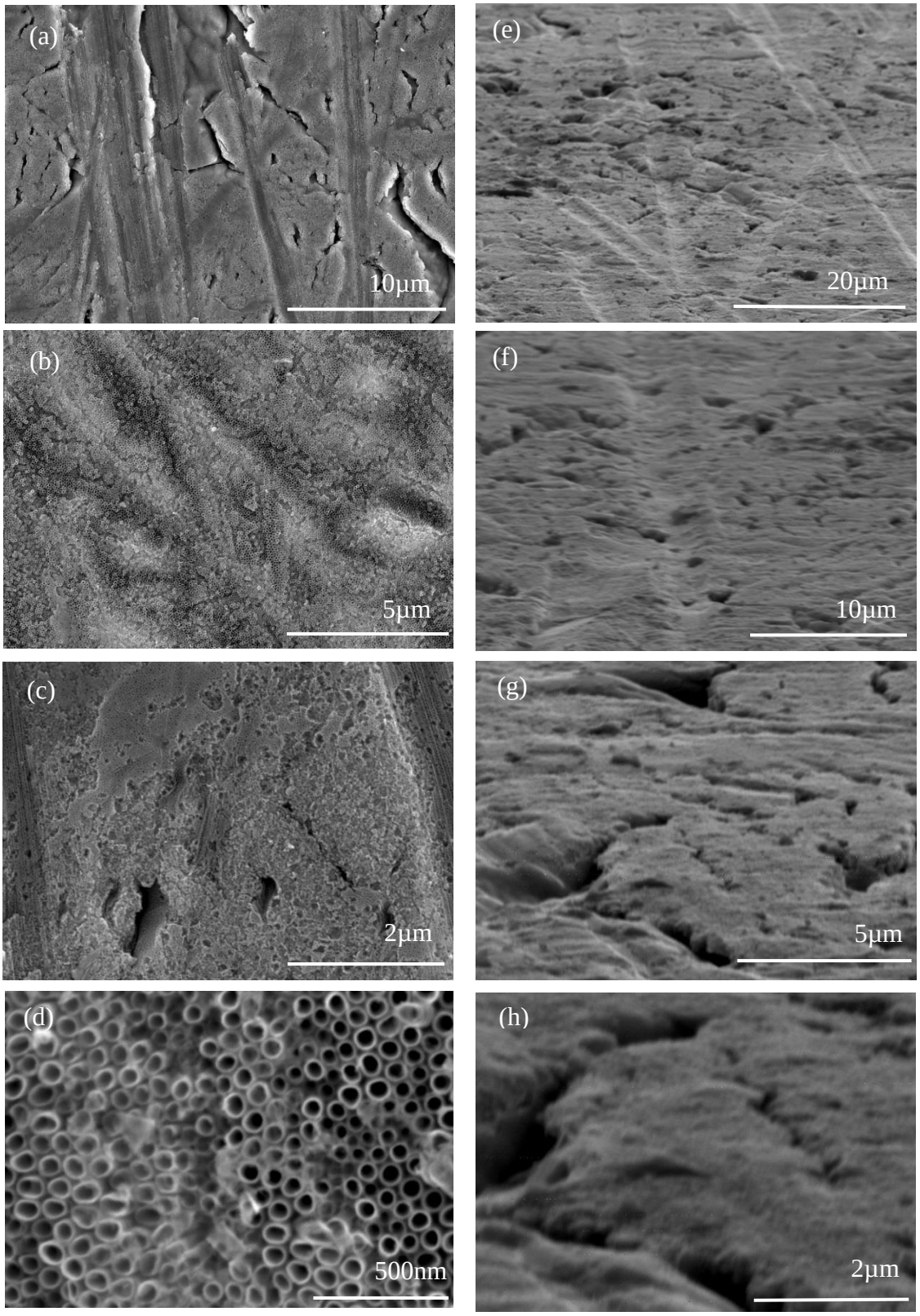

Figure 4.30 SEM images for TiNT showing normal planar views (a)-(d) and 80˚ tilt side angle views(e)-(h) at magnifications of (a) x4.5k, (b) x10k, (c) x22k (d) x90k, (e) x2.5k, (f) x4.5k, (g) x10k, and (h) x22k. Note higher magnification used to image nanotubular microstructure

4.5.4 AFM Analysis

The 2D and 3D AFM scans for TiNT are shown in Figure 4.31. Unfortunately, there is some interference and noise present due to fluctuation of the tip on this very rough surface. Moreover, the scale on which these substrates were scanned is not sensitive enough to detect the individual nanotubular structures but does allow for an overall roughness of the surface. These data sets do allow an estimate of surface roughness to be made when compared to the previous samples. The corresponding average Ra and Rq data are shown in Table 4.10 and show a high standard deviation. Whereas, these AFM images do show a roughened morphology reflective of the nanotube topography, the lines and grooves on the Ti surface due to processing are still present. It is assumed that the lines and grooves are the main reason that the nanotubes appear on different levels within the SEM images and also then cause the issues with the noise in the AFM scans reported here.

Table 4.10 Average Ra and Rq values (n = 18) and image surface area difference in % (n = 3) for TiNT surfaces calculated from AFM images (n = 3) with standard deviation included

Sample Type	Ra (nm) ± Standard Deviation	Rq (nm) ± Standard ± Standard Deviation	Image Surface Area Difference % ± Standard Deviation
TiNT	55.24 ± 21.98	70.23 ± 33.95	32.83 ± 20.41

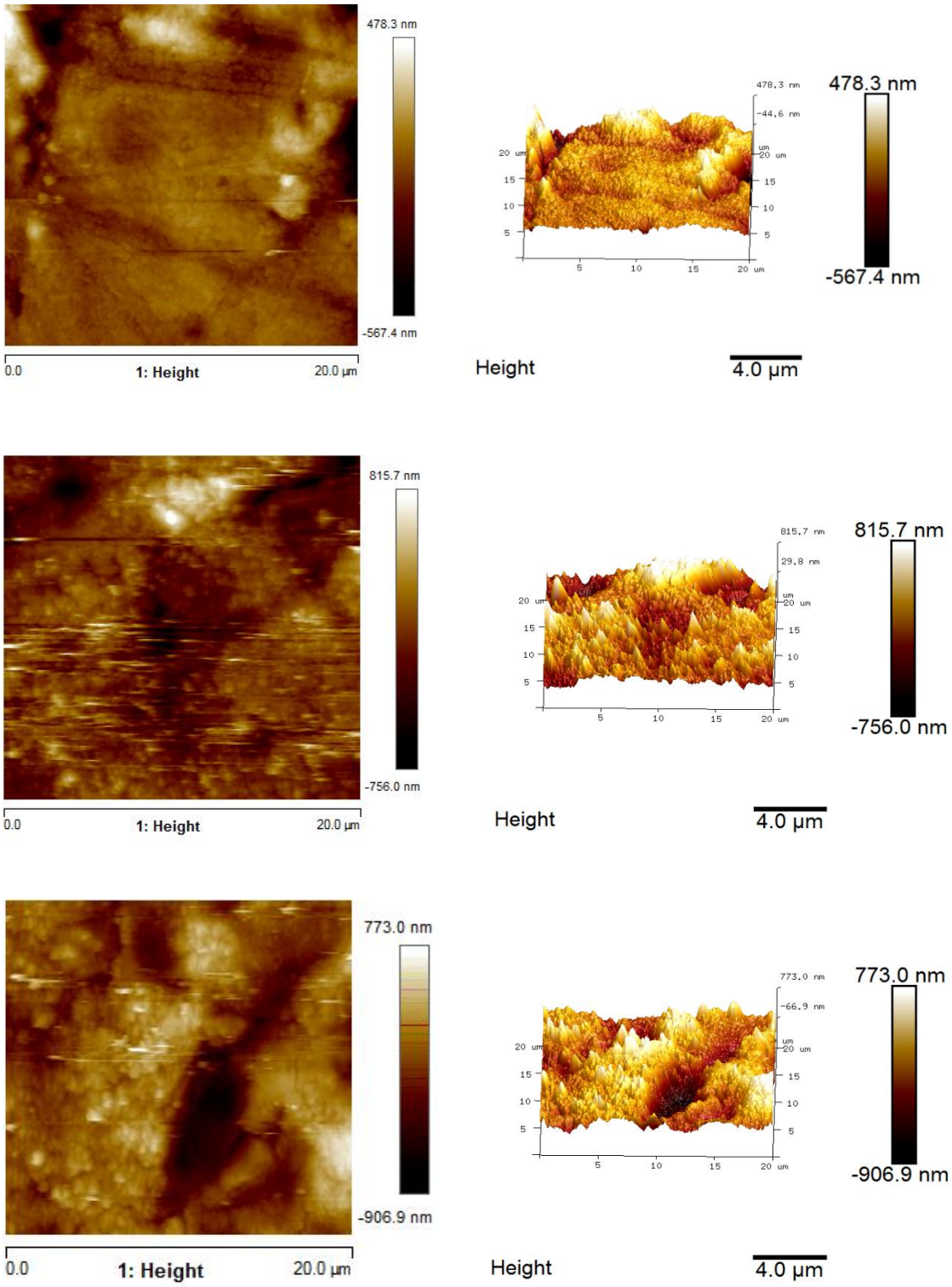

Figure 4.31 Pseudo- colour 20 µm x 20 µm 2D and 3D AFM images and corresponding 3D plots of TiNT

4.6 Discussion

The purpose of the work reported in this chapter is to understand how chemical etching of titanium changes surface properties in regard to control of dissolution of as deposited CaP thin film coatings thereon. It is proposed that chemically etched titanium surfaces can be readily applied as a simple means to deliver this effect. However, as they have not been studied previously in this context, a detailed level of characterisation is required. Moreover, the identification of appropriate controls to compare with the behaviour of these etched samples is also important. Native titanium, either in a pristine (unannealed) or thermally annealed state is the most obvious control sample, but since both sputtered deposited and anodised titanium have been used in previous studies[29,31,115], comparison with one or other of them is warranted. An understanding of the surface chemical and morphological properties of all these surfaces, before and after annealing, is required.

When comparing the pristine (unannealed) titanium surfaces with the thermally annealed titanium samples, few differences were notable. The WESS for both sample types presented similar signals, and only upon quantification were differences in carbon, oxygen and titanium presence on the surface observed. The aTi displayed a reduction in surface carbon, with a significant increase in oxygen and titanium, as expected with the growth of the oxide layer due to the thermal annealing. As the thermal annealing was undertaken at 500 ˚C, no changes in crystallinity occurred, as shown in the XRD data with both sample types presenting x-ray diffractograms corresponding to semi-crystalline titanium[205], with anatase and rutile phases present. Notably, the intensity of the rutile phases increases after thermal annealing. There was what looked to be ‘smoothing’ of the surface when comparing SEM images of the aTi to Ti, indicative of the oxide growth with thermal annealing. When the surface microstructure is examined at higher resolution using AFM the Ti and aTi samples showed very similar roughness, with little difference between the average Ra and Rq values. The image surface area difference % almost doubled after the Ti was annealed to aTi, but the standard deviation was large and so overlapped with the Ti measurements. Therefore, it is suggested that the extra annealing step does not give rise to any desirable changes in the surface chemistry or morphology of the titanium sample, and so the unannealed titanium (Ti) is thought to be a suitable control.

XPS data at the WESS level for chemically etched titanium showed little variation compared to that of the surface chemistry for pristine Ti. The associated high-resolution spectral plots for the etched samples do show some changes that may affect how sputter deposited CaP thin films behave thereon. The most significant difference is the presence

of a carbide signal on the 3eTi surface. The associated SEM and AFM images suggest that this has formed predominantly along the lines and grooves that are present on the surface due to machining of the pristine material, as well as around the edges of minor pits that had formed across the surface. This nucleation could in turn be the cause of the high standard deviation measured for both Ra and Rq values. The corresponding 24eTi sample showed a more promising morphology, in addition to a well-defined surface chemistry, which is similar to that seen for aTi. This surface presents a lower amount of carbon, as well as a higher oxygen and titanium concentration when compared to that of the pristine Ti, with no other peaks present suggestive of contamination. The SEM images gathered present a 'honeycomb' pitted topography that was found to be present across the substrate surface. The subsequent AFM measured a roughness (Ra & Rq) higher than that of the other samples, as well as a low standard deviation, suggestive of an offset orientated but repeatable morphology from sample-to-sample[189]. The 24eTi samples also had the third highest image surface area difference %, but the lowest standard deviation indicating repeatability of roughness between samples. Hence, it is deemed that this chemically etched surface should not present any negative effects on cells *in vitro*. These data suggest that the 24eTi provides a more desirable surface chemistry and morphology compared to that of the 3eTi. Literature describes how an offset orientated topography rather than an ordered topography provides a surface onto which cells can adhere and proliferate more readily (REFS). It is believed that the 'honeycomb' pitting morphology on the 24eTi surface will provide a topography onto which CaP thin films can be deposited in an amorphous state, and in turn allow a degree of control over the dissolution of the CaP thin film when placed in aqueous solution.

In respect of the control samples, the surface chemical properties of radio frequency (RF) magnetron sputtered PolyTi samples were similar to that of both the Ti and aTi, with no unexpected peaks present in the XPS spectra data. It was found that aPolyTi250 showed a small decrease in surface carbon content, with a slight increase in oxygen content, confirming that surface oxidation occurred from PolyTi250 to aPolyTi250, due to thermal annealing. This was further evident when comparing the AFM measurements which showed little change between the two samples. PolyTi400 has a surface chemistry similar to the aTi sample, whilst thermal annealing to give aPolyTi400 actually led to an increase in carbon content with a decrease in oxygen content, despite the enhanced oxide layer growth. This surface chemistry suggested both of the sputtered samples, PolyTi250 and PolyTi400 have the potential to act as comparator samples. Interestingly, these results suggest that PolyTi400 has a surface chemistry similar to that

of aTi without the need of an annealing step. However, when comparing the XRD of both samples, PolyTi250 presented a surface crystallinity similar to that of the pristine Ti, as expected, with both anatase and rutile phases present indicative of semi-crystalline titanium. Notwithstanding, the PolyTi400 x-ray diffractogram displayed a singular peak at $2\theta = 36.4^{\circ}$, which corresponds to the Miller index (hkl) orientation in the 004 plane[205]. This peak is indicative of TiO_2 and suggests that the PolyTi400 surface has a significantly increased oxide layer which is thick enough to mask the detection of any other crystallographic planes for titanium. This interpretation is supported by the XPS quantification for this sample, which showed high oxygen and titanium contributions. A possible explanation for this is offered by Duffy[224], where he states that increased roughness and heights of morphology can lead to strong dominant crystallographic planes. It is thought here that the sputtering of PolyTi400 has more pronounced highly oriented TiO_2 growth on the surface than that seen for the other PolyTi samples. No significant differences between these samples was discerned from the SEM images, with the lines and grooves present on both surfaces. The PolyTi400 did present a higher occurrence of nucleation of material, seen predominantly along these lines and grooves present on the surface. When further characterised, it was found that the PolyTi250 exhibited more desirable morphology and roughness than that of the PolyTi400. The characterisation data gathered suggested that PolyTi250 may be more beneficial as a morphology to control the dissolution of CaP thin films thereon.

When comparing these samples with titania nanotubes (TiNT), a similar surface chemistry is presented in the XPS spectra, with the addition of a fluorine signal. This is further confirmed upon XPS quantification, with the highest surface carbon concentration of all the samples, as well as the lowest titanium content measured. The fluorine that is present on the surface is in small amounts and it is believed that at these levels there should be no issues with subsequent cell activity *in* vitro. The x-ray diffractogram for the TiNT presents a combination of semi-crystalline titanium and anatase titanium dioxide[116,197,205]. In tandem with the XPS data, this indicates that there was an increased oxide layer on this surface. This increased oxide layer is expected due to the process of the electrochemical anodisation reaction, where the oxide layer is continually anodised and regrown throughout the reaction, leading to areas of thicker oxide content[22,196]. The SEM images showed that the TiNT did present a roughened morphology. The nanotubes became visible at a higher magnification and showed a homogeneity for the tubular diameter. However, these nanotubular features were found to have varying heights suggesting that although the nanotubes have a desirable surface chemistry and roughness,

the latter are not repeatable across the required sample set. This was further confirmed by the AFM of the TiNT surfaces, which did display a relatively high surface roughness. However, the standard deviations were high, leading to the assertion that although these surfaces do provide areas of desirable roughness and tubular structures capable of retaining CaP thin films, the repeatability of these surfaces in particular is not feasible.

In summary, the chemically etched surface for 24 hr (24eTi) was found to be the superior chemically etched sample when comparing all characterisation data gathered and comparison to literature. These surfaces presented a desirable surface chemistry, as well as a roughened surface morphology, and it is believed that this particular surface roughness will play a role in the control of dissolution of CaP thin films thereon. Pristine titanium was shown to be an obvious control choice, as there was no data gathered that suggested that the thermal annealing yielded any elevated surface chemistry or morphology properties compared to the unannealed titanium sample. It is important that the comparative sample is repeatable, so as to allow for an accurate comparison with not only the 24eTi, but also with the Ti control. Therefore, PolyTi250 samples were found to be the surface comparator of choice. These samples exhibited a surface chemically similar to that of the Ti, but with a more pronounced surface roughness higher than that of the Ti but lower than the 24eTi surfaces. It is believed that these surfaces, particularly the 24eTi samples, will exhibit desirable properties from which the control of sputtered CaP thin films will be possible thereon, to give rise to an enhanced bioactive response *in vitro.*

Chapter 5: Calcium Phosphate Thin Film Coatings on Etched Titania Morphologies

5.1 Introduction

This chapter provides a detailed analysis of calcium phosphate (CaP) thin films sputter deposited from both hydroxyapatite (HA) and strontium substituted hydroxyapatite (SrHA) targets onto 24 hr etched titanium substrates. Coatings produced from SrHA have been shown previously to have an increased rate of dissolution compared to those from HA due to the larger atomic radius of strontium compared to that of the calcium ions[182,225,226]. The core objective of this work is to determine the effectiveness of the etched titania morphology in controlling the subsequent dissolution of the two coating chemistries and to investigate their relative rates of dissolution. To this end, HA and SrHA coatings similarly deposited on pristine and polycrystalline (sputter deposited) titanium surfaces are used as comparators. All coated substrates were subjected to a 7-day dissolution study in cell culture medium and the changes to surface chemistry and topography measured to determine the capabilities of the various surfaces to retain remnants of the respective CaP thin films at a level that can impart a bioactive response.

The nomenclature for the various samples employed here are provided below. It should be noted that sputter deposited CaP coatings are not chemically identical to the precursor HA and SrHA target materials and hence these terms are used here for convenience of identification:

- TiHA - Titanium with HA thin film
- 24eTiHA- 24 hr piranha etched titanium with HA thin film
- PolyTi250HA - 250 W polycrystalline titanium with HA thin film
- TiSrHA- Titanium with SrHA thin film
- 24eTiSrHA- 24 hr etched titanium with SrHA thin film
- PolyTi250SrHA - 250 W polycrystalline titanium with SrHA thin film

All substrates were subjected to surface analysis before and after the 7-day dissolution process using x-ray photoelectron spectroscopy (XPS), time of flight secondary ion mass spectrometry (ToFSIMS), x-ray diffraction (XRD) and scanning electron microscopy (SEM).

5.2 Pristine Titanium with HA and SrHA Coatings

Pristine titanium was used here as a control sample. It is noted here that this substrate surface is not completely 'smooth' but rather it has a minor surface topography derived from processing that is significantly different to that of the etched and polycrystalline surfaces. Previous literature has shown that CaP thin films will quickly dissipate completely on flat surfaces[29,160]. Hence, creation of a specific form of surface roughness on the titanium surfaces created here seeks to provide a convenient means to control the dissolution of the CaP (HA and SrHA) thin films thereon.

5.2.1 XPS of HA and SrHA Coated Pristine Titanium

XPS was carried out on all CaP sputter coated thin films on pristine titanium substrates to ensure that a coating from either the HA or SrHA targets was achieved under the deposition conditions employed. The estimated film thickness created using the deposition conditions employed here was approximately 111nm. However, it is recognised that due to the conformal nature of the coating process, the uniformity of the layer thickness depends on the substrate morphology present.

Figure 5.1 (a) – (e) shows the XPS spectra for TiHA, with peaks observed in the wide energy survey scan (WESS) labelled accordingly (Figure 5.1 (a)). As expected, peaks associated with the CaP thin film produced from the HA are present as calcium (Ca 2p, Ca 2s, Ca 3s and Ca 3p) and phosphorus (P 2p and P 2s) signals. The lack of any discernible titanium (Ti 2p or Ti 2s) signals in this spectrum confirms that film thickness is greater than the relevant photoelectron inelastic mean free path, i.e. ca. 10 nm. The lowest binding energy (BE) component (C-C, C-H) in the carbon (C 1s) envelope (Figure 5.1 (b)) is assigned to adventitious carbon and set at a BE of 284.8 eV[203] and then used to calibrate all other present peaks for the effects of residual surface charging (low energy electrons were used to neutralise major charging effects during spectral acquisition). The remaining three peaks present in the C 1s region are assigned to C-O, C=O and O-C=O at 286.3 eV, 287.7 eV and 288.7 eV, respectively. The corresponding O 1s plot (Fig 5.1 (c)) comprises two peaks with that at 531.0 eV attributed to lattice oxide bonding and the 532.8 eV contribution assigned to hydroxide bonding (OH^-). Figure 5.1 (d) shows the Ca 2p region with the expected Ca $2p_{3/2}$ and Ca $2p_{1/2}$ doublet components at 347.4 eV and 350.9 eV, respectively. The corresponding P 2p region is provided in Figure 5.1 (e) with the unresolved doublet centred at 133 eV, which when peak fitted results in P $2p_{3/2}$ and P $2p_{1/2}$ contributions at 133.4 eV and 134.4 eV, respectively. The calculated carbon to oxygen ratio (C/O) for these substrates is 0.42,

which is slightly lower than that for aTi which had a C/O of 0.47. Given the lack of titanium signals detected, the oxygen here is assumed to emanate from the CaP (TiHA) coating which is formed from the HA target ($Ca_{10}(PO_4)_6(OH)_2$). The Ca/P ratio for these TiHA samples is calculated as 0.99, which suggests an almost 1:1 Ca and P content on the surface rather than the 1.67 ratio (10:6) expected for the stoichiometric HA target material[32,202].

Figure 5.2 (a) – (e) shows the WESS and high-resolution plots for the corrseponding TiSrHA samples. In general, the signals present in the WESS scan (Figure 5.2 (a)) are similar to those observed for TiHA with the addition of the expected strontium contribution. The lowest binding energy contribution in the high resolution C 1s plot (Figure 5.2 (b)) is again assigned to adventitious carbon at 248.8 eV and used to calibrate other signal bands for surface charging. The remaining three peaks present at 286.4 eV, 287.9 eV and 288.9 eV are again indicative of C-O, C=O and O-C=O bonding, respectively. The O 1s high resolution region (Figure 5.2 (c)) shows two peaks at 531.1 eV and 533.0 eV indicative of lattice oxide bonding and hydroxide bonding, respectively. The Ca 2p region (Figure 5.2 (d)) shows a single doublet with Ca $2p_{3/2}$ and Ca $2p_{1/2}$ at 347.6 eV and 351.0 eV, respectively. The P 2p region (Figure 5.2 (e)) shows a doublet with P $2p_{3/2}$ at 133.5 eV and P $2p_{1/2}$ at 135 eV. The Sr region (Figure 5.2 (f)) shows a Sr 3p doublet comprising Sr $3p_{3/2}$ at 269.0 eV and Sr $3p_{1/2}$ at 279.7 eV. The C/O ratio calculated for the TiSrHA samples was 0.46 which is slightly higher than the 0.42 value recorded for the TiHA samples. As before, the oxygen detected here is assumed to emanate from the CaP (TiSrHA) coating which is formed from the SrHA target ($Ca_{10x}Sr_x(PO_4)_6(OH)_2$). The Ca/P ratio calculated for the TiSrHA samples was 0.35, with a combined (Sr + Ca)/P ratio of 0.45. This Ca/P ratio is much lower than the 0.99 value calculated for TiHA and the 1.67 expected for the SrHA target material. The XPS quantification data for the TiHA and TiSrHA samples are presented in Table 5.1.

Table 5.1 XPS quantification data (n = 9) for TiHA and TiSrHA samples with standard deviation included

	TiHA			TiSrHA		
Element	Binding Energy (eV)	Atomic concentration %	Total Atomic Concentration %	Binding Energy (eV)	Atomic Concentration %	Total Atomic Concentration %
C 1s	284.8	15.35 ± 2.56	19.65 ± 3.54	284.8	15.31 ± 0.04	18.36 ± 3.17
	286.3	2.45 ± 2.39		286.4	2.26 ± 0.43	
	287.7	0.75 ± 0.42		287.9	0.38 ± 0.13	
	287.7	1.00 ± 0.19		288.9	0.54 ± 0.21	
O 1s	531.0	27.88 ± 4.75	47.14 ± 2.40	531.1	29.76 ± 4.08	40.07 ± 1.78
	532.8	19.20 ± 7.10		533.0	10.22 ± 5.72	
Ca 2p	347.4	11.31 ± 0.69	16.53 ± 0.28	347.6	6.86 ± 0.73	10.03 ± 1.03
	350.9	5.30 ± 1.17		351.0	3.23 ± 0.32	
P 2p	133.4	11.29 ± 0.92	16.68 ± 0.92	133.5	19.05 ± 1.32	28.64 ± 2.16
	134.4	5.47 ± 0.15		135.0	9.52 ± 0.66	
Sr 3p	-	-	-	269.0	2.08 ± 0.47	2.90 ± 0.58
	-	-	-	279.7	0.76 ± 0.13	

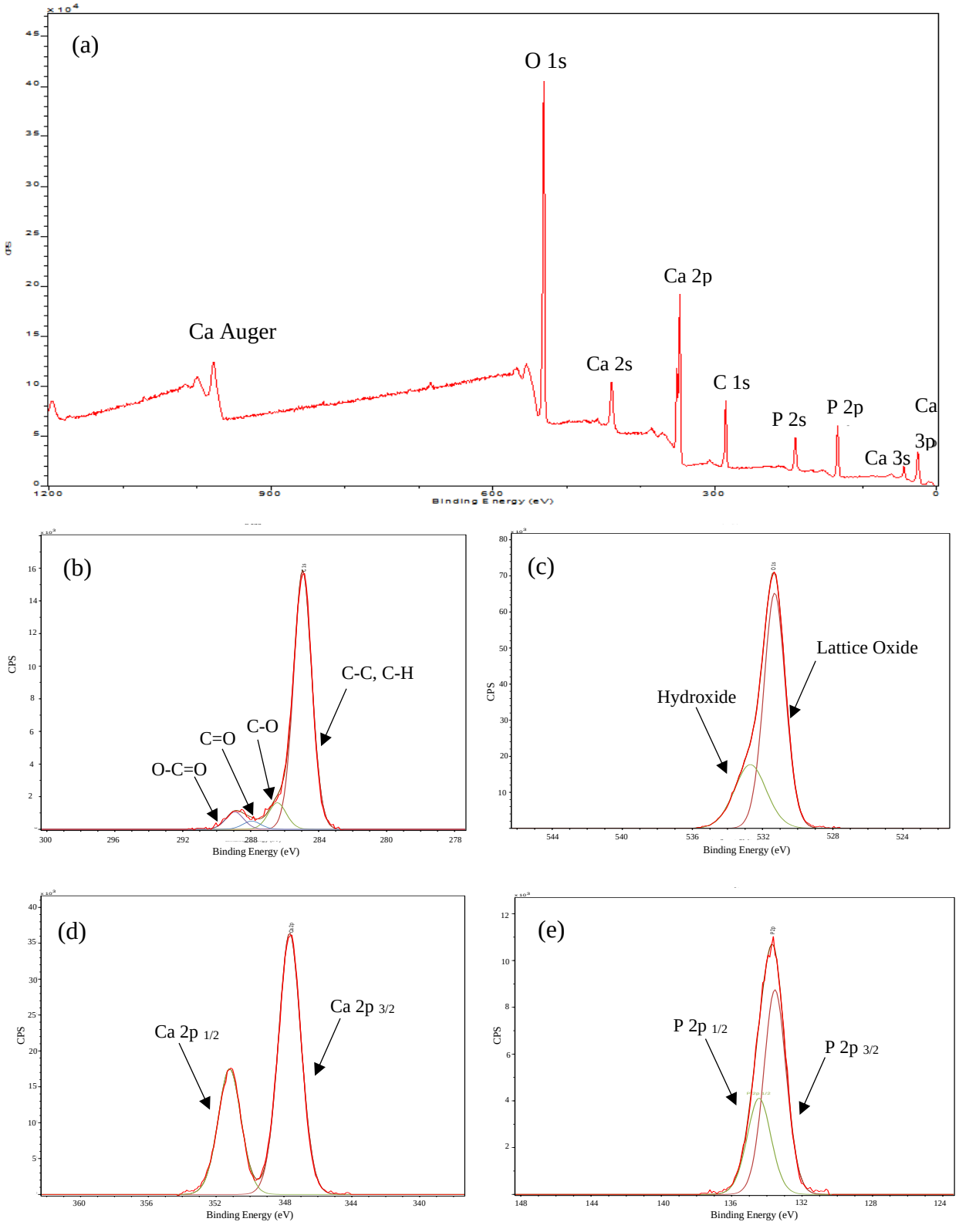

Figure 5.1 XPS spectra for TiHA surface showing (a) WESS, and high-resolution spectra for (b) C 1s, (c) O 1s, (d) Ca 2p and (e)P 2p regions

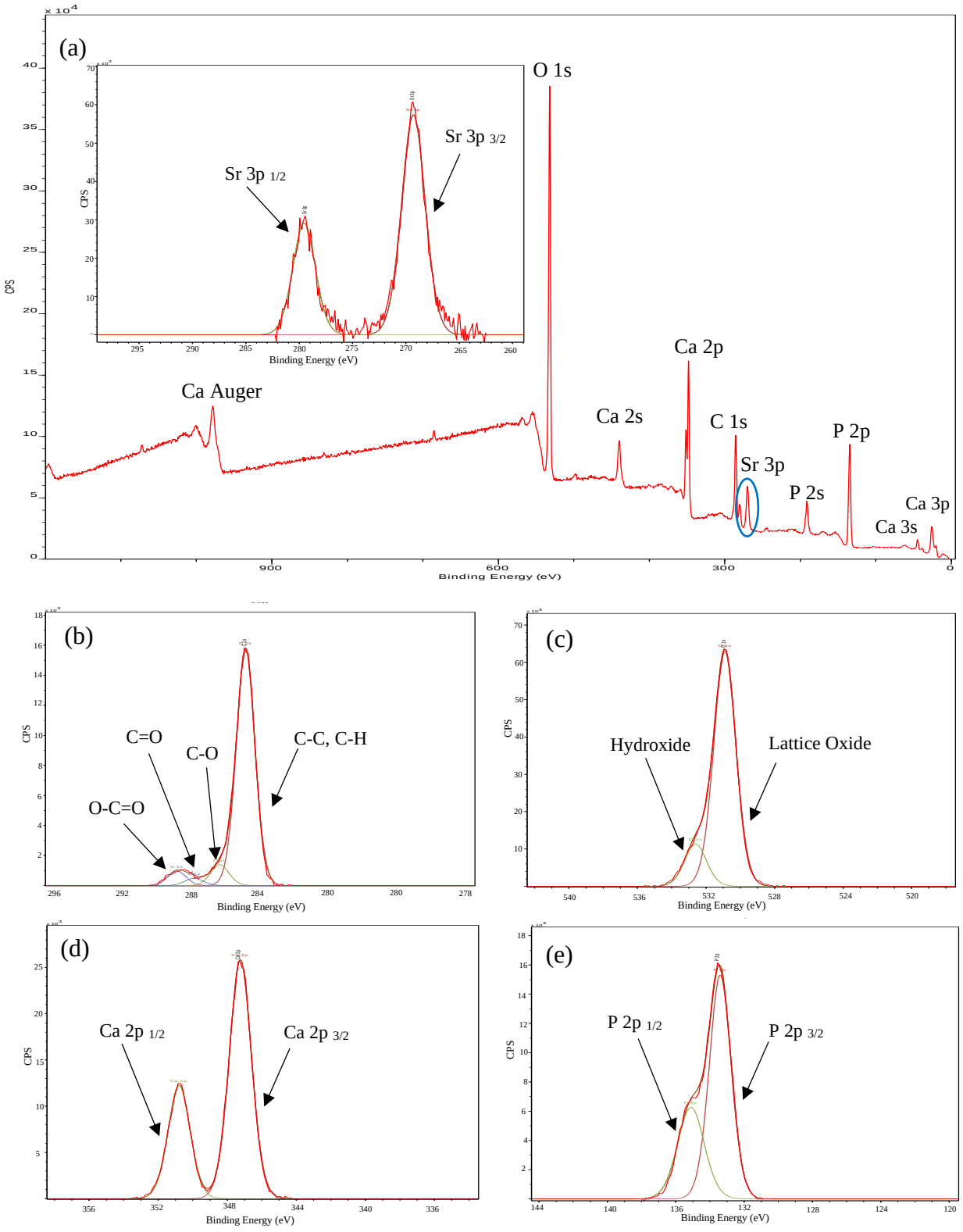

Figure 5.2 XPS spectra for TiSrHA surface showing (a) WESS, and high-resolution spectra for (b) C 1s, (c) O 1s, (d) Ca 2p, (e)P 2p and Sr 3p (insert within WESS plot) regions

5.2.2 ToFSIMS of Titanium with CaP Thin Film Coatings

Time of flight secondary ion mass spectrometry (ToFSIMS) has been used to further investigate the HA and SrHA coatings on the pristine titanium substrate surfaces with particular reference to investigating thin film integrity. For this purpose, positive ion spectra and associated mapping have been utilised to display ions indicative of the CaP coatings and to provide details of the distribution of the elements present on the substrate surface.

Figure 5.3 shows a positive ion mass spectrum for TiHA in the 0 to 300 mass-to-charge ratio (m/z) range with evidence of organic and inorganic substances present. Major peaks at 40 m/z and 57 m/z show the presence of calcium ions (Ca^+) and calcium hydroxide ions ($CaOH^+$), respectively. These are followed in decreasing relative intensity by ions of calcium monohydride (CaH^+) and calcium phosphate ions in varying forms ($CaPO_2^+$, $Ca_2PO_4^+$, $CaPO_3^+$, $Ca_2PO_3^+$, $Ca_3PO_5^+$ and $Ca_4PO_6^+$), as well as indicating the presence of calcium oxide in the form of a divalent cation (Ca_2O^+). There is also the presence of sodium (Na^+) and potassium (K^+) at 23 m/z and 39 m/z, respectively (These are commonly seen in ToFSIMS as contaminants, usually from handling). Notably, there is an absence of Ti^+ at 48 m/z. The corresponding positive ion maps for Ca^+, CaH^+, $CaOH^+$, Ca_2O^+, $CaPO_2^+$, $CaPO_3^+$, $Ca_2PO_3^+$, $Ca_2PO_4^+$, $Ca_3PO_5^+$ and $Ca_4PO_6^+$ are provided in Figure 5.4 as a means of showing the spatial distribution of these positive ions across a representative area of the substrate surface. Plots of total ion count are also provided as reference.

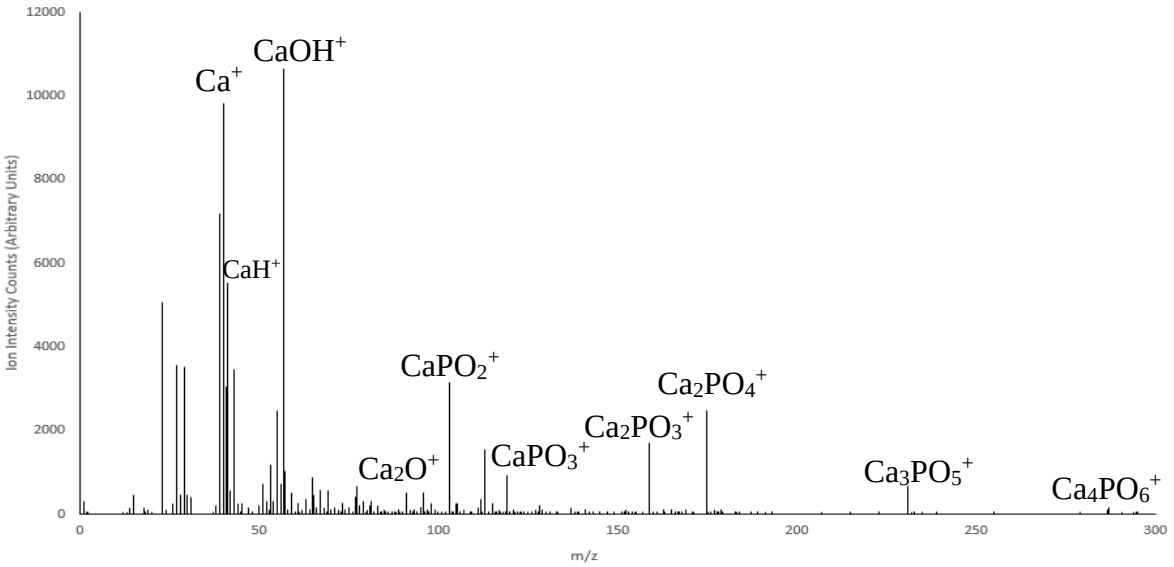

Figure 5.3 Positive ToFSIMS spectra for TiHA surface with positive ion signals indicative of a CaP thin film labelled

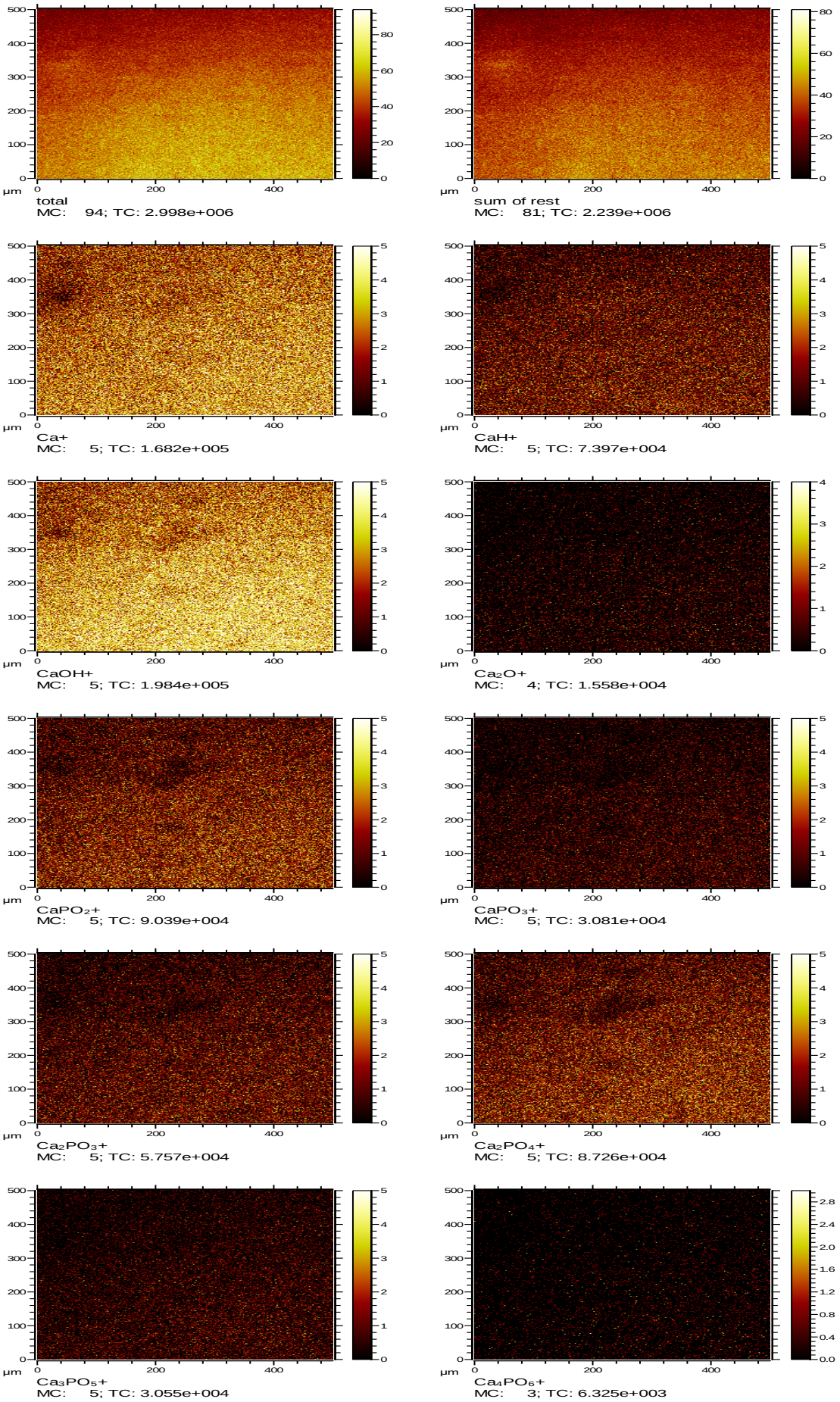

Figure 5.4 ToFSIMS positive ion maps of total ion count (TIC), Ca^+, CaH^+, $CaOH^+$, Ca_2O^+, $CaPO_2^+$, $CaPO_3^+$, $Ca_2PO_3^+$, $Ca_2PO_4^+$, $Ca_3PO_5^+$ and $Ca_4PO_6^+$ for TiHA

The positive ion mass spectrum for TiSrHA is provided in Figure 5.5 and again Ca^+, CaH^+ and $CaOH^+$ are the most dominant peaks, indicative of a CaP thin film coating. As expected, a strontium ion (Sr^+) signal is present at 89 m/z. As before, there is no signal for titanium was detected at 48 m/z confirming a homogenous CaP coating on this substrate. There is a large signal present at 23 m/z indicative of sodium ions, again attributed to contaminants from handling of the sample. Notably, there are less calcium phosphate ion groups ($CaPO_2^+$, $Ca_2PO_4^+$, $CaPO_3^+$, $Ca_2PO_3^+$, $Ca_3PO_5^+$ and $Ca_4PO_6^+$) present in this TiSrHA spectrum. The corresponding positive ion maps in Figure 5.6 display the distribution of the main positive ions present on the substrate surface including that for Sr^+. The absence of the more complex calcium phosphate phases seen previously for the TiHA samples is evident across the substrate surface maps.

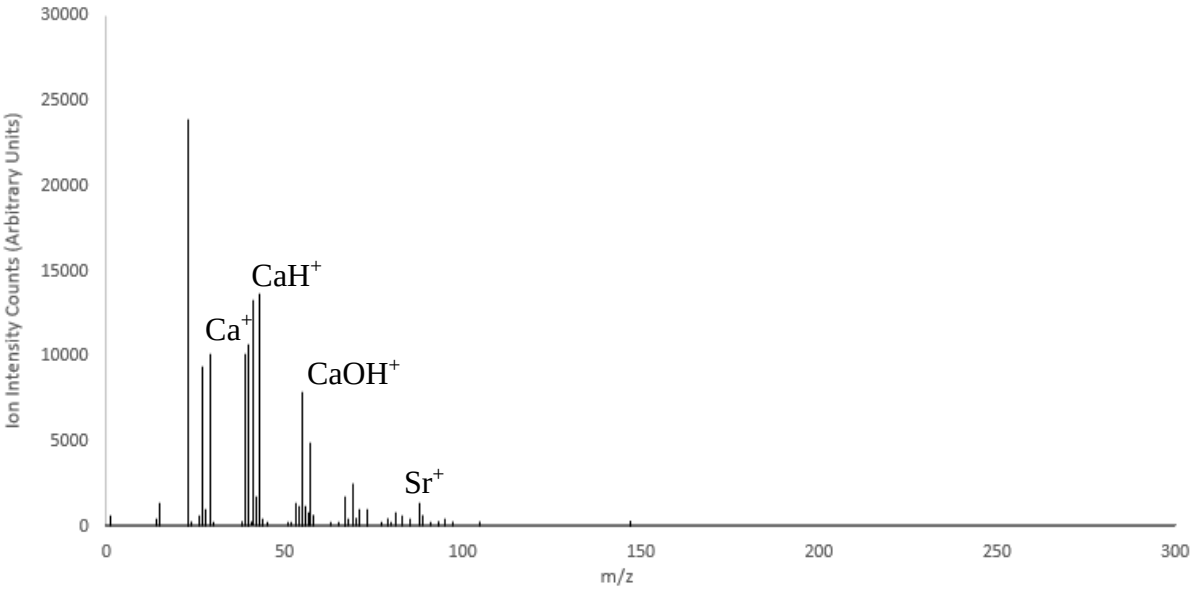

Figure 5.5 Positive ion ToFSIMS spectrum for TiSrHA surface with positive ion signals indicative of a CaP thin film labelled

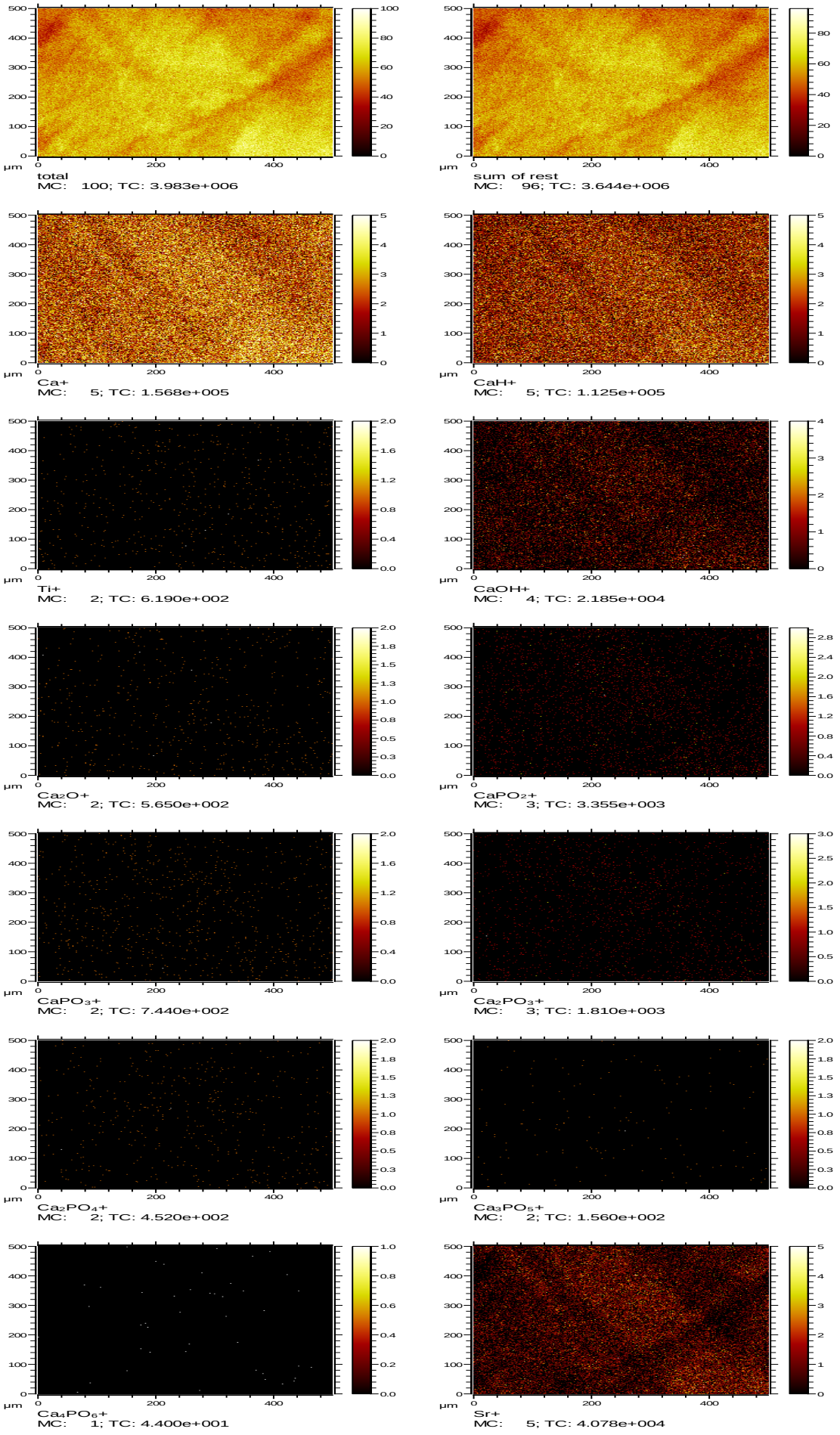

Figure 5.6 ToFSIMS positive ion maps of total ion count (TIC), Ca^+, CaH^+, Ti^+, $CaOH^+$, Ca_2O^+, $CaPO_2^+$, $CaPO_3^+$, $Ca_2PO_3^+$, $Ca_2PO_4^+$, $Ca_3PO_5^+$, $Ca_4PO_6^+$ and Sr^+ for TiSrHA

5.2.3 XRD of HA and SrHA Coated Pristine Titanium

The sputtered CaP (TiHA and TiSrHA) thin films produced here are in the as-deposited state; therefore, they are understood to be amorphous as no subsequent thermal annealing step has taken place. Nonetheless, it was deemed important to confirm this condition and so x-ray diffractograms were generated for the thin film coated samples as shown in Figure 5.7 (a) for TiHA and Figure 5.7 (b) for TiSrHA with all of the peaks detected labelled accordingly. The main peaks for TiHA are seen at 2θ = 35˚, 38.3˚, 40.1˚ and 53.1˚ corresponding to Miller indices (hkl) in the 100, 002, 101 and 102 planes, respectively. Peaks present in the TiSrHA scan are at 2θ = 35˚, 38.2˚, 40.1˚ and 52.8˚ corresponding to Miller indices (hkl) in the 100, 002, 101 and 102 planes, respectively. In both cases, the spectra conform to the ICDD file 00-044-1294 for semi-crystalline titanium[205,227]. This indicates that the thin film coatings derived from either HA or SrHA sputter targets on pristine titanium surfaces are indeed amorphous.

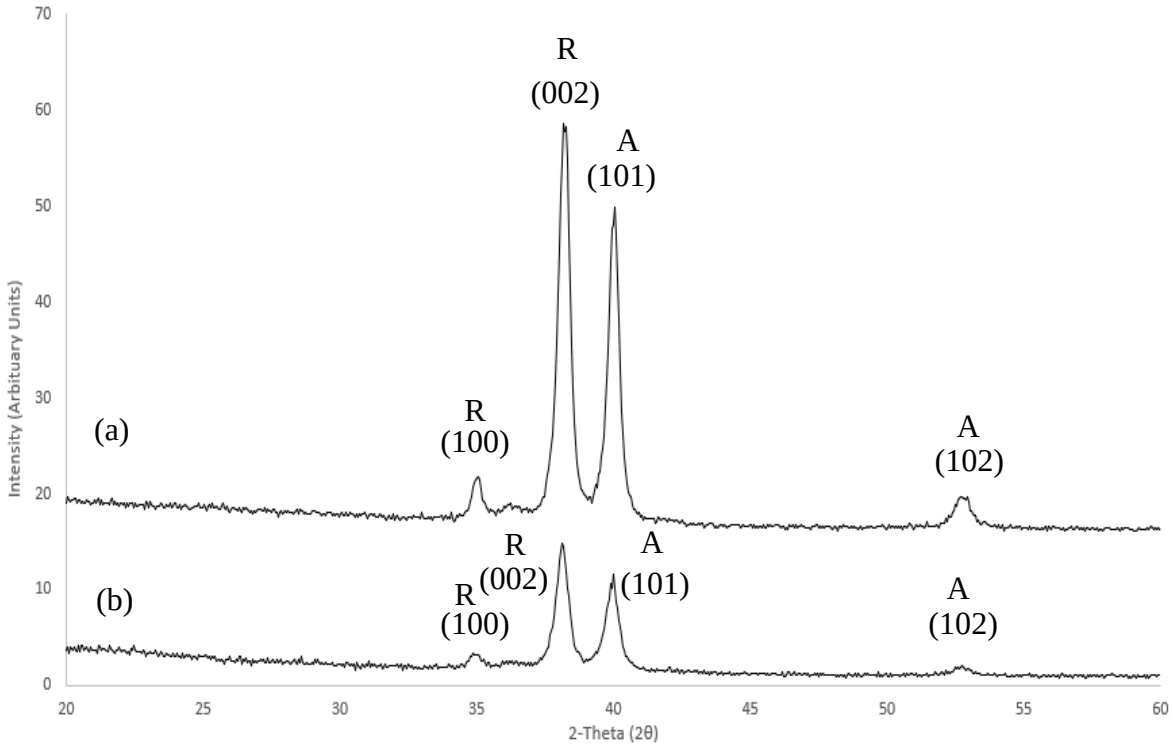

Figure 5.7 X- ray diffractograms for HA and SrHA CaP sputtered coatings on pristine titanium (a) TiHA and (b) TiSrHA with Miller index assignments labelled according to ICDD file 00-044-1294. Anatase (A) and rutile (R) phases also labelled

5.2.4 SEM analysis of HA and SrHA Coated Pristine Titanium

Figure 5.8 shows scanning electron microscopy (SEM) images for TiHA samples at magnifications of (a) x400, (b) x2.5k, (c) x4.5k (d) x8k with corresponding 80° tilt image views (e) x400, (f) x2.5k, (g) x4.5k and (h) x8k. At lower magnifications, there are no significant differences observed between the TiHA samples and the corresponding pristine Ti samples seen in Chapter 4.2.3 (Figure 4.4). The lines and grooves seen previously on the pristine Ti surface are still present. When magnification is increased to x30k, as provided in Figure 5.9, the presence of CaP (HA) particles becomes visible particularly along the lines and grooves present on the substrate. The underlying distinguishing titanium topography is still clearly visible in all of these SEM images.

Figure 5.10 shows the corresponding planar view and 80° tilted view images for TiSrHA at magnifications of (a) x400, (b) x2.5k, (c) x4.5k (d) x8k, (e) x400, (f) x2.5k, (g) x4.5k and (h) x8k. As before, there are no discernible differences between the Ti uncoated and TiSrHA samples at lower magnification. At higher magnification the presence of the sputtered SrHA material can be seen across the surface, especially along any lines, grooves and pits. In this regard, Figure 5.11 shows an SEM image of a typical TiSrHA surface at x30k and clearly shows that the coating nucleates and grows on these pronounced surface features.

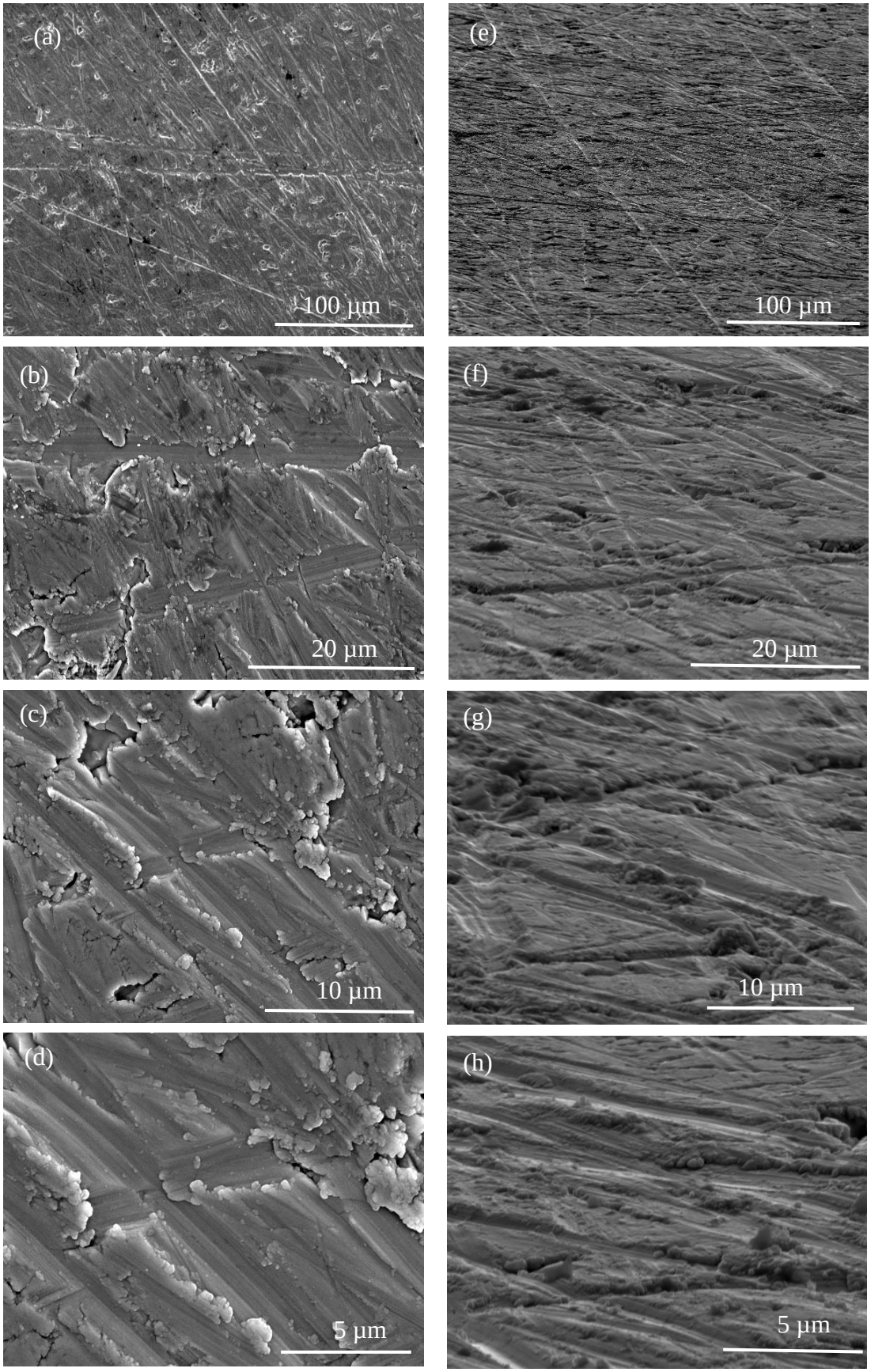

Figure 5.8 SEM images for TiHA showing normal planar views (a) – (d), and 80° tilt side angle views (e) – (h) at magnifications of (a) x400, (b) x2.5k, (c) x4.5k, (d) x8k, (e) x400, (f) x2.5k, (g) x4.5k and (h) x8k

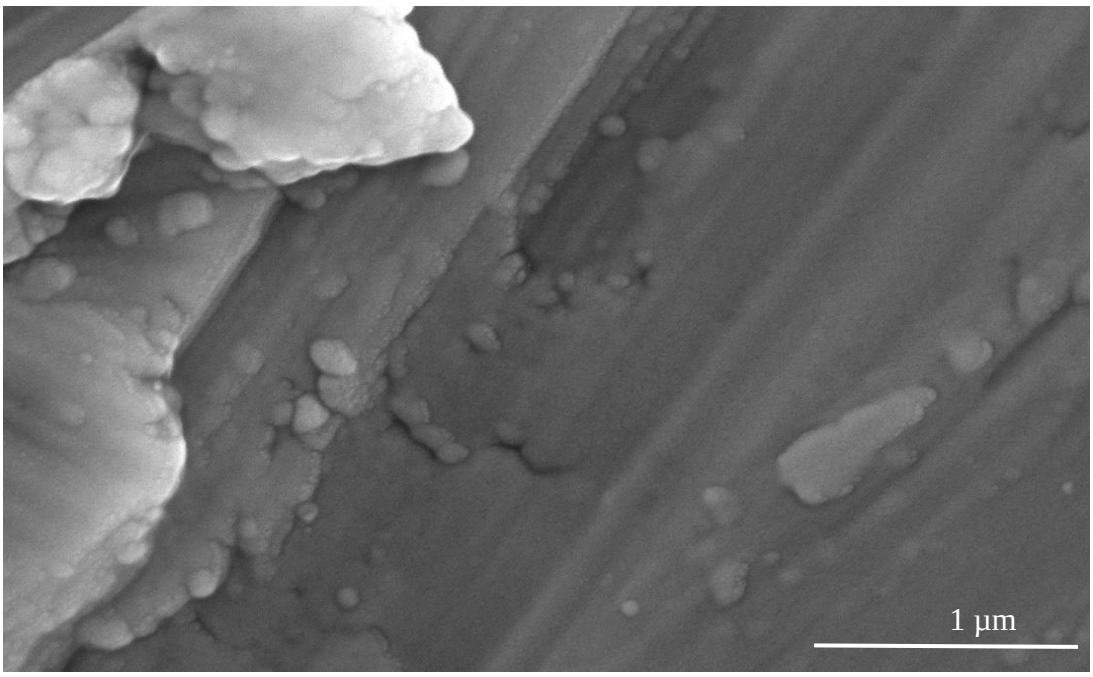

Figure 5.9 SEM planar view image of TiHA at x30k magnification

A comparison of Figure 5.8 (d) with Figure 5.10 (d) samples (x8k) suggests that TiHA has more areas of 'pull out' and surface nucleation than are observed for TiSrHA. Overall, the TiSrHA samples have a 'smoother' surface and although the lines and grooves are still present there are no areas of coating material build-up of the type seen for the TiHA samples. However, at higher magnification (x30k) both sample surfaces are very similar.

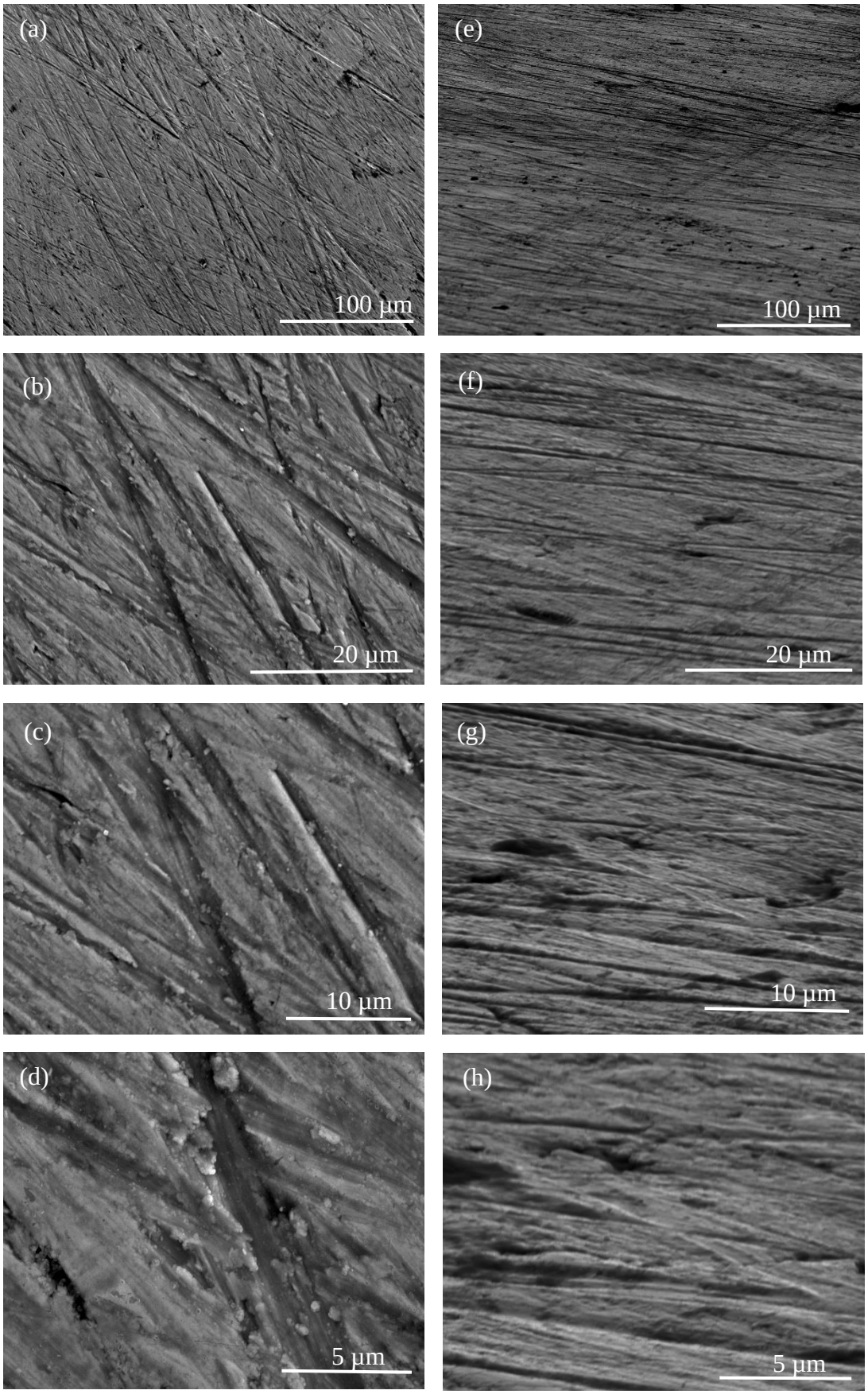

Figure 5.10 SEM images for TiSrHA showing normal planar views (a) – (d), and 80° tilt side angle views (e) – (h) at magnifications of (a) x400, (b) x2.5k, (c) x4.5k, (d) x8k, (e) x400, (f) x2.5k, (g) x4.5k and (h) x8k

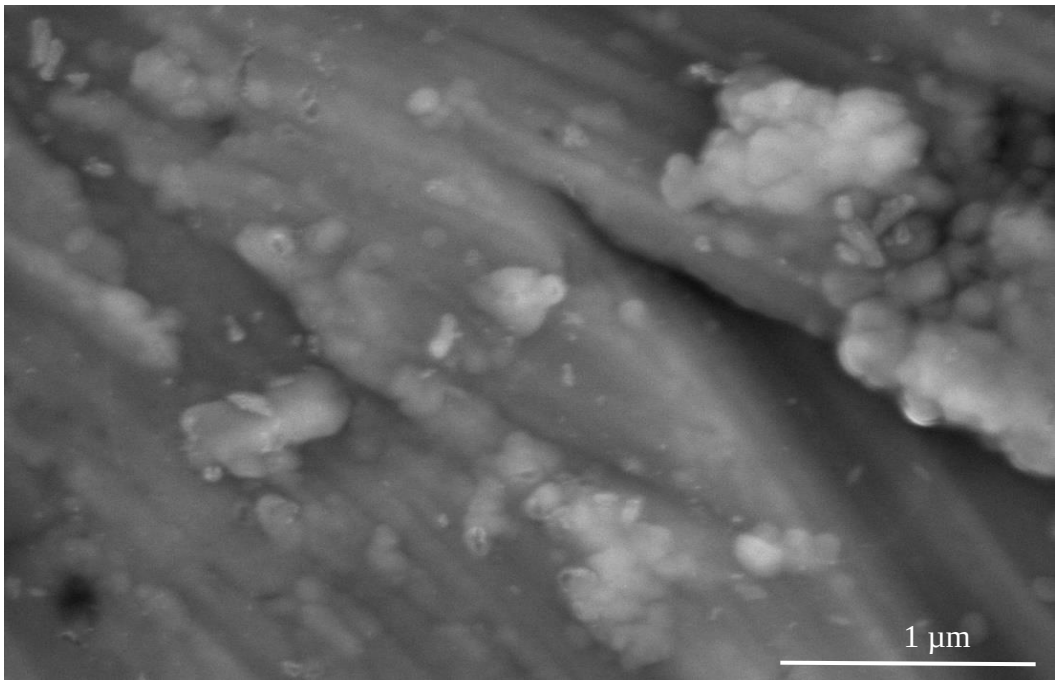

Figure 5.11 SEM planar view image of TiSrHA at x30k magnification

5.3 HA and SrHA Coatings on 24 hr Etched Titanium

The morphology created on the 24eTi surface is thought to have the potential to provide the type of offset orientated roughness that can control the dissolution of HA or SrHA sputtered films thereon. To this end, the surface chemistry (XPS, ToFSIMS, XRD) and morphology (SEM) that results from adding a CaP bioactive sputter deposited coating to the underlying etched titanium surface have been determined.

5.3.1 XPS of HA and SrHA Coated 24 hr Etched Titanium

The XPS spectra for 24eTiHA is presented in Figure 5.12. In general, the WESS (Figure 5.12 (a)) is similar to that observed for TiHA (Figure 5.1 (a)). There are again no titanium signals detected indicating that the CaP (HA) coating is thicker than the inelastic mean free path of the photoelectrons from the underlying substrate. Given that the etching process has been shown to create significant surface roughness, the lack of Ti 2p signals also confirms that HA deposits as a continuous HA coating on this surface. The high-resolution spectra plots (Figure 5.12 (b) – (e)) show the presence of carbon (C 1s), oxygen (O 1s), calcium (Ca 2p) and phosphorus (P 2p) signals. Figure 5.12 (b) shows the C 1s region, with the lowest binding energy again charge corrected to 284.8 eV, indicative of C-C and C-H bonding. The three remaining peaks present in this C 1s envelope correspond to C-O, C=O and O-C=O bonding which are fitted to 286.5 eV, 287.7 eV and 288.7 eV, respectively. The O 1s region in Figure 5.12 (c) comprises the lattice oxide peak at 531.0 eV and the corresponding hydroxide bonding peak present at 532.1 eV. Presence of the HA thin film coating was confirmed through the quantifiable Ca 2p and P 2p signals. The doublet peak shown for Ca 2p in Figure 5.12 (d) is present at 347.8 eV and 351.4 eV for Ca $2p_{3/2}$ and Ca $2p_{1/2}$, respectively. The P 2p signal (Figure 5.12 (e)) is fitted to P $2p_{3/2}$ and P $2p_{1/2}$ peaks at 133.6 eV and 134.6 eV, respectively. The C/O ratio here was calculated as 0.42 which is again indicative of a higher oxygen content on the surface expected with the HA thin film. This C/O ratio is the same as that recorded for TiHA but lower than the 0.46 calculated for TiSrHA. The Ca/P ratio for 24eTiHA was calculated as 0.91, which is also lower than that calculated for the TiHA and the typical 1.67 expected for HA.

Figure 5.13 (a) – (e) shows the WESS and high-resolution plots for 24eTiSrHA samples. The peaks present in the WESS (Figure 5.13(a)) are again similar to those seen for the TiHA, with the addition of strontium here, as expected. The C 1s region was charge corrected to 284.8 eV, with the corresponding carbon peaks for C-O, C=O and O-C=O fitted to 286.3 eV, 287.8 eV and 288.8 eV, respectively. The O 1s region (Figure 5.13 (c))

present at 531.5 eV and 533.1 eV once again correspond to lattice bonding and hydroxide bonding, respectively. The Ca 2p doublet in Figure 5.13 (d) can be fitted to Ca $2p_{3/2}$ and Ca $2p_{1/2}$ at 347.7 eV and 351.3 eV, respectively. The unresolved P 2p doublet displayed in Figure 5.13 (e) shows contributions for P $2p_{3/2}$ at 133.8 eV and P $2p_{1/2}$ at 135.5 eV. The Sr 3p doublet (Figure 5.13 (insert within WESS)) comprises the Sr $3p_{3/2}$ at 269.7 eV and the Sr $3p_{1/2}$ at 279.8 eV. There are no titanium signals present in the WESS indicating again that the sputter coating is thicker than that of the relevant photoelectron inelastic mean free path. The C/O ratio is calculated as 0.33 which is lower than that of the TiHA, TiSrHA and 24eTiHA samples. The Ca/P ratio for these is 0.31, with a combined (Sr + Ca) / P ratio of 0.40. These ratios are lower than those calculated for TiSrHA and suggest a higher content of phosphorus than calcium on the sample surface.

The XPS quantification data for the 24eTiHA and 24eTiSrHA samples can be seen in Table 5.2.

Table 5.2 XPS quantification data (n = 9) for 24eTiHA and 24eTiSrHA samples with standard deviation included

	24eTiHA			24eTiSrHA		
Element	Binding Energy (eV)	Atomic concentration %	Total Atomic Concentration %	Binding Energy (eV)	Atomic Concentration %	Total Atomic Concentration %
C 1s	284.8	13.64 ± 0.47	19.77 ± 3.65	284.8	11.08 ± 2.80	14.69 ± 0.97
	286.5	3.89 ± 1.93		286.3	2.40 ± 1.25	
	287.7	1.24 ± 1.21		287.8	0.52 ± 0.67	
	288.7	0.95 ± 0.29		288.8	0.71 ± 0.25	
O 1s	531.0	22.46 ± 4.66	47.50 ± 1.20	531.5	31.90 ± 1.81	44.43 ± 5.47
	532.1	25.02 ± 3.81		533.1	13.00 ± 6.51	
Ca 2p	347.8	10.08 ± 1.58	15.59 ± 2.20	347.7	6.24 ± 1.66	9.17 ± 2.20
	351.4	5.49 ± 1.27		351.3	2.96 ± 0.62	
P 2p	133.6	11.49 ± 0.73	17.15 ± 1.13	133.8	19.48 ± 1.19	29.25 ± 1.72
	134.6	5.74 ± 0.37		135.5	9.74 ± 0.60	
Sr 3p	-	-	-	269.7	1.71 ± 0.53	2.47 ± 0.88
	-	-	-	279.8	0.70 ± 0.32	

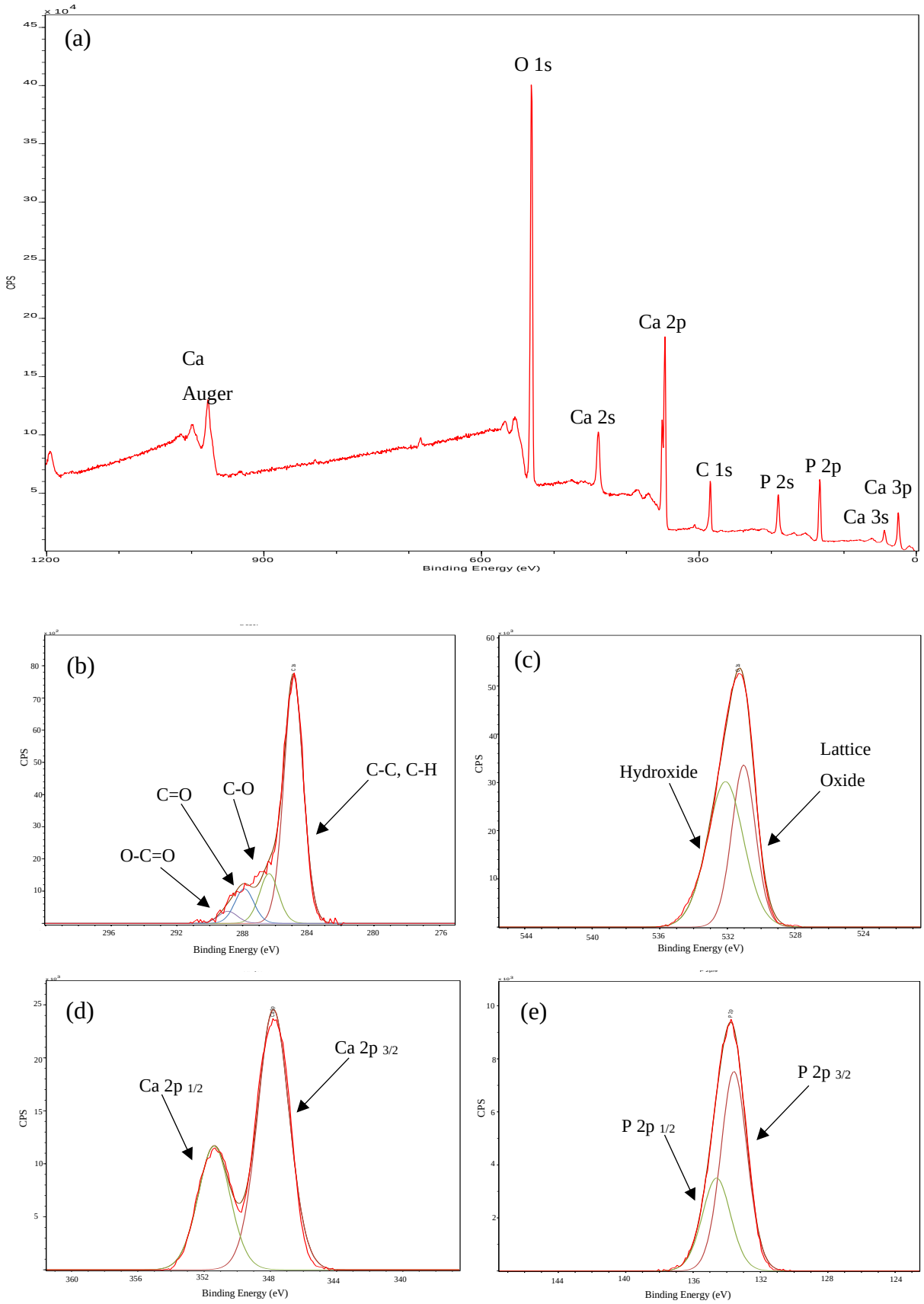

Figure 5.12 XPS spectra for 24eTiHA surface showing (a) WESS, and high-resolution spectra for (b) C 1s, (c) O 1s, (d) Ca 2p and (e) P 2p regions

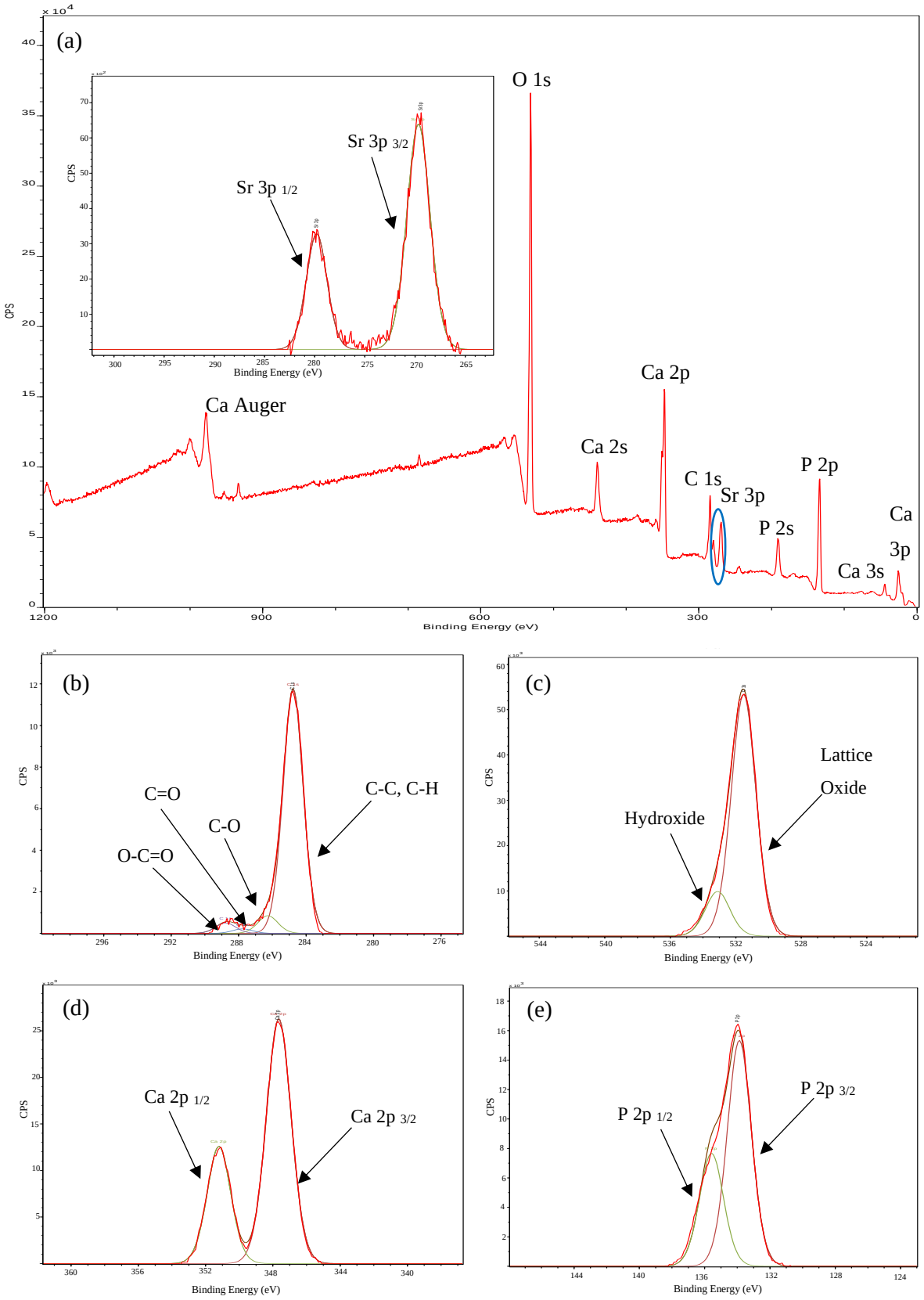

Figure 5.13 XPS spectra for 24eTiSrHA surface showing (a) WESS, and high-resolution spectra for (b) C 1s, (c) O 1s, (d) Ca 2p, (e)P 2p and Sr 3p (insert within WESS plot) regions

5.3.2 ToFSIMS of HA and SrHA Coated 24 hr Etched Titanium

Figure 5.14 shows the positive ion mass spectrum for 24eTiHA in the range 0-300 m/z. Two major signals are detected at 40 m/z and 57 m/z indicative of calcium and calcium hydroxide ions, respectively. There is no signal detected at 48 m/z for titanium indicating that the CaP thin film is homogeneous across the surface. There are also various of calcium phosphate ions detected with lower intensity: CaH^+, $CaPO_2^+$, $Ca_2PO_4^+$, $CaPO_3^+$, $Ca_2PO_3^+$, Ca_2O^+ and $Ca_3PO_5^+$. These ions are all indicative of a CaP (HA) thin film on the substrate surface. Positive ion maps for the main peaks are presented in Figure 5.15 indicative of their spatial distribution over representative areas of the sample surface.

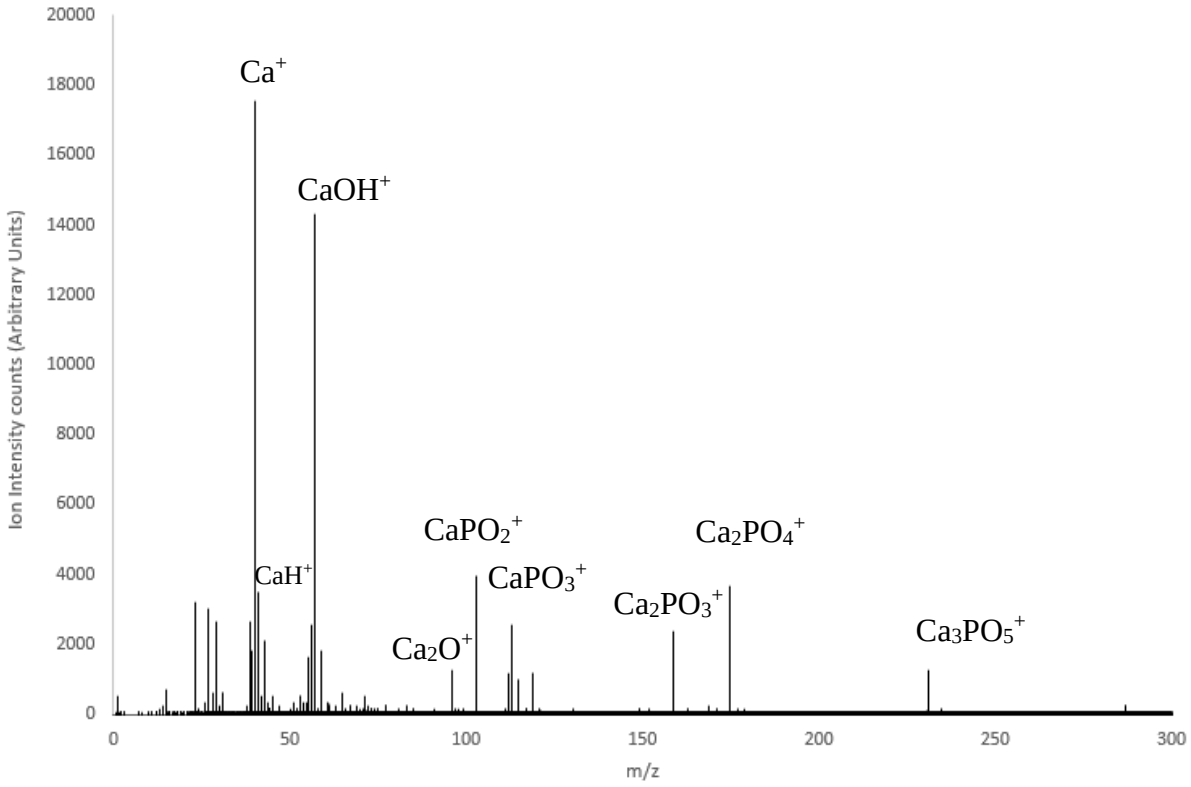

Figure 5.14 Positive ion ToFSIMS spectrum for 24eTiHA surface with positive ion signals indicative of a CaP thin film labelled

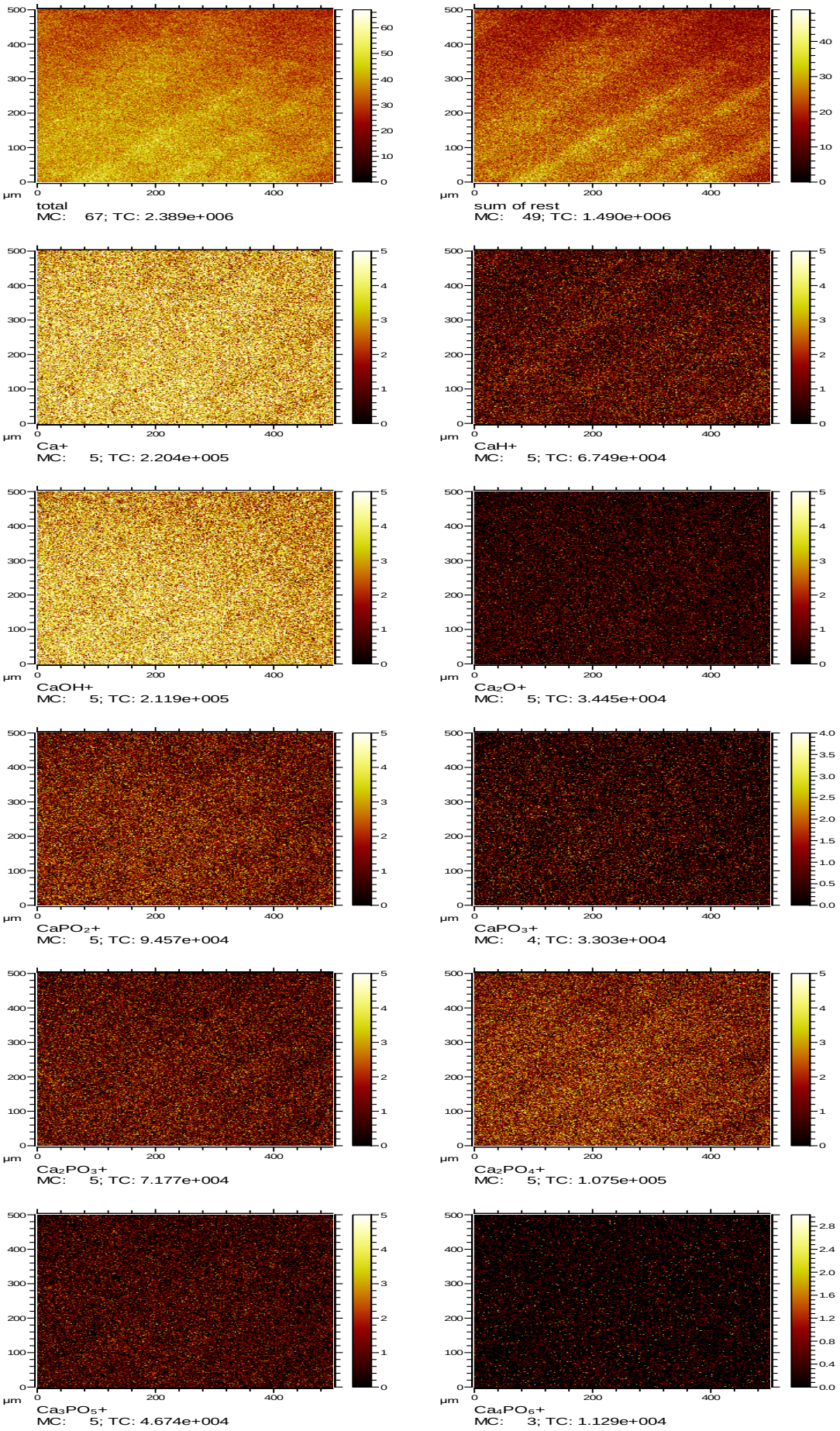

Figure 5.15 ToFSIMS positive ion maps of total ion count (TIC), Ca^+, CaH^+, $CaOH^+$, Ca_2O^+, $CaPO_2^+$, $CaPO_3^+$, $Ca_2PO_3^+$, $Ca_2PO_4^+$, $Ca_3PO_5^+$, and $Ca_4PO_6^+$ for 24eTiHA

Figure 5.16 displays the corresponding positive ion mass spectrum for 24eTiSrHA. Again, the dominant peaks here are Ca^+ at 40 m/z and $CaOH^+$ at 57 m/z. There is a strontium signal present at 88 m/z, as expected. As before, no signal is detected for titanium at 48 m/z in the positive ion spectra. However, small titanium signals are detected in the positive ion maps. Overall, the spectrum for 24eTiSrHA show similarities to that for TiSrHA (Figure 5.5) with both displaying calcium ions associated with HA coatings. When comparing these latter positive ion spectra to those for 24eTiHA and 24eTiSrHA (Figures 5.14 and Figure 5.16, respectively) it is noted that the 24eTiHA shows the presence of many more CaP phases than that of the 24eTiSrHA samples.

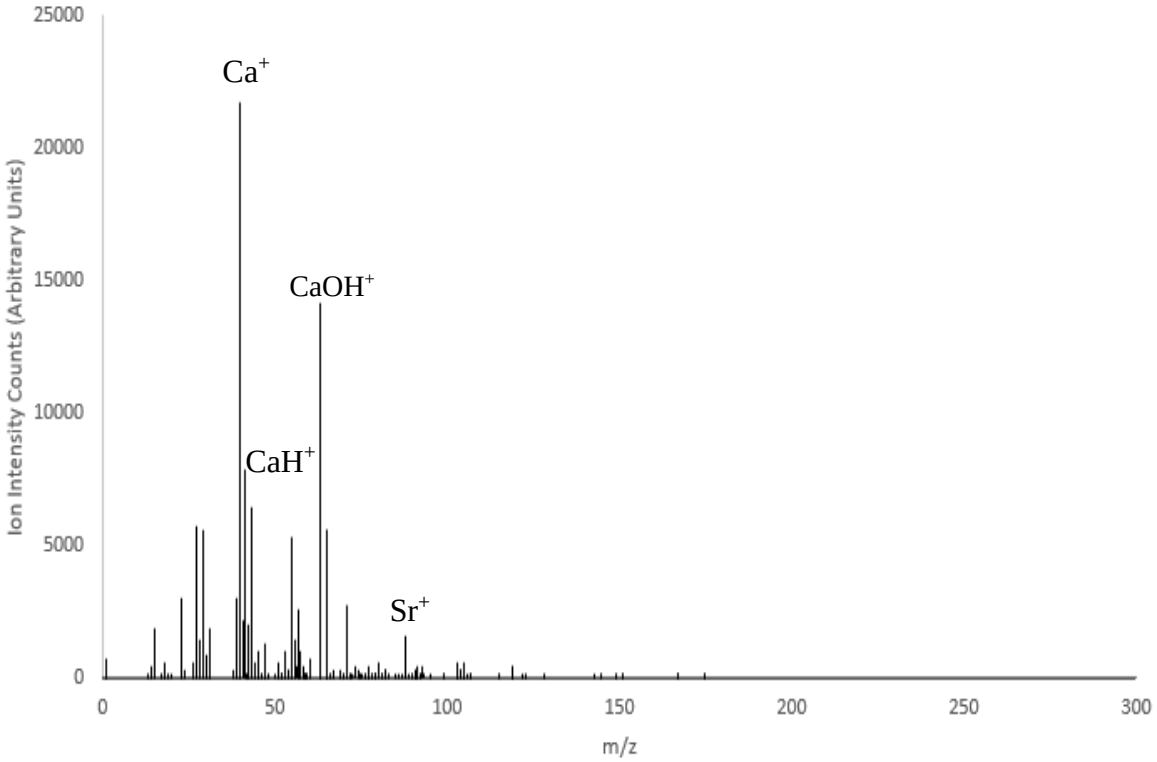

Figure 5.16 Positive ion ToFSIMS spectrum for 24eTiSrHA surface with positive ion signals indicative of a CaP thin film labelled

Figure 5.17 provides the positive ion maps for 24eTiSrHA with intensities that are similar to those for TiHA (Figure 5.6). The corresponding positive ion maps for 24eTiSrHA show the absence of many of the CaP phases noted in the 24eTiHA but do show the presence of calcium and calcium hydroxide, with lesser amounts of simpler CaP phases. As before, no peaks were detected for titanium.

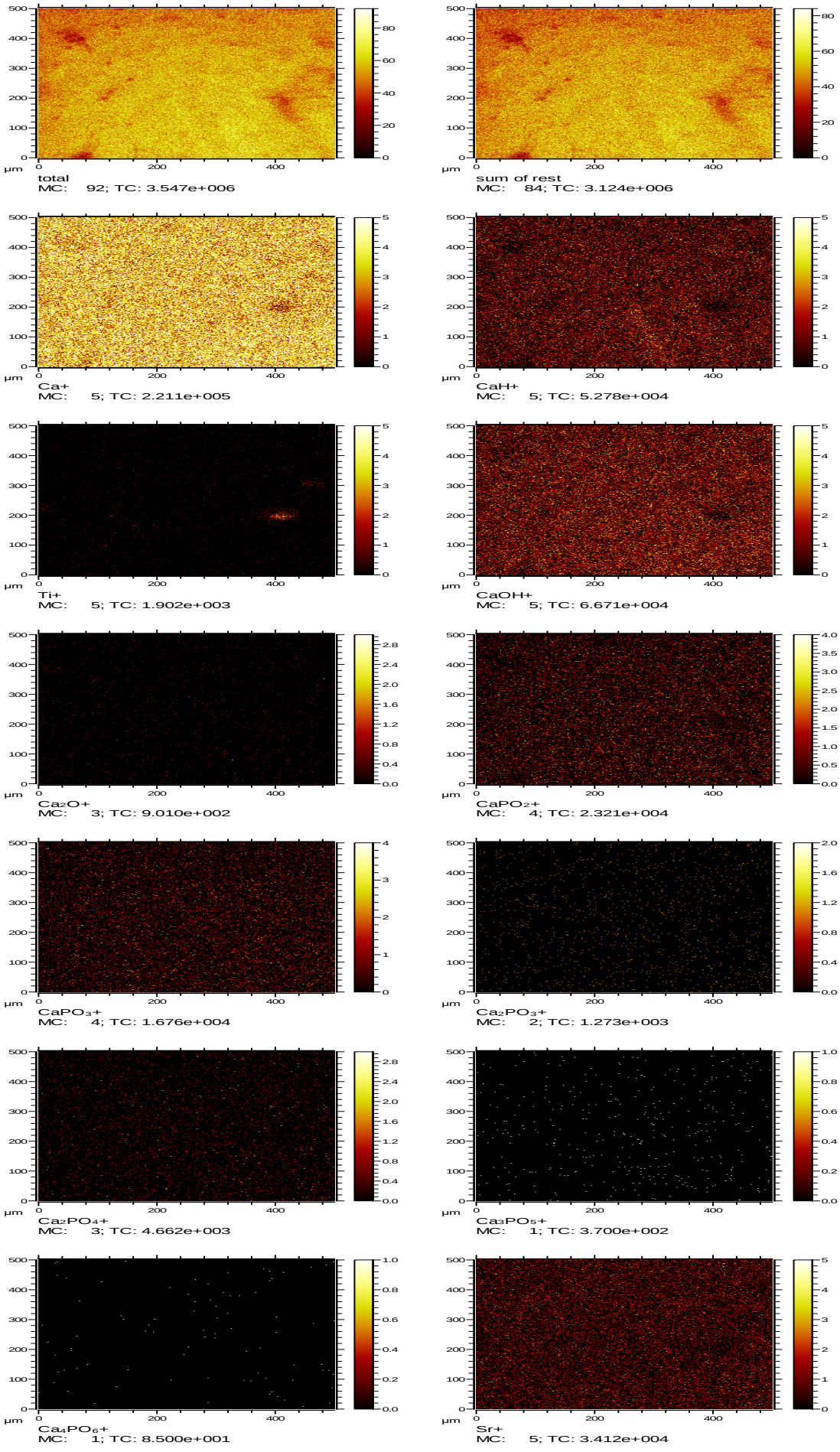

Figure 5.17 ToFSIMS positive ion maps of total ion count (TIC), Ca^+, CaH^+, Ti^+, $CaOH^+$, Ca_2O^+, $CaPO_2^+$, $CaPO_3^+$, $Ca_2PO_3^+$, $Ca_2PO_4^+$, $Ca_3PO_5^+$, $Ca_4PO_6^+$and Sr^+ for 24eTiSrHA

5.3.3 XRD of HA and SrHA Coated 24 hr Etched Titanium

Figure 5.18 displays x-ray diffractograms for (a) 24eTiHA and (b) 24eTiSrHA with all peaks present labelled accordingly. For the 24eTiHA sample, Figure 5.18 (a) displays peaks at 2θ = 35.2°, 38.5°, 40.2° and 53.0° which correspond to the Miller index (hkl) orientation in the 100, 002, 101 and 102 planes respectively. These peaks correspond to the ICDD file 00-044-1294 for semi-crystalline titanium[205,227]. No peaks indicative of HA was found to be present.

Figure 5.18 (b) shows the x-ray diffractogram collected for the 24eTiSrHA sample. Peaks were found to be present at 2θ = 35.1°, 38.5°, 40.2° and 53.1° which correspond to the Miller index (hkl) orientation in the planes of 100, 002, 101 and 102 respectively. These samples also show no indication of peaks associated with HA or SrHA. The diffraction planes again correspond to the semi-crystalline titanium ICDD file 00-044-1294[205,227]. These x-ray diffractograms are similar to those for TiHA and TiSrHA (Figure 5.7 (a) – (b)), showing orientation planes indicative of semi- crystalline titanium.

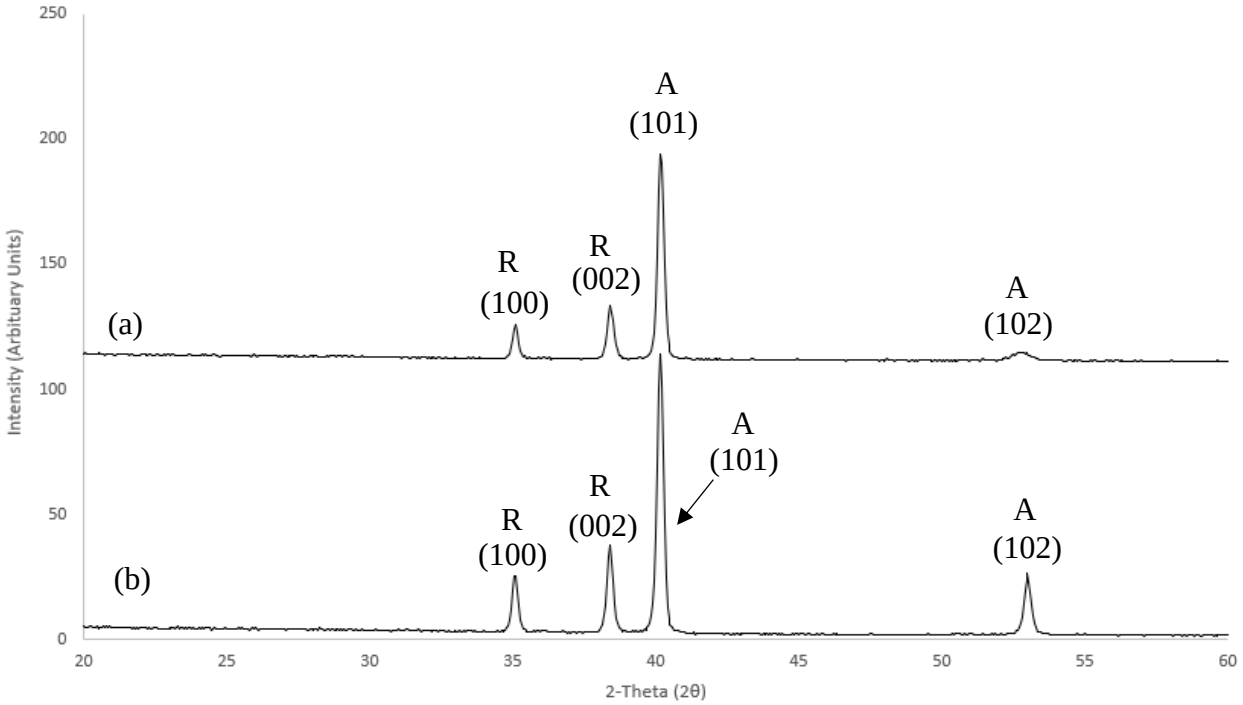

Figure 5.18 X-ray diffractograms for HA and SrHA CaP sputter coatings on 24 hr etched titanium (a) 24eTiHA and (b) 24eTiSrHA with Miller index assignments labelled according to ICDD file 00-044-1294. Anatase (A) and rutile (R) phases also labelled

5.3.4 SEM of Etched Titanium with CaP Thin Film Coatings

Figure 5.19 displays SEM images for 24eTiHA in both plane and 80° tilted angle views to allow for better visualisation of the CaP coating on the etched titanium surface. The distinctive 'honeycomb' pitting morphology previously observed for the underlying 24eTi surface (Figure 4.12) is still clearly visible across the sample surface. Nucleation of the HA material is partially visible at x8k (Figure 5.19 (d)) but is much clearer in Figure 5.20 which shows this sample at x30k. At this magnification, nucleation of the material across the surface and in the pitted areas is clearly visible, with the particles of the HA clearly visible. As such, the HA has not altered the morphology of the surface but in fact conformed to the underlying topography, as expected.

The corresponding SEM images for 24eTiSrHA are presented in Figure 5.21. At x400 (Figure 5.21 (a)) the pitting morphology is not as prominent as it was in the 24eTiHA images nor the original 24eTi surface, but the lines and grooves that were seen on the pristine Ti are still visibly present. Upon higher magnification (Figure 5.21 (b) – (d)) nucleation of the SrHA material becomes apparent as there is what looks to be 'smoothing' of the pitting features on this surface. The 80° tilted images (Figure 5.21 (e) – (h)) show similarities to their equivalents for the 24eTiHA sample, with the pitting visible across the surface. However, the 24eTiSrHA sample does show a greater build-up of the nucleated coating material along certain parts of the sample surface compared to that for 24eTiHA. Figure 5.22 depicts the x30k magnification image for 24eTiSrHA with the individual CaP particles visible across the surface.

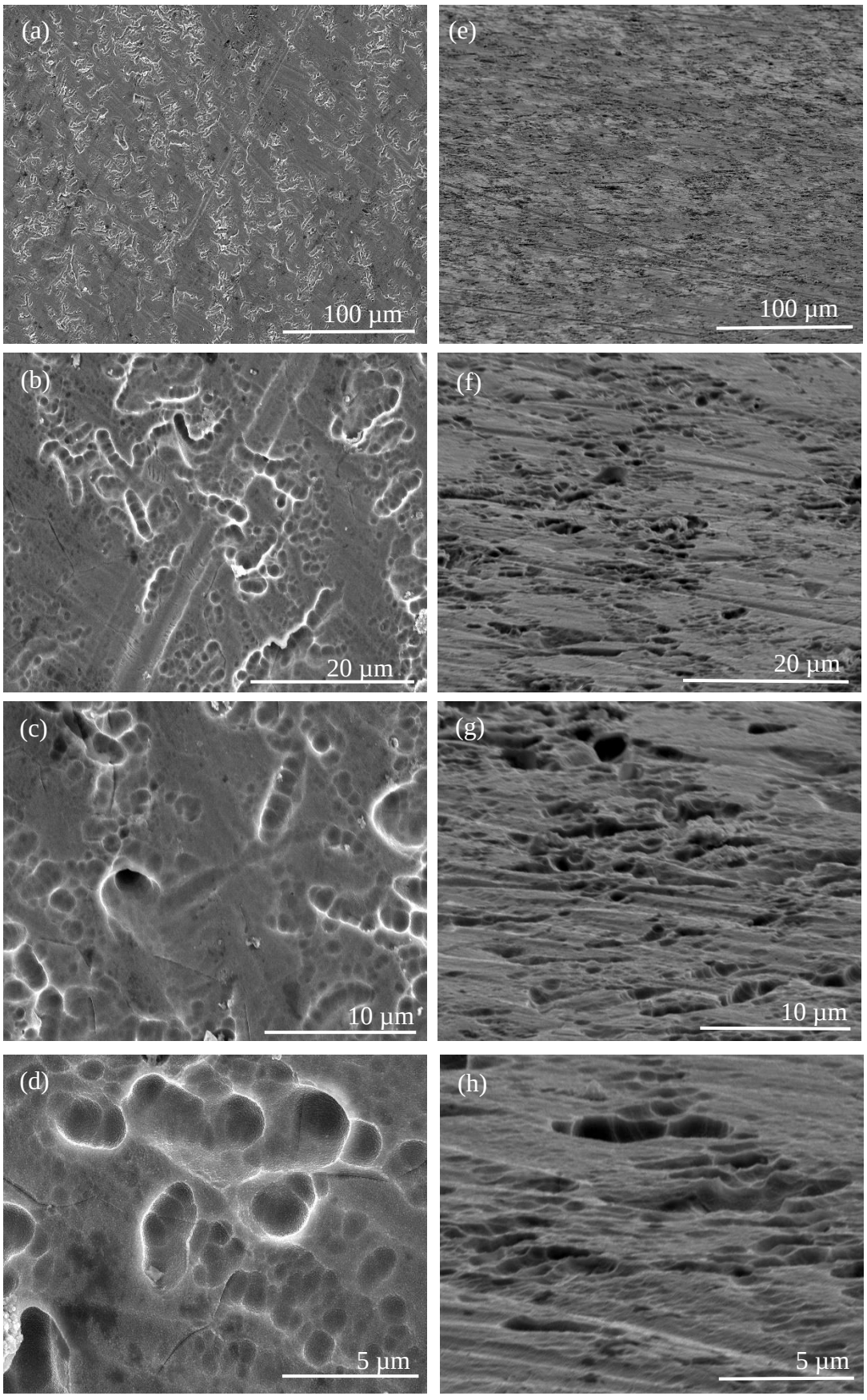

Figure 5.19 SEM images for 24eTiHA showing normal planar views (a) – (d), and 80° tilt side angle views (e) – (h) at magnifications of (a) x 400, (b) x 2.5k, (c) x 4.5k, (d) x 8k, (e) x 400, (f) x 2.5k, (g) x 4.5k and (h) x 8k

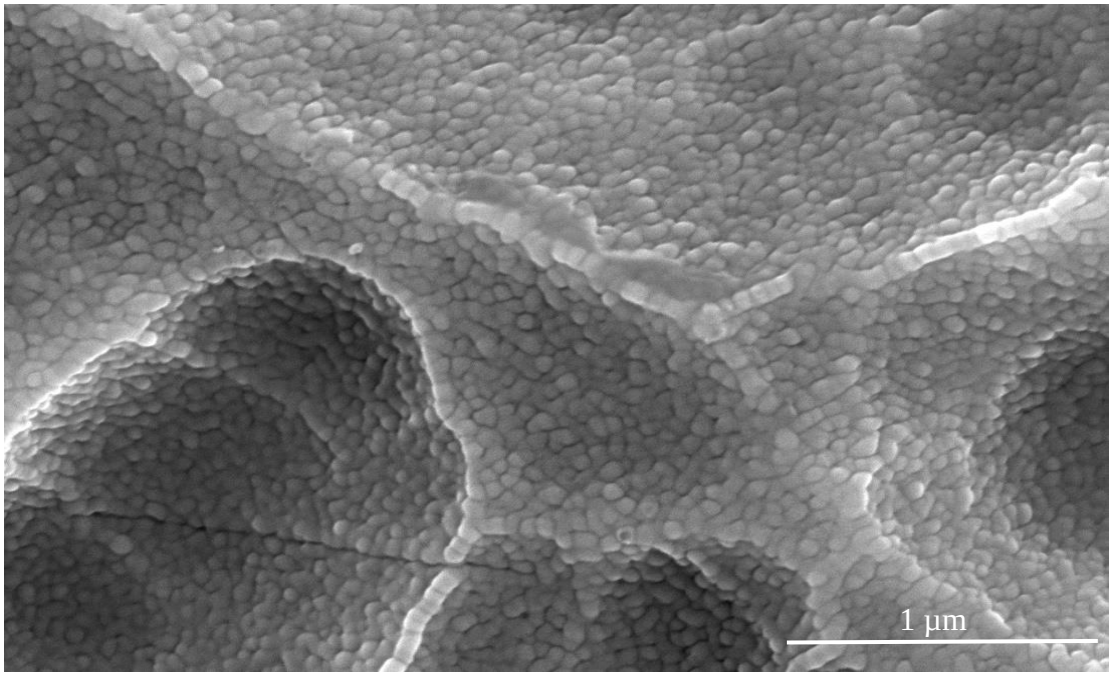

Figure 5.20 SEM planar view image of 24eTiHA at x 30k magnification

Both the 24eTiHA and 24eSrHA samples show nucleation of the coating materials (HA and SrHA) onto the etched sample surface. Both types of sample do still show a dominant underlying 'honeycomb' pitted morphology, which is much more prominent for 24eTiHA samples compared to 24eTiSrHA. Interestingly, a build-up of particles in certain sample areas is evident on the 24eTiSrHA samples, both in the planar view images and the 80° tilted images.

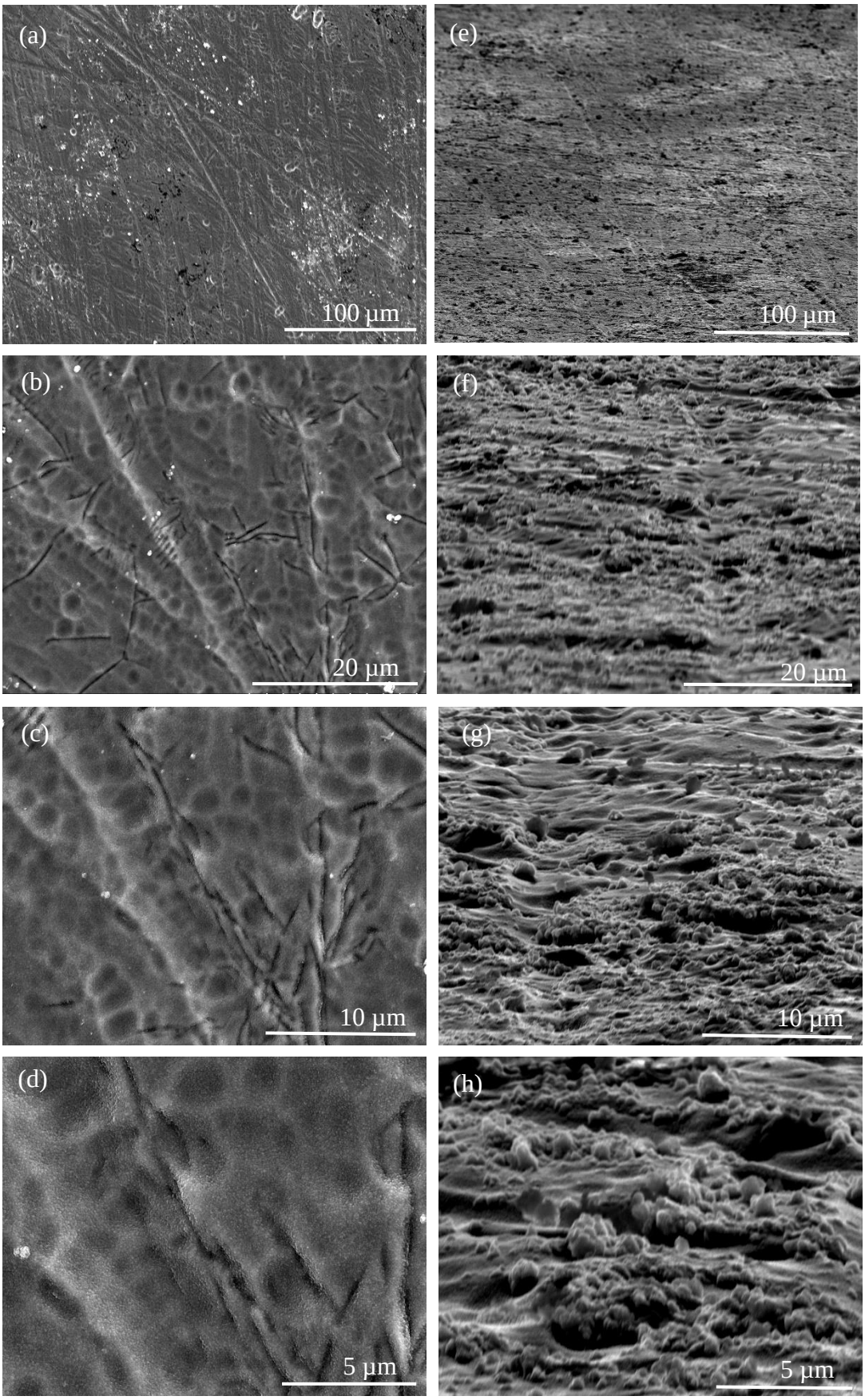

Figure 5.21 SEM images for 24eTiSrHA showing normal planar views (a) – (d), and 80° tilt side angle views (e) – (h) at magnifications of (a) x 400, (b) x 2.5k, (c) x 4.5k, (d) x 8k, (e) x 400, (f) x 2.5k, (g) x 4.5k and (h) x 8k

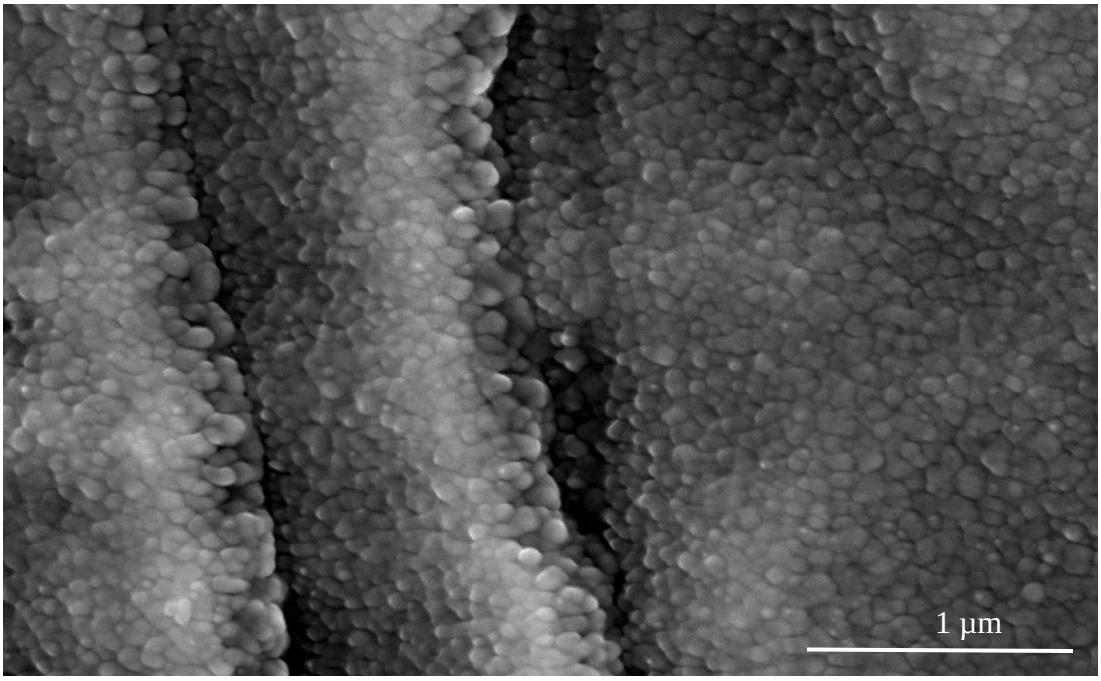

Figure 5.22 SEM planar view image of 24eTiSrHA at x 30k magnification

5.4 HA and SrHA Coatings on Polycrystalline Titanium

Titanium surfaces created by RF magnetron sputtering from a pure titanium target have been coated with HA and SrHA as a comparator for the 24 hr etched substrates. These polycrystalline surfaces have been shown previously to extend the time taken for dissolution of as-deposited sputtered CaP thin films coatings thereon[28,29].

5.4.1 XPS of HA and SrHA Coatings on Polycrystalline Titanium

The XPS spectra for PolyTi250HA are displayed in Figure 5.23 with the WESS in Figure 5.23 (a) and the corresponding high-resolution plots for the C 1s, O 1s, Ca 2p and P 2p regions shown in Figure 5.23 (b) – (e), respectively. The WESS shows the presence of the HA thin film in the form of calcium (Ca 2p) and phosphorus (P 2p) signals, with the absence of any titanium (Ti 2p) signal notable. This absence of titanium signals again suggests that the coating is thicker than that of the inelastic mean free path of the respective photoelectrons. Figure 5.23 (b) shows the C 1s region, where the lowest BE peak was charge corrected to 284.8 eV for adventitious carbon, with the three remaining peaks assigned to C-O, C=O and O-C=O seen at 286.1 eV, 287.6 eV and 288.6 eV respectively. The O 1s region shows two peaks due to lattice bonding and hydroxide bonding at 531.0 eV and 532.3 eV, respectively. The Ca 2p doublet in Figure 5.23 (d) shows Ca $2p_{3/2}$ at 347.7 eV and Ca $2p_{1/2}$ at 351.1 eV. The P 2p region in Figure 5.23 (e) shows P $2p_{3/2}$ and P $2p_{1/2}$ contribution to the doublet at 133.4 eV and 134.5 eV, respectively. The C/O ratio calculated from these data is 0.74 which is much higher than that for the TiHA, 24eTiHA, TiSrHA and 24eTiSrHA samples. The Ca/P value is 0.93, which is again lower than that of TiHA and the expected 1.67 for HA.

Figure 5.24 (a) presents the WESS for the PolyTi250SrHA surface. The lowest BE peak of the C 1s region in Figure 5.24 (b) is designated as due to adventitious carbon at 284.8 eV and all other peaks charge corrected accordingly. The remaining three peaks in this envelope are seen at 286.3 eV, 287.8 eV and 288.8 eV corresponding to C-O, C=O and O-C=O respectively. The O 1s region (Figure 5.24 (c)) has two discernible peaks at 531.0 eV and 532.3 eV which are as before, indicative of lattice bonding and hydroxide bonding, respectively. The Ca 2p region (Figure 5.24 (c)) shows a doublet at 347.7 eV and 351.3 eV assigned to Ca $2p_{3/2}$ and Ca $2p_{1/2}$, respectively. Figure 5.24 (e) shows the P 2p region which is fitted to show P $2p_{3/2}$ and P $2p_{1/2}$ at 133.9 eV and 135.8 eV, respectively. The Sr 3p region (Figure 5.24 (insert within WESS)) presents a doublet fitted for Sr $3p_{3/2}$ at 269.9 eV and Sr $3p_{1/2}$ at 280.0 eV. The C/O ratio calculated here is 0.43, which is lower than that for TiSrHA but higher than that calculated for 24eTiSrHA.

The Ca/P ratio is calculated to be 0.32 with a combined (Sr + Ca)/P ratio of 0.42 which is higher than the 24eTiSrHA but lower than the corresponding ratios calculated for TiSrHA. All XPS quantification for the PolyTi250HA and PolyTi250SrHA samples is presented in Table 5.3.

Table 5.3 XPS quantification data (n = 9) for PolyTi250HA and PolyTi250SrHA with standard deviation included

	PolyTi250HA			PolyTi250SrHA		
Element	**Binding Energy (eV)**	**Atomic concentration %**	**Total Atomic Concentration %**	**Binding Energy (eV)**	**Atomic Concentration %**	**Total Atomic Concentration %**
C 1s	284.8	24.04 ± 9.68	30.72 ± 12.11	284.8	15.66 ± 3.03	17.70 ± 2.26
	286.1	3.85 ± 1.09		286.3	1.80 ± 0.66	
	287.6	0.96 ± 0.55		287.8	0.18 ± 0.27	
	288.6	1.86 ± 0.80		288.8	0.21 ± 0.15	
O 1s	531.0	23.93 ± 6.09	41.69 ± 6.63	531.0	30.32 ± 2.68	41.17 ± 1.45
	532.3	17.86 ± 1.07		532.3	10.67 ± 3.99	
Ca 2p	347.7	8.91 ± 2.00	13.29 ± 2.75	347.7	6.54 ± 0.58	9.38 ± 0.81
	351.1	4.46 ± 0.86		351.3	2.86 ± 0.31	
P 2p	133.4	4.13 ± 1.17	14.24 ± 3.23	133.9	19.35 ± 0.54	28.99 ± 0.83
	134.5	9.99 ± 2.05		135.8	9.67 ± 0.27	
Sr 3p	-	-	-	269.9	2.06 ± 0.40	2.76 ± 0.50
	-	-	-	280.0	0.68 ± 0.14	

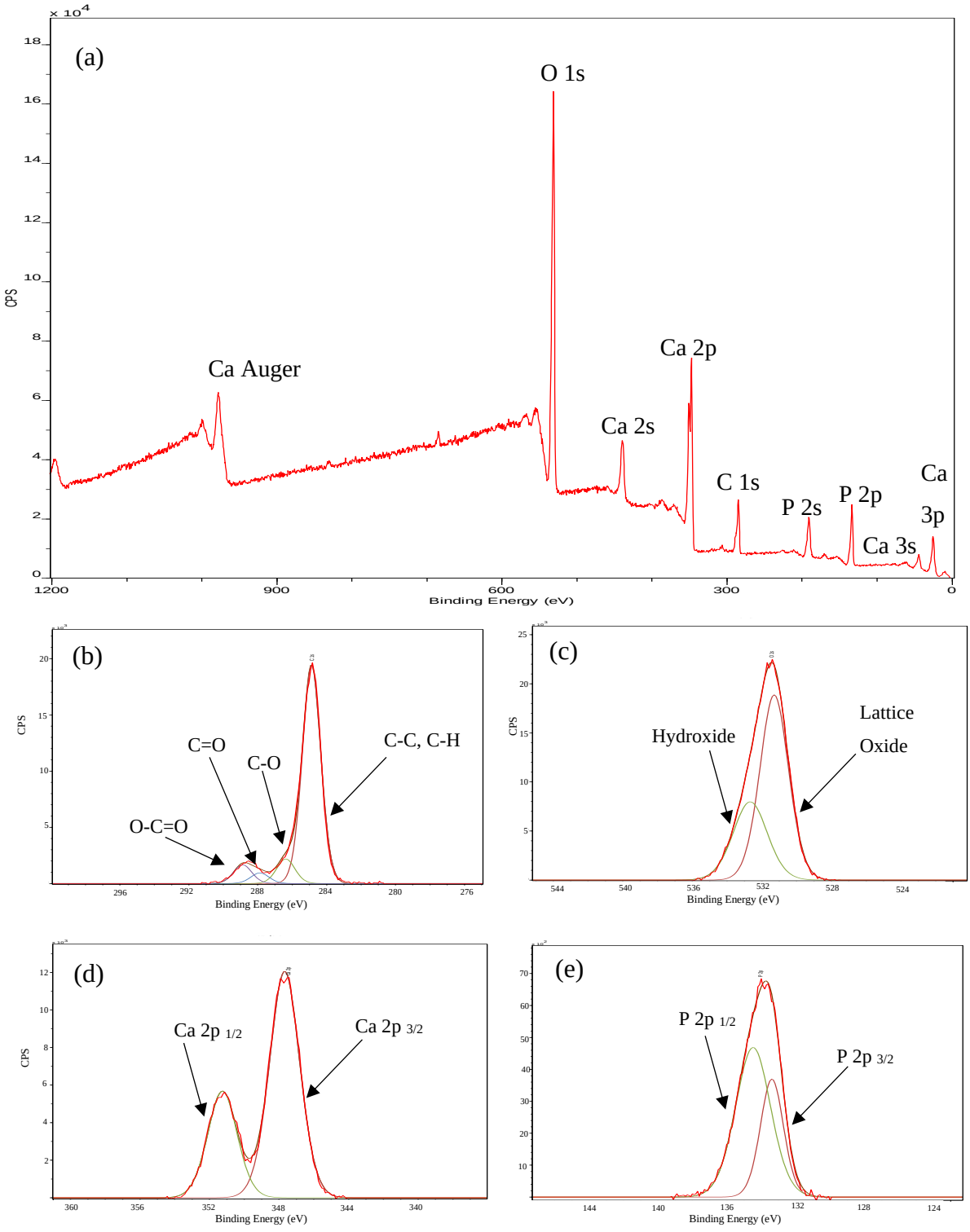

Figure 5.23 XPS spectra for PolyTi250HA showing (a) WESS, and high-resolution spectra for (b) C 1s, (c) O 1s, (d) Ca 2p and (e)P 2p regions

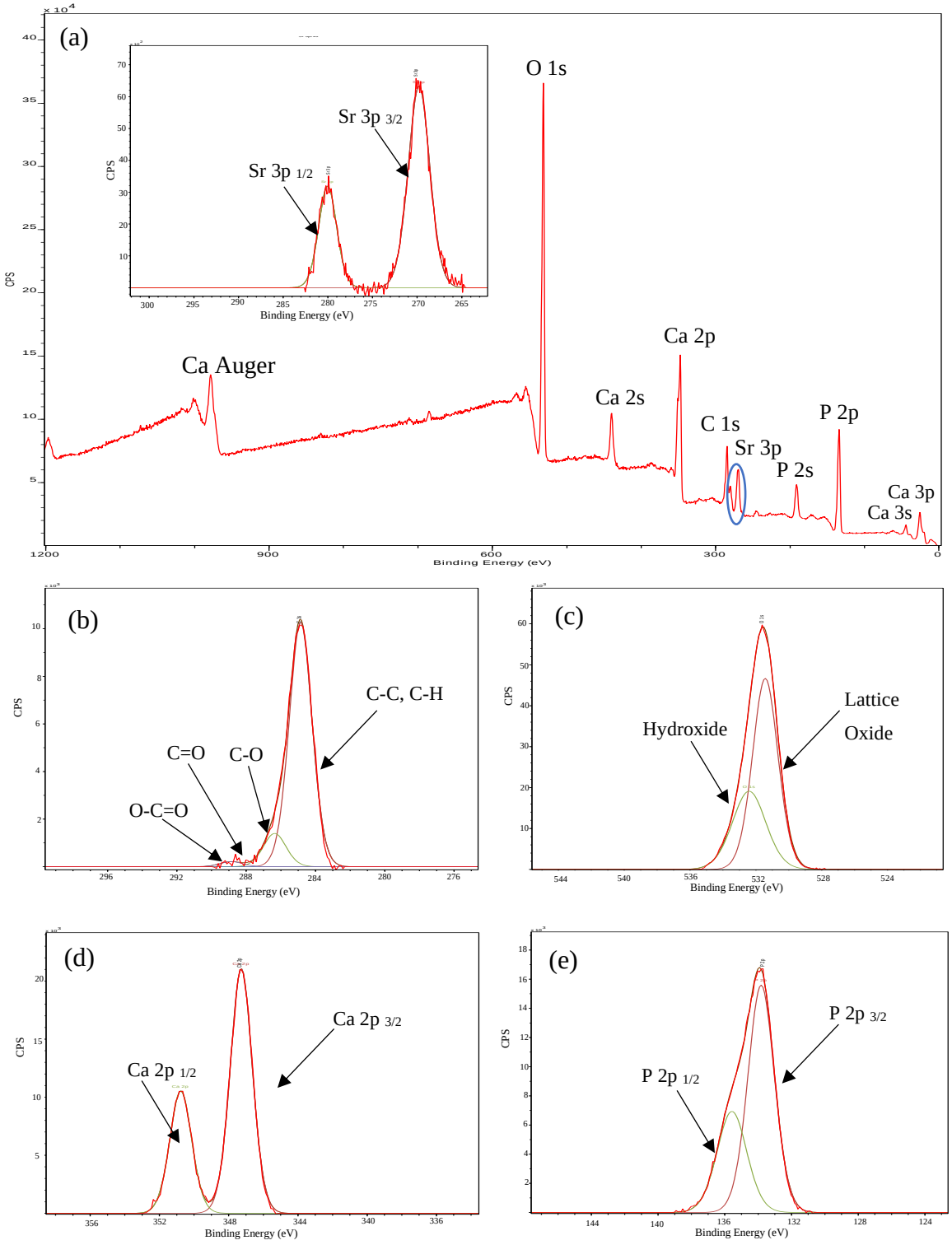

Figure 5.24 XPS spectra for PolyTi250SrHA surface showing (a) WESS, and high-resolution spectra for (b) C 1s, (c) O 1s, (d) Ca 2p, (e)P 2p and (f) Sr 3p (insert within WESS) regions

5.4.2 ToFSIMS of HA and SrHA Coatings on Polycrystalline Titanium

Figure 5.25 shows the ToFSIMS positive ion spectrum for PolyTi250HA. Ions due to calcium, calcium hydroxide and various calcium phosphate groups are clearly present, indicative of a CaP (HA) coating. The most dominant peaks are those for Ca^+ at 40 m/z and $CaOH^+$ at 57 m/z. There is some surface contamination in the form of Na^+ at 23 m/z and K^+ at 39 m/z, which as was the case previously thought to be from handling of the samples. Various forms of calcium phosphate ions are present across the surface but there is an absence of Ti^+. The associated PolyTi250HA positive ion maps for Ca^+, CaH^+, $CaOH^+$, Ca_2O^+, $CaPO_2^+$, $CaPO_3^+$, $Ca_2PO_3^+$, $Ca_2PO_4^+$, $Ca_3PO_5^+$and $Ca_4PO_6^+$ are provided in Figure 5.26 and confirm that the CaP (HA) forms a continuous thin film layer across the substrate surface.

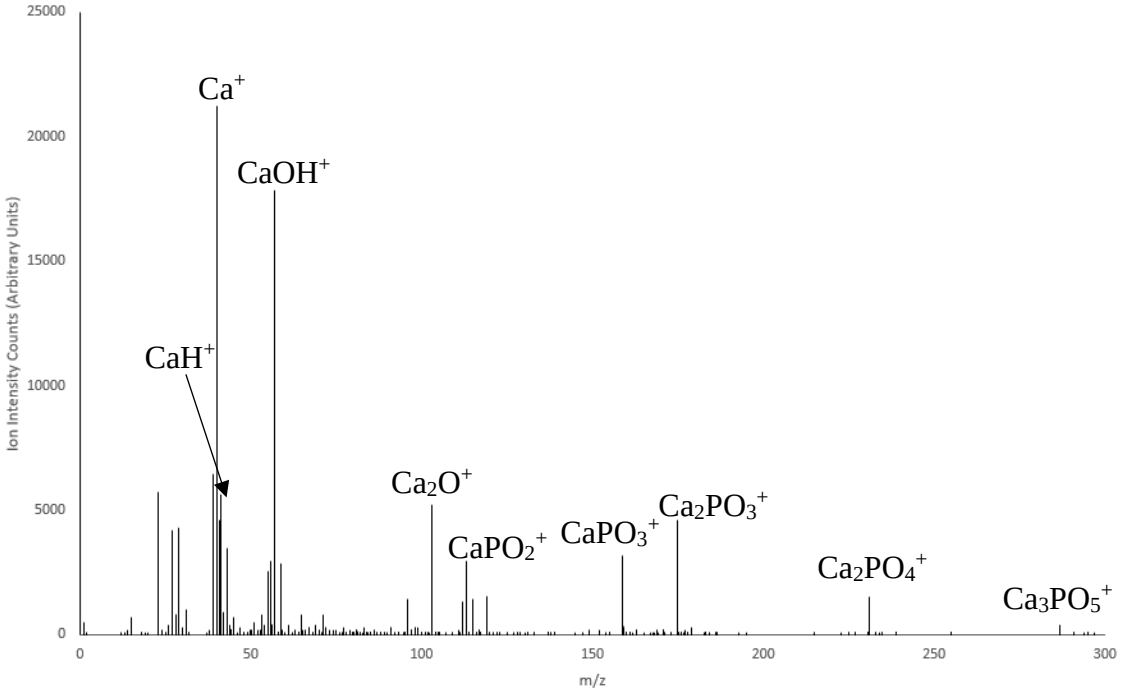

Figure 5.25 ToFSIMS positive ion spectrum for PolyTi250HA with positive ion signals indicative of a CaP thin film labelled

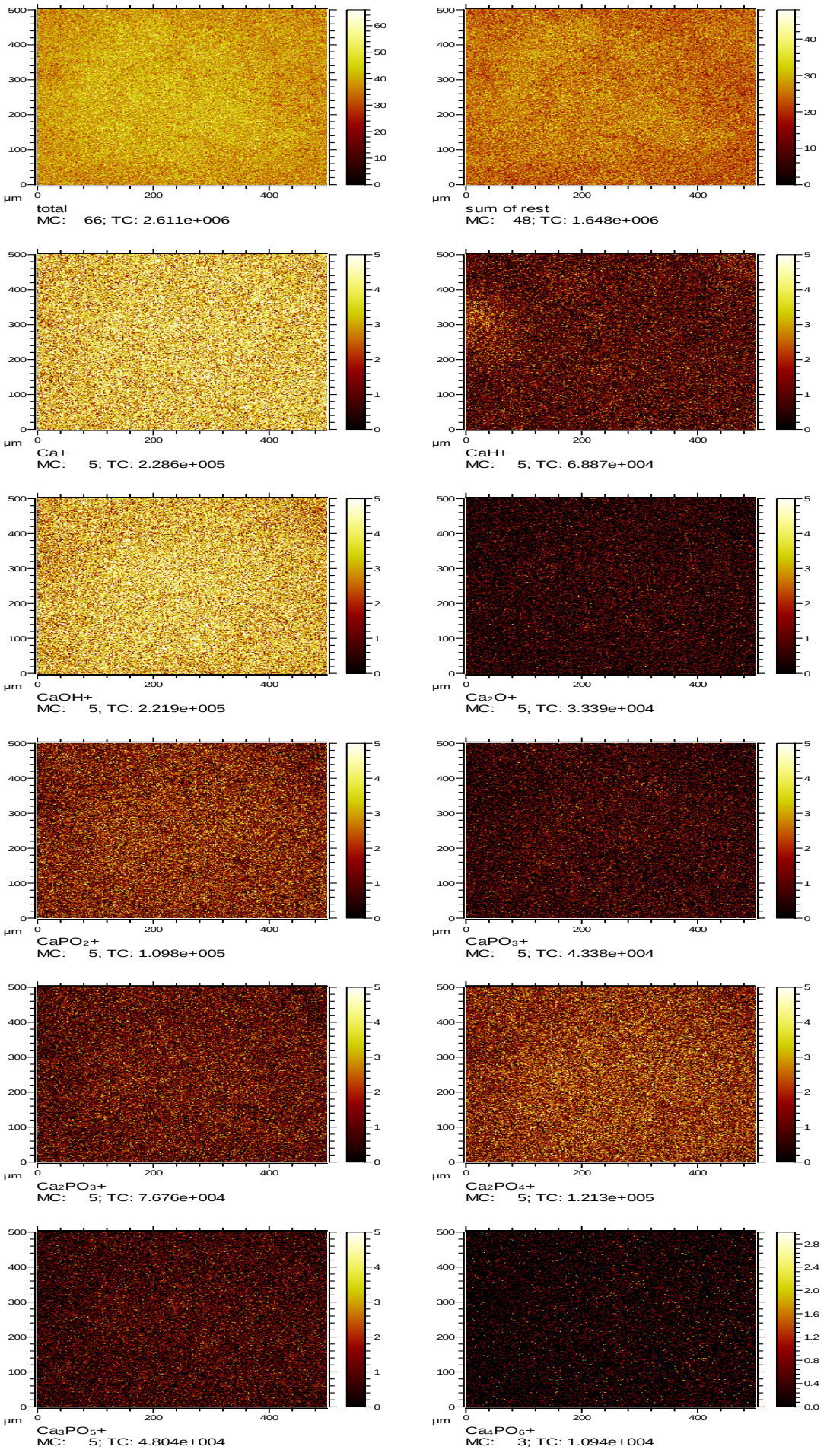

Figure 5.26 ToFSIMS positive ion maps of total ion count (TIC), Ca^+, CaH^+, $CaOH^+$, Ca_2O^+, $CaPO_2^+$, $CaPO_3^+$, $Ca_2PO_3^+$, $Ca_2PO_4^+$, $Ca_3PO_5^+$ and $Ca_4PO_6^+$ for PolyTi250HA

The ToFSIMS positive ion spectrum for PolyTi250SrHA is presented in Figure 5.27. As seen before, calcium, calcium hydroxide and various calcium phosphate groups are the main species present with some minor Na^+ and K^+ acquired contamination. Again, calcium (Ca^+) and calcium monohydride (CaH^+) ions are present at 40 m/z and 41 m/z, respectively. A signal for $CaOH^+$ is detected at 57 m/z and for Sr^+ at 88 m/z. The positive ion maps for this surface are shown in Figure 5.28 and confirm the presence of a continuous CaP (SrHA) thin film on the PolyTi250 sample surface.

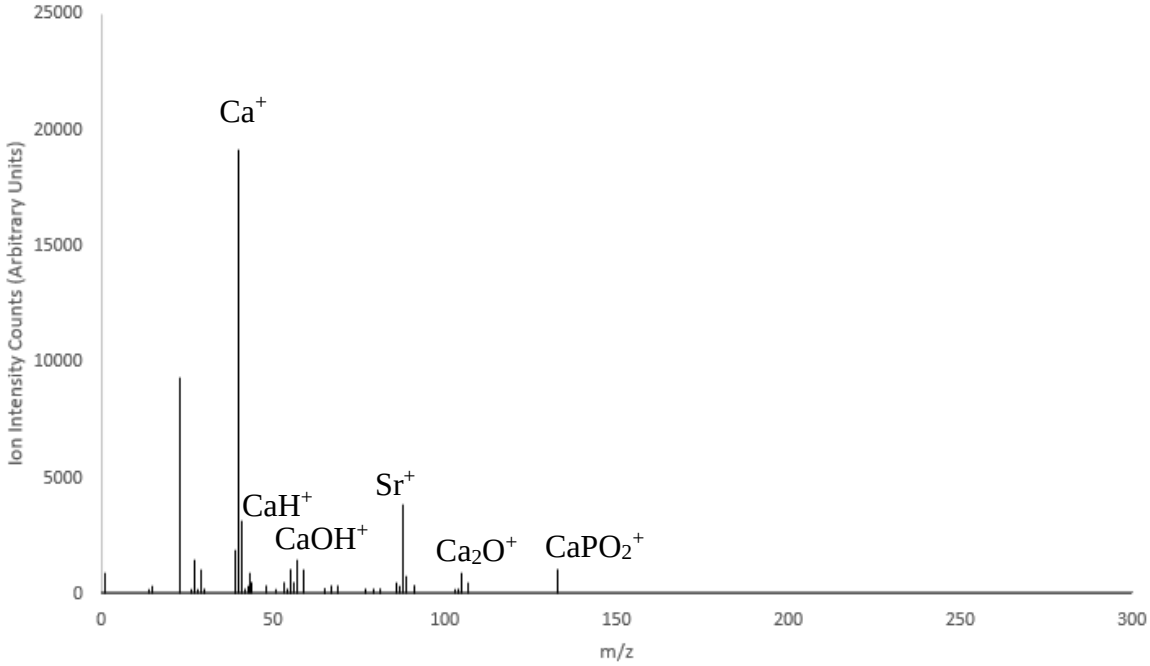

Figure 5.27 ToFSIMS positive ion spectrum for PolyTi250SrHA with positive ion signals indicative of a CaP (SrHA) thin film labelled

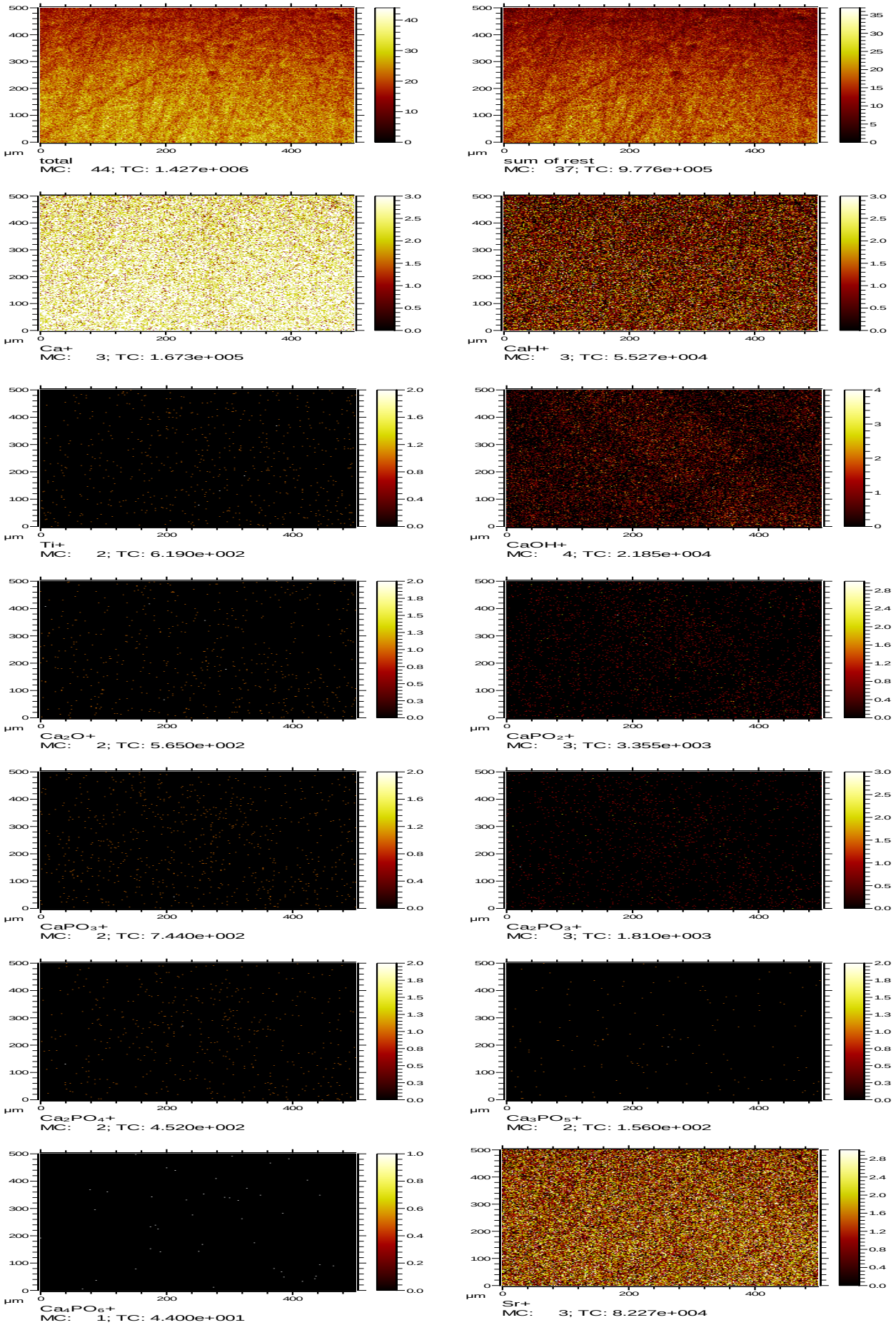

Figure 5.28 ToFSIMS positive ion maps of total ion count (TIC), Ca^+, CaH^+, Ti^+, $CaOH^+$, Ca_2O^+, $CaPO_2^+$, $CaPO_3^+$, $Ca_2PO_3^+$, $Ca_2PO_4^+$, $Ca_3PO_5^+$, $Ca_4PO_6^+$ and Sr^+ for PolyTi250SrHA

5.4.3 XRD of HA and SrHA Coatings on Polycrystalline Titanium

X-ray diffractograms for PolyTi250HA and PolyTi250SrHA are shown in Figure 5.29 (a) and (b), respectively. The scan for PolyTi250HA (Figure 5.29 (a)) displays peaks at 2θ = 35.1°, 38.3°, 40.1°, 43.3° and 53.0° which correspond to Miller index (hkl) orientation in the 100, 002, 101, 101 and 102 planes, respectively. As before, these data correspond to that of semi-crystalline titanium as described in ICDD file 00-044-1294[205,227].

Figure 5.29 (b) displays the spectrum graph for PolyTi250SrHA, with peaks at 2θ = 35.1°, 38.2°, 40.0° and 52.7° which correspond to Miller Index (hkl) orientation in the 100, 002, 101 and 102 planes, respectively. Again, these plane orientations correspond to those in the ICDD file 00-044-1294 for semi-crystalline titanium.

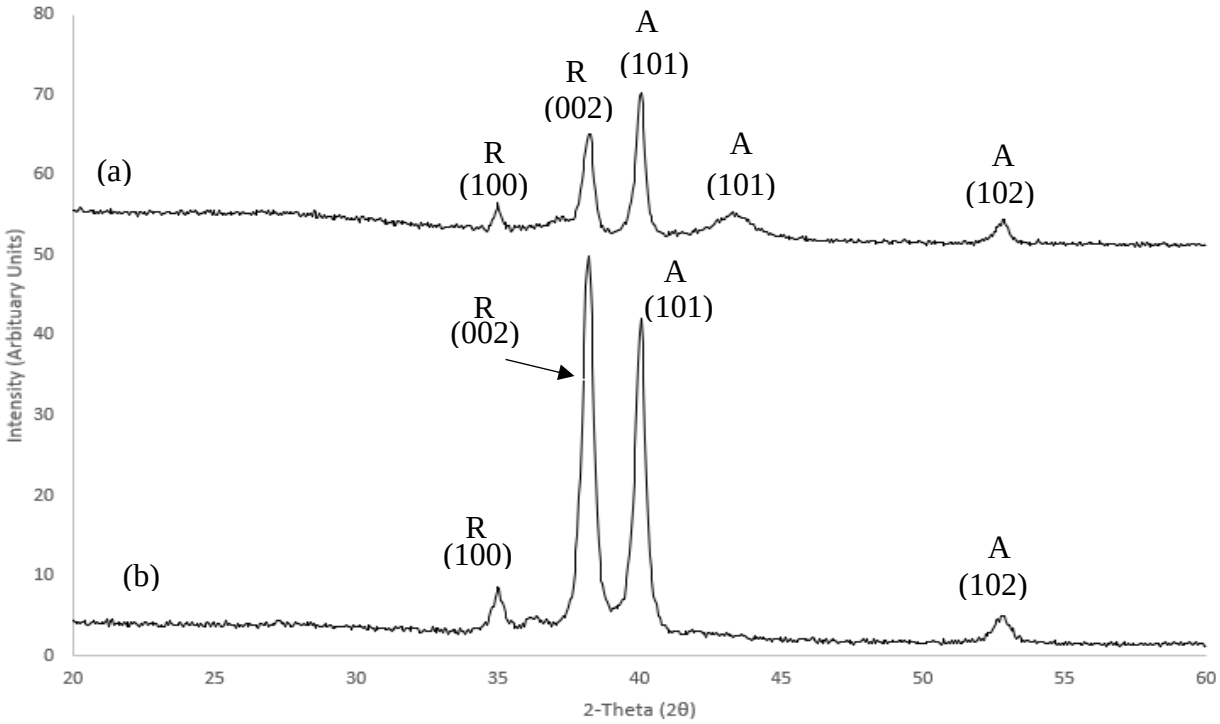

Figure 5.29 X-ray diffractograms for CaP (HA and SrHA) coatings on polycrystalline titanium (a) PolyTi250HA and (b) PolyTi250SrHA, with Miller index assignments labelled according to ICDD file 00-044-1294. Anatase (A) and rutile (R) phases also labelled

5.4.4 SEM Analysis of HA and SrHA Coatings on Polycrystalline Titanium

Figure 5.30 shows SEM images for PolyTi250HA samples, at both planar and 80° tilt views with magnifications of x400, x2.5k, x4.5k and x8k, to allow for visualisation of the CaP (HA) material on the polycrystalline titanium surface. These images bear a strong resemblance to the PolyTi250 surface and the aTi surfaces seen previously. There are some areas which seem to contain a build-up of the coating material and are particularly prominent where lines or grooves occur on the surface. Figure 5.31 provides a higher x30k magnification of this surface and allows for a clear indication of the growth of the HA on this surface. However, individual particles of coating material seen previously (TiHA and TiSrHA) are not present here. Overall, the coating material appears to have better conformed to the underlying surface causing a 'smoothing' effect in certain areas.

Figure 5.32 (a) – (h) shows the corresponding planar image and 80° tilt image views for PolyTi250SrHA at magnifications of x400, x2.5k, x4.5k and x8k. Once again lines and grooves are dominant on this surface with these features visible across all of the images. There are some areas where there is clear evidence of the coating material being present, which as before, occurs specifically along the more dominant lines and grooves of the surface. Figure 5.33 provides a x30k magnification image for this surface and shows that the particles have amalgamated into denser regions of CaP.

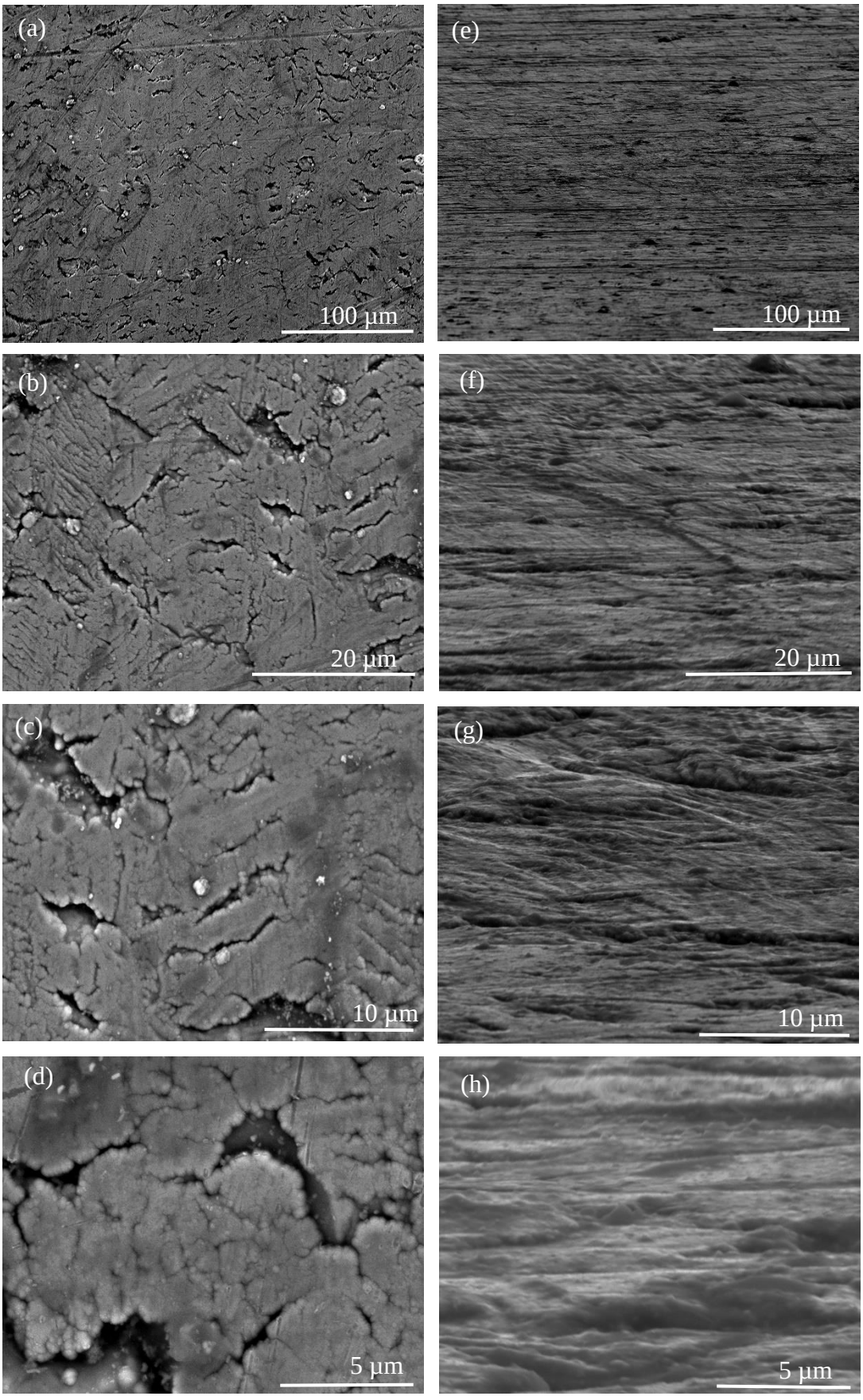

Figure 5.30 SEM images for PolyTi250HA showing normal planar views (a) – (d), and 80° tilt side angle views (e) – (h) at magnifications of (a) x400, (b) x2.5k, (c) x4.5k, (d) x8k, (e) x400, (f) x2.5k, (g) x4.5k and (h) x8k

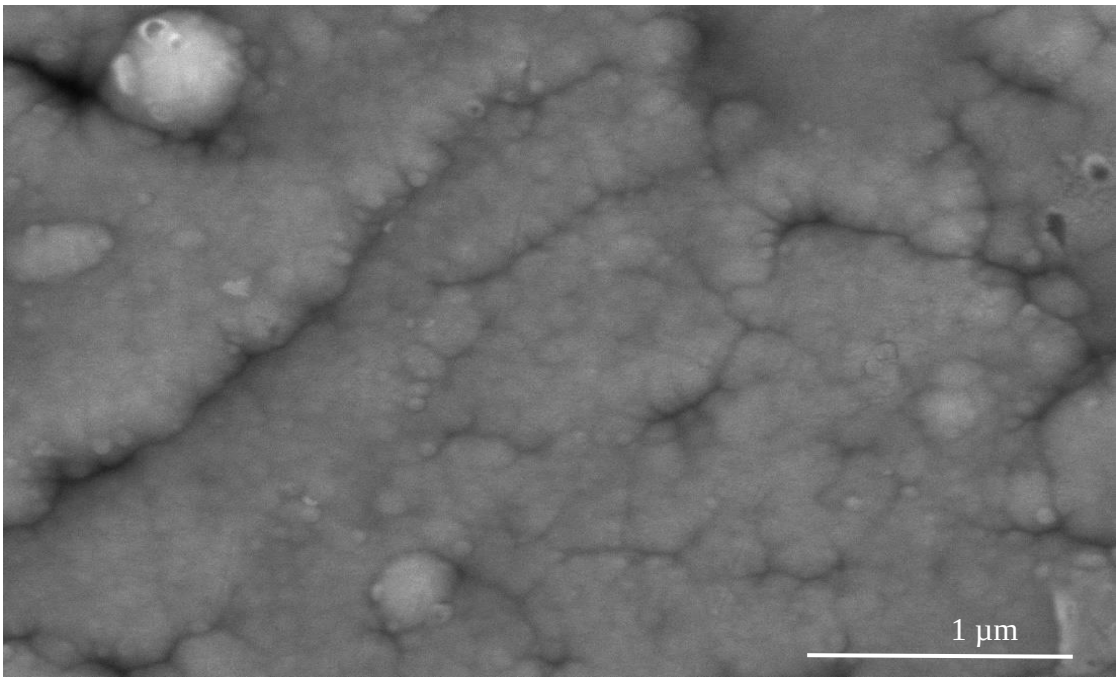

Figure 5.31 SEM planar view image of PolyTi250HA at x30k magnification

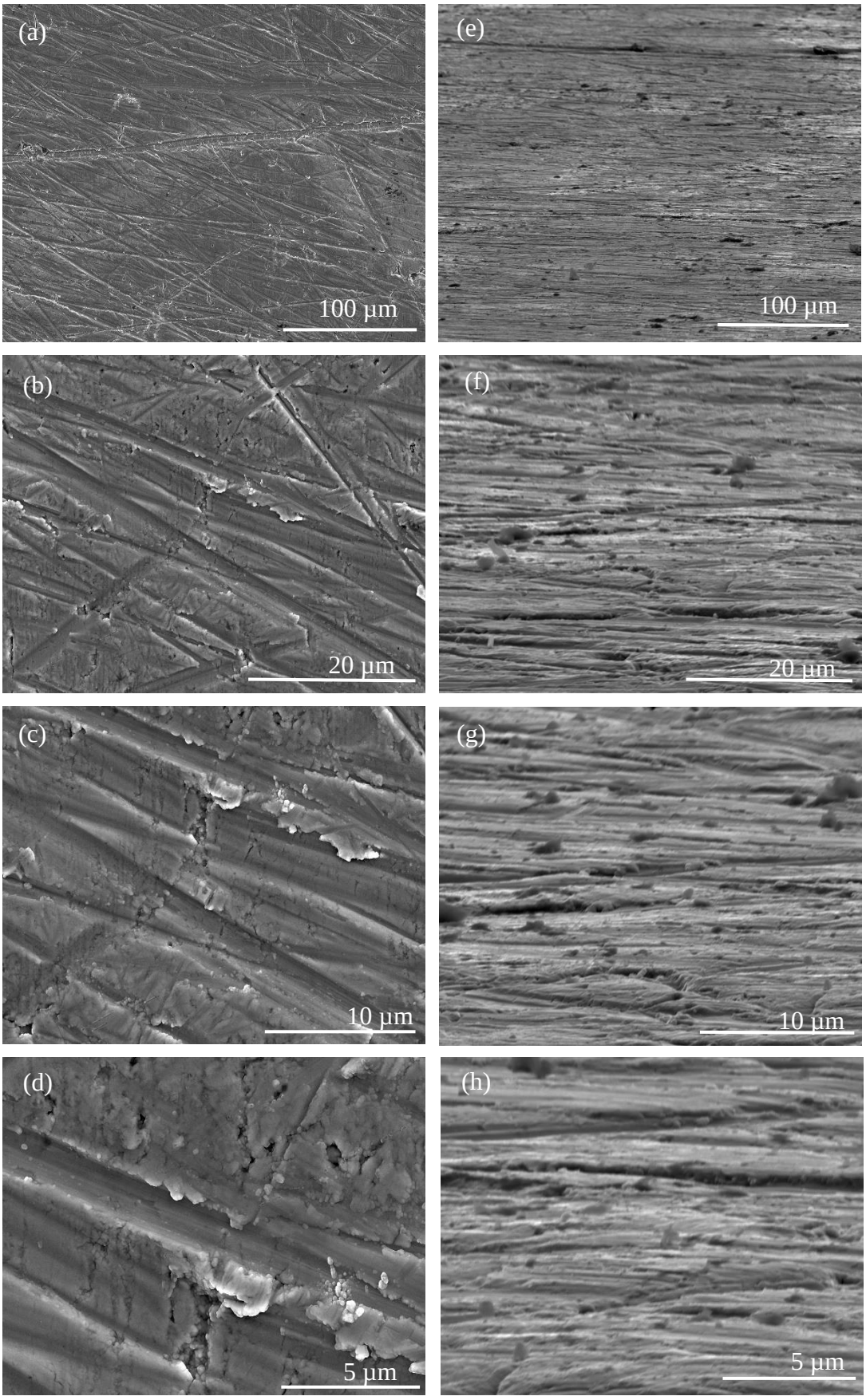

Figure 5.32 SEM images for PolyTi250SrHA showing normal planar views (a) – (d), and 80° tilt side angle views (e) – (h) at magnifications of (a) x400, (b) x2.5k, (c) x4.5k, (d) x8k, (e) x400, (f) x2.5k, (g) x4.5k and (h) x8k

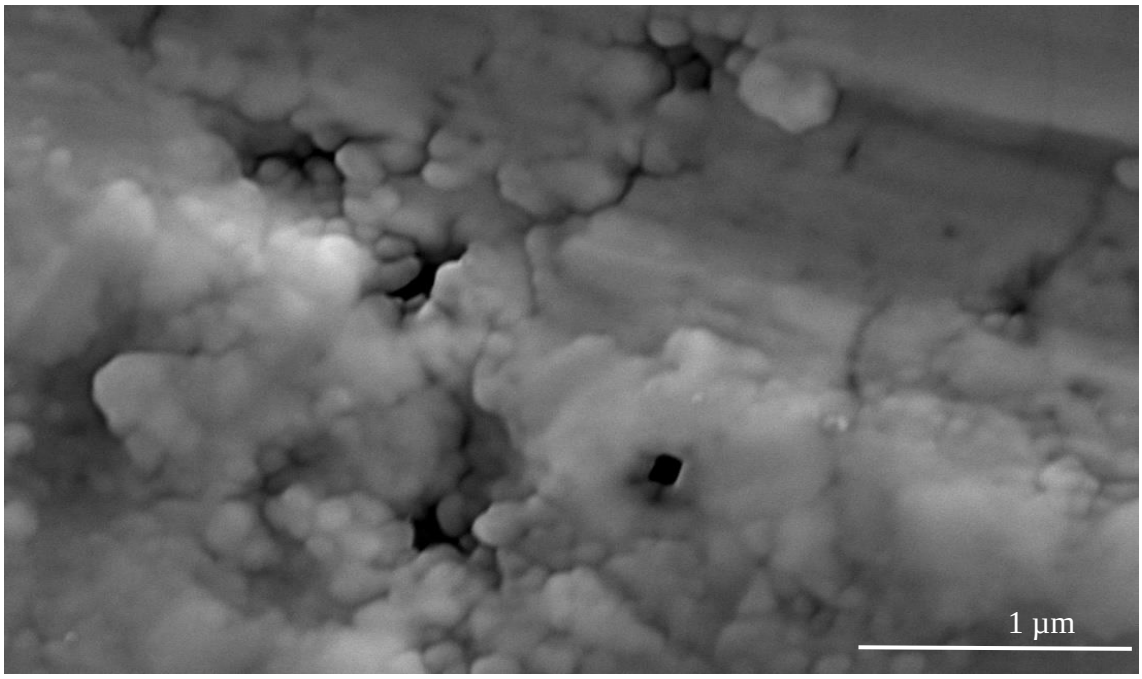

Figure 5.33 SEM planar view image of PolyTi250SrHA at x30k magnification

5.5 Dissolution Studies of HA and SrHA Coatings on Pristine, Etched and Polycrystalline Titanium

As stated earlier, sputtered CaP thin films are amorphous in the as-deposited state thereby making them readily soluble in aqueous solution i.e. culture and bodily fluids. Factors that can directly affect or alter the rate at which such thin film coatings dissolve include any catatonic or anionic substitutions[228] (as is the case in SrHA), the porosity of the thin film and the coating particle size[130]. In terms of indirect factors that can influence dissolution, the topography of the substrate surface onto which the coating is deposited also plays an important role. Specifically, the ability to create specific features on the surface that can physically 'entrap' and protect the soluble CaP film from intimate contact with the aqueous environment provides a means of slowing dissolution. This means that some of the bioactive material should then be available to subsequently stimulate cell response, in this case bone cells, thereon. Hence, in this work the ability of etched titanium surfaces to maintain an appropriate quantity of sputter deposited CaP capable of engendering enhanced cell activity after exposure to culture media is considered. The nature of the CaP dissolution process on 24 hr etched titanium has been compared to that of coatings on both the pristine and polycrystalline metal surfaces.

All substrates were subjected to a 7-day dissolution study by submerging them in 2 ml of cell culture medium and storing in an incubator at 37 ˚C with 5 % CO_2. Samples, in triplicates, were recovered from the media at day 1 and day 7 timepoints and analysed by XPS, ToFSIMS and SEM. The presence or otherwise of the HA or SrHA coatings is then used to qualify the various samples for subsequent bone cell culture studies.

5.5.1 XPS of CaP Coatings on Pristine, Etched and Polycrystalline Titanium Surfaces After Exposure to Cell Culture Media

TiHA and TiSrHA

Figure 5.34 presents the typical WESS plots for TiHA (Figure 5.34 (a)) and TiSrHA (Figure 5.34 (b)) after exposure to culture media for 7 days. Table 5.4 (a) presents the XPS quantitative data for TiHA before the dissolution and after days 1 and 7 with values before exposure to media included again here for convenience. The main peaks detected are carbon (C 1s), oxygen (O 1s), calcium (Ca 2p) and phosphorus (P 2p), but high-resolution plots are not presented here. There is also a sodium peak (Na 1s) present which is assumed to have been deposited from the media. The C/O ratio for the sample prior to exposure to media was 0.42 which rises to 2.47 at day 1 and 4.99 at day 7,

indicating a significant increase in the amount of carbon present on the surface as a function of exposure time. The Ca/P ratio is 0.99 pre-exposure which increases very little after the 1-day exposure timepoint despite a significant decrease in the total amount off calcium and phosphorus detected on the surface. At day 7, the Ca/P ratio has increased to 1.80 which is close to the stoichiometric value for HA (1.67) and both calcium and phosphorus present on the surface have increased slightly. Interestingly, no signal for titanium (Ti 2p) was detected in these post immersion samples. Hence, after 7-days exposure there is a continuous CaP thin film present that masks the underlying substrate chemistry.

The XPS spectra for TiSrHA post 7-days exposure to culture media is presented in Figure 5.35 (b) with the corresponding quantitative data shown in Table 5.4 (b). Again, the spectrum shows signals from carbon (C 1s), oxygen (O 1s), calcium (Ca 2p) and phosphorus (P 2p), with a peak now detected for strontium (Sr 3p) and a sodium peak (Na 1s) is also again detected. Prior to dissolution the C/O ratio was 0.46 which rises to 3.85 at the 1-day timepoint and 4.38 after 7 days, indicating increasing carbon content with exposure to media. The Ca/P and (Sr + Ca)/P ratios were originally 0.35 and 0.45, respectively, increasing to 1.42 and 2.27 at day 1 and 2.67 and 1.84 at day 7, respectively, with an associated decrease in the total calcium and phosphorus content. As was found for the TiHA, no titanium signal was detected here after 7 days in culture media and so there is still enough of a thin film present to mask the underlying substrate chemistry.

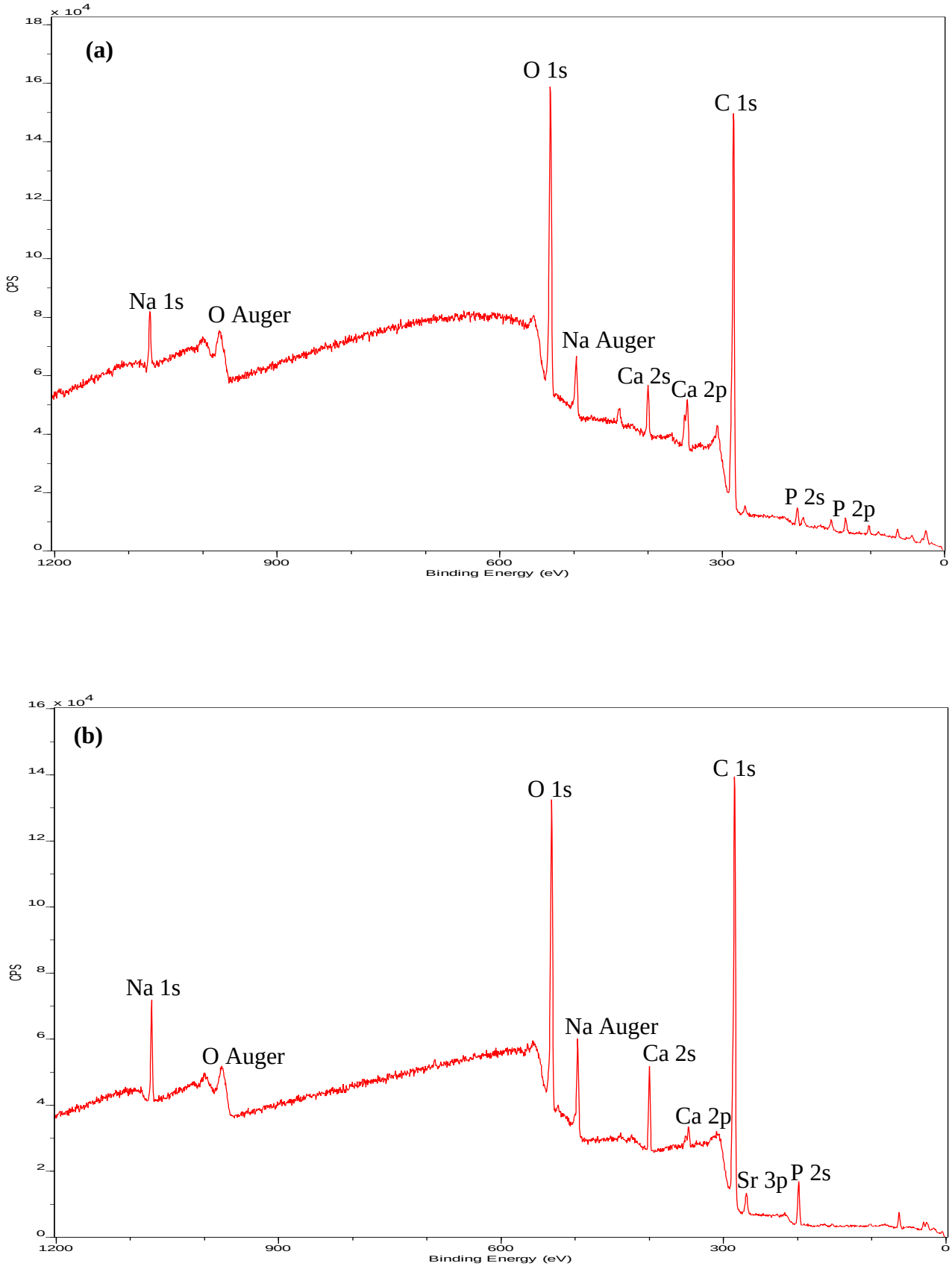

Figure 5.34 XPS WESS spectra for (a) TiHA and (b) TiSrHA surfaces after 7-days to exposure to cell culture media

Table 5.4 XPS quantitative data (n = 9) for (a) TiHA and (b) TiSrHA after exposure to cell culture media with standard deviation included

(a)	**TiHA**		
	Before Dissolution	**Day 1**	**Day 7**
Element	**Total Atomic Concentration %**	**Total Atomic Concentration %**	**Total Atomic Concentration %**
C 1s	19.65 ± 3.54	69.32 ± 2.92	80.47 ± 4.58
O 1s	47.14 ± 2.40	28.10 ± 2.77	16.14 ± 3.53
Ca 2p	16.53 ± 0.28	1.13 ± 0.03	2.19 ± 0.63
P 2p	16.68 ± 0.92	1.13 ± 0.03	1.22 ± 0.84
Ca/P	**0.99**	**1.00**	**1.80**

(b)	**TiSrHA**		
	Before Dissolution	**Day 1**	**Day 7**
Element	**Total Atomic Concentration %**	**Total Atomic Concentration %**	**Total Atomic Concentration %**
C 1s	18.36 ± 3.17	77.67 ± 0.65	80.23 ± 0.93
O 1s	40.07 ± 1.78	20.18 ± 1.53	18.31 ± 0.74
Ca 2p	10.03 ± 1.03	0.94 ± 0.27	0.88 ± 0.15
P 2p	28.64 ± 2.16	0.66 ± 0.05	0.33 ± 0.14
Sr 3p	2.90 ± 0.58	0.56 ± 0.62	0.28 ± 0.07
Ca/P	**0.35**	**1.42**	**2.67**
Sr + Ca/P	**0.45**	**2.27**	**1.84**

24eTiHA and 24eTiSrHA

A typical XPS WESS for 24eTiHA after 7-days exposure to cell culture media is presented in Figure 5.35 (a). As before for the TiHA, the main peaks present are carbon (C 1s), oxygen (O 1s), calcium (Ca 2p) and phosphorus (P 2p). Sodium (Na 1s) is also present and is thought to be attributable to the culture media. Table 5.5 (a) shows the quantitative XPS dissolution data gathered over the 7-day study for the 24eTiHA. Before the dissolution study, the C/O ratio for this sample was 0.42 (the same as TiHA) which rises to 2.83 at day 1 and 4.44 at day 7, indicating again a significant increase in the carbon present on the surface post immersion. The original Ca/P ratio of 0.91 decreases to 0.78 after day 1 and is accompanied by a decrease in the total amount of calcium and phosphate detected on the surface. At day 7 this Ca/P ratio has increased to 1.50, with both the calcium and phosphorus content present on the surface now being slightly greater compared to that seen at day 1. As was for the Ti and TiSrHA samples, no Ti 2p peaks are observed here indicating that the coating thickness is greater than the inelastic mean free path for these photoelectrons.

The corresponding WESS spectrum for 24eTiSrHA is shown in Figure 5.35 (b) and the associated quantitative data in Table 5.5. As before, the peaks present here are carbon (C 1s), oxygen (O 1s), calcium (Ca 2p) and phosphorus (P 2p), with the addition of a strontium (Sr 3p) signal, as expected. Sodium (Na 1s) signals were again detected here, attributed to the cell culture media. Initially this sample had a C/O ratio calculated to be 0.33 (lower than that of the TiHA, TiSrHA and 24eTiHA samples) which at day 1 increases to 4.03, indicative of a large increase of carbon now being present on this surface. At day 7, the C/O ratio increases again only slightly to 4.38. The original Ca/P and Sr + Ca/P ratios were calculated as 0.31 and 0.40, respectively and increased to 1.44 and 2.39 at day 1, respectively. At day 7, the Ca/P ratio increases to 1.48 whilst the (Sr + Ca)/P ratio decreases to 1.83, associated with a slight increase in calcium and phosphorus but a decrease in strontium content. Again, there is no signal detected for Ti 2p indicating that the thickness of the CaP thin film is still greater than their inelastic mean free path.

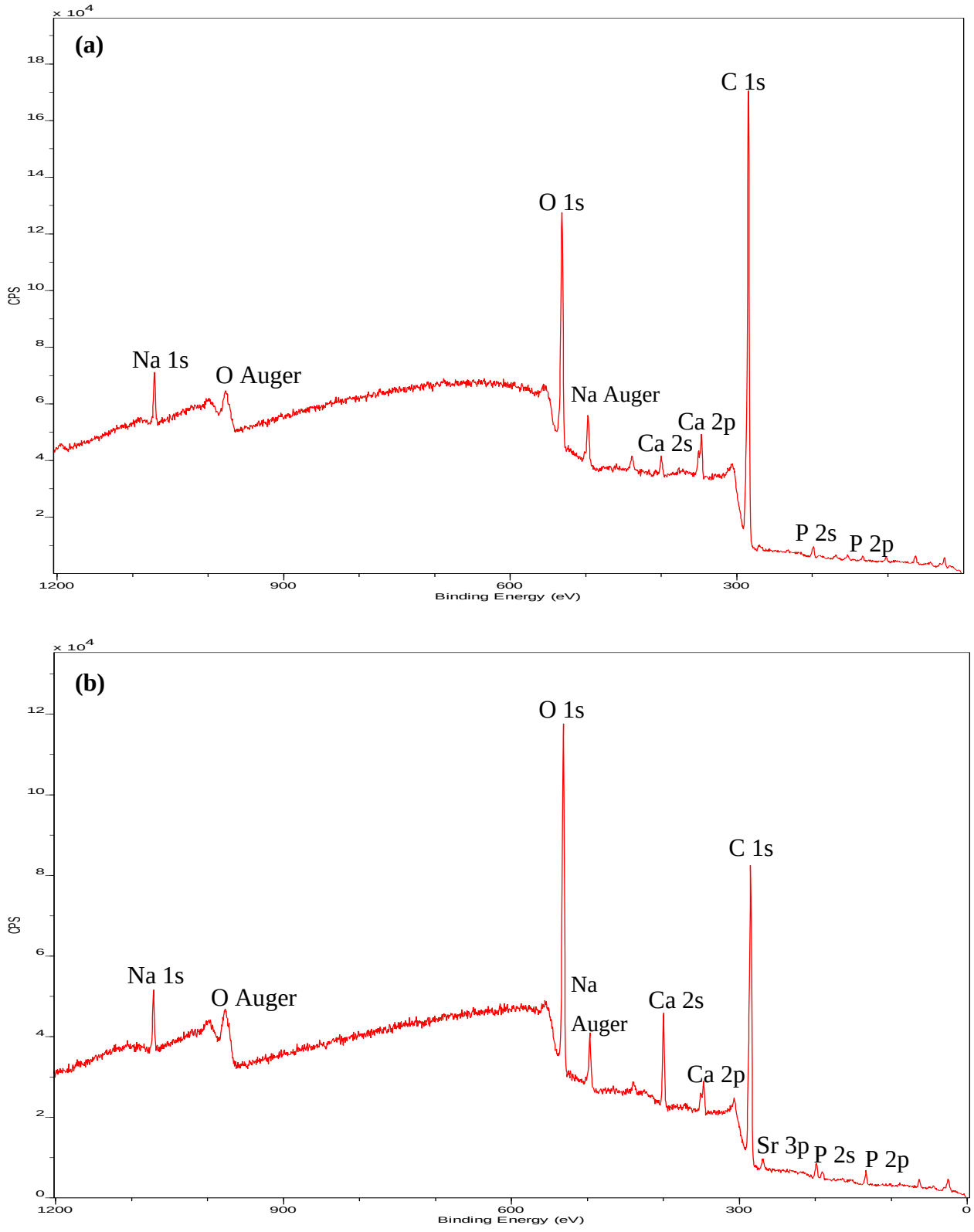

Figure 5.35 XPS WESS spectra for (a) 24eTiHA and (b) 24eTiSrHA after 7-days exposure to cell culture media

Table 5.5 XPS quantitative data (n = 9) for (a) 24eTiHA and (b) 24eTiSrHA after exposure to cell culture media with standard deviation included

(a)	24TiHA		
	Before Dissolution	Day 1	Day 7
Element	Total Atomic Concentration %	Total Atomic Concentration %	Total Atomic Concentration %
C 1s	19.77 ± 3.65	71.33 ± 2.30	79.09 ± 0.43
O 1s	47.50 ± 1.20	25.22 ± 0.62	17.80 ± 1.00
Ca 2p	15.59 ± 2.20	1.04 ± 0.29	1.99 ± 0.67
P 2p	17.15 ± 1.13	1.34 ± 0.22	1.33 ± 0.39
Ca/P	**0.91**	**0.78**	**1.50**

(b)	24eTiSrHA		
	Before Dissolution	Day 1	Day 7
Element	Total Atomic Concentration %	Total Atomic Concentration %	Total Atomic Concentration %
C 1s	14.69 ± 0.97	78.32 ± 1.82	80.79 ± 1.39
O 1s	44.43 ± 5.47	19.43 ± 2.67	17.83 ± 4.24
Ca 2p	9.17 ± 2.20	0.95 ± 0.29	1.45 ± 0.71
P 2p	29.25 ± 1.72	0.66 ± 0.05	0.98 ± 0.53
Sr 3p	2.47 ± 0.88	0.63 ± 0.56	0.34 ± 0.21
Ca/P	**0.31**	**1.44**	**1.48**
Sr + Ca/P	**0.40**	**2.39**	**1.83**

PolyTi250HA and PolyTi250SrHA

The XPS spectra presented in Figure 5.36 shows the WESS for (a) PolyTi250HA and (b) PolyTi250SrHA after 7-days exposure to cell culture media. The associated quantitative data are displayed in Table 5.6 (a) for PolyTi250HA and (b) PolyTi250SrHA. The spectra for PolyTi250HA (Figure 5.36 (a)) show peaks for carbon (C 1s), oxygen (O 1s), calcium (Ca 2p) and phosphorus (P 2p) and again showing the presence of sodium (Na 1s). The C/O ratio for PolyTi250HA increases from 0.74 (the highest of all the original HA coated samples) to 3.17 at day 1 due again to increased carbon present on the sample surface. After 7-days exposure the C/O ratio decreases slightly to 3.05. Before dissolution the Ca/P ratio for PolyTi250HA was 0.93 which is lower than the stoichiometric ratio of the HA target material (1.67) and remains at this value after 1-day of exposure to media despite there being a significant decrease in the calcium and phosphorus content on the surface. At day 7, the Ca/P ratio increases slightly to 1.05 with a further decrease in calcium and phosphorus surface content observed. Again, there is no titanium signal detected in the XPS WESS, indicating that the thin film on this surface is still thicker than that of the inelastic mean free path of Ti 2p photoelectrons.

The XPS WESS for the corresponding PolyTi250SrHA (Figure 5.36 (b)) shows the main carbon (C 1s), oxygen (O 1s), calcium (Ca 2p) and phosphorus (P 2p) peaks, with the addition of strontium (Sr 3p), as expected. Once again, sodium (Na 1s) is present in the spectrum and again attributed to the cell culture media. In the case of PolyTi250SrHA the original C/O ratio of this sample was calculated to be 0.43 and increases significantly to 4.53 at day 1 and further to 5.11 at day 7, which once again indicates increased carbon content on the surface. The Ca/P and combined (Sr + Ca)/P ratios pre-dissolution were calculated as 0.32 and 0.42, respectively. After 1-day exposure to culture media these both increased to 1.48 and 1.83, respectively, despite the loss of calcium, phosphorus and strontium from the surface. The ratios both increase again to 1.54 and 1.88, respectively, after 7-days exposure with a slight increase in the total calcium content observed but a decrease in the total strontium and phosphorus content. As is the case with all of the samples investigated, no titanium signals were detected for PolyTi250SrHA post immersion, indicating that there is a continuous thin film on this surface that prevents the escape of the substrate photoelectrons.

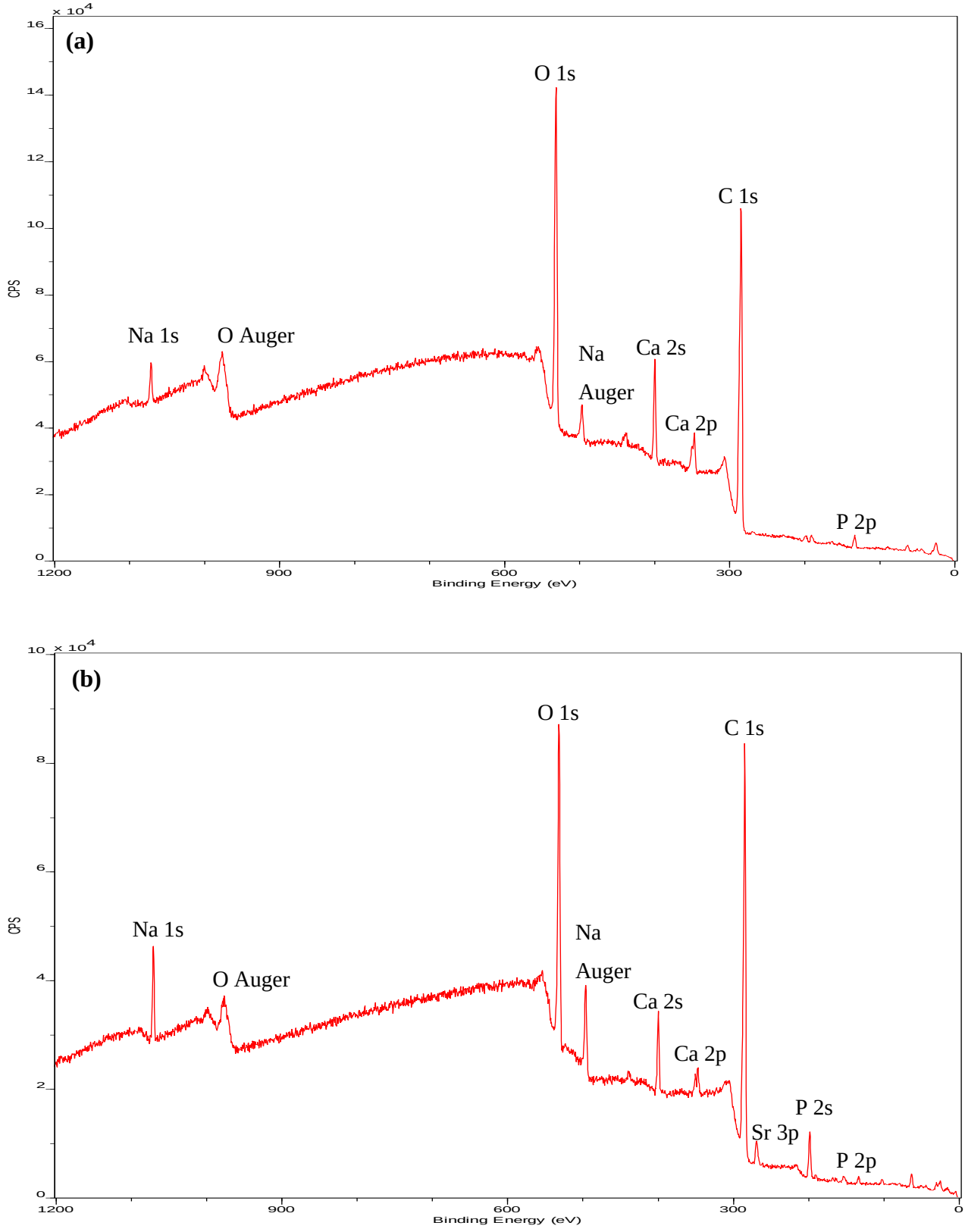

Figure 5.36 XPS WESS spectra for (a) PolyTi250HA and (b) PolyTi250SrHA after 7-days exposure to cell culture media

Table 5.6 XPS quantitative data (n = 9) for (a) PolyTi250HA and (b) PolyTi250SrHA after exposure to cell culture media with standard deviation included

(a)	PolyTi250HA		
	Before Dissolution	Day 1	Day 7
Element	Total Atomic Concentration %	Total Atomic Concentration %	Total Atomic Concentration %
C 1s	30.72 ± 12.11	73.34 ± 2.27	48.47 ± 2.33
O 1s	41.69 ± 6.63	23.17 ± 2.60	15.88 ± 1.72
Ca 2p	13.29 ± 2.75	1.68 ± 0.29	1.30 ± 0.93
P 2p	14.24 ± 3.23	1.81 ± 0.27	1.23 ± 0.67
Ca/P	**0.93**	**0.93**	**1.05**

(b)	PolyTi250SrHA		
	Before Dissolution	Day 1	Day 7
Element	Total Atomic Concentration %	Total Atomic Concentration %	Total Atomic Concentration %
C 1s	17.70 ± 2.26	80.79 ± 1.39	80.80 ± 1.56
O 1s	41.17 ± 145	17.83 ± 4.24	15.82 ± 2.15
Ca 2p	9.38 ± 0.81	1.45 ± 0.71	1.48 ± 0.66
P 2p	28.99 ± 0.83	0.98 ± 0.53	0.96 ± 0.41
Sr 3p	2.76 ± 0.50	0.34 ± 0.21	0.32 ± 0.16
Ca/P	**0.32**	**1.48**	**1.54**
Sr + Ca/P	**0.42**	**1.83**	**1.88**

5.5.2 ToFSIMS of CaP Coatings on Pristine, Etched and Polycrystalline Titanium Surfaces after Exposure to Cell Culture Media

TiHA and TiSrHA

ToFSIMS was utilised to further investigate the chemistry and integrity of the CaP (HA or SrHA) thin films after 7-days exposure to cell culture media (spectra were not recorded for samples at day 1). The positive ion spectrum for TiHA is provided in Figure 5.37 and shows the presence of both organic and inorganic signals. Peaks assigned to Ca^+ at 40 m/z, CaH^+ at 41 m/z and $CaOH^+$ at 57 m/z are still detected. As seen in the XPS spectra (Figure 5.34 (a)), there is a higher carbon content on the surface after 7-days exposure and that is supported here with high relative intensity peaks for carbon species including $C_2H_5^+$ at 29 m/z and CH_3CO^+ at 43 m/z. As for the original pre-dissolution sample (Figure 5.3), there is an absence of a Ti^+ signal that would be expected at 48 m/z. The associated positive ion maps showing the spatial distribution of the key ions detected in the spectrum are provided in Figure 5.38. There is still a high coverage of both Ca^+ and CaH^+ ions across the TiHA substrate surface, with small traces of Ti seen in the positive ion maps. Overall, there would seem to be a significant decrease in the number of ions originating from CaP on this surface after 7-days exposure to cell culture media which is consistent with the XPS analysis.

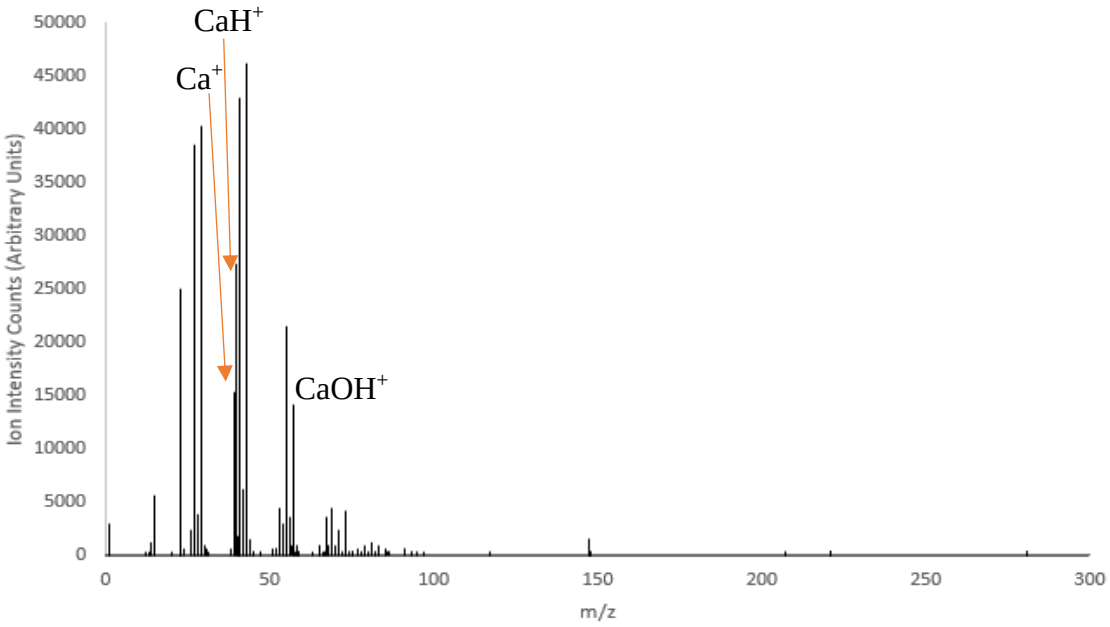

Figure 5.37 ToFSIMS positive ion spectrum for TiHA after 7-days exposure to culture media with positive ion signals indicative of a CaP thin film labelled

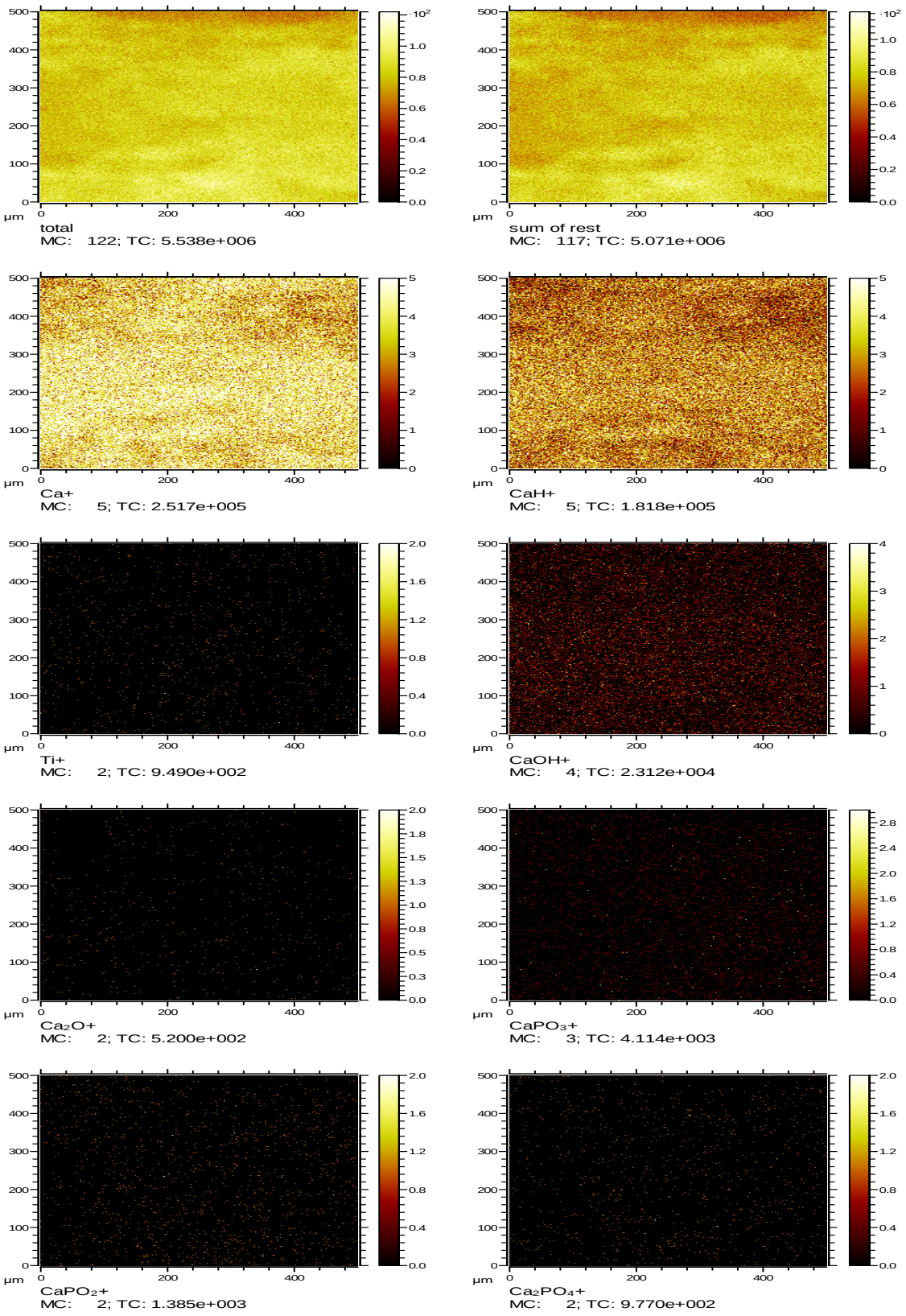

Figure 5.38 ToFSIMS positive ion maps of total ion count (TIC), Ca^+, CaH^+, Ti^+, $CaOH^+$, Ca_2O^+, $CaPO_3^+$, $CaPO_2^+$ and $Ca_2PO_4^+$ for TiHA

The positive ion spectra for TiSrHA at day 7 is presented in Figure 5.39. The most intense peak in this spectra at 23 m/z corresponds to Na^+. There are signals for Ca^+, CaH^+ and $CaOH^+$ detected at 40 m/z, 41 m/z and 57 m/z, respectively as well as an increase in carbon species present including $C_2H_3^+$, $C_2H_5^+$ and CH_3CO^+ at 27 m/z, 29 m/z and 43 m/z, respectively. There is also a small signal for Sr^+ at 88 m/z. Again, no signal is detected for Ti^+ at 48 m/z in the spectra. The corresponding positive ion maps are shown in Figure 5.40 and indicate that the distribution of the Ca^+ and CaH^+ ions are not homogeneous across the surface, when compared to the TiSrHA pre-exposure or for TiHA after day 7 immersion. Small amounts of titanium are also noted here in the ion maps. Although Sr^+ is detected in the corresponding maps there is a decrease in the amount present compared to that for TiSrHA after 7 days in culture media.

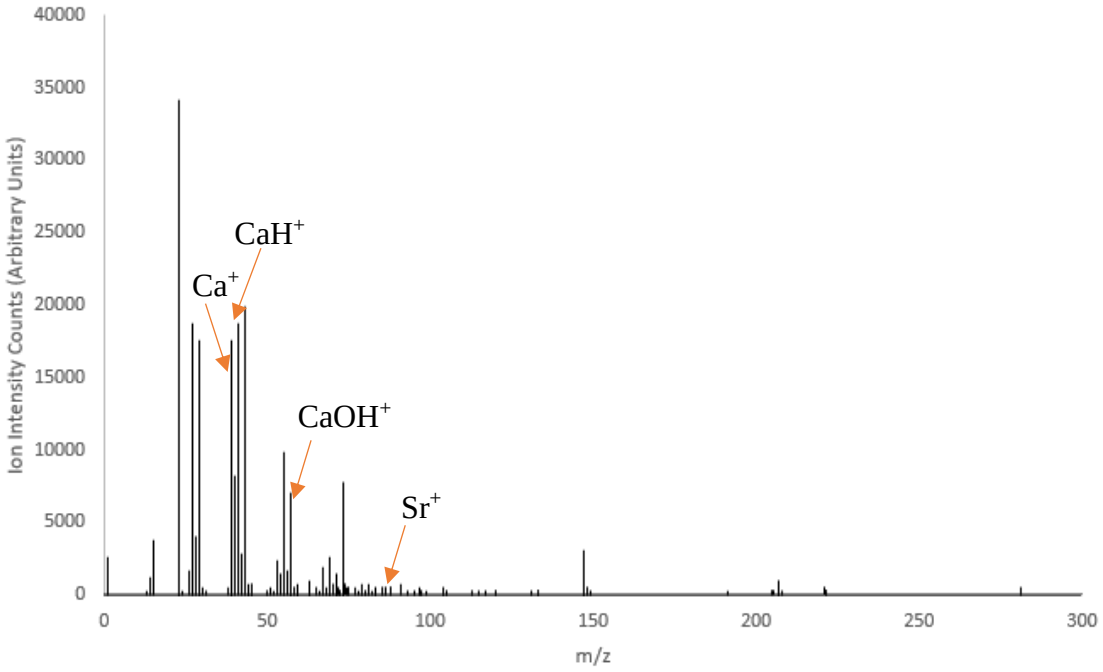

Figure 5.39 ToFSIMS positive ion spectrum for TiSrHA after 7-days exposure to culture media with positive ion signals indicative of a CaP thin film labelled

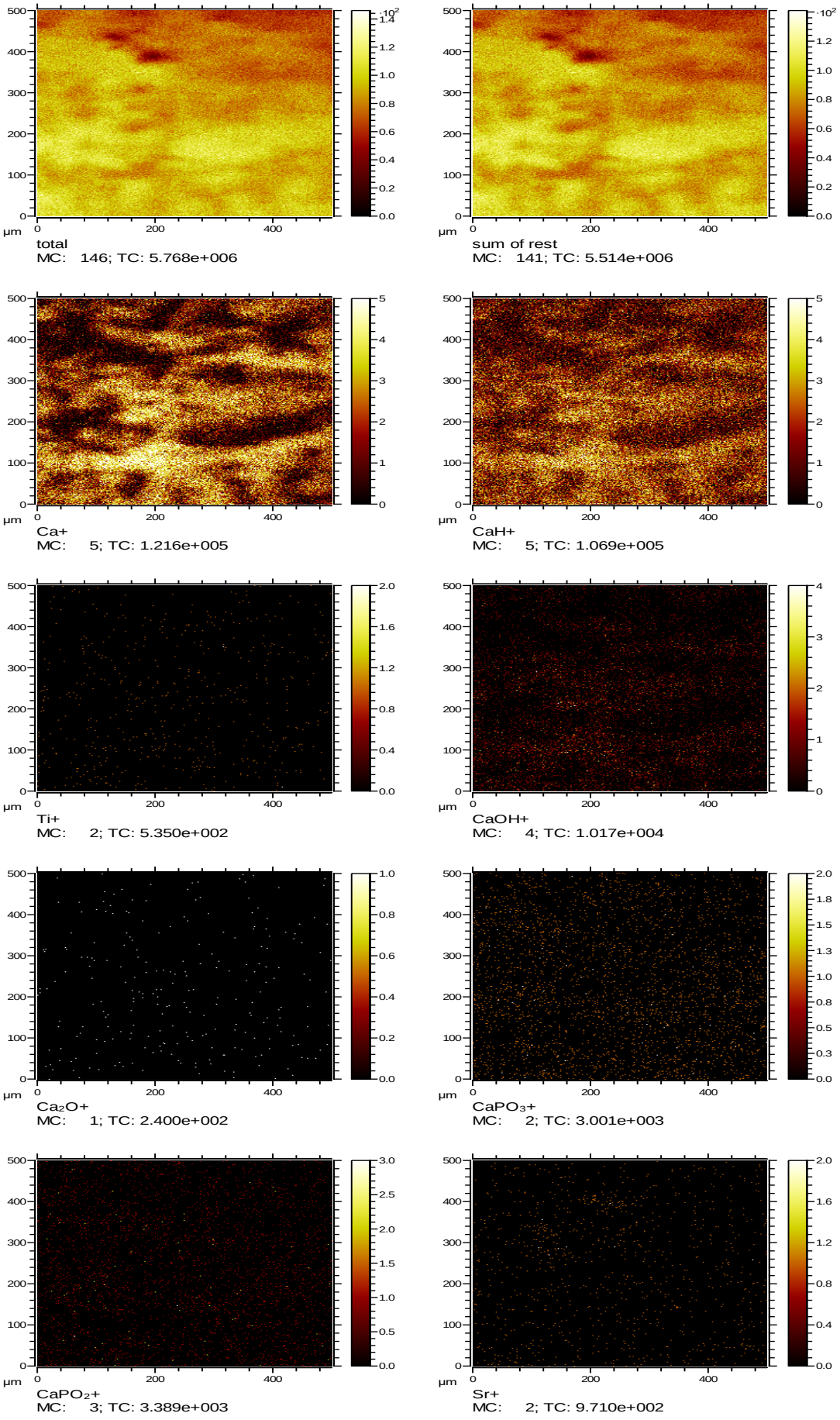

Figure 5.40 ToFSIMS positive ion maps of total ion count (TIC), Ca^+, CaH^+, Ti^+, $CaOH^+$, Ca_2O^+, $CaPO_3^+$, $CaPO_2^+$ and Sr^+ for TiSrHA

24eTiHA and 24eTiSrHA

The ToFSIMS spectra for 24eTiHA after 7-days exposure to cell culture media is presented in Figure 5.41, with again both organic and inorganic signals detected. The expected Ca^+ and CaH^+ are present at 40 m/z and 41 m/z, respectively. Although the more complex CaP ions seen in the original sample are much less intense, there is still an appreciable calcium hydroxide ion signal at 57 m/z. Again, there is an increase in the relative intensity of carbon species (as seen previously in the XPS data) including $C_2H_3^+$ at 27 m/z, $C_2H_5^+$ at 29 m/z and CH_3CO^+ at 43 m/z. The absence of Ti^+ at 48 m/z is also noted here. The positive ion maps for this sample are provided in Figure 5.42 and indicate a homogenous surface distribution of both Ca^+ and CaH^+, similar to that seen for pre-dissolution samples. Whilst there are no titanium signals present in the spectra, small traces of titanium ions are noted in the positive ion maps.

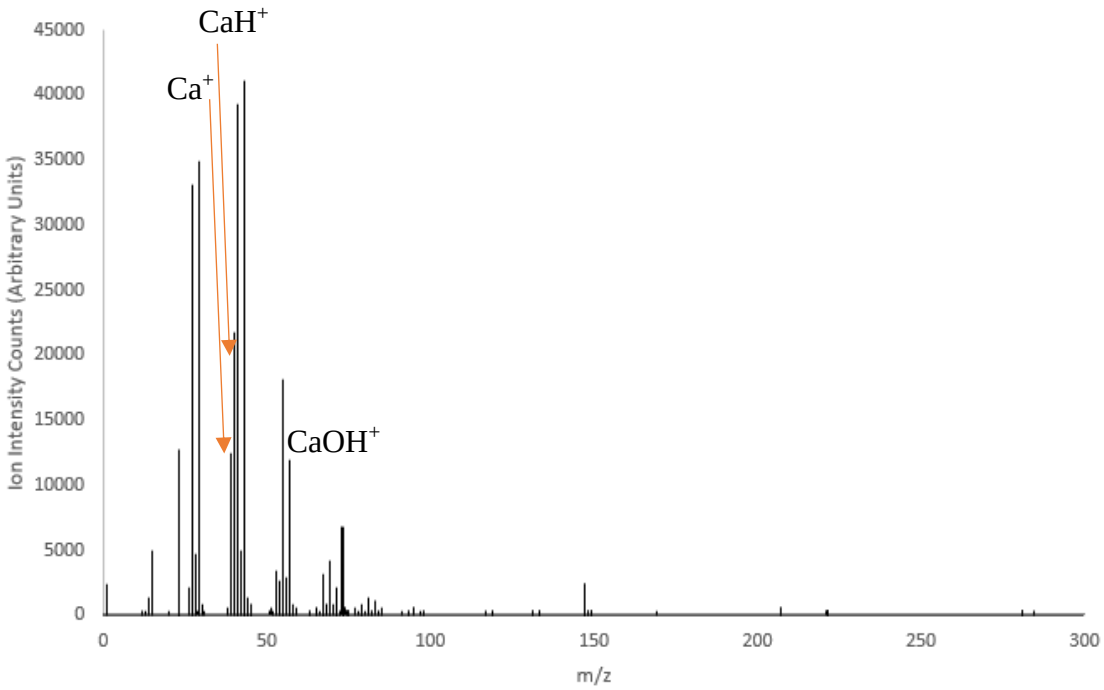

Figure 5.41 ToFSIMS positive ion spectrum for 24eTiHA after 7-days exposure to culture media with positive ion signals indicative of a CaP thin film labelled

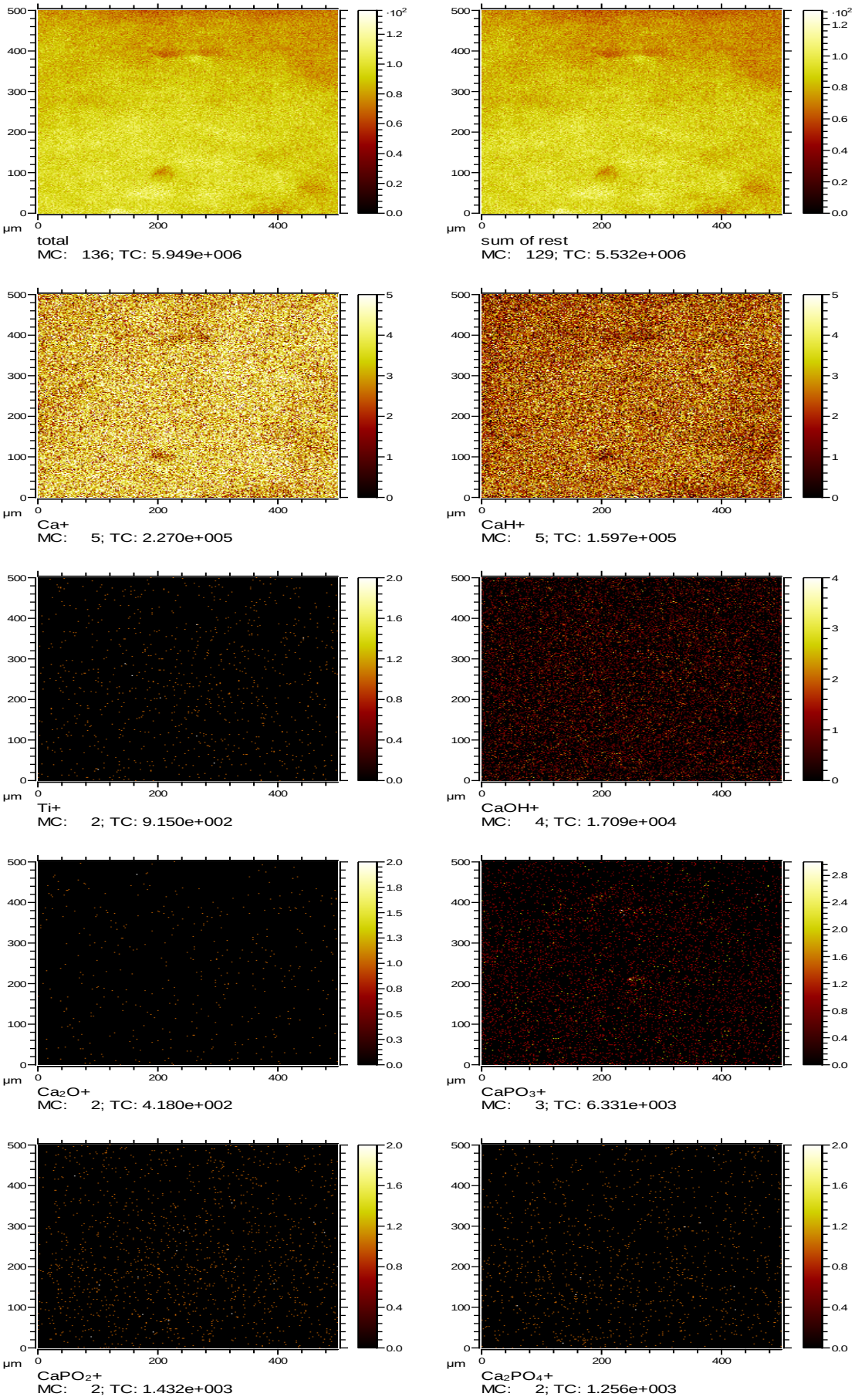

Figure 5.42 ToFSIMS positive ion maps of total ion count (TIC), Ca^+, CaH^+, Ti^+, $CaOH^+$, Ca_2O^+, $CaPO_3^+$, $CaPO_2^+$ and $Ca_2PO_4^+$ for 24eTiHA

Figure 5.43 displays the ToFSIMS positive spectrum for the 24eTiSrHA samples at day 7. There are several clear similarities here with the data obtained for the HA coating on the etched Ti (24eTiHA). However, the presence of Sr^+ ions is evident at 88 m/z. The expected Ca^+ and CaH^+ ions are detected at 40 m/z and 41 m/z, respectively. Calcium hydroxide is again present at 57 m/z. Carbon species are present in the spectrum at high relative intensities (as seen in the XPS data) including $C_2H_3^+$, $C_2H_5^+$ and CH_3CO^+ ions at 27 m/z. 29 m/z and 43 m/z, respectively. The ion maps for this sample are shown in Figure 5.44 and indicate that the distribution of the calcium and calcium monohydride ions after immersion in media for 7 days is less homogenous across the surface than it is for 24eTiHA. There are then indications that the underlying topography is beginning to emerge. However, there is no titanium ion signal detected that would be expected at 48 m/z suggesting that although the distribution of the ions on the surface has decreased, the thin film remaining at this point still masks the detection of the underlying titanium substrate. Small traces of titanium are seen in the positive ion maps in Figure 5.44.

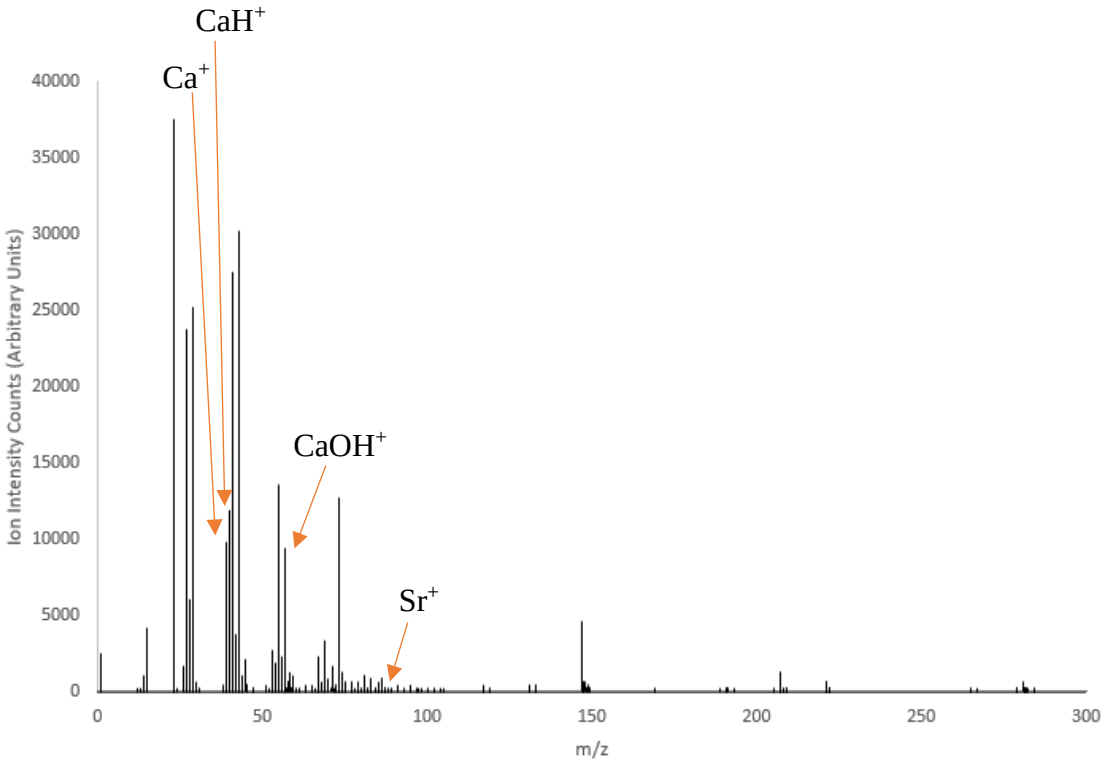

Figure 5.43 ToFSIMS positive ion spectrum for 24eTiSrHA after 7-days exposure to culture media with positive ion signals indicative of a CaP thin film labelled

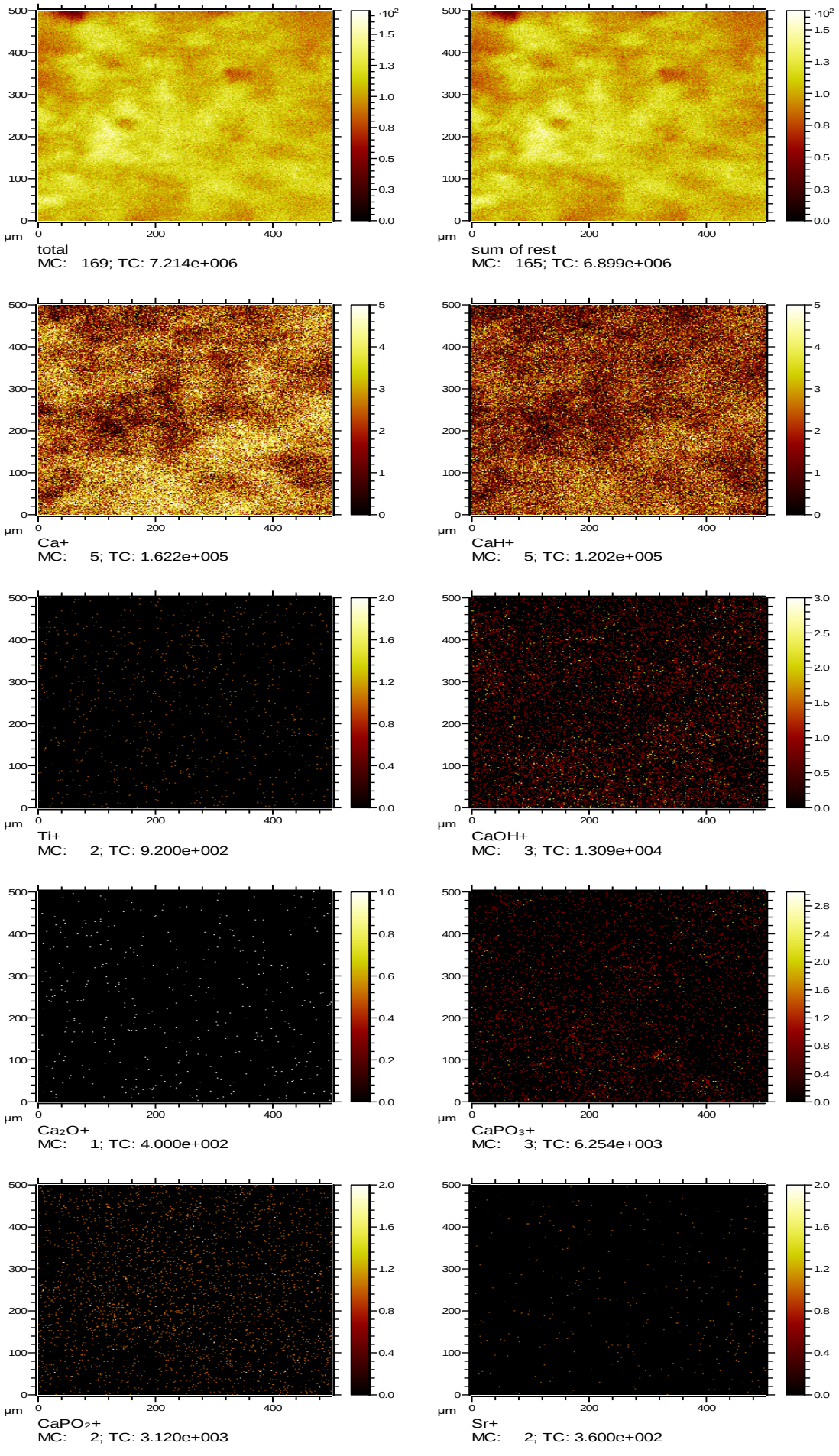

Figure 5.44 ToFSIMS positive ion maps of total ion count (TIC), Ca^+, CaH^+, Ti^+, $CaOH^+$, Ca_2O^+, $CaPO_3^+$, $CaPO_2^+$ and Sr^+ for 24eTiSrHA

PolyTi250HA and PolyTi250SrHA

The ToFSIMS positive ion spectrum for PolyTi250HA is provided in Figure 5.45 and as before, indicates the presence of Ca^+, CaH^+ and $CaOH^+$ ions at 40 m/z, 41 m/z and 57 m/z, respectively, with the presence of carbon species at higher relative intensities for $C_2H_3^+$, $C_2H_5^+$ and CH_3CO^+ ions at 27 m/z, 29 m/z and 43 m/z, respectively. There is again no signal detected at 48 m/z for titanium. This spectrum closely resembles that for the original surface with the exception of the significant reduction of ion signal intensity for the more complex CaP phases. The positive ion maps are provided in Figure 5.46 and confirm that there is still a significant covering of calcium and calcium monohydride on the PolyTi250 substrate surface, with small traces of Ti detected.

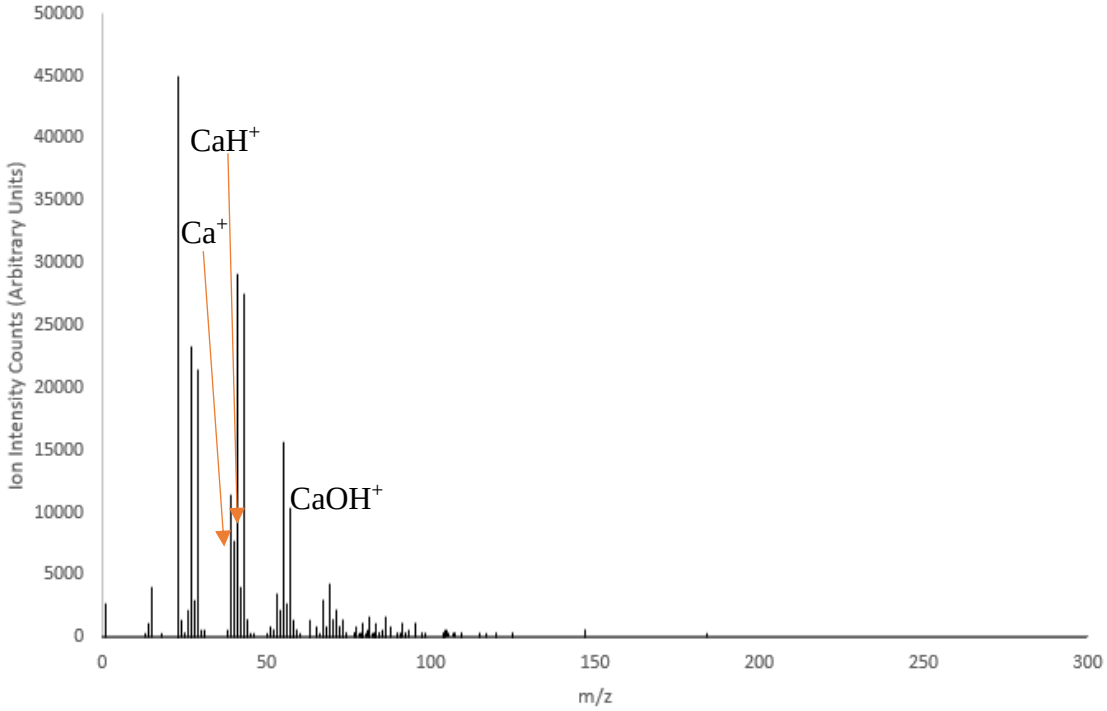

Figure 5.45 ToFSIMS positive ion spectrum for PolyTi250HA after 7-days exposure to culture media with positive ion signals indicative of a CaP thin film labelled

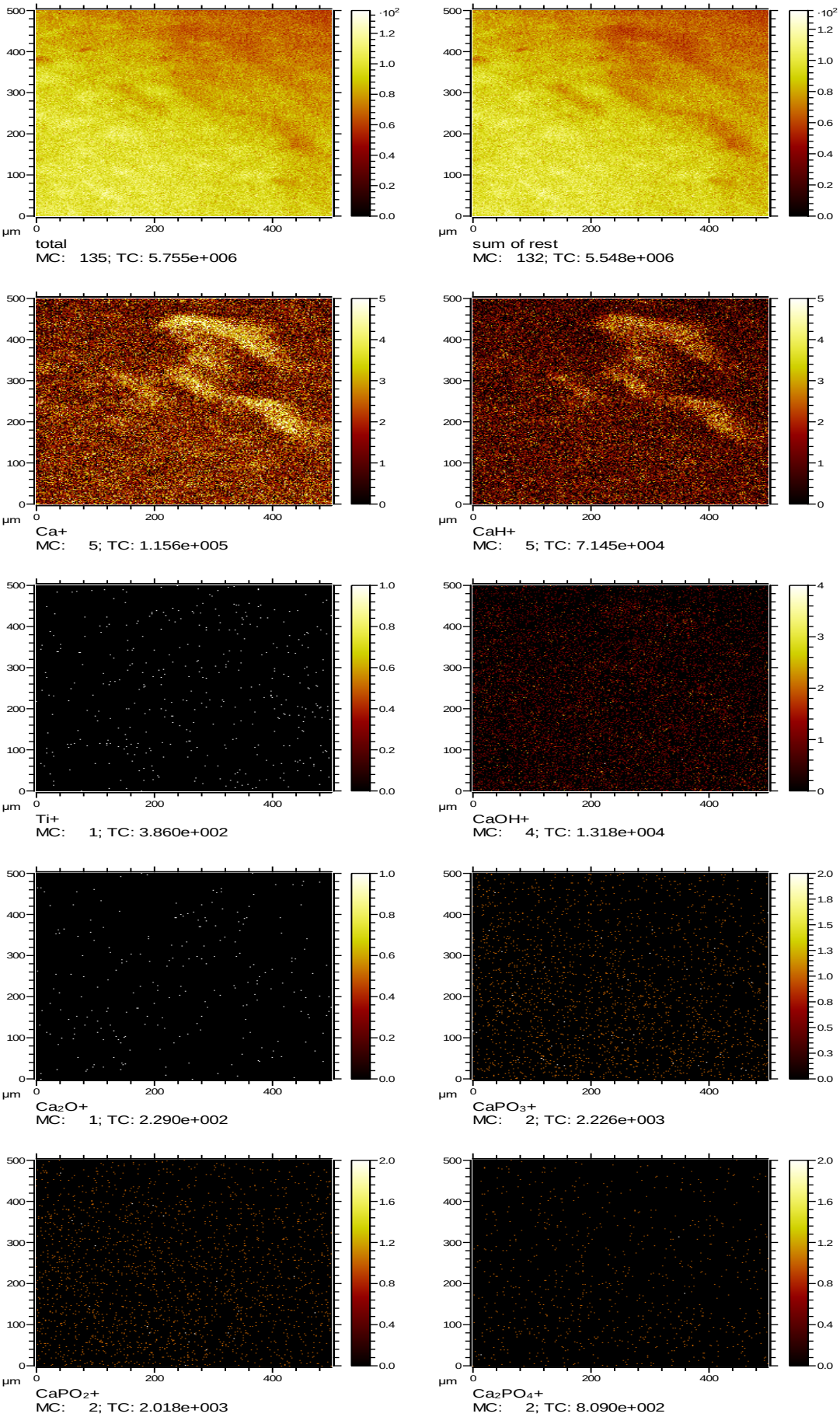

Figure 5.46 ToFSIMS positive ion maps of total ion count (TIC), Ca^+, CaH^+, Ti^+, $CaOH^+$, Ca_2O^+, $CaPO_3^+$, $CaPO_2^+$ and $Ca_2PO_4^+$ for PolyTi250HA

The ToFSIMS spectrum for PolyTi250SrHA at day 7 is presented in Figure 5.47 and shows similar features to those for the previous SrHA coated samples exposed to culture media. Specifically, calcium, calcium monohydride and calcium hydroxide ions are detected at 40 m/z, 41 m/z and 57 m/z, respectively and strontium is present at 88 m/z, as expected. High relative intensity signals are present for Na^+ at 23 m/z and carbon species $C_2H_3^+$, $C_2H_5^+$ and CH_3CO^+ at 27 m/z, 29 m/z and 43 m/z, respectively. This increase in carbon species after 7-days exposure is supported by the XPS data. Again, there is no signal at 48 m/z for Ti^+ ions detected in the positive ion spectra. However, trace amounts of Ti are seen in the corresponding positive ion maps, provided in Figure 5.48. These maps also show that there are calcium and calcium monohydride ions present across the complete surface area imaged. However, the distribution of these ions does not appear to be as homogenous as seen in original samples.

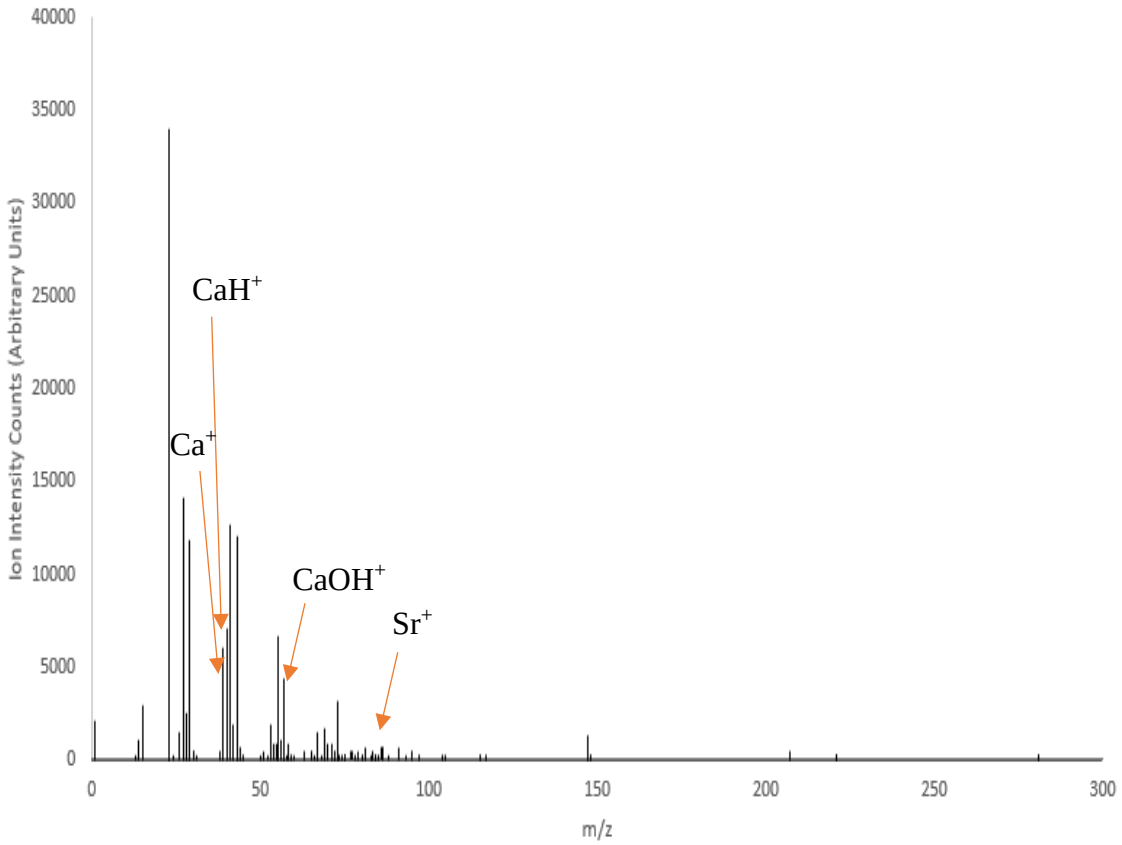

Figure 5.47 ToFSIMS positive ion spectrum for PolyTi250SrHA after 7-days exposure to culture media with positive ion signals indicative of a CaP thin film labelled

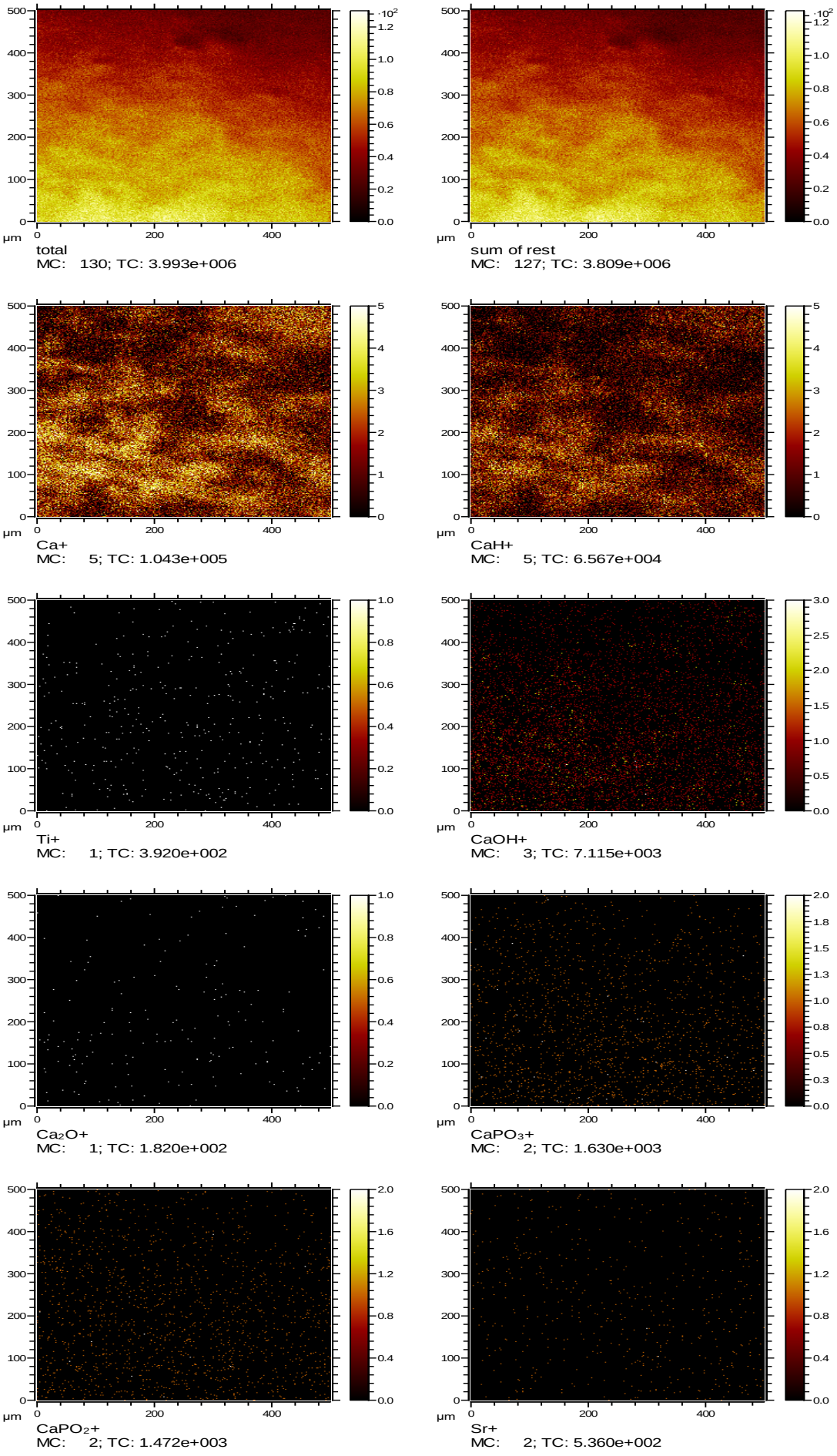

Figure 5.48 ToFSIMS positive ion maps of total ion count (TIC), Ca^+, CaH^+, Ti^+, $CaOH^+$, Ca_2O^+, $CaPO_3^+$, $CaPO_2^+$ and Sr^+ for PolyTi250SrHA

5.5.3 SEM Analysis of CaP Coatings on Pristine, Etched and Polycrystalline Titanium Surfaces after Exposure to Cell Culture Media

TiHA and TiSrHA

SEM has been used to visualise the CaP thin film integrity on the various substrate surfaces after 7-days exposure to cell culture media. The data for TiHA are shown in Figure 5.49 (a) – (c) with the images from the original surfaces at the same magnification provided in Figure 5.49 (d) – (f) for convenience of comparison. At x2.5k magnification both the pre- and post-dissolution samples are similar with the dominant lines and grooves visible on the surface in both cases. Upon higher magnification, at x8k and x30k, the post dissolution samples present similar morphologies, with the post-dissolution samples showing a higher build-up of coating material on the surface.

Figure 5.50 presents SEM images for the TiSrHA samples (a) – (c) post immersion in cell culture media and (d) – (f) shows the original surfaces. The underlying topography of processing lines and grooves are again visible in both sets of images. After exposure to media for 7 days (Figure 5.50 (a) – (c)) there is a significant build-up of additional material visible across the surface that is a consequence of the dissolution process.

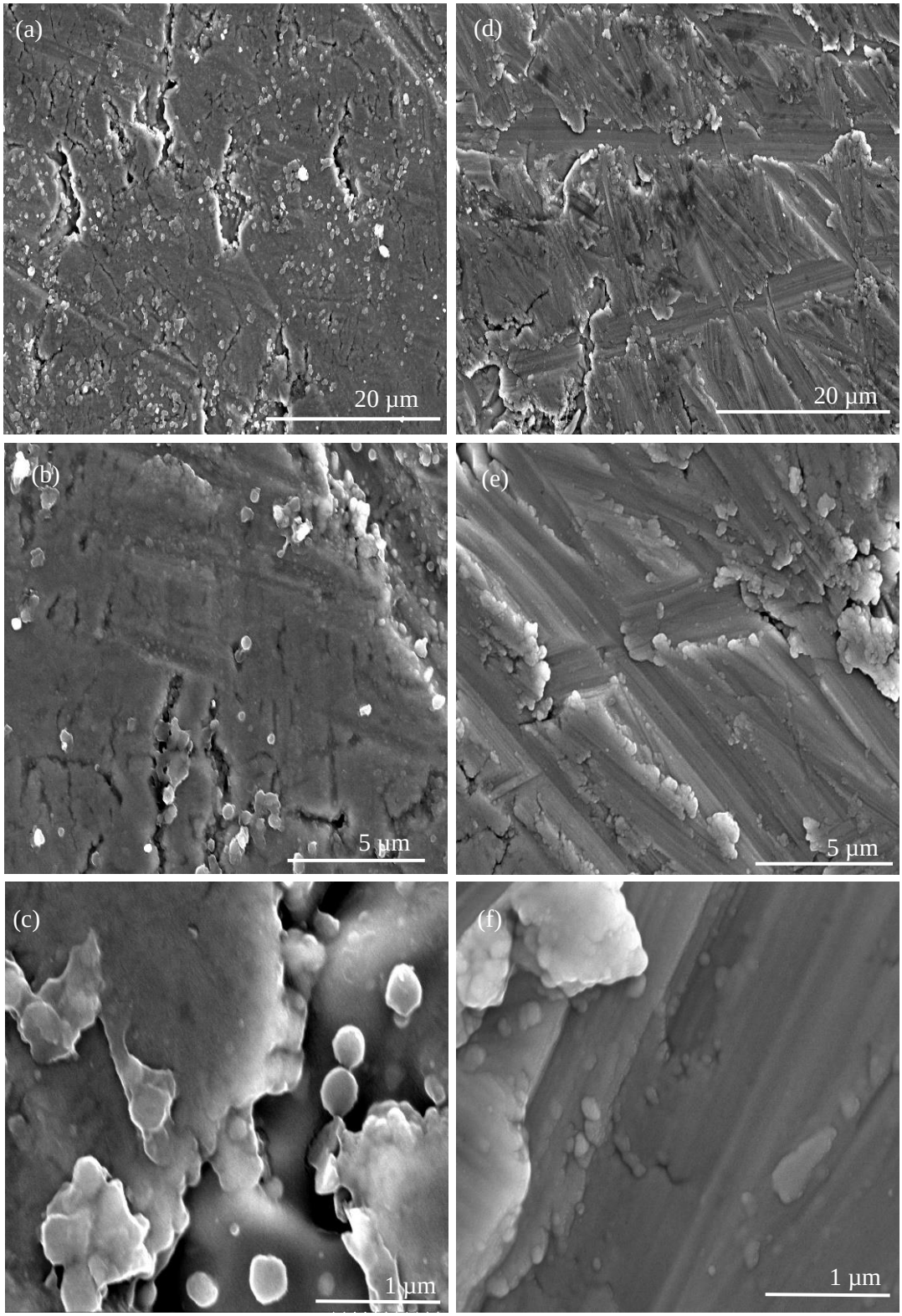

Figure 5.49 SEM images in normal planar view for TiHA (a) – (c) after 7-day exposure to cell culture media with original images reproduced in (d) – (f) at magnifications of (a) x2.5k, (b) x8k, (c) x30k, (d) x2.5k, (e) x8k, and (f) x30k

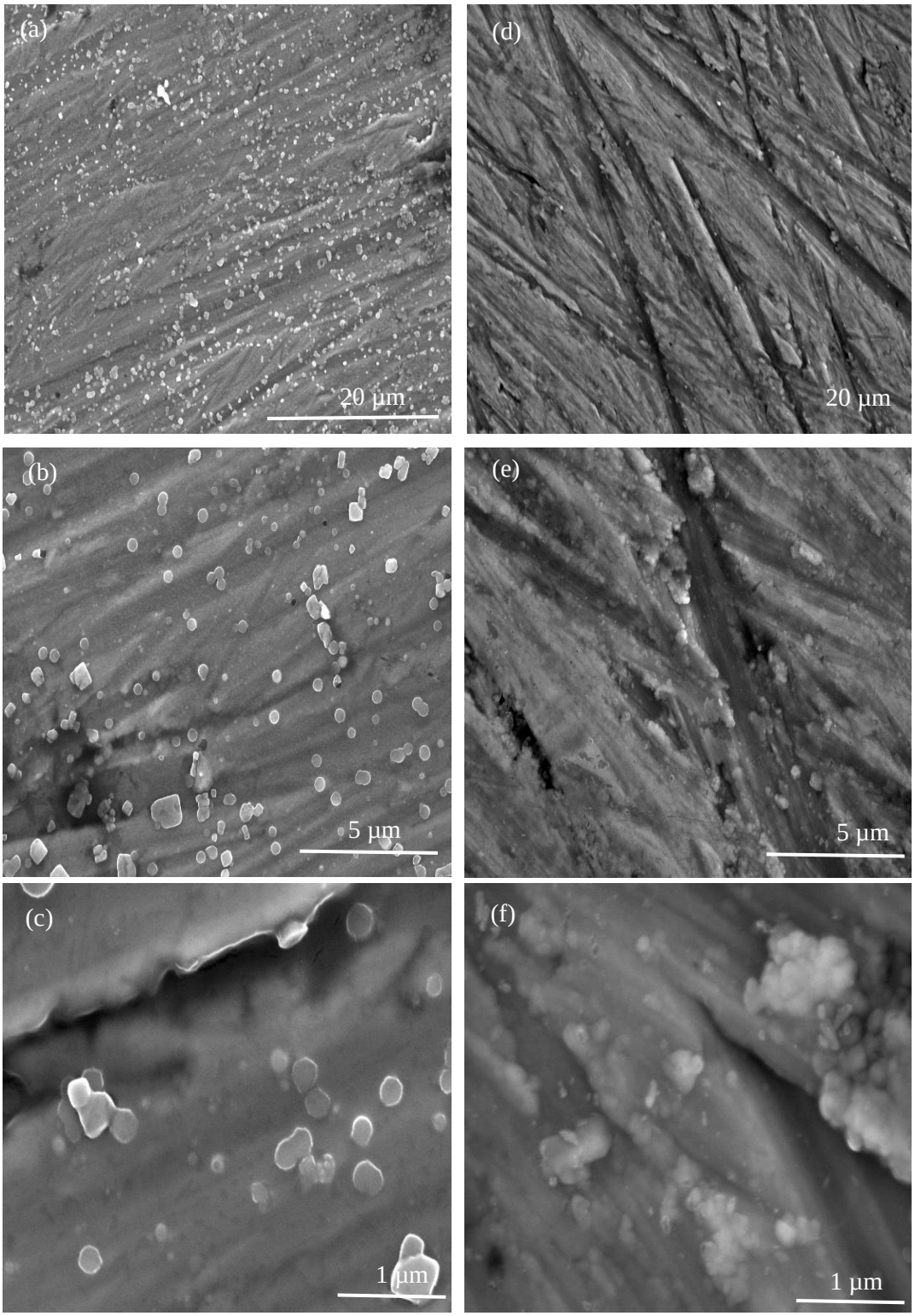

Figure 5.50 SEM images in normal planar view for TiSrHA (a) – (c) after 7-day exposure to cell culture media with original images reproduced in (d) – (f) at magnifications of (a) x2.5k, (b) x8k, (c) x30k, (d) x2.5k, (e) x8k, and (f) x30k

24eTiHA and 24eTiSrHA

SEM images for 24eTiHA at day 7 are seen in Figure 5.51 (a) – (c) with the originals presented again in Figure 5.51 (d) – (f) to allow direct comparison. At a magnification of x2.5k, clear differences can be seen between the two samples. Although the dominant underlying topography can be seen in both samples, there is clearly a build-up of material across the sample surface after exposure to media. This build-up becomes more visible as the magnification is increased and occurs predominantly in the pitting morphology across the surface that has been caused by the etching process.

The corresponding SEM images for 24eTiSrHA post immersion in media for 7 days are provided in Figure 5.52 (a) – (c) with the originals again shown in (d) – (f) for comparison. As was found for the 24eTiHA, the etched morphology of the substrate is still evident after contact with the culture media, with a build-up of additional material across the surface. Again, this occurs predominantly along the lines and grooves, as well as the pitted morphology across the surface.

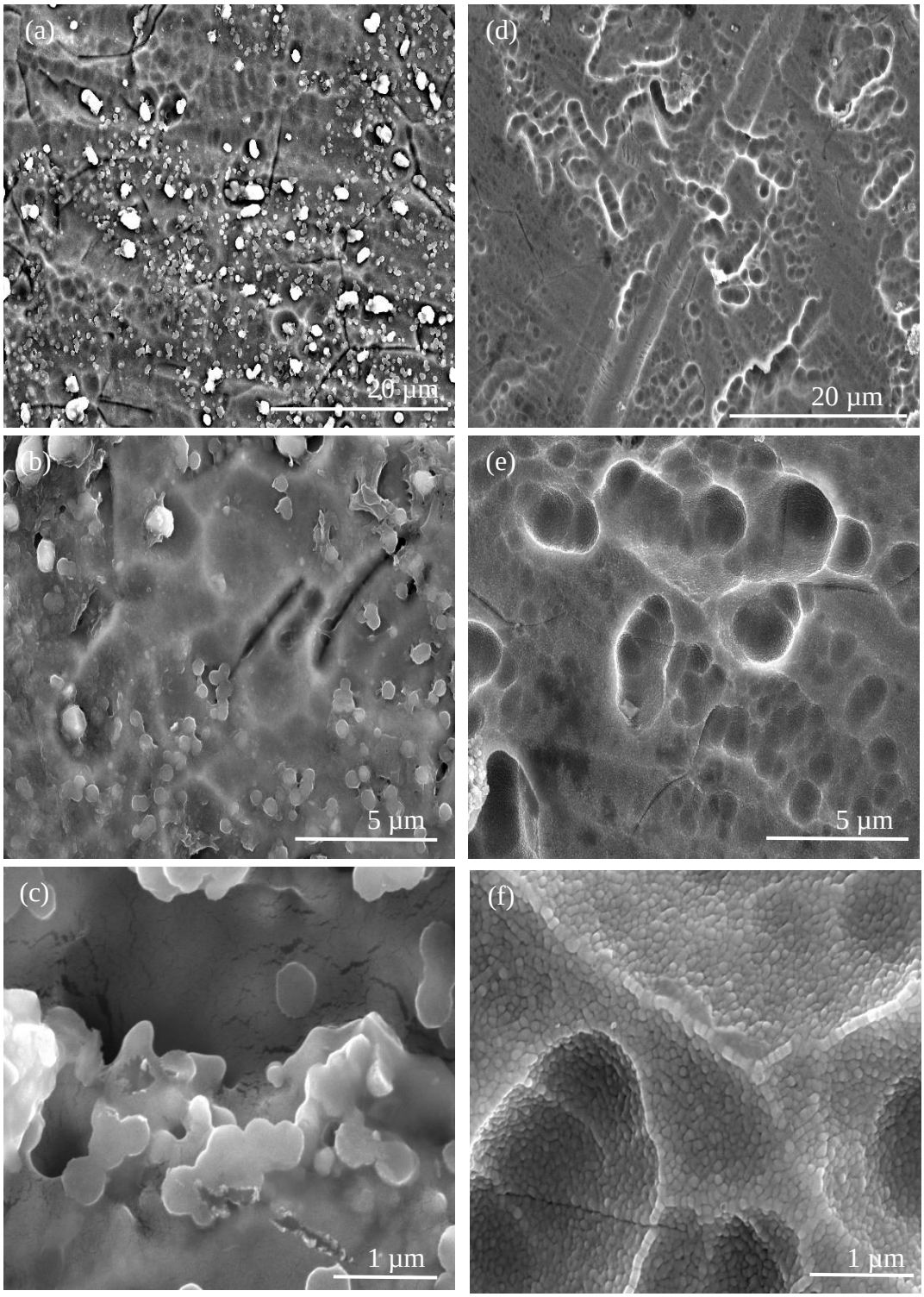

Figure 5.51 SEM images in normal planar view for 24eTiHA (a) – (c) after 7-day exposure to cell culture media with original images reproduced in (d) – (f) at magnifications of (a) x2.5k, (b) x8k, (c) x30k, (d) x2.5k, (e) x8k, and (f) x30k

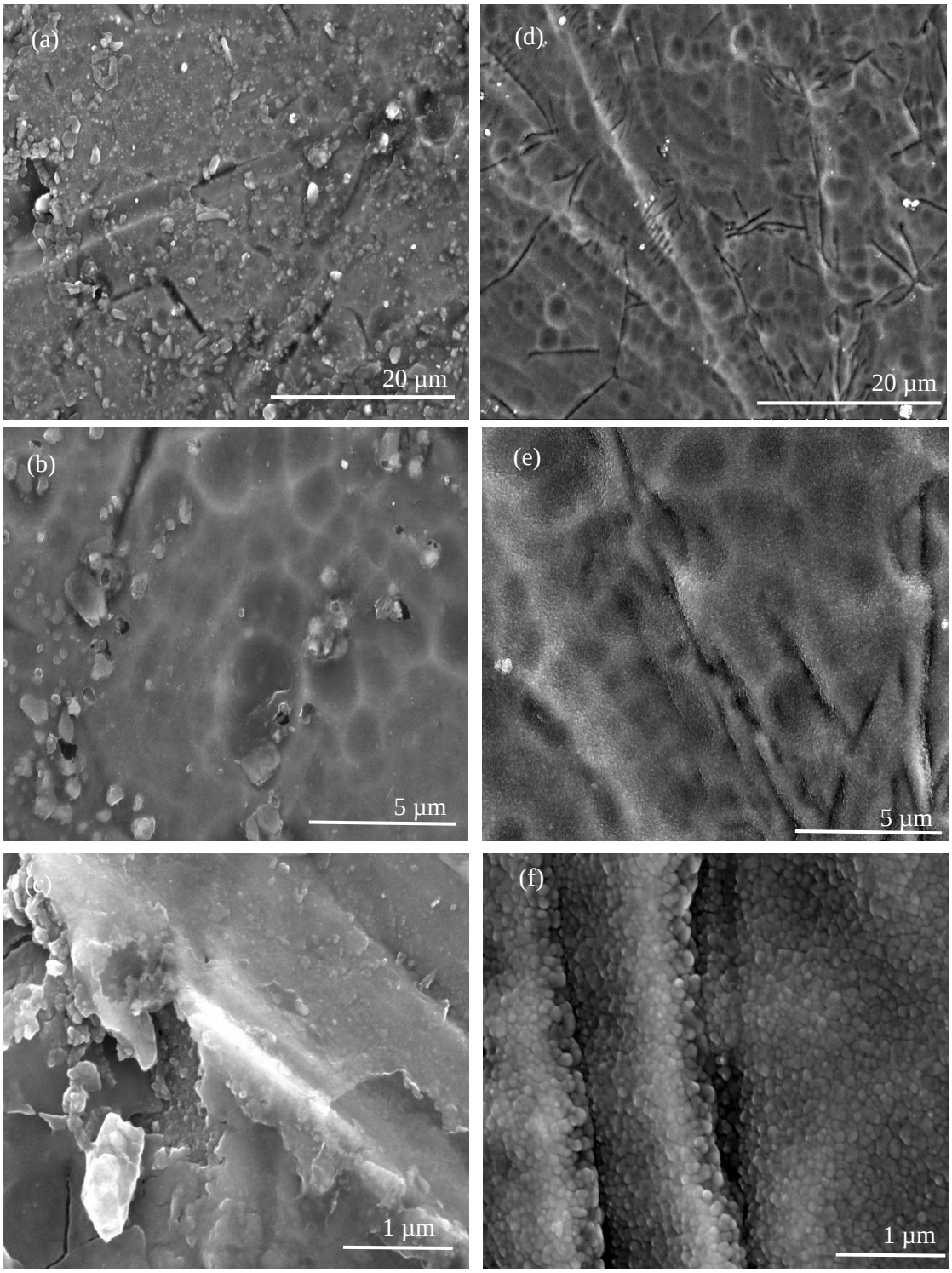

Figure 5.52 SEM images in normal planar view for 24eTiSrHA (a) – (c) after 7-day exposure to cell culture media with original images reproduced in (d) – (f) at magnifications of (a) x2.5k, (b) x8k, (c) x30k, (d) x2.5k, (e) x8k, and (f) x30k

PolyTi250HA and PolyTi250SrHA

The SEM images in Figure 5.53 compare the PolyTi250HA after 7-day exposure to cell culture media (a) – (c) and the original samples (d) – (f) for comparison. Again, there is a build-up of additional material on the surface after exposure to the cell culture media for 7 days which is predominantly present at the lines, groves and on the rougher areas on the sample surface.

Finally, the equivalent for PolyTi250SrHA are provided in Figure 5.54 for post 7-day exposure to cell media (a) – (c) and the original samples (d) – (f), for convenience and to allow for direct comparison. As per the previous PolyTi250HA samples, there is little change here after exposure to media except for the build-up of additional material along the predominant lines and grooves on the sample surface.

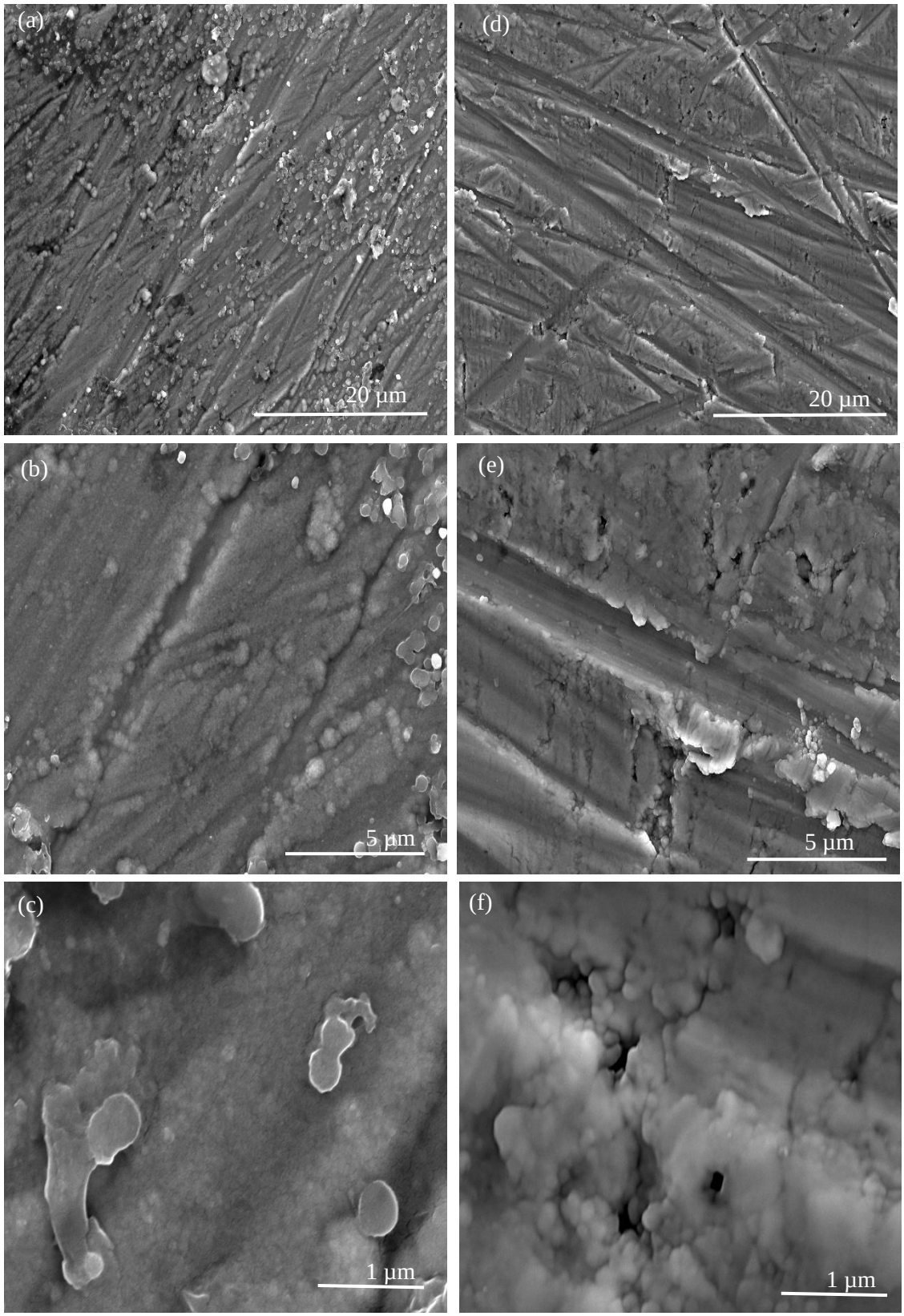

Figure 5.53 SEM images in normal planar view for PolyTi250HA (a) – (c) after 7-day exposure to cell culture media with original images reproduced in (d) – (f) at magnifications of (a) x2.5k, (b) x8k, (c) x30k, (d) x2.5k, (e) x8k, and (f) x30k

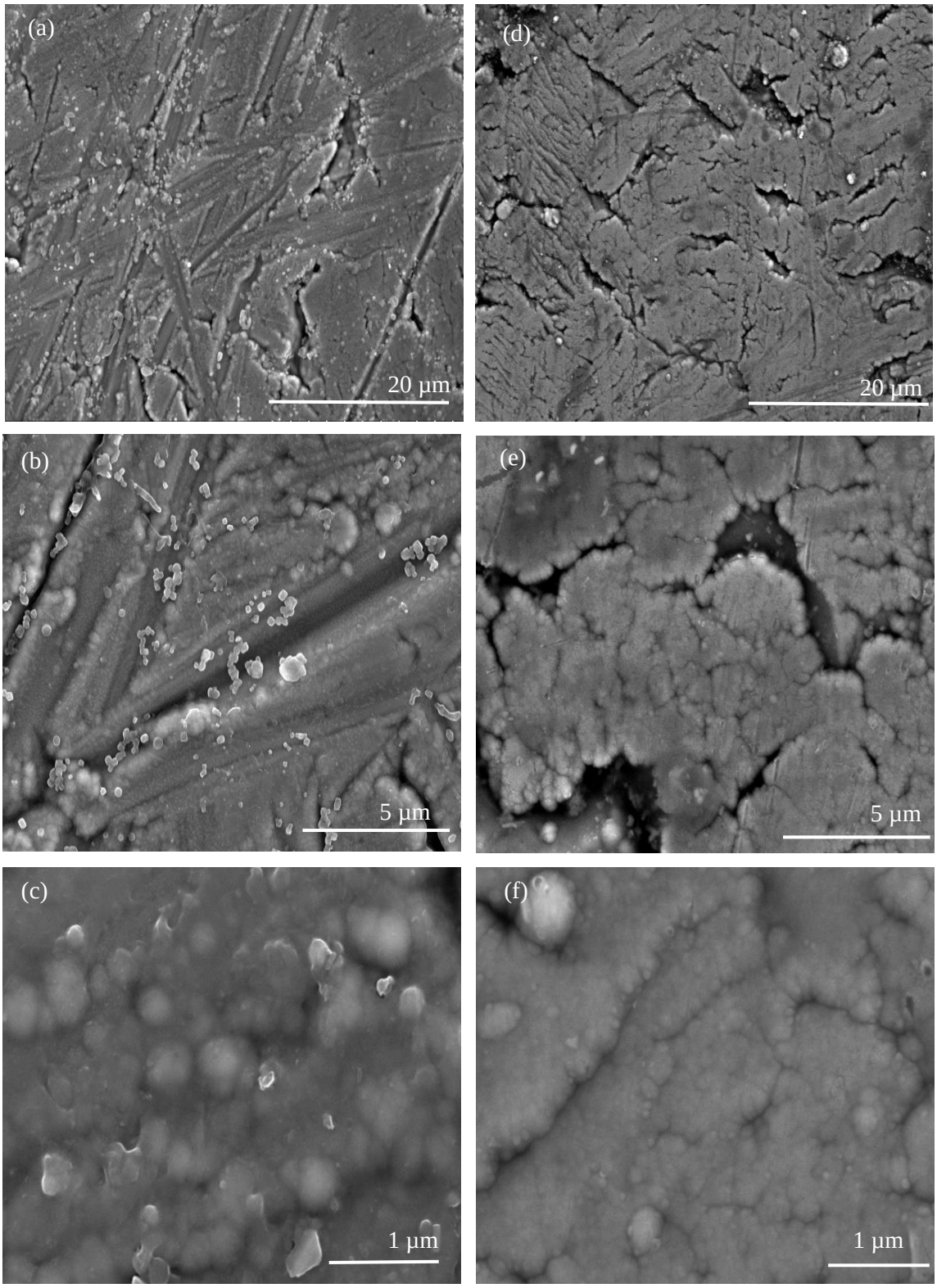

Figure 5.54 SEM images in normal planar view for PolyTi250SrHA (a) – (c) after 7-day exposure to cell culture media with original images reproduced in (d) – (f) at magnifications of (a) x2.5k, (b) x8k, (c) x30k, (d) x2.5k, (e) x8k, and (f) x30k

5.6 Discussion

The aim of the work presented in this chapter was to investigate the chemistry and microstructure of sputter deposited calcium phosphate (CaP) coatings (HA and SrHA) on titanium coupons that had been chemically etched for 24 hrs (24eTi), and to determine how these surfaces respond when exposed to cell culture media (at 37 °C) for 7 days. In order to better understand the nature and scale of the response of the 24eTiHA and 24eTiSrHA samples to media, data have also been obtained for the same CaP coatings on the titanium sheet material (Ti) as a pristine control and also on polycrystalline titanium sputter deposited at 250 W (PolyTi250) as a comparator surface. The chemistry of the various surfaces before and after exposure to media has been determined by XPS and ToFSIMS and their initial as-deposited amorphous nature confirmed by XRD (original samples only). Changes to the corresponding microstructure after exposure to media has then been examined by SEM.

Chemical investigation (XPS and ToFSIMS) of the CaP coatings (HA or SrHA) on the 24eTi surfaces indicated the presence of both calcium and phosphorus ions, with the elimination of any titanium ion signals in both cases, indicating that they are at least 100 nm thick (Chapter 3.3.5). XPS quantitative data showed a higher phosphorus than calcium content for 24eTiHA, leading to an almost 1:1 stoichiometric ratio. The 24eTiSrHA surface yielded much lower calcium content, some but not all of which is due to the substitution of the Sr ions for the Ca ions in the HA lattice[147,229,230]. This lower than expected Ca/P ratio for both HA and SrHA coatings is attributed to the energetics encountered during the sputtering process producing thin films in the as-deposited amorphous state that are known to be calcium deficient[129,231]. However, it should also be noted that when such thin films are deposited onto rough surfaces the variation in distribution across the various features makes it difficult to accurately measure the Ca/P ratio. Therefore, the values calculated here are used only as a guide and in a sample-to-sample comparative manner. The 24eTiHA and 24eTiSrHA samples had a relatively low average carbon contribution to the XPS spectra. Moreover, the standard deviation calculated for the XPS quantitative data from HA and SrHA coated surfaces showed little variation, indicating that the coating chemistry is continuous across the sample surfaces. The TiHA and TiSrHA samples both showed similar chemical composition to the 24eTiHA and 24eTiSrHA coated samples, indicating the presence of calcium and phosphorus as well as oxygen and a relatively low carbon content. Once again, there were no titanium signals detected for either sample suggesting that the coating was thicker than

that of the electrons inelastic mean free path. The Ca/P ratio of the TiHA surface was again found to be an almost 1:1 stoichiometric ratio. As seen for the 24eTiSrHA, the TiSrHA displayed a decrease in calcium content, with a rise in phosphorus content and the addition of a strontium signal. By comparison, PolyTi250HA samples showed a higher amount of carbon on the sample surface compared to that for both the TiHA and 24eTiHA samples. The calcium and phosphorus present on this surface where found to be at lower concentrations that that of both the 24eTiHA and TiHA, but still presented a Ca/P ratio close to that of the previous 1:1 stoichiometric ratio of the previous HA coated samples. The relative carbon content present on the PolyTi250SrHA is at a level similar to that seen for the 24eTi, 24eTiSrHA, TiHA and TiSrHA samples. As seen for the other SrHA coated substrates, the calcium content is much lower than that of the phosphorus, thought to be partially attributable to the presence of strontium. Again, all of the surfaces coated with a CaP thin film (HA or SrHA) showed no titanium signals in the XPS acquisition, suggesting that these coatings were thicker than the inelastic mean free path of the titanium photoelectrons (i.e. coating thickness in the region of 50 to 100 nm)[232,233]. Original thickness of the coatings was estimated to be 111 nm (Chapter 3.3.5). However, this is an estimate and it is expected that film thickness will vary slightly across the surface dependant on any topography present. Overall, all substrates, except for PolyTi250HA, showed a similar chemical composition, with calcium, phosphorus, carbon and oxygen present on the surface.

The XRD spectra for all of the coated titanium substrates confirmed that the CaP coatings (HA and SrHA) are as expected, in the amorphous phase. No signals indicative of the presence of a CaP coating were observed in the x-ray diffractograms, with the peaks present indicative of semi-crystalline titanium, noted previously in Chapter 4[205]. These results are as expected due to the deposition process used for these thin films coatings and their as-deposited amorphous state[45,234,235].

Further chemical investigation of the 24eTiHA and 24eTiSrHA surfaces was carried out using ToFSIMS. In this regard, only positive ion spectra were recorded to identify the presence of the main ions indicative of the CaP thin films[236–238]. Mapping of the distribution of these ions confirmed that a continuous CaP thin film was created in both cases. A high calcium content in the surface region of 24eTiHA is again confirmed by the presence of various calcium phases that are not as evident in the 24eTiSrHA. The 24eTiSrHA spectra show the addition of strontium signals, as expected. No signals for titanium were detected on the 24eTiHA nor the 24eTiSrHA positive ion graphs. However, trace amounts of titanium are present in the positive ion maps of the 24eTiSrHA. Low

amounts of sodium are seen to be present in all of the ToFSIMS spectra and are attributed to low level contamination acquired during handling of the samples. By comparison, the positive ion spectra for TiHA show a lower relative calcium content compared to that of the 24eTiHA but with various calcium phases present. The corresponding positive ion maps indicate a continuous CaP thin film has been deposited across the surface. The TiSrHA sample shows the presence of calcium ions with the addition of strontium ions, but the more complex calcium phases seen for the 24eTiHA and TiHA are absent here. The positive ion maps for this sample again indicate a continuous thin film on the surface of the substrate. As seen in the 24eTiHA and TiHA positive ion spectra, the presence of calcium ions and various calcium phases were again detected for the PolyTi250HA surface. The corresponding positive ion maps are, as before, indicative of a homogenous and continuous CaP coating across the substrate surface. The PolyTi250SrHA spectra shows similarities to those for 24eTiSrHA and TiHA, but with fewer calcium phases observed than for the HA coated samples. As expected, signals assigned to strontium ions are detected. Hence, when comparing the data for the 24eTiHA with those for TiHA and PolyTi250HA, no significant differences in the spectra or positive ion maps are noticeable. This is the same when comparing the SrHA coated samples, which all show a decrease in the amount of calcium phases present, and the addition of strontium into the spectra. The positive ion maps for all of the CaP coated substrates (HA and SrHA) show a homogenous and continuous thin film coating across the surface, with no underlying titanium detected. These data, taken in tandem with the XPS results, confirm the lower calcium content of the SrHA coated samples. The trace amounts of Ti seen in the positive ion graphs for the samples, particularly the SrHA coated samples, are thought to be due in part to the roughened underlying surface causing the CaP coating (HA or SrHA) to be thinner in parts.

Previous work carried out at Ulster University on sputter deposited CaP thin films have involved a number of substrate surface conditions. For example, McLister[29] sputtered CaP films at 50 W for 9 hrs onto (1) glass, (2) a polycrystalline titanium interlayer sputtered onto glass and (3) titanium nanotube surfaces. The calculated Ca/P ratio for these CaP coated substrates was close to the stoichiometric 1.67, typical of stoichiometric HA. Similarly, McCafferty[160]created sputter deposited CaP thin films on (1) glass and (2) a sputtered titanium interlayer on glass at 150 W for 10 hrs, both of which exhibited a Ca/P ratio of ~1.75 – 1.83. Although there are key differences in the sputter conditions used in these previous studies and those employed here which may lead to the differences in the Ca/P ratio values, these are not thought to be the main influence.

Rather, as mentioned earlier, it is suggested here that the titanium (sheet) substrate morphology that is present here causes the XPS data to be unreliable for these calculations as compared to the smooth glass base surface utilised in the earlier studies. Hence, it is not the case that the CaP stoichiometry is necessarily lower than might be expected but rather that the pronounced surface roughness of the samples examined here causes shadowing effects that suggest a 1:1 Ca/P ratio.

The microstructure of the various CaP coated titanium sample surfaces was visualised using SEM. These images confirmed that the layers sputtered from HA or SrHA targets conform to the underlying morphology of the substrates, as hypothesised. A build-up of material is visible along these distinctive topography features, i.e. lines and grooves present on the surface. In the case of 24eTi, the CaP layers clearly conformed to the 'honeycomb' pitted morphology on the etched titanium surface. Interestingly, higher magnification images for 24eTiHA suggest that there are areas where the CaP material has coalesced as ridges on this surface. This form of build-up of material is not obvious in the SEM images of the Ti and PolyTi250 surfaces with HA coatings, even though the underlying Ti pristine surface markings are still seen in all SEM images. The TiSrHA sample shows a similar form of thin film growth on the surface, with the underlying topography visible and evidence of the coating occurring predominantly at these surface features. The PolyTi250HA sample showed similarities to TiHA, with coating build-up mainly at surface features, when compared to that of the uncoated PolyTi250. This was also the case for PolyTi250SrHA, which shows less build-up as seen for the other samples.

To confirm if chemical etching of the Ti surface will allow for partial retention of the CaP material, samples were immersed in aqueous media along with pristine and polycrystalline titanium, shown previously to be capable of this type of behaviour[29,160,239]. In this regard, the chemistry of the CaP coated (HA and SrHA) samples was again characterised by XPS and ToFSIMS, and the associated microstructure by SEM after 7-days immersion in cell culture media at 37 °C. After 1-day in solution, the majority of the CaP on the 24eTiHA surface had dissolved, as indicated by a reduction in the calcium detected by XPS, with an associated decrease in phosphorus and oxygen content also noted. There was also a large increase in carbon content present on this surface. After 7-days immersion in media the oxygen levels had further decreased with a slight increase in the relative carbon, calcium and phosphorus surface content thought to be due in part to reprecipitation of the CaP thin film, as well as protein adhesion occurring (Chapter 2.7.1). The presence of sodium was also noted in the XPS WESS of 24eTiHA at this time

point. For the 24eTiSrHA sample, XPS quantitative data after day 1 of immersion indicated a steep increase in surface carbon content, with a significant decrease in oxygen, calcium and phosphorus content, as well as a decrease in the strontium detected. After 7-days in cell culture media, both the calcium and phosphorus concentrations increased coupled with a further decrease in strontium and oxygen content. Interestingly, despite the low calcium and phosphorus concentrations in the XPS data for both the 24eTiHA and 24eTiSrHA at day 7, no titanium signals were detected across these surfaces. This suggests that whilst parts of the film had dissipated and the CaP concentration had decreased significantly, there were still enough remnants of the CaP thin film present to mask the detection of the underlying substrate. By comparison, TiHA showed a similar response to 24eTiHA over the duration of the immersion study, with a decrease in oxygen, calcium and phosphorus content on the surface, but a significant increase in carbon. The TiSrHA illustrated a similar significant increase in carbon from days 1 to 7, whilst oxygen, calcium, phosphorus and strontium all showed a decrease over the 7-days. As before, no titanium signals were detected after 7-days immersion in the aqueous solution. The PolyTi250HA sample showed a significant increase in carbon content on the surface after 1-day immersion in cell culture media, with the oxygen, calcium and phosphorus contributions all exhibiting a large decrease in relative concentrations, as seen for previous samples at this time point. The carbon content on PolyTi250HA decreases after 7-days, unlike the increase that was seen for 24eTiHA, 24eTiSrHA, TiHA and TiSrHA samples, whilst the oxygen, calcium and phosphorus concentrations in this case all show the expected further decrease after 7-days in cell culture media. The corresponding PolyTi250SrHA sample showed a significant decrease in oxygen, calcium and phosphorus content on the substrate surface after 1-day in the aqueous solution, with again an increase in carbon. After 7-days in cell culture media, little change was found in the relative concentrations of carbon, oxygen, calcium and phosphorus present on this sample surface. As was the case for the previous samples, no titanium signals were present after 7-days for PolyTi250HA or PolyTi250SrHA.

The increase in carbon can be attributed to the adhesion of proteins (Chapter 2.7.1) which have been found to increase surface carbon contributions[22,169].The increase in the calcium and phosphorus contributions measured via the XPS quantitative data at day 1 and day 7 may be explained by the process of reprecipitation of these ions onto the substrate surface due to an increased degree of saturation of these elements in the surrounding static environment[123,129]. As discussed in Chapter 2.7.1, salt electric bilayers can form on the surfaces when in aqueous environments, leading to a protective layer

which could slow the dissolution of the CaP film from the surface. Overall, these data suggest that the 24eTi and Ti substrates provide the most effective morphology to retain residual CaP (HA) compared to that of the PolyTi250 samples. The SrHA coated surfaces show the highest amount of dissolution of CaP occurs after 1-day in cell culture media with the increase after 7-days being the lowest of the samples studied here, thereby confirming that the SrHA films dissolve more quickly than HA films in aqueous solution. However, as before, these data indicate that whilst there has been a significant loss of calcium and phosphorus present on all of the coated surfaces, there is still a continuous thin film coating that is preventing the detection of the underlying titanium substrate.

Further chemical characterisation of samples after immersion in cell culture media was also evaluated by ToFSIMS. The positive ion spectrum for 24eTiHA after 7-days in aqueous solution shows calcium and calcium hydroxide present but a noticeable loss of several other calcium phases. However, despite this decrease in calcium concentration, titanium ions are still not detected in the positive ion spectra, with only trace Ti detected in the positive ion maps. This suggests that there is a still a continuous CaP thin film on the surface at this time point. There is also an increase in organic signals detected in the spectra which is consistent with the high carbon content that was detected in the corresponding XPS data. The positive ion maps for these samples confirm that there is indeed still a continuous CaP thin film coating on the surface. The positive ion spectra for the 24eTiSrHA after 7-days in dissolution presents a spectrum similar to that for the 24eTiHA. Calcium and calcium hydroxide are again present, as well as organic and sodium contamination. Signals assigned to titanium ions are once again absent from this spectrum and suggesting that there is still a continuous CaP thin film on this surface. However, the corresponding positive ion maps observed indicate that there are areas of lower relative calcium intensity than that of other areas across the surface. By comparison, the positive ion spectrum for TiHA after 7-days in cell culture media resembles that for the 24eTiHA at the same time point, i.e. there is a notable absence of various calcium phases that are seen pre-dissolution, but calcium and calcium hydroxide are still present on the surface. There is again an increase in the carbon and sodium ions detected, with titanium once again absent from the spectrum, suggesting that there is still a continuous coating present on the surface. The TiSrHA positive ion spectrum shows similarities to that for 24eTiSrHA, with calcium, calcium hydroxide, organic carbon and sodium species once again detected, as well as strontium ions. Again, the corresponding positive ion maps indicate areas with much lower calcium coverage than that of other areas on the surface. This is indicative of the more pronounced dissolution of the thin film coating at particular

areas on the surface. However, there is still no titanium signal present in the spectra which again indicates that although there has been significant loss in the calcium content on the surface, there is still a thick enough coating across the surface which prevents the detection of the underlying titanium substrate. The positive ion spectrum for PolyTi250HA after 7-days immersion is like that seen for the corresponding 24eTiHA and TiHA substrates at the same time point, i.e. there is calcium, calcium hydroxide, sodium and carbon detected on the surface, with the notable absence of titanium. As before, the positive ion maps for PolyTi250HA at 7-days show a continuous coating across the surface. By comparison, the maps for the PolyTi250SrHA sample indicate that the coating has undergone more dissolution than that seen for the 24eTiSrHA and TiSrHA after 7-days in media. This can be explained by the expected faster dissolution of the SrHA coatings that occurs when the larger strontium ion substitutes for the calcium in HA, thereby 'stretching' the ionic lattice, making it more susceptible to dissolution when placed in aqueous solution[47,229,240].

The data here suggest that whilst all substrates indicate that there is still a continuous coating present after 7-days in aqueous solution, there is evidence that some have undergone dissolution more readily than others. This is particularly evident for the 24eTiSrHA, TiSrHA and PolyTi250SrHA surfaces. The 24eTiHA and the TiHA samples both exhibit higher amounts of residual calcium after 7-days, as confirmed by the XPS, compared to that of the PolyTi250HA. Both the XPS and ToFSIMS data suggest that there is an increased presence of carbon and sodium on all of the surfaces after immersion in media. Low levels of sodium contamination are expected from handling of the samples and are most evident in ToFSIMS, which is sensitive to very low levels. However, the increased sodium from days 1 to day 7 is thought to be attributable to the cell culture media utilised here, which has sodium bicarbonate in the solution[241]. Likewise, the increased carbon contribution is deemed to be due to the organic component of the media and protein adsorption on the sample surfaces. Therefore, it is suggested that the interaction of the substrate with the surrounding environment has led to the deposition of both sodium and carbon on the surface over the 7-days dissolution. Moreover, Diez-Escudero *et al.*[128] found that the incorporation or 'doping' of carbonate ions with CaP can decrease the solubility of the thin film in aqueous media and so this may also play a role in the dissolution behaviour observed here. Overall, when comparing the chemistry of the HA coated samples after immersion in media, the TiHA and 24eTiHA samples display similar amounts of CaP retention, with an increase in calcium content from days 1 to days 7 and little change in the phosphorus content. The PolyTi250HA sample showed a

decrease in CaP content across the 7-days study, with no increase measured between days 1 and 7. On the other hand, when comparing the SrHA coated samples, both the 24eTiSrHA and PolyTi250SrHA show the highest retention after 7-days, with the TiSrHA showing the lowest value.

SEM imaging of the 24eTiHA and 24eTiSrHA surfaces after 7-days immersion in cell culture media indicated that both displayed a build-up of material across the surface, thought to be due to reprecipitation of the dissolved CaP material. It is suggested that the underlying 'honeycomb' pitted morphology is the cause of the build-up ridges of material on this surface. At high magnification, particles can be seen on the as-deposited CaP film. The SEM images for the 24eTiSrHA surface after exposure to media suggests that this surface undergoes less reprecipitation of coating material, as supported by the lower CaP concentration seen in the related XPS and ToFSIMS data. By comparison, images for TiHA after 7-days in cell culture media indicate that there is a lower build-up of coating material than that seen for 24eTiHA, with the most of it concentrated here in areas along the surface features (lines and grooves) present. The TiSrHA sample exhibits a similar build-up of material which is again concentrated along the lines and grooves visible on the surface. The PolyTi250HA, after 7-days immersion, also display this reprecipitated CaP material. However, there is less precipitated material than that seen for the 24eTiHA and TiHA samples. This lower amount of surface reprecipitation is again supported by the XPS and ToFSIMS data. In contrast, PolyTi250SrHA display a higher build-up of material on the surface after 7-days in cell culture media, again concentrated on the surface features present. The XPS and ToFSIMS data are again indicative of there being significant retention of CaP material on these surfaces.

Overall, these data show that the 24eTi substrate has a surface chemistry with properties that are similar to native titanium. The addition of a bioactive element in the form of a CaP coating (HA or SrHA) has been successfully undertaken by sputter coating. A study of the dissolution of this as-deposited CaP layer shows that the 24eTi surface morphology is capable of retaining both HA and SrHA derived thin films post-dissolution. Moreover, the CaP retention noted on these surfaces was higher than that on either the Ti or PolyTi250 substrates. This preservation of the bioactive CaP material after 7-days is of particular interest for enhancing cell interactions thereon, as no annealing step was necessary to slow the dissolution of the thin film. This is particularly important as high processing temperatures can lead to degradation of the mechanical properties of the substrates[25,191]. Previous work carried out at Ulster University[28,29,160] has evaluated how CaP thin film coatings on flat surfaces (i.e. glass substrates) will dissolve

almost immediately after immersion in aqueous solution. However, the addition of the roughened morphology created by chemically etching titanium substrates has been shown here to slow the dissolution of the CaP thin film. It should be noted that unlike in the case of the work on glass, all of the substrates employed in this thesis have a degree of surface roughness which is thought to contribute to the preservation of the CaP coating throughout. Yokota *et al.*[129] sputtered an as-deposited amorphous CaP thin film onto titanium screws which were tested *in vivo*. It was found that the amorphous CaP thin film was still present after 1-week implantation *in vivo*. However, it was found to be absent after further evaluation at weeks 2 and 4. This supports the findings in this thesis, where the CaP thin films (approximately 0.111 µm thick) are still seen to be present after 7-days immersion in aqueous solution.

As an outcome of the results discussed here, it is further hypothesised that the partial dissolution of CaP coatings (HA or SrHA) on the 24eTi substrate will prove beneficial to cell interactions thereon, due to an increase in the local concentration of both Ca and P ions in the surrounding environment, leading to enhanced bioactivity[3,22,129]. In particular, the presence of strontium has been shown to provide enhanced cellular response at low concentrations[37,242–244], and so its availability is of special interest. It is also thought that the underlying roughened topography of the chemically etched surfaces (24eTi) will also contribute to an elevated cell response. Hence, to investigate the nature and scale of these biological responses, a series of *in vitro* bone cell culture studies have been designed and implemented. As presented in the next chapter, this work seeks to understand how the ‘controlled’ dissolution of the CaP thin films on 24eTi direct affects cell response in comparison to the behaviour of the same cells on CaP coated pristine and polycrystalline titanium substrates.

Chapter 6: *In Vitro* Evaluation Calcium Phosphate Coatings on Etched Titanium

6.1 Introduction

Cells are known to respond to the physical and chemical cues that they encounter directly, or in some cases indirectly, in their environment. Previous studies have shown that bone cells respond positively to surface chemistries and morphologies in which the features have a degree of offset orientation. In addition, the presence of bioactive elements on such surfaces can lead to positive effects such as enhanced propagation and differentiation and, under the correct conditions, impart antimicrobial effects. However, it is also clear that negative effects including the inhibition of certain cellular processes and even cell death can occur, depending on the nature of the chemical species present and their respective concentrations. This chapter reports the results of an *in vitro* study of U-2 OS bone-like osteosarcoma cells on chemically etched titanium with and without an as-deposited calcium phosphate (CaP) coating (HA and SrHA). Based on the findings from the characterisation studies presented in Chapter 5, the data obtained for the etched samples (24eTi) have been compared to that obtained for the equivalent pristine (Ti) and polycrystalline titanium (PolyTi250) substrates. The cell culture work is grouped into three separate but intercorrelated studies: Cell Study A provides baseline data from a 7-day study of U-2 OS cells on Ti, 24eTi and PolyTi250 substrates; Cell Study B evaluates the day 3 response of U-2 OS cells to CaP coated (HA and SrHA) Ti, 24eTi and PolyTi250 substrates, and Cell study C comprises a more considered appraisal of the response of U-2 OS cells to CaP coated (HA and SrHA) Ti, 24eTi and PolyTi250 substrates over a 28-day period. Cell studies A and B utilise the MTT assay as a measure of the metabolic rate of those cells removed from each of the substrates at each time point. The PicoGreen™ assay was employed to measure the DNA concentration present from cells that were attached to the substrate surfaces at the same time points. Cell counting was also undertaken using DAPI staining of the cell nuclei to allow for visualisation of cells directly attached to the various surfaces. Finally, SEM imaging of adhered cells was used to give an indication of their morphology and how this reflects the cellular response to these various surfaces. In addition, Cell Study C measured the total protein concentration from cells that had been present on each substrate surface, as well as specifically measuring for ALP as an indication of differentiating osteoblast activity. The various samples evaluated in this chapter are as described previously and abbreviated as follows:

- Ti – Titanium control
- 24eTi – 24 hr etched titanium
- PolyTi250 – 250 W polycrystalline titanium
- TiHA – Titanium with HA thin film
- 24eTiHA – 24 hr piranha etched titanium with HA thin film
- PolyTi250HA – 250 W polycrystalline titanium with HA thin film
- TiSrHA – Titanium with SrHA thin film
- 24eTiSrHA – 24 hr etched titanium with SrHA thin film
- PolyTi250SrHA – 250 W polycrystalline titanium with SrHA thin film

6.2 Cell Study A – 7-Day Evaluation of Uncoated Substrates

As indicated above, an evaluation of the response of U-2 OS cells to the Ti, 24eTi and PolyTi250 substrates was undertaken in Cell Study A to provide baseline data and as a way to better gain a basic understanding of how each of the different topographies influence the initial stages of cell response.

6.2.1 Cellular Metabolic Activity

The MTT assay data for U-2 OS cells exposed to the Ti, 24eTi and PolyTi250 native substrate surfaces after 1, 3 and 7 days in culture are presented in Figure 6.1. The absorbance data presented is an indication of the viability of the cells as a measure of their metabolic rate and show there is a statistically significant difference between the values obtained for cells on Ti and on 24eTi, with the etched samples showing an elevated response at all three time points: $P < 0.0001$ = **** at days 1 and 3 and $P < 0.001$ = *** at day 7. A comparison between the PolyTi250 and Ti samples indicates no statistically significant difference at day 1. However, significant values of $P < 0.001$ = *** at day 3 and $P < 0.05$ = * at day 7 were calculated. A comparison of the 24eTi with PolyTi250 shows $P < 0.01$ = ** at day 1 but no statistically significant difference at days 3 and 7. These data therefore suggest that the cells on the PolyTi250 surface have a lower initial response (day 1) with a lower absorbance for metabolic activity measured when compared to the 24eTi samples but that by day 3 the cell response on each surface is similar, with both showing elevated levels of absorbance when compared to those from the cells on the Ti control substrate surface.

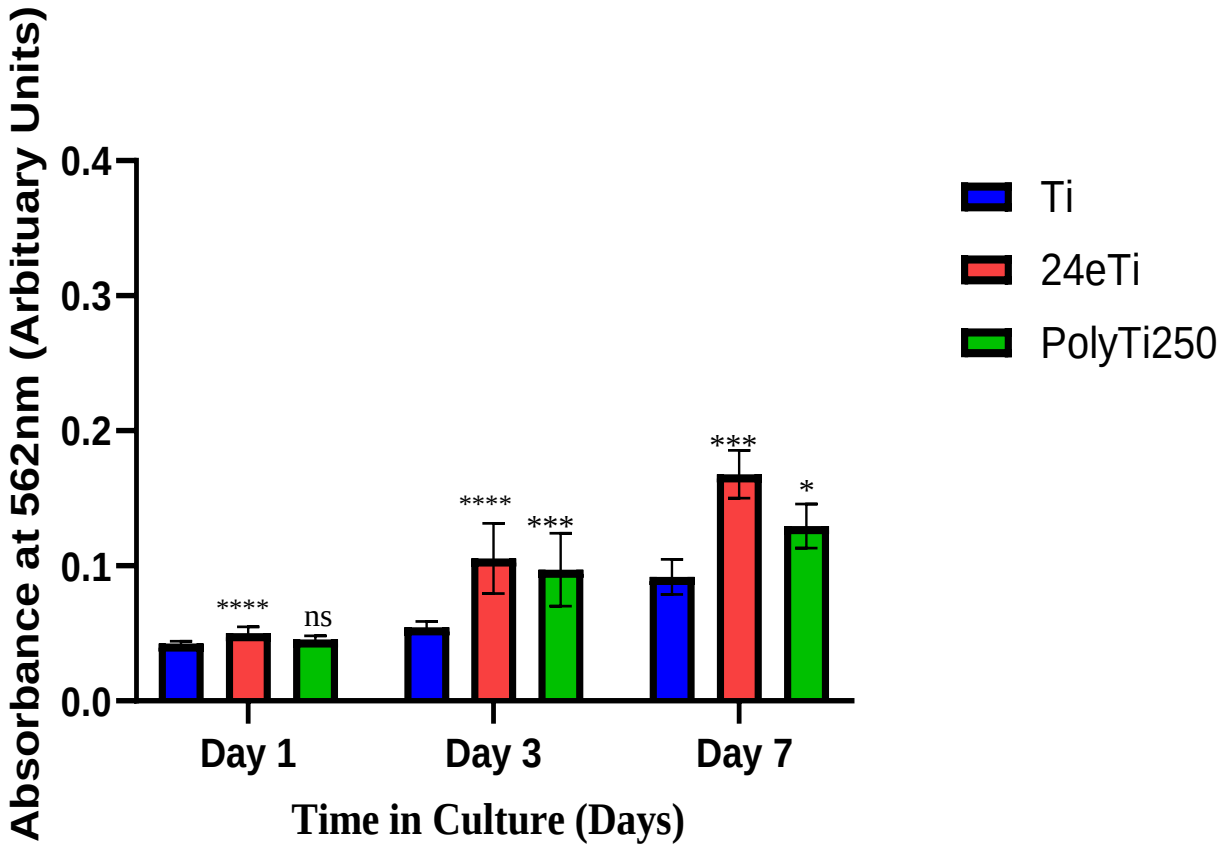

*Figure 6.1 MTT absorbance values for U-2 OS cells cultured on Ti, 24eTi and PolyTi250 substrates at days 1, 3 and 7 with statistically significant difference (P > 0.05= ns, P < 0.05 = *, P < 0.01 = **, P < 0.001 = *** and P < 0.0001 = ****) for 24eTi and PolyTi250 when compared to Ti*

6.2.2 DNA Quantification

Figure 6.2 shows the Pico Green DNA quantification data for the substrates of interest at each of the three timepoints over the 7-day study, with measured concentrations given in nanograms per millilitre (ng/ml). The day 1 data shows that there is no statistically significant difference between the 24eTi and PolyTi250 substrates when each is compared to the Ti control. In addition, there are no distinct statistically significant differences between the 24eTi and PolyTi250 substrates when compared directly to each other. At day 3 all substrates show a statistically significant increase in DNA concentration when compared to the day 1 results and a statistically significant difference recorded between Ti and 24eTi ($P < 0.001$ = ***), with the Ti showing a higher value for DNA concentration. However, there is no statistically significant difference between the measurements obtained from cells on the Ti and PolyTi250 samples. A statistical difference of $P < 0.05$ = * was determined when comparing 24eTi to PolyTi250 with the higher concentration calculated for the PolyTi250. At day 7, a statistically significant increase in DNA concentration was again observed across all samples compared to the earlier timepoints, with 24eTi samples showing the greatest increase when compared to the other samples ($P < 0.01$ = **). When compared to Ti, PolyTi250 showed a value of $P < 0.05$ = *, indicative of a DNA concentration higher than that of the Ti control. A comparison of 24eTi to PolyTi250 gave a value of $P < 0.05$ = * with the 24eTi presenting the highest positive increase at day 7. The PolyTi250 samples showed a similar response to that for Ti at all 3 timepoints with no statistically significant difference detected until day 7 where $P < 0.05$ = * was calculated, indicative of PolyTi250 having a higher response than Ti. Overall, these data suggest that whilst the 24eTi samples initially have a lower DNA concentration than the other samples, they have the largest value by day 7. By comparison, the PolyTi250 and Ti samples show a steady increase in the measured DNA concentration from days 1 to 7 with no discernible difference determined between them.

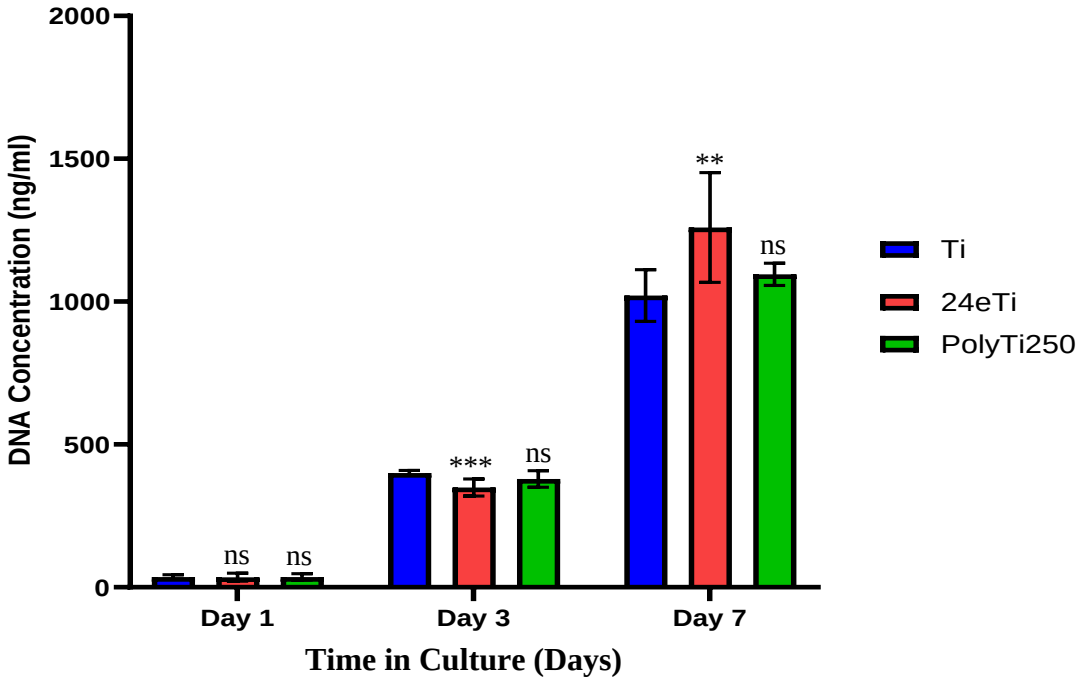

*Figure 6.2 DNA concentration values for U-2 OS cells cultured on Ti, 24eTi and PolyTi250 substrates at days 1,3 & 7 with statistically significant difference (P > 0.05 = ns, P < 0.05 = *, P < 0.01 = **, P < 0.001 = *** and P < 0.0001 = ****) for 24eTi and PolyTi250 when compared to Ti*

6.2.3 Metabolic Activity Normalised to DNA Concentration

In order to allow clearer visualisation of the cellular metabolic rate according to the cell density present, MTT results (Chapter 6.2.1) were normalised to cell number according to the DNA concentration at the particular timepoint (Chapter 6.2.2). Figure 6.3 shows the normalised data, and a clear trend is visible across all three substrates. Whilst the 24eTi samples appear t display the higher values, no significant difference is calculated for 24eTi and PolyTi250 at days 1,3 or 7 when compared to Ti. At each timepoint, no significant difference is seen when comparing 24eTi and PolyTi250.

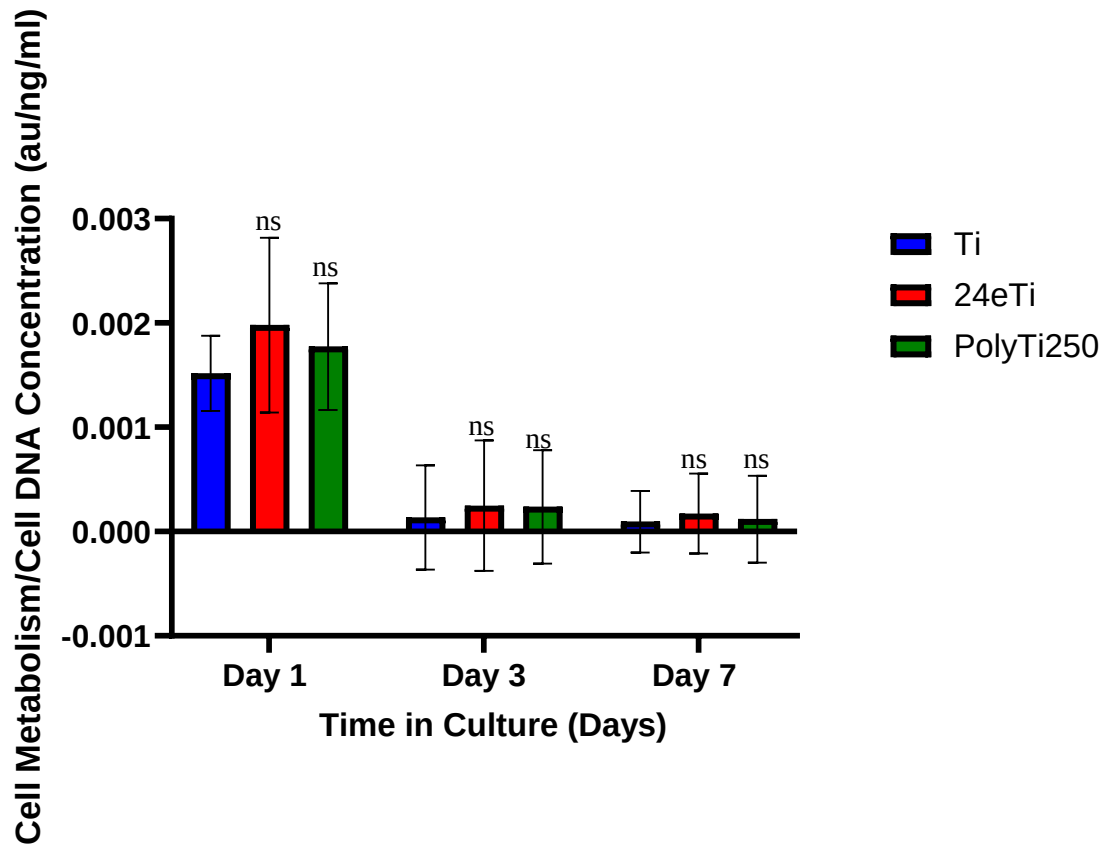

*Figure 6.3 Normalised cell metabolism to DNA concentration values for U-2 OS cells cultured on uncoated substrates at days 1, 3 & 7 with statistically significant difference (P > 0.05 = ns, P < 0.05 = *, P < 0.01 = **, P < 0.001 = *** and P < 0.0001 = ****) for 24eTi and PolyTi250 when compared to Ti*

6.2.4 Cell Nuclei Staining using DAPI

Figure 6.4 shows the fluorescence microscopy images of DAPI stained U-2 OS cell nuclei on (a) Ti, (b) 24eTi and (c) PolyTi250 substrate surfaces at days 1, 3 and 7. There is a clear trend observed from day 1 to day 7, with an increase in the number of cell nuclei over time evident across all samples. At day 1, the images indicate that all substrate surfaces have cells present with no clear visible difference in the numbers on each. Average cell coverage reported as the number of cells/cm^2, for the surfaces after 1 day in culture indicate that Ti has the lowest coverage (11.92 ± 11.10) with 24eTi (23.31 ± 23.30) and PolyTi250 (37.12 ± 25.30) showing significantly more cell coverage than this control surface. The day 3 substrate surfaces all show a significant increase in the number of blue nuclei staining present compared to that seen on the substrate surfaces at day 1. Again, the numbers of nuclei on each type of surface is similar. At day 3, average cell coverage (cells/cm^2) calculated for Ti was 46.29 ± 30.91, 24eTi was 39.47 ± 20.66 and PolyTi250 was 57.05 ± 18.23. By day 7 the cell numbers of cell nuclei have increased again with the cells appearing to show areas of 'clumping', most especially on the 24eTi and PolyTi250 surfaces. Average cell coverages after 7-days in culture have increased to 84.46 ± 10.72 for Ti, and 47.09 ± 27.96 for 24eTi but have now decreased to 42.57 ± 15.54 for PolyTi250. In general, the numbers of cells that are present on the various substrates at each timepoint are consistent with the trends that were seen previously for the MTT and DNA data (Figure 6.1 - Figure 6.3, respectively).

When using the ImageJ cell counter plugin, cell numbers display a similar trend. At day 1 Ti cell numbers were averaged at 522.67 ± 398.33, with 24eTi (326.67 ± 165.62) and PolyTi250 (402.17 ± 143.70) displaying lower cell counts but lower standard deviation. Day 3 numbers show an increase across all samples, as expected, with PolyTi250 giving the highest cell count (2097.83 ± 1034.87), with 24eTi (1610 ± 360.33) and Ti (1512.50 ± 513.01) displaying lower cell counts but a lower standard deviation. Day 7 displays a decrease in numbers for both the PolyTi250 (1510.67 ± 434.16) and 24eTi (728 ± 648.58) but an increase for Ti (1744.50 ± 629.0).

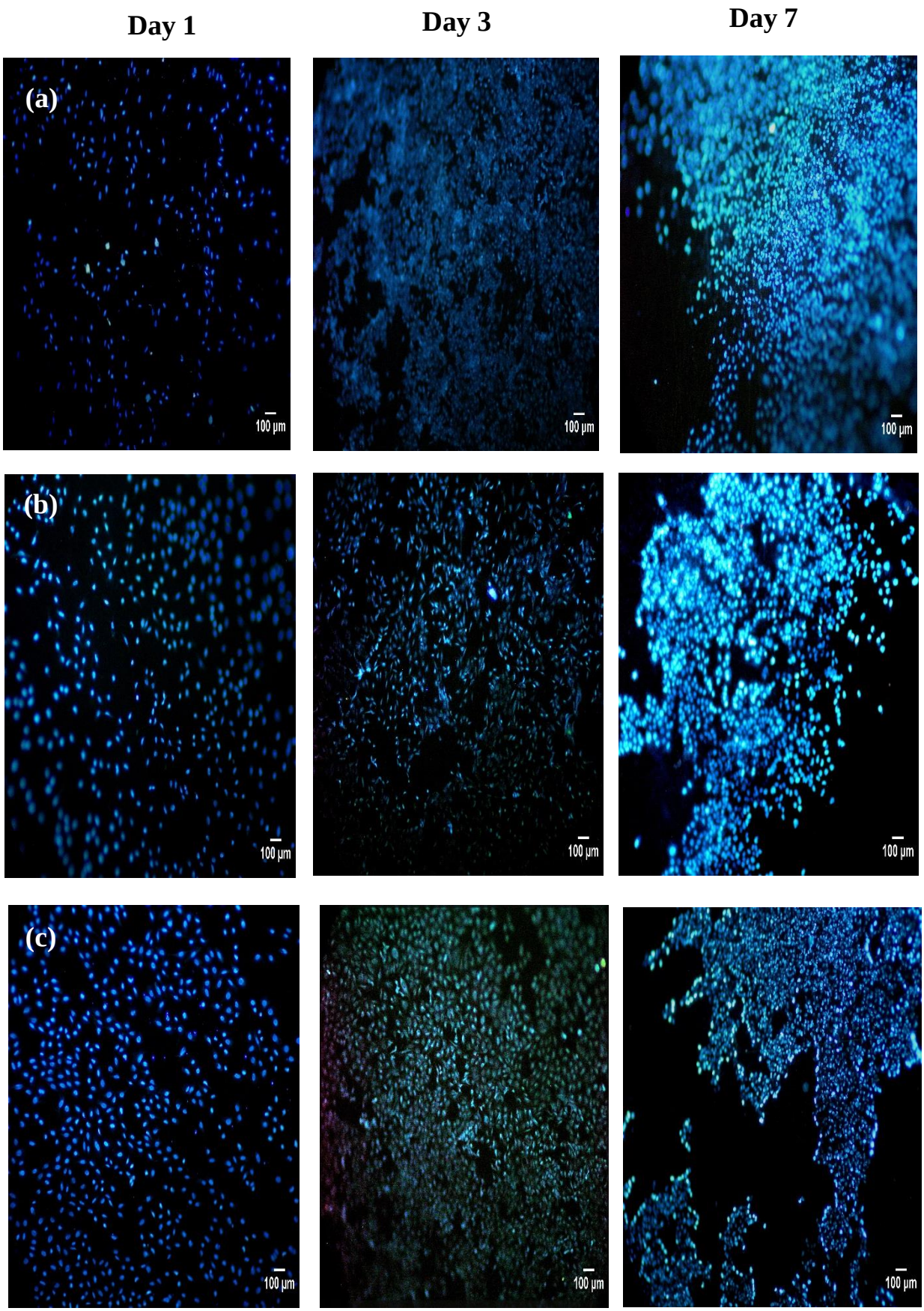

Figure 6.4 Fluorescence images of DAPI stained U-2 OS cells (x10 objective lens) on (a) Ti, (b) 24eTi and (c) PolyTi250 surfaces at days 1,3 and 7

6.2.5 SEM Imaging of Adhered Cells

SEM images at days 1, 3 and 7 for adhered U-2 OS cells on (a) Ti, (b) 24eTi and (c) PolyTi250 surfaces are presented in Figure 6.5. The cells on the Ti substrates at day 1 are primarily concentrated towards the centre of the image and comprise a mixture of both flattened and rounded morphologies, with rounded cells appearing to be more commonly present. Filopodia can be seen spreading from the cells to the substrate surface. In comparison, cells on the 24eTi sample are generally flatter in the centre of the image with a few rounded cells observed towards the periphery. The cells on this etched sample also show filopodia spreading to the surface as well as indications of cell elongation. The PolyTi250 substrate appears to have fewer cells present across the surface with the majority that are present located in the centre. There appears to be a greater number of rounded cells present on this substrate with more spacing between them as compared to others, although some cell flattening is also observed here. At day 3, the cells present on all of the surfaces have primarily a flattened morphology with less evidence of any with a rounded shape being observed. The amount of lamellipodia and filopodia present has increased significantly in all cases with indications of cell elongation across substantial regions of the surfaces with some areas where the commencement of cell splitting is occurring. Although the cell numbers present on the 24eTi sample at day 3 appear to be lower than that for the Ti sample, there are areas of visible cell ‘clumping’ on this surface. The cell numbers on PolyTi250 appear to be higher than those on both the Ti and 24eTi and are primarily found in the centre, with only a few cells migrating towards the edges when compared to the other two samples. The flattened cells in the centre of the sample are closely packed with filopodia emanating from these cells to the surface. At day 7, all three substrates show a further increase in cell numbers as well as more cell spreading and increased filopodia. The Ti samples show an increase in the number of rounded cells present with some areas of cells raised off the surface evident here. Cell stretching and elongation, as well as stretching of the filopodia is also evident. Similar types of cell morphology are present on 24eTi, although there appears to be more areas of empty space observed between them when compared to the Ti control. The flattened and clumped cells present here are mainly in the centre with more rounded cells migrating outwards from the centre to the edges. Once again, cell elongation and stretching is observed, as well as an increased presence of stretched filopodia. The PolyTi250 substrate follows a similar pattern to that seen for both the Ti and 24eTi samples with areas of cell ‘clumping’ spreading outwards from the centre of the sample. Filopodia are once again present with cell stretching and elongating observed and have lamellipodia stretching from cell to cell.

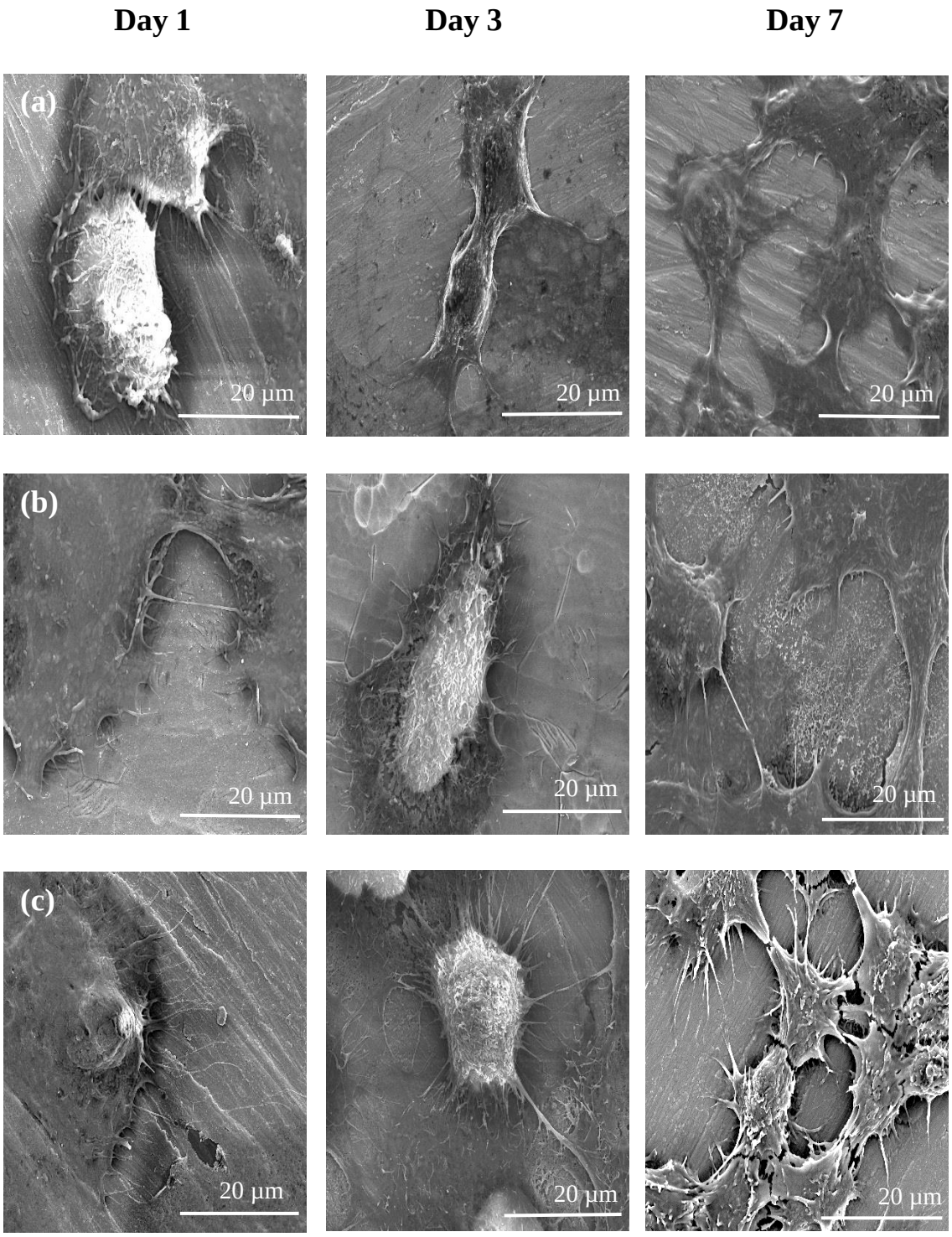

Figure 6.5 SEM planar view images (x 2.5k magnification) for fixed U-2 OS cells on (a) Ti, (b) 24eTi and (c) PolyTi250 substrates at days 1, 3 and 7

6.3 Cell Study B – Day 3 Evaluation of Calcium Phosphate Coated Substrates

As previously described, Cell Study B evaluates cell response of sputter coated CaP (HA and SrHA) on the various titanium substrates at day 3. An MTT assay of cell metabolic activity, a PicoGreen™ DNA quantification assay, DAPI cell nuclei staining and SEM imaging of adhered cells have once again been performed. The key objective here is to understand how U-2 OS cells respond to these bioactive coatings on Ti, 24eTi and PolyTi250 substrate surface morphologies. As well as providing a comparison between the uncoated and coated substrates, differences between cell response to the HA and SrHA coating chemistries were assessed.

6.3.1 Cellular Metabolic Activity

The MTT assay data for U-2 OS cells exposed to TiHA, 24eTiHA and PolyTi250HA substrate surfaces at day 3 are shown in Figure 6.6. As before, the absorbance data provides an indication of the viability of the cells as a measure of their metabolic activity. The results show that there is no statistically significant difference between the absorbance values for cells on TiHA when compared to 24eTiHA ($P = 0.8451$), nor is there any statistically significant difference when the value for TiHA is compared to that for PolyTi250HA ($P = 0.6335$). In addition, there is no statistically significant difference when 24eTiHA is compared to PolyTi250HA ($P > 0.9999$). When comparing the HA coated samples to the uncoated samples there is no statistically significant difference between Ti and TiHA ($P = 0.3287$), 24eTiHA ($P = 0.9943$) or PolyTi250HA ($P = 0.9999$). However, there is a statistically significant difference in the values for 24eTiHA when compared to 24eTi ($P < 0.0001$ = ****) with the higher absorbance measured for the uncoated substrate. In addition, when comparing the PolyTi250 with the PolyTi250HA there is also a statistically significant difference ($P < 0.0001$ = ****) with the uncoated substrate once again having an increased absorbance value

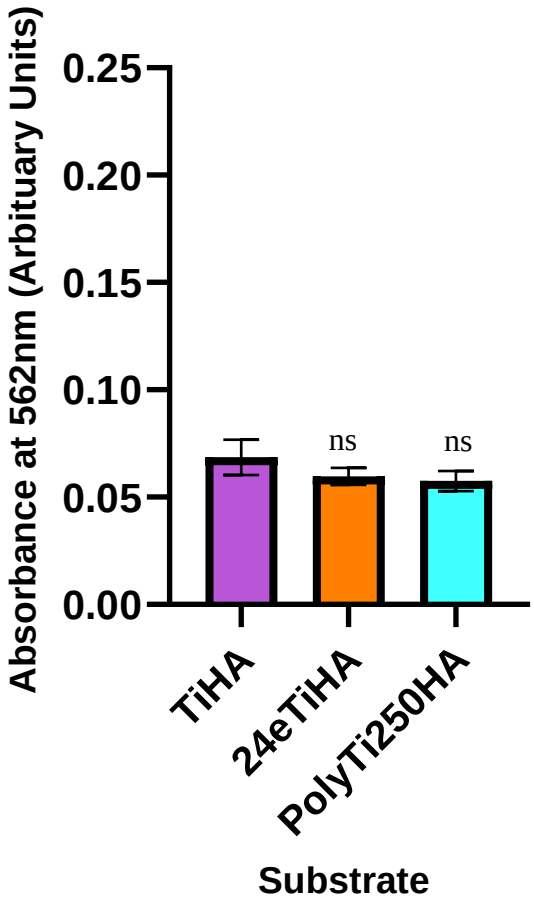

*Figure 6.6 MTT absorbance value for U-2 OS cells cultured on HA coated substrates at day 3 with statistically significant difference (P > 0.05 = ns, P < 0.05 = *, P < 0.01 = **, P < 0.001 = *** and P < 0.0001 = ****) for 24eTiHA and PolyTi250HA when compared to TiHA*

Figure 6.7 shows the results obtained from the MTT assay of U-2 OS cells exposed to TiSrHA, 24eTiSrHA and PolyTi250SrHA substrate surfaces. Once again, there is no statistically significant difference between the absorbance values for cells on TiSrHA when compared to those on 24eTiSrHA ($P = 0.5538$). Likewise, no statistically significant difference is observed when TiSrHA is compared to PolyTi250SrHA ($P = 0.9659$) nor between 24eTiSrHA and PolyTi250SrHA ($P = 0.9950$). On comparing the SrHA coated substrates to that of the uncoated substrates at day 3, there is no statistically significant difference when Ti is compared to TiSrHA ($P = 0.7984$), 24eTiSrHA ($P > 0.9999$) or PolyTi250HA ($P > 0.9999$). However, when 24eTi is compared to 24eTiSrHA there is a statistically significant difference ($P < 0.0001$ = ****) with the higher result obtained for the 24eTi substrate. Comparing PolyTi250 with PolyTi250SrHA gives a statistically significant difference ($P < 0.0001$ = ****) with the higher result obtained for the PolyTi250 substrate.

There is a statistically significant difference ($P < 0.01$ = **) between TiHA and TiSrHA, with the higher result obtained for the TiHA substrate value. There is no statistically significant difference between TiHA and 24eTiSrHA ($P = 0.5153$) or PolyTi250SrHA ($P = 0.1029$). Comparison of 24eTiHA with 24eTiSrHA shows no statistically significant difference ($P = 0.9998$), nor is there a statistically significant difference between PolyTi250HA and PolyTi250SrHA ($P = 0.9015$). Albeit, in general there is no statistically significant difference between the HA and SrHA coated samples when compared to their uncoated counterpart but the TiSrHA samples exhibited the lowest absorbance values when compared to all the other samples. Both the HA and SrHA coated substrates gave absorbance values similar to those for the native Ti, 24eTi and PolyTi250 surfaces at day 1 (Figure 6.1) suggesting that at day 3, the cells on HA and SrHA coated surfaces are responding at a similar rate to that of their uncoated counterpart.

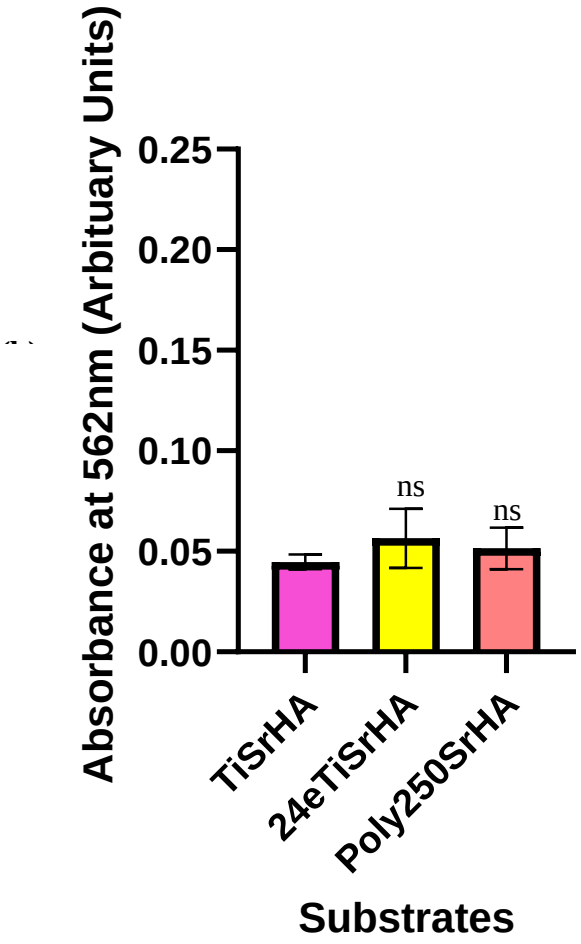

*Figure 6.7 MTT absorbance values for U-2 OS cells cultured on SrHA coated surfaces at day 3 with statistically significant difference (P > 0.05= ns, P < 0.05 = *, P < 0.01 = **, P < 0.001 = *** and P < 0.0001 = ****) for 24eTiSrHA and PolyTi250SrHA when compared to TiSrHA*

6.3.2 DNA Quantification

Figure 6.8 shows the DNA quantification data obtained from U-2 OS cells cultured on each of the HA coated substrates at day 3, with the concentrations given in nanograms per millilitre (ng/ml), along with measurements previously obtained for their uncoated counterparts for direct comparison. The values for TiHA show no statistically significant difference when compared to 24eTiHA (P = 0.9948) or PolyTi250HA (P = 0.0731) substrates. When comparing 24eTiHA to PolyTi250HA a statistically significant difference (P < 0.01 = **) is obtained with the higher DNA concentration measured for the 24eTiHA substrate. Despite there being no statistically significant difference between PolyTi250HA and TiHA, the former exhibited the lowest DNA concentration measurements, with 24eTiHA showing the highest values. Comparing the HA coated samples with their uncoated counterpart indicates a statistically significant difference between Ti and TiHA (P < 0.001 = ***), 24eTiHA (P < 0.01 = **) and PolyTi250HA (P < 0.0001 = ****) with the uncoated Ti having higher concentration values.

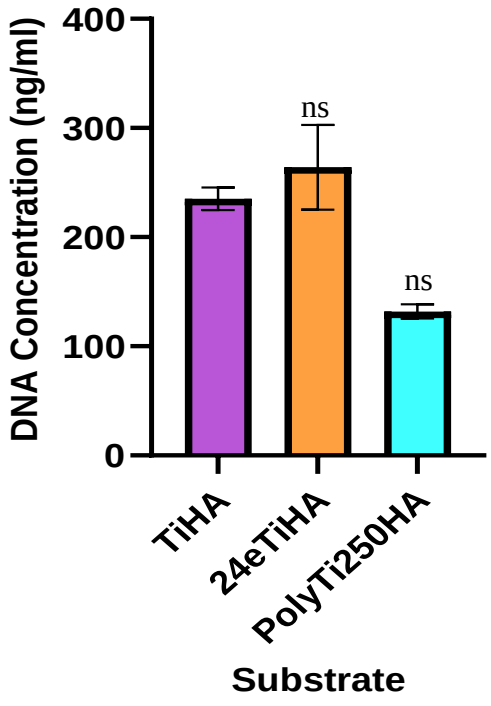

*Figure 6.8 DNA concentration values for U-2 OS cells cultured on HA coated substrates at day 3 with significant difference (P > 0.05 = ns, P < 0.05 = *, P < 0.01 = **, P < 0.001 = *** and P < 0.0001 = ****) for 24eTiHA and Polyi250HA when compared to TiHA*

Figure 6.9 displays the DNA concentration measurements for the TiSrHA, 24eTiSrHA and PolyTi250SrHA coated substrates at day 3 along with measurements previously obtained for their uncoated counterparts for direct comparison. There is a statistically significant difference between the values for TiSrHA when compared to 24eTiSrHA ($P < 0.0001$ = ****) but no statistically significant difference for TiSrHA when compared to PolyTi250SrHA ($P = 0.3826$). However, there is a statistically significant difference when 24eTiSrHA is compared with PolyTi250SrHA ($P < 0.0001$ = ****). The DNA concentration for the SrHA coated samples compared to that for the uncoated samples at day 3 show no statistically significant difference between Ti and TiSrHA ($P = 0.1414$), or PolyTi250SrHA ($P = 0.9999$). However, a statistically significant difference is observed when Ti is compared to 24eTiSrHA ($P < 0.0001$ = ****). When comparing 24eTi to 24eTiSrHA there is a statistically significant difference ($P < 0.01$ = **) with 24eTi exhibiting the higher value. In addition, comparison of PolyTi250 and PolyTi250SrHA gives a statistically significant difference ($P < 0.0001$ = ****) with the PolyTi250 having the highest value.

Comparing TiHA to TiSrHA shows a statistically significant difference ($P < 0.0001$ = ****) with TiSrHA giving the higher value. There are also statistically significant differences when comparing TiHA with 24eTiSrHA ($P < 0.05$ = *) and PolyTi250SrHA ($P < 0.0001$ = ****). In addition, comparison of 24eTi with 24eTiSrHA gives a statistically significant difference ($P < 0.01$ = **), and 24eTi gives a statistically significant difference when compared to PolyTi250SrHA ($P < 0.001$ = ***), with the uncoated etched substrate giving the higher value in both cases. Although the highest values appear to come from TiSrHA and PolyTi250SrHA, there is no statistically significant difference for these substrates when compared to that of the Ti control. The 24eTiSrHA substrates presents the lowest DNA concentration at day 3, with no statistically significant difference ($P > 0.05$) when compared to the PolyTi250HA substrate.

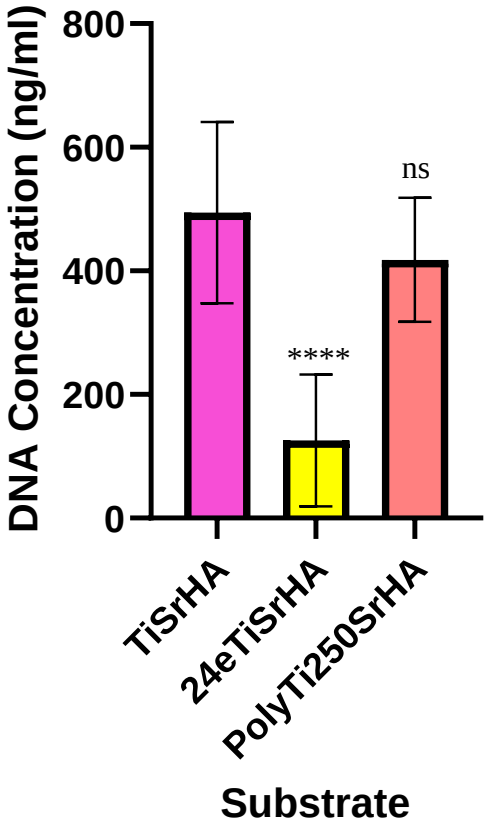

*Figure 6.9 DNA concentration values for U-2 OS cells cultured on SrHA coated substrates at day 3 with statistically significant difference (P > 0.05 = ns, P < 0.05 = *, P < 0.01 = **, P < 0.001 = *** and P < 0.0001 = ****) for 24eTiSrHA and PolyTi250SrHA when compared to TiSrHA*

6.3.3 Metabolic Activity Normalised to DNA Concentration

As stated previously in Chapter 6.2.3, the MTT data collected for HA and SrHA coated samples at day 3 was normalised using the DNA concentration to allow a clearer visualisation of the cellular metabolic rate according to the cell density present at the timepoint. Figure 6.10 displays the normalised data for HA coated samples. No significant difference ($P > 0.05$) is noted when comparing the 24eTiHA and PolyTi250HA to TiHA, as well as when comparing the 24eTiHA with PolyTi250HA. Comparing the HA coated substrates to their uncoated counterparts, no significant difference ($P > 0.05$) is calculated at day 3 for any of the substrates.

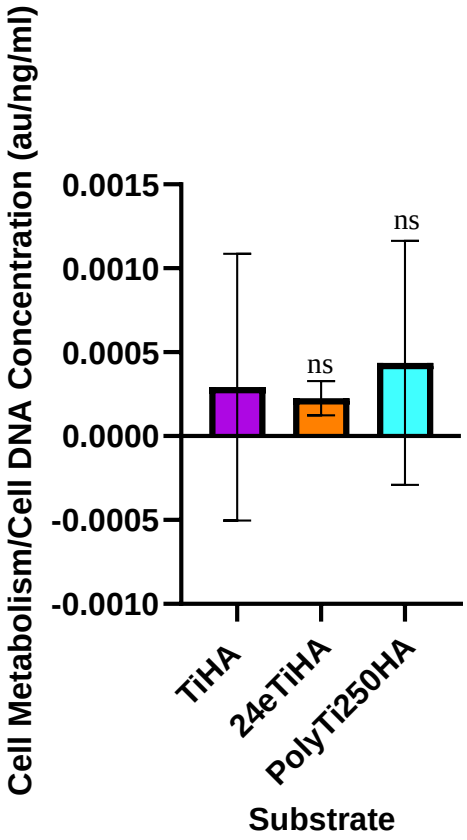

*Figure 6.10 Normalised cell metabolism to DNA concentration values for U-2 OS cells cultured on HA coated substrates at day 3 with significant difference (P > 0.05 = ns, P < 0.05 = *, P < 0.01 = **, P < 0.001 = *** and P < 0.0001 = ****) for 24eTiHA and Polyi250HA when compared to TiHA*

Figure 6.11 displays the normalised data for the SrHA coated samples. There is a significant difference (P < 0.05 = *) when comparing the 24eTiSrHA samples with the TiSrHA but no significant difference (P > 0.05) when comparing PolyTi250SrHA with the TiSrHA samples. No significant difference is calculated between 24eTiSrHA and PoluYi250SrHA samples. No significant differences (P > 0.05) are calculated when the uncoated substrates are compared to the SrHA coated substrates. When comparing the SrHA to their HA counterparts there is a significant difference (P < 0.001 = ***) when comparing the TiHA and TiSrHA samples. No significant difference (P > 0.05) is calculated between 24eTiAH and 24eTiSrHA samples. PolyTi250HA compared to PolyTi250SrHA gives a significant difference (P < 0.05 = *).

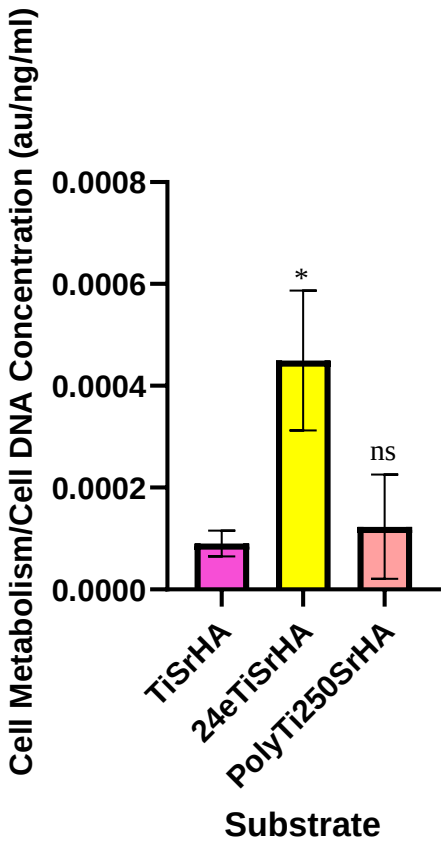

*Figure 6.11 Normalised cell metabolism to DNA concentration values for U-2 OS cells cultured on SrHA coated substrates at day 3 with statistically significant difference (P > 0.05 = ns, P < 0.05 = *, P < 0.01 = **, P < 0.001 = *** and P < 0.0001 = ****) for 24eTiSrHA and PolyTi250SrHA when compared to TiSrHA*

6.3.4 Cell Nuclei Staining using DAPI

Figure 6.11 shows DAPI stained U-2 OS cell nuclei on (a) TiHA, (b) 24eTiHA and (c) PolyTi250HA surfaces at day 3. All these substrates clearly show a high level of blue staining across the surface, thereby indicating the presence of a high number of cells. Visually the 24eTiHA samples show an elevated cell amount with little spacing when compared to that for PolyTi250HA and TiHA. The positive cell response indicated here is consistent with the MTT and DNA data reported previously. After 3 days in culture the average number of cells per cm^2 was measured using ImageJ to count pixels and produce histograms for all samples. Cell numbers on TiHA was calculated as 43.16 ± 9.72, with both 24eTiHA (80.05 ± 11.28) and PolyTi250HA (65.58 ± 14.53) eliciting higher cell coverage values and 24eTiHA showing the highest coverage across the surface. When using the ImageJ cell counter plugin, cell numbers display the same trend, with HA coated samples presenting the higher coverage. Cell numbers for TiHA at day 3 were averaged at 1779 ± 416.50, with 24eTiHA (2727.17 ± 493.59) and PolyTi250HA (2639 ± 709.65) eliciting higher cell counts.

The DAPI staining of U-2 OS nuclei on SrHA coated substrates is presented in Figure 6.12. Both the 24eTiSrHA and PolyTi250SrHA substrates have the lowest cell coverage when compared to TiSrHA. On comparing to the HA substrates (Figure 6.11) there is a substantial difference in cell nuclei numbers with considerable decline on SrHA substrates. The average cell coverage measurements (cells/cm^2) after 3 days in culture were 3.53 ± 3.80 for TiSrHA, 0.81 ± 0.89 for 24eTiSrHA and 0.69 ± 0.50 for PolyTi250SrHA. Using the ImageJ cell counter plugin, cell numbers for SrHA coated samples again display the same trend, with TiSrHA having the highest coverage (87.17 ± 113.31). Cell numbers for 24eTiSrHA at day 3 were averaged at 32 ± 47.24 and PolyTi250HA averaged at 10.67 ± 9.22.

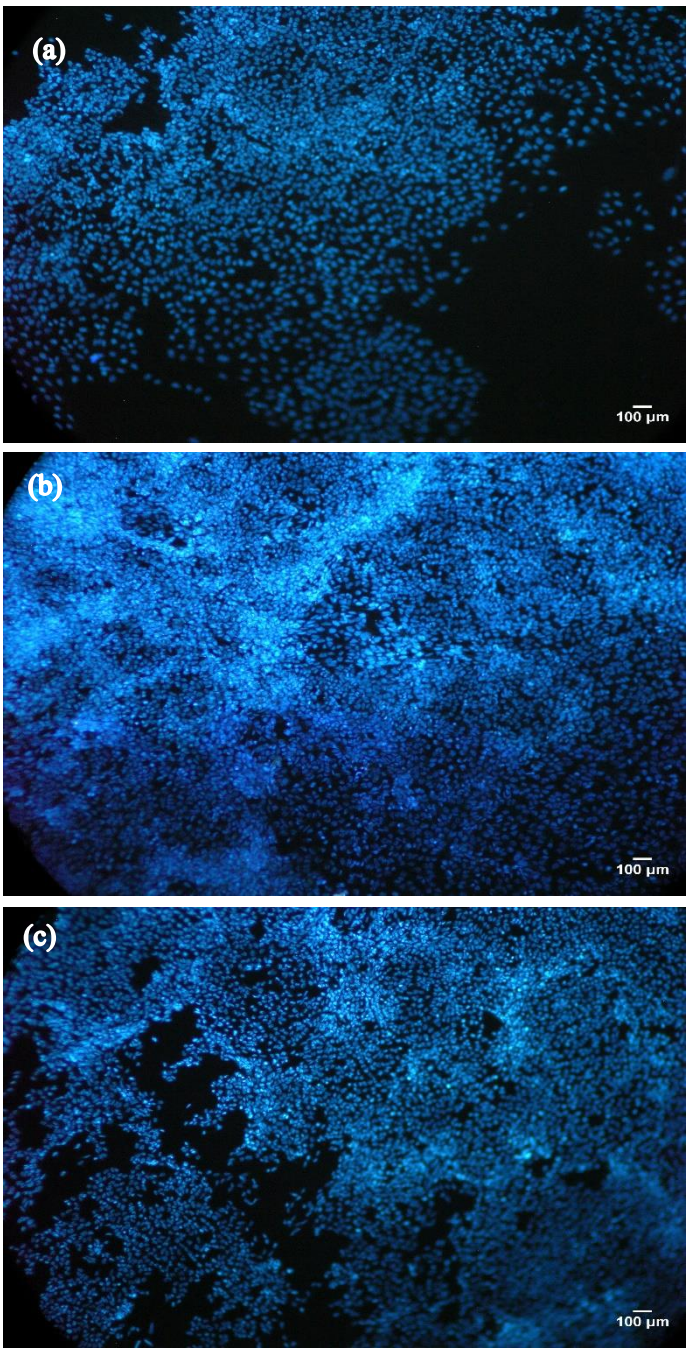

Figure 6.11 Fluorescence images of DAPI stained U-2 OS cells on (a) TiHA, (b) 24eTiHA and (c) PolyTi250HA surfaces at day 3

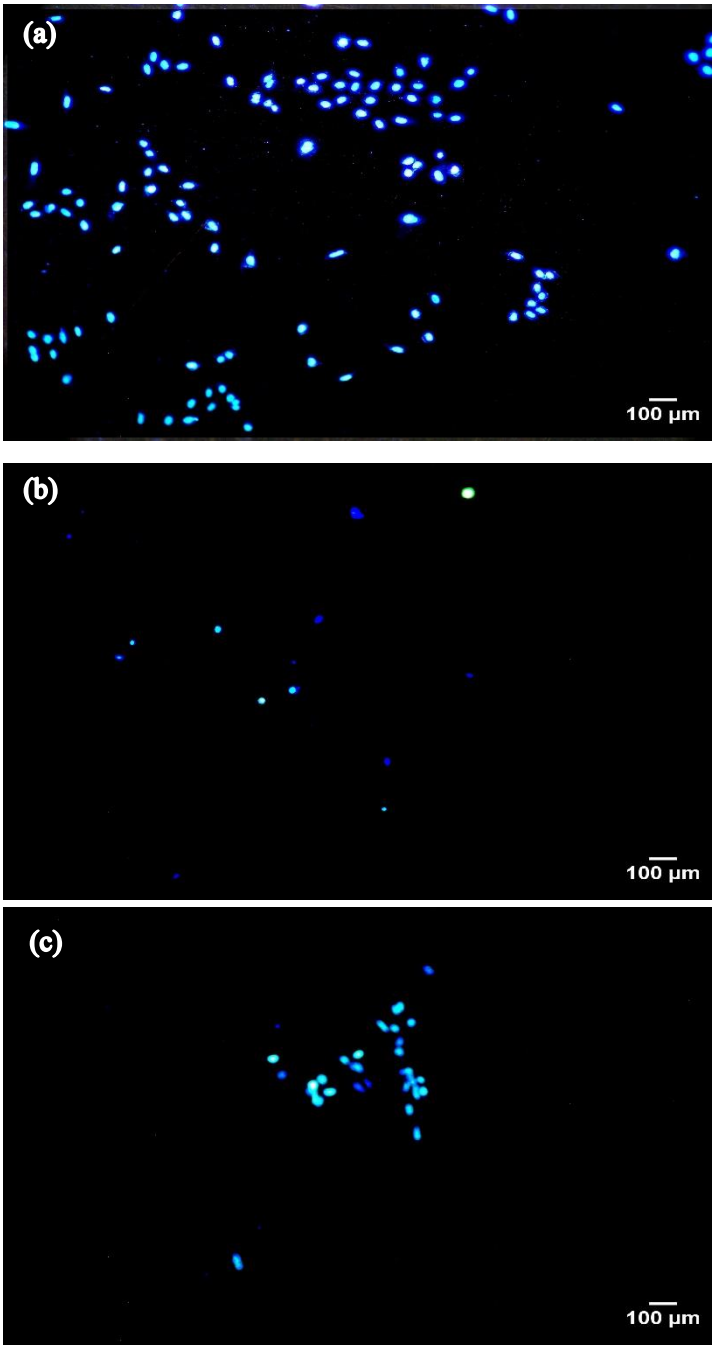

Figure 6.12 Fluorescence images of DAPI stained U-2 OS cells on (a) TiSrHA, (b) 24eTiSrHA and (c) PolyTi250SrHA surfaces at day 3

6.3.5 SEM Imaging of Adhered Cells

SEM images obtained for U-2 OS cells on (a) TiHA, (b) 24eTiHA and (c) PolyTi250HA at day 3 are presented in Figure 6.13. The HA coated substrates show an abundance of cells across the surfaces. The cells observed on the TiHA substrate are spread across the sample surface and comprise a mixture of both flattened and rounded morphologies. There are some lamellipodia between cells and filopodia reaching from the cells onto the substrate surface. By comparison, cells on 24eTiHA are generally more flattened and concentrated in the centre of the image with a few rounded cell bodies observed towards the periphery. This sample also shows lamellipodia and filopodia spreading from cell to cell and onto the coated surface with some cell stretching visible. By comparison, the PolyTi250HA substrate appears to have fewer flattened cells across the surface, with the majority having a more rounded cell body morphology. There are lamellipodia and filopodia present, with some areas of cell clumping visible.

SEM images of U-2 OS cells on (a) TiSrHA, (b) 24eTiSrHA and (c) PolyTi250SrHA at day 3 are presented in Figure 6.14. In general, when comparing the SrHA coated substrates with those for their equivalent HA coated counterparts there are notably less cells present across all surfaces which is consistent with the findings from the DAPI stained nuclei images (Figure 6.12). At day 3, cells on TiSrHA are concentrated towards the edges of the substrate and comprise a mixture of both flattened and rounded morphologies with pronounced cell bodies. Filopodia and cell stretching are visible. The cells on 24eTiSrHA are more sparsely distributed and fewer in number in comparison to TiSrHA. The cells are more round in shape, concentrated towards the substrate edges and filopodia are present. The cells on PolyTi250SrHA are spread across the substrate. Once again, more cells are concentrated at the substrate edges. The cells are round and flat in shape, and lamellipodia and filopodia are visible.

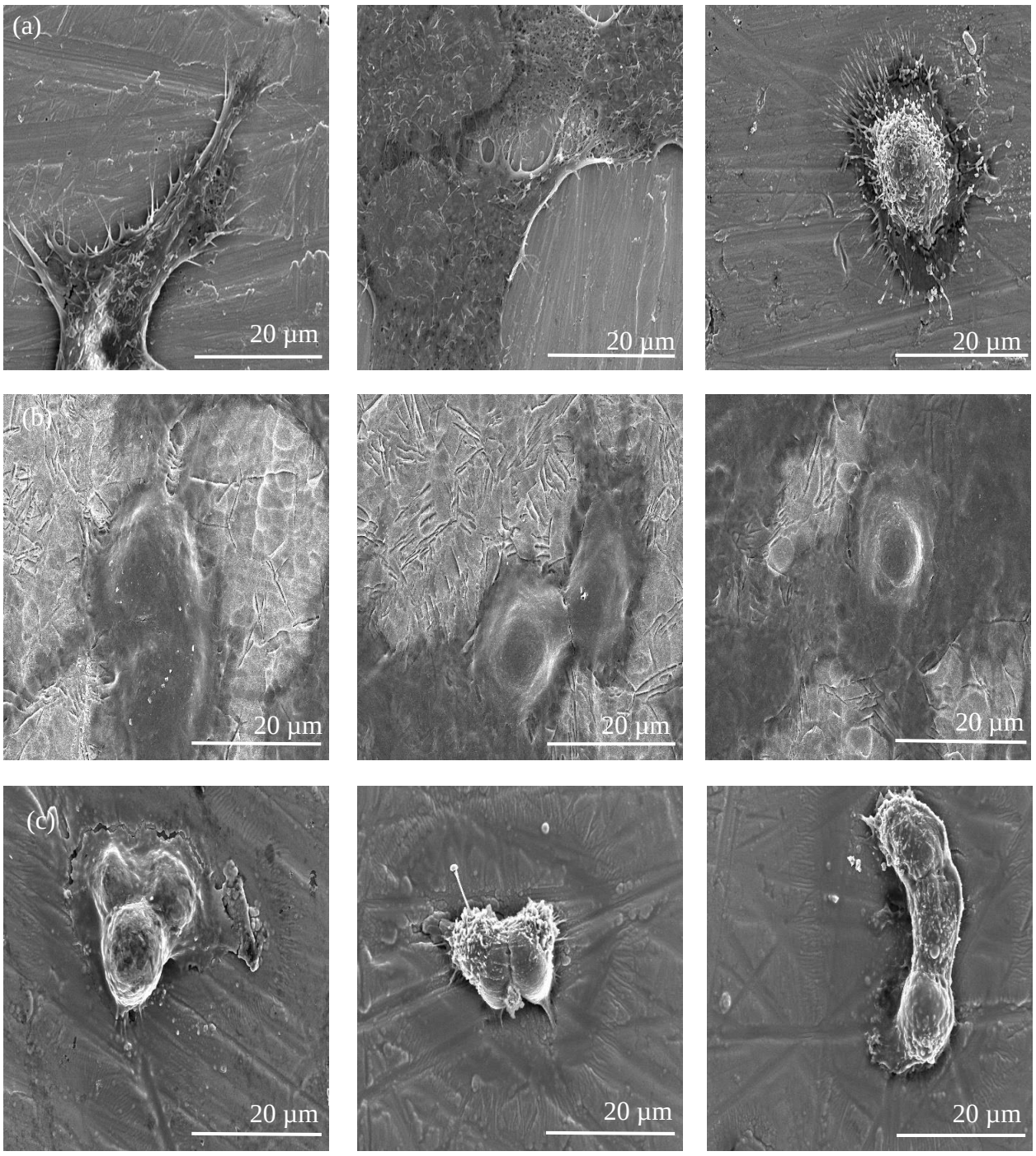

Figure 6.13 SEM planar view images (x 2.5k magnification) for U-2 OS cells on (a) TiHA, (b) 24eTiHA and (c) PolyTi250HA surfaces at day 3

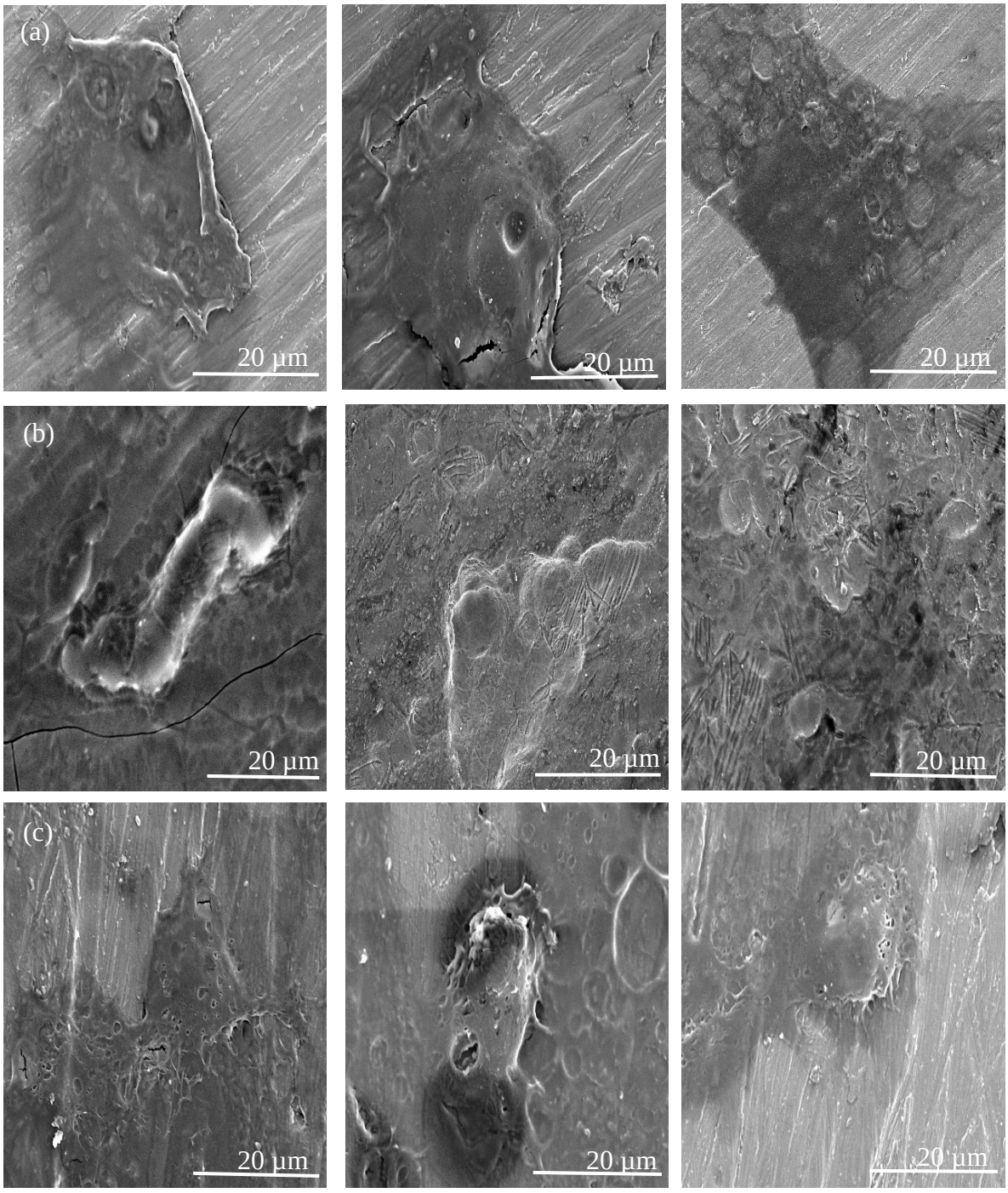

Figure 6.14 SEM planar view images (x 2.5k magnification) for fixed U-2 OS cells on (a) TiSrHA, (b) 24eTiSrHA and (c) PolyTi250SrHA surfaces at day 3

6.4 Cell Study C (28-day Evaluation CaP Coated Titanium Substrates)

As described previously in Chapter 3.5.6 and 3.5.7, measurements from ALP and BCA total protein content assays were obtained from U-2 OS cells cultured on both HA and SrHA coated 24eTi, Ti and PolyTi250 substrates over 28 days. Figure 6.15 shows ALP concentrations from U-2 OS cells cultured on HA coated substrates over 28 days in nanograms per millilitre (ng/ml). These data suggest that at day 7 cells on TiHA express higher ALP than those of the other HA coated substrates, with 24eTiHA and PolyTi250HA eliciting a similar response to one another. An increasing trend in the values exists from day 7, to 21 and then measurements decrease for all substrates at day 28 to measurements similar to those at day 14. On comparing TiHA to 24eTiHA, there is no statistically significant difference at day 7 ($P = 0.9979$), day 14 ($P = 0.9831$), day 21 ($P > 0.9999$) or day 28 ($P = 0.6821$). The same outcome exists on comparing TiHA with PolyTi250HA at day 7 ($P = 0.7726$), day 14 ($P = 0.9702$), day 21 ($P = 0.9994$) and day 28 ($P = 0.4196$). Finally, there is no statistically significant difference found between 24eTiHA and PolyTi250HA: day 7 ($P = 0.9507$), day 14 ($P = 0.6836$), day 21 ($P > 0.9999$) and day 28 ($P = 0.9977$).

Figure 6.16 shows the ALP concentrations from U-2 OS cells cultured on SrHA coated substrates over 28 days in ng/ml. Both TiSrHA and PolyTi250SrHA show a general increase in ALP concentration from day 7 to 21 before the value decreases at day 28. However, while 24eTiSrHA shows elevated concentrations at day 7 and 14, they decrease at day 21 and 28 to concentrations lower than those for TiSrHA and PolyTi250SrHA at the same timepoints. There is no statistically significant difference between TiSrHA and 24eTiSrHA at day 7 ($P = 0.7417$) and 14 ($P > 0.9999$). After 21 days, there is a decrease in the concentration for 24eTiSrHA ($P < 0.01$ = **), and a further decrease after 28 days ($P < 0.001$ = ***). There is no statistically significant difference between TiSrHA and PolyTi250SrHA at day 7 ($P = 0.9616$), day 14 ($P > 0.9999$) or day 21 ($P = 0.7344$). However, after 28 days there is a statistically significant difference between these substrates ($P < 0.05$ = *). There is no significant difference between 24eTiSrHA and PolyTi250SrHA at day 7,14, 21 and 28 ($P = 0.2400$, $P = 0.9997$, $P = 0.1541$ and $P = 0.8893$, respectively).

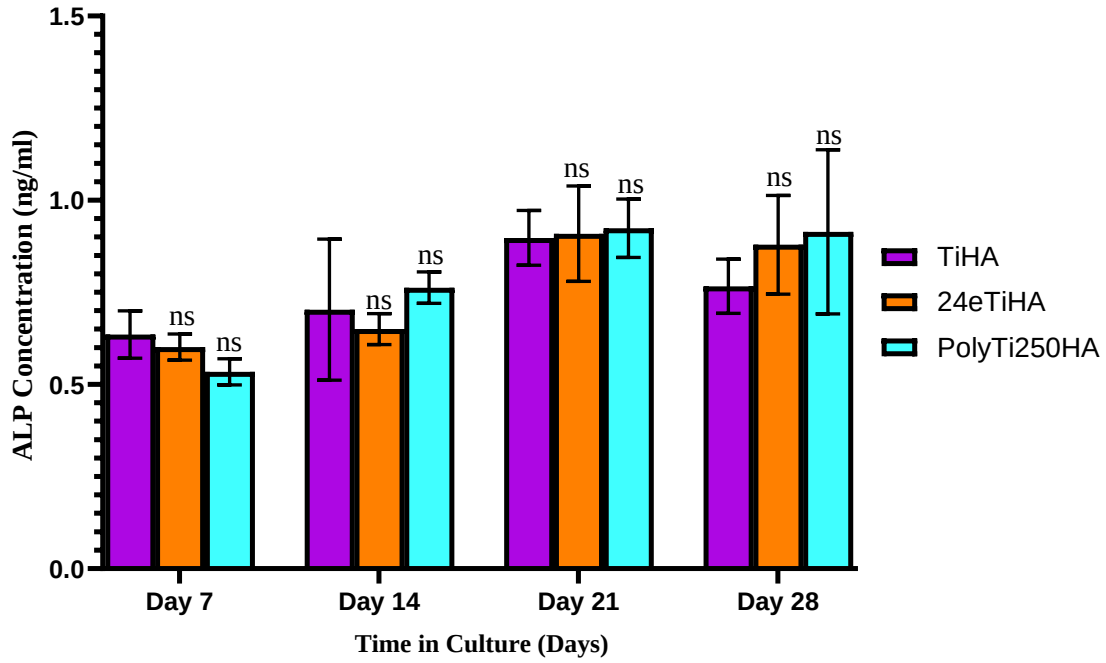

*Figure 6.15 ALP concentrations for U-2 OS cells after 7, 14, 21 and 28 days in culture with HA coated titanium substrates showing significant difference (P > 0.05 = ns, P < 0.05 = *, P < 0.01 = **, P < 0.001 = *** and P < 0.0001 = ****) for 24eTiHA and PolyTi250HA when compared to TiHA*

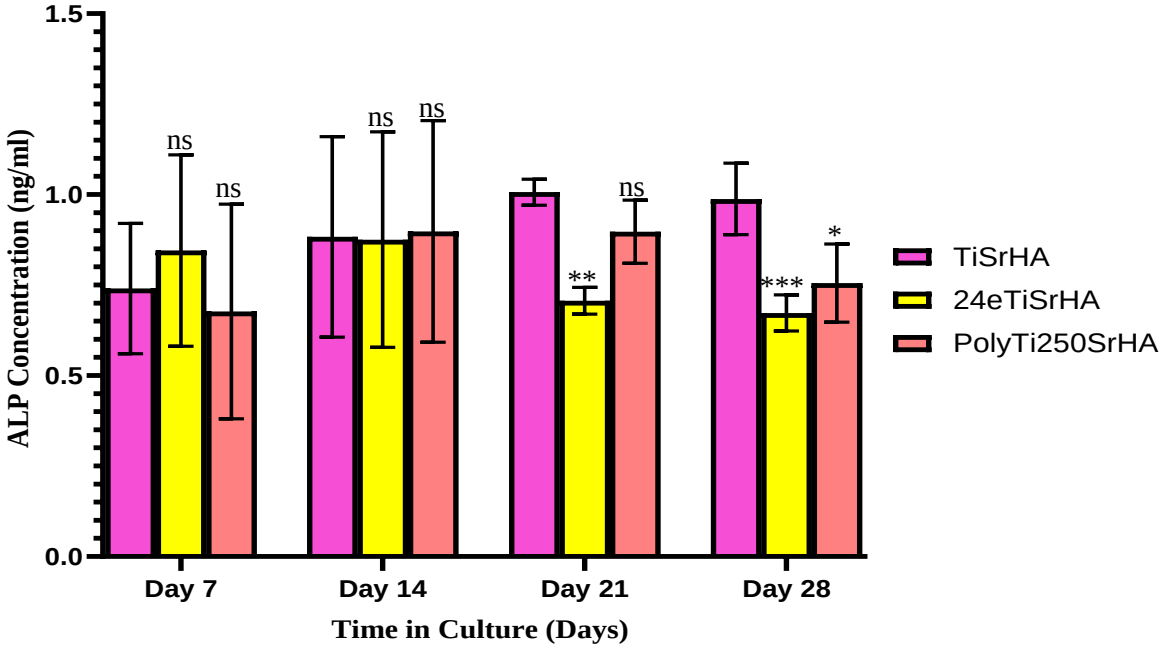

*Figure 6.16 ALP concentrations for U-2 OS cells after 7, 14, 21 and 28 days in culture with SrHA coated titanium substrates showing significant difference (P > 0.05 = ns, P < 0.05 = *, P < 0.01 = **, P < 0.001 = *** and P < 0.0001 = ****) for 24eTiSrHA and PolyTi250SrHA when compared to TiSrHA*

Comparing the ALP measurements from cells cultured on SrHA coated substrates to those for TiHA, there is no statistically significant difference at days 7, 14 and 21 ($P = 0.7428$, $P = 0.1771$ and $P = 0.7122$, respectively). After 28 days in culture, there is a statistically significant difference ($P < 0.05 = *$) between the values for these samples, with the TiSrHA displaying the highest value. Although the average ALP values for 24eTiSrHA at days 7 and 14 are higher than those for TiHA, there is no statistically significant difference at these or subsequent 21-day and 28-day time points. Comparing the TiHA and PolyTi250SrHA indicates no statistically significant difference across any of the four timepoints. In the case of the 24eTiHA and 24eTiSrHA, there is a statistically significant difference at days 7 and 14 ($P < 0.05 = *$ in each case) but no statistically significant difference between these samples at day 21 and day 28, despite a higher value being recorded from the cells on the 24eTiHA at these later time points. Finally, no statistically significant difference was found for ALP values from cells at any of the timepoints when comparing PolyTi250HA and PolyTi250SrHA.

Figure 6.17 displays the BCA whole cell protein concentration values measured from U-2 OS cells cultured on HA coated samples at each of the four timepoints over the 28-day period in micrograms per millilitre (µg/ml). All of the HA coated samples show a general increase in BCA across each timepoint, with PolyTi250HA displaying the highest increase from day 7 to day 28. No statistically significant difference is seen between TiHA and 24eTiHA across days 7,14, 21 and 28 despite TiHA seeming to have a higher value. A lack of statistically significant difference is also observed when comparing TiHA and PolyTi250HA samples at days 7,14 and 21. However, at the 28-day time point the difference in the BCA measurements is now statistically significant ($P < 0.0001 = ****$) with the PolyTi250HA showing a pronounced increase in total cell protein concentration. Similarly, when comparing 24eTiHA to PolyTi250HA, there is no statistically significant difference until day 28 ($P < 0.001 = ***$) with PolyTi250HA again having the higher value.

The corresponding BCA assay data for the SrHA coated substrates across the 28-day study are presented in Figure 6.18. All SrHA coated substrates display an increase from day 7 to day 28, with 24eTiSrHA samples showing the lowest values across all four time points. The TiSrHA samples elicit the highest values after the 28-days in culture. After 7-days in culture there is no statistically significant difference between the BCA values for TiSrHA and 24eTiSrHA nor between the TiSrHA and PolyTi250SrHA. A statistically significant difference ($P < 0.05 = *$) is seen between TiSrHA and 24eTiSrHA at day 14 with TiSrHA having the higher concentration. However, there is no significant

difference between the values for TiSrHA and PolyTi250SrHA at any time point. There is a statistically significant difference between TiSrHA and 24eTiSrHA at day 21 (P < 0.0001 = ****) only, but TiSrHA and PolyTi250SrHA exhibit no statistically significant differences at any time point. At day 28, the statistically significant difference between the TiSrHA and 24eTiSrHA remains at P < 0.0001 = ****, with the 24eTiSrHA eliciting a lower concentration. There is no statistically significant difference between TiSrHA and PolyTi250SrHA. Consideration of comparison between 24eTiSrHA and PolyTi250SrHA indicates that there is no statistically significant difference at days 7 and 14, but after 21 days there is at a value of P < 0.01 = ** which then further increases to P < 0.0001 = **** at day 28.

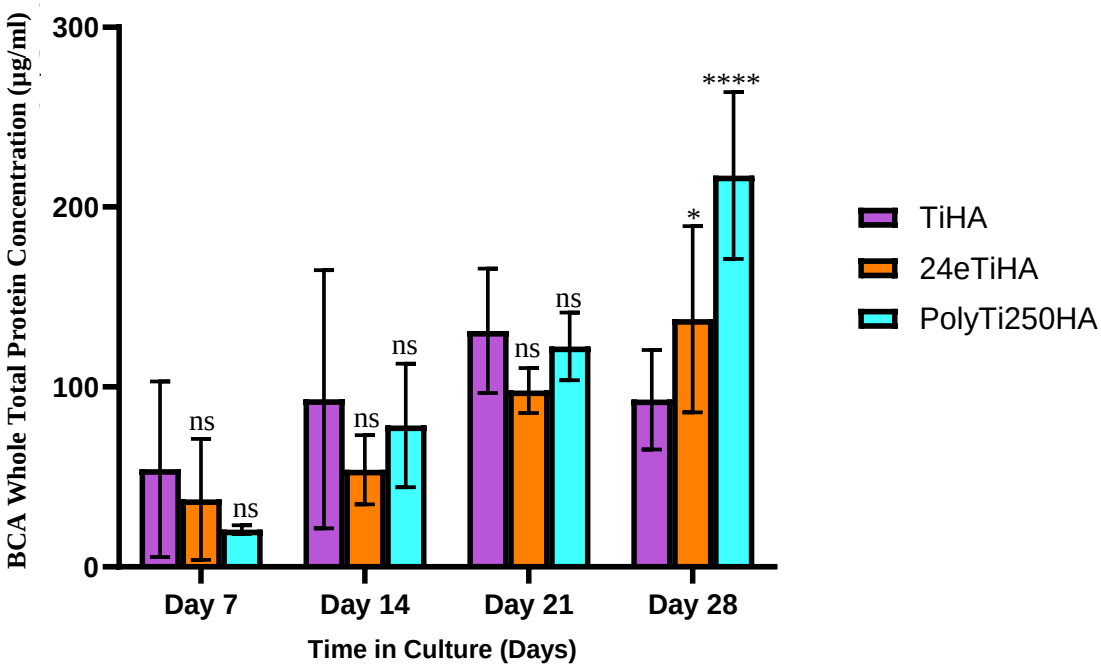

*Figure 6.17 BCA whole cell protein concentrations for U-2 OS cells after 7, 14, 21 and 28 days in culture with HA coated titanium substrates showing significant difference (P > 0.05 = ns, P < 0.05 = *, P < 0.01 = **, P < 0.001 = *** and P < 0.0001 = ****) for 24eTiHA and PolyTi250HA when compared to TiHA*

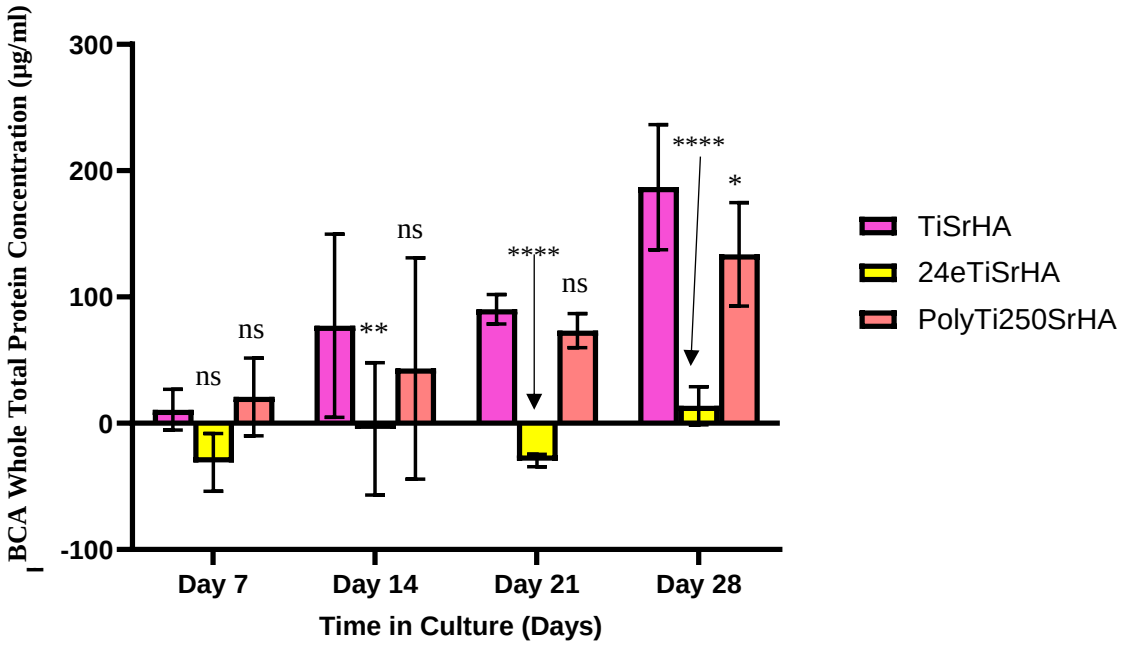

*Figure 6.18 BCA whole cell protein concentrations for U-2 OS cells after 7, 14, 21 and 28 days in culture with SrHA coated titanium substrates showing significant difference (P > 0.05 = ns, P < 0.05 = *, P < 0.01 = **, P < 0.001 = *** and P < 0.0001 = ****) for 24eTiSrHA and PolyTi250SrHA when compared to TiSrHA*

Comparing the BCA values from cells cultured on the TiHA and TiSrHA samples at days 7, 14 and 21 indicates that there are no significant differences (P = 0.9987, P = 0.9999 and P = 0.2466, respectively). However, after 28 days there is a statistically significant difference between the values expressed on these surfaces (P < 0.0001 = ****). In general, the TiSrHA samples have higher measured BCA values than the TiHA samples throughout the 28-day study but is only significantly different at day 28. No statistically significant difference is found between the TiHA and 24eTiSrHA at days 7 and 14, but statistically significant values are calculated at day 21 (P < 0.0001 = ****) and day 28 (P < 0.005 = ***). The TiHA and PolyTi250SrHA surfaces show no significant difference at days 7, 14 and 28. However, a statistically significant difference (P < 0.05 = *) was observed for this surface at day 21. Comparison of 24eTiHA with 24eTiSrHA shows no statistically significant difference at days 7 and 14, but at days 21 and 28 a statistically significant difference (P < 0.0001 = ****) is found for both time points. When comparing PolyTi250HA and PolyTi250SrHA, no measurable significant difference is calculated at days 7, 14 and 21 but after 28 days there is a statically significant difference between them (P < 0.0001 = ****). Although the PolyTi250HA samples show a significant increase in the value for BCA concentration, no statistically significant difference is found between it and values for the 24eTiHA and PolyTi250HA samples.

6.5 Alizarin Red Staining

Alizarin red staining of the U-2 OS cells after culturing for 28 days on the various surfaces was utilised to visualise any indication of mineralisation that might be present as a consequence of maturation. As described in Chapter 3.5.8, this technique stains areas within the cells that contain calcium, resulting in a reddish/brown colouration within optical micrographs. Cells seeded onto tissue culture plastic were also stained as a control.

As expected, no staining occurred of cells grown on the tissue culture plastic (data not shown). Figure 6.19 (a) – (i) shows the optical micrographs for stained U-2 OS cells on (a) Ti, (b) 24eTi, (c) PolyTi250, (d) TiHA, (e) 24eTiHA, (f) PolyTi250HA, (g) TiSrHA, (h) 24eTiSrHA and (i) PolyTi250SrHA samples at day 28. Clearly the Ti and 24eTi surfaces (Figure 6.19 (a) – (b)) show the greatest amount of red staining indicating the presence of substantive calcium typically associated with bone cell mineralisation. The PolyTi250 surface (Figure 6.19 (c)) has some areas of red staining from cells on the surface but it is significantly less than that seen for both Ti and 24eTi.

The TiHA and 24eTiHA samples (Figure 6.19 (d) – (f)) display dense areas of red staining which are smaller and more spread out when compared to the more localised intense red staining of cells on PolyTi250HA.

The SrHA coated samples (Figure 6.19 (g) – (i)) display the least amount of red staining across the respective surfaces. The TiSrHA samples shows staining similar to that on the pristine Ti sample with red colouration spread across the surface. The 24eTiSrHA show little to no red staining across the sample surface while the PolyTi250SrHA sample has localised areas of dense red staining.

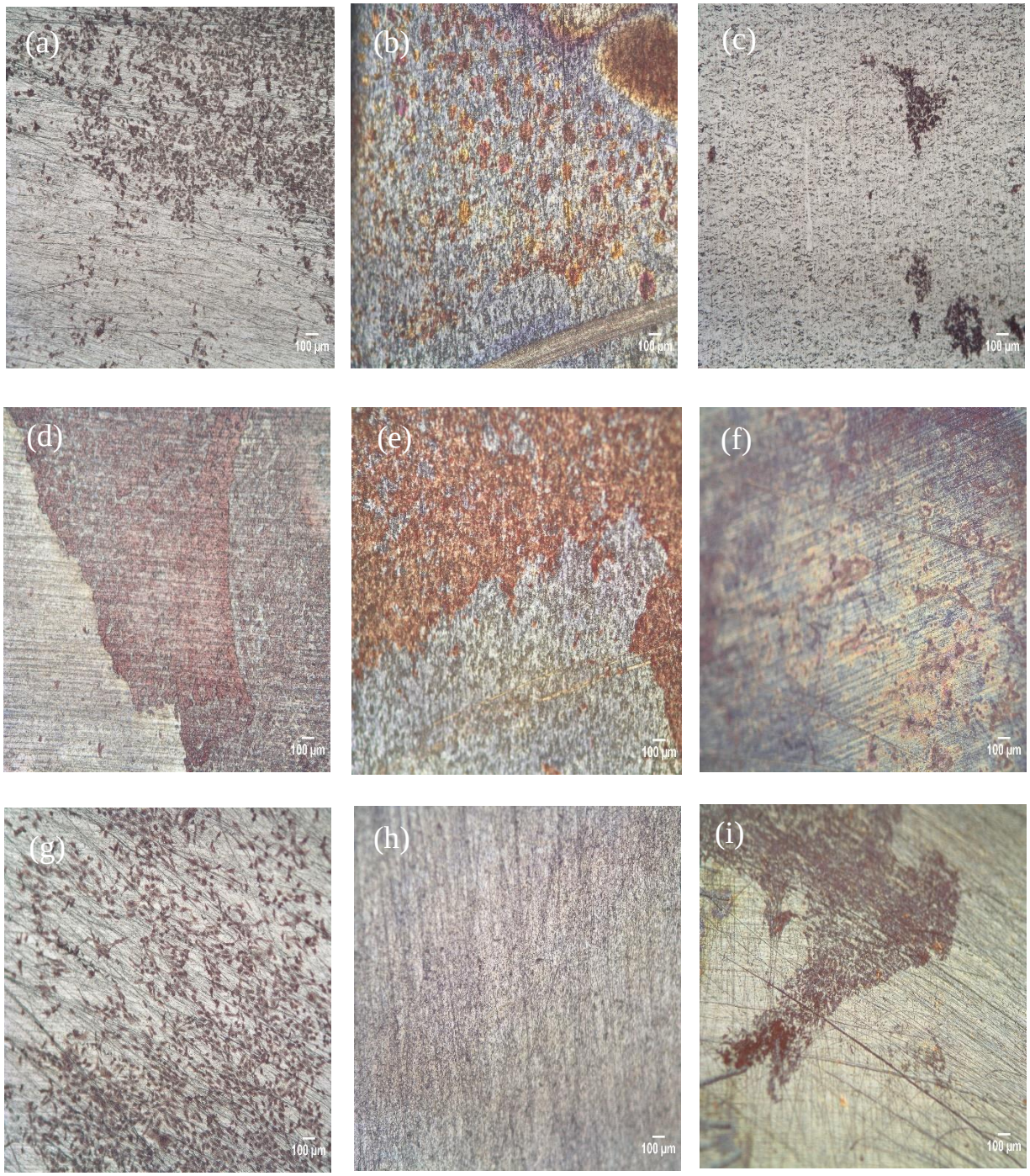

Figure 6.19 Optical micrographs showing Alizarin red staining of U-2 OS cells after 28 days in cell culture on (a) Ti, (b) 24eTi, (c) PolyTi250, (d) TiHA, (e) 24eTiHA, (f) PolyTi250HA, (g)TiSrHA, (h) 24eTiSrHA and (i) PolyTi250SrHA samples

6.6 Discussion

The data presented in this chapter seeks to investigate the capabilities of the chemically etched (24eTi) surfaces to interact with bone cells *in vitro*, compared to that of the pristine control (Ti) and the comparator (PolyTi) samples. Dalby *et al.*[27] have discussed in detail how the interplay between cells and surface features plays a key role in their subsequent response. Whereas, their studies have addressed how modified surfaces can influence key aspects of differentiation, the effects that augmentation with a soluble bioactive component has not yet been considered in detail. Hence, the work reported here provides new insight into how the combination of pronounced surface morphology and a liable calcium phosphate coating can affect cell interactions thereon. An initial evaluation was carried out on the uncoated substrates to understand how their respective chemistry and microstructure affected U-2 OS cell response. The MTT assay, which measures the amount of tetrazolium salt reduced by the mitochondria of the cells removed from the surface[217,245,246], has been used here to compare the viability of cells cultured on the various surfaces of interest for various periods of time. Given that other enzymes that are present in the cells can also reduce this salt[216], the results are only considered here as an estimation of the number of viable cells on each surface. The PicoGreen™ assay, which provides a direct measurement of the DNA from viable cells removed from the sample surfaces[218,247,248], is subject to less variation and so has been used here to give a better indication of the number of cells present on each substrate at a given timepoint. Hence, the data from the MTT and PicoGreen™ assays has been considered here in combination to allow for a better evaluation of the various results obtained. In addition, DAPI staining of U-2 OS cell nuclei has been employed as a means of directly measuring the number of cells on each surface at each time point. The nature of cell-surface and cell-cell interactions has been studied by SEM imaging of adhered cells on all surfaces. As previously stated, it is hypothesised in this work that the 24eTi samples will elicit an elevated cell response compared to pristine Ti due to the high degree of offset roughness that is created on the substrate by the chemical etching process. In order to better qualify the scale of this effect, the cell response to 24eTi was compared to that on PolyTi250, a surface that has been shown previously to support enhanced bone cell response *in vitro*.

The MTT and PicoGreen™ assay measurements for U-2 OS cells exposed to 24eTi and Ti samples in a 7-day culture study (Cell Study A) showed statistically significant differences, with more viable cells detected on the etched titanium than on the control surface. No statistically significant differences were found for MTT measurements obtained between the 24eTi and PolyTi250 after 7-days. However, there was a statistical

difference in the PicoGreen™ measurements when comparing the values for 24eTi and PolyTi250, with the 24eTi eliciting the higher response. The normalised MTT to DNA data for the uncoated substrates showed a decreasing trend over the 7-days of average cell metabolic activity per attached cell. This decreasing trend over the 7-days can be explained by the consumption of the resources available as cells proliferate, namely surface area and nutrients. A comparison of the number of DAPI stained cell nuclei and SEM imaging of fixed cells on the various titanium surfaces confirmed that the 24eTi samples has similar numbers of cells present to both the Ti and PolyTi250 surfaces. Moreover, the U-2 OS cells on the etched substrate had a mostly flattened morphology while those on the Ti and PolyTi250 surfaces exhibited a predominantly more rounded shape. Hence, these data suggest that chemical etching of the titanium sheet material produces surface features (chemical and topographical) that directly promote a higher degree of bone cell propagation and cell-surface interactions thereon as compared to those on the pristine Ti or PolyTi250 surfaces.

A key consideration in this work is the ability of the etched titanium surface features to support calcium phosphate (CaP) coatings, created by sputter deposition from hydroxyapatite (HA) or strontium substituted hydroxyapatite (SrHA) targets, in a way that engenders an enhanced cell response due to the presence of these known bioactive agents[242,249,250]. To determine the initial (early stage) effects of such coatings a 3-day cell culture study was carried out (Cell Study B), the results of which were then used to prime a longer 28-day study. It is known that the addition of strontium into the HA lattice can be beneficial in appropriate (relatively small) concentrations to enhance *in vitro* osteoblast response[147,149,251,252]. Previous work carried out with the commercial SrHA material used here indicates that the actual substituent concentration can be lower than that expected and it has also been reported that the final concentration in sputter deposited coatings is typically lower than that of the original substitution concentration in the target[30,45,47,224]. Hence, the concentration of the Sr ions in the SrHA coatings applied here is assumed to be well below the level that has been seen to lead to any negative effects on bone cells. Therefore, it is hypothesised herein that chemically etched titanium surfaces coated with a SrHA thin film can promote an earlier onset of cellular processes as compared to that seen for uncoated substrate surfaces.

An evaluation of U-2 OS cells cultured on CaP coated substrates 24eTi substrates for 3-days (24eTiHA and 24eTiSrHA) was carried out using the MTT assay, PicoGreen™ assay, DAPI cell nuclei staining and SEM imaging of adhered cells (Cell Study B). As before, these data were compared with those attained for the TiHA/TiSrHA and

PolyTi250HA/PolyTi250SrHA samples. In addition, these results correlate with those from the cells on the uncoated substrates (24eTi, Ti and PolyTi250). Whilst U-2 OS cells on all CaP coated (HA or SrHA) substrates elicited a positive response, the MTT and PicoGreen™ values were found to be lower than those obtained for the uncoated substrates. The MTT measurements at day 3 for the HA coated samples showed no statistically significant differences between the 24eTiHA, TiHA and PolyTi250HA surfaces. The day 3 PicoGreen™ measurements again showed no statistically significant difference between the 24eTiHA and TiHA samples (despite the value for 24eTiHA appearing to show a higher response than TiHA). However, there was a statistically significant difference noted when comparing 24eTiHA and PolyTi250HA, with the etched surface displaying the higher value overall. The normalised data showed no significant difference between the samples when compared to the TiHA .Subsequent cell counting via DAPI cell nuclei staining indicated that whilst all the HA coated surfaces had presented high levels of cells after 3-days in culture, 24eTiHA showed the highest overall coverage (cell/cm^2) when compared to that for both the TiHA and PolyTi250HA surfaces, with the TiHA surfaces having the lowest cell coverage after 3 days in culture. The 24eTiHA sample also showed higher levels of cell coverage across the surface than that seen for the 24eTi surfaces which suggests that after 3-days in culture media, the presence of HA has a positive influence on cell response[202,220]. SEM imaging of adhered cells shows that those on the 24eTiHA sample exhibited a mostly flattened cell morphology. By comparison, cells on the TiHA surface had both rounded and flattened morphologies and those on PolyTi250HA exhibited mostly rounded cell bodies. By comparison, the MTT measurements from U-2 OS cells on the SrHA coated samples at day 3 show no statistically significant differences between 24eTiSrHA and TiSrHA, or 24eTiSrHA and PolyTi250SrHA. It should also be noted that, whereas the MTT measurements for 24eTiSrHA and PolyTi250SrHA are lower than those from the equivalent uncoated (24eTi and PolyTi250) surfaces, there was a statistically significant difference between the coated and uncoated counterparts. Likewise, the corresponding PicoGreen™ measurements for the SrHA coatings showed values that are much lower than those recorded for the HA coated substrates and the corresponding uncoated samples. The reason for this lower MTT and PicoGreen™ response is evident when comparing the images for the DAPI stained cell nuclei which show a very significant decrease in coverage on all SrHA coated surfaces. The TiSrHA sample shows the highest cell coverage followed by 24eTiSrHA and PolyTi250SrHA, respectively. This behaviour is further confirmed by SEM imaging of adhered cells where TiSrHA again showed the

highest number cells present on the surface, with evidence of flattening apparent, PolyTi250SrHA had slightly less cell coverage with those present having a similar morphology to those on TiSrHA but with less cell spreading. The 24eTiSrHA surface had the least number of cells for this set of samples with those present having more rounded cell bodies sparsely spread across the substrate surface. In the context of the objectives of this work, the SrHA coated samples did not elicit the type of early stage cell response that might originally have been expected, but rather present a slower response than that of both the HA coated and uncoated samples. Whilst the normalised data for the SrHA coated substrate showed a significant difference between the TiSrHA and the 24eTiSrHA, the corresponding DAPI and SEM suggest a lower attachment of cells on the surface compared to that of the TiSrHA.

It is recognised that the effects of a bioactive CaP (HA or SrHA) coating on bone cell differentiation may only be seen after more than 21 days in culture[134,200,253,254]. Hence, a 28-day culture study was employed to measure ALP and BCA activity of cells on the coated 24eTi substrates with the values again compared to those from Ti and PolyTi250 (Cell Study C). When looking at the ALP results, all substrates (HA and SrHA coated) showed an increase in the values measured across days 7, 14 and 21, with a decrease then observed for all of the surfaces after 28-days. No statically significant differences where measured when comparing the HA coated substrates to each other. There is a similar trend for the SrHA coated substrates, with again no statistically significant difference noted between these samples at days 7 and 14. However, after 21-days the 24eTiSrHA and PolyTi250SrHA samples showed a decrease in the concentration of ALP measured. Moreover, 24eTiSrHA showed statistically significant differences at days 21 and 28 when compared to the TiSrHA, with the latter exhibiting higher values. Hence, the TiSrHA samples elicited the highest expression of ALP compared to that of either 24eTiSrHA or PolyTi250SrHA. Overall, there was no statistically significant difference between the ALP values measured at day 21 and day 28 for the various HA and SrHA coated samples. The BCA total protein concentrations values were found to increase for all CaP coated (HA and SrHA) samples across the 28-day culture period, with the lowest value noted for 24eTiSrHA, which is consistent with earlier findings (Cell Study B) in that there are lower numbers of cells on this surface. After 28-days in culture both the 24eTiHA and PolyTi250HA samples exhibited higher total protein concentrations compared to that observed for TiHA, with statistically significant differences noted for both. At days 7, 14 and 21, all HA coated surfaces elicited similar BCA measurements. By comparison, the TiSrHA surface exhibited the highest total protein concentration after 28-days in cell

culture, with statistically significant differences noted for this value and those from both 24eTiSrHA and PolyTi250SrHA.

Alizarin red staining solution was employed here to investigate the presence (or otherwise) of calcium deposits in the U-2 OS cells, indicative of cell mineralisation[255,256] having occurred on the various surfaces after 28-days in cell culture. All three uncoated substrate surfaces (Ti, 24eTi and PolyTi250) exhibited red areas of stained cells across the respective surfaces, suggesting that the U-2 OS bone-like cells have undergone differentiation by day 28, with calcium present on these uncoated surfaces due to the associated mineralisation. The 24eTi surface showed the most intense amount of localised red staining and PolyTi250 the least for this set of samples. The HA coated substrates also showed positive staining for calcium deposits, with the 24eTiHA surface displaying the densest areas of red, followed in intensity by TiHA and PolyTi250HA, respectively. By comparison, the 24eTiSrHA samples showed little or no staining, which is consistent with U-2 OS cells on the 24eTiSrHA coated substrate having the lowest ALP values across the 28-days. Whereas, there are localised areas of low intensity red staining visible for PolyTi250SrHA and TiSrHA, any red staining is barely detectable om 24eTiSrHA suggesting a lack of differentiation and subsequent mineralisation of U-2 OS cells on the etched surface after 28-days in culture. The U-2 OS osteosarcoma cells utilised for this thesis have been found previously to show a preference to attach to roughened surface morphology[174,214] For example, Mutreja *et a.l*[31,115] found that there was a higher degree of cell spreading evident on uncoated titanium substrates but the cells that were present showed a better initial cell response when there were CaP (HA) coatings on these substrates. Brugge *et al*.[257] also found that U-2 OS cells attached more readily to roughened substrates when compared to smoother surfaces. However, there are generally conflicting results in the literature detailing the performance of U-2 OS cells *in vitro.* Several studies have found that these cells express proteins and markers that are similar to those from native osteoblast cells[214,258]. However, it has also been found that U-2 OS cells can exhibit low basal ALP activity and inhibited mineralisation when compared to other human osteosarcoma cell lines, such as MG-63 and Saos-2 cells[87]. The culture studies carried out here (Cell Study C) found that low but positive concentrations of ALP were present across the 28-day study. In addition, positive calcium staining associated with their mineralisation was found on all surfaces except 24eTiSrHA.

Overall, the uncoated substrates present higher values associated with cell activity than those measured for the HA coated samples. However, comparing the DAPI stained cell nuclei and SEM images of cells adhered to the 24eTi and 24eTiHA samples indicates

that there is a clear difference not only in the cell coverage, but in the morphology of those cells present, with the 24eTiHA surface exhibiting a higher cell coverage with flattened cell bodies that are spread across the surface. In this regard, surfaces that encourage increased cell adhesion tend to show enhanced propagation[31,112,200,259]. However, although higher in number, these cells may not differentiate as efficiently when compared to surfaces that initially exhibited fewer attached cells but have improved differentiation at later time points. By comparison, PolyTi250HA and TiHA samples displayed higher cell coverage than the associated uncoated substrates, with both rounded and flattened cell bodies present on both of these surfaces, as evident from the alizarin red staining image analysis. Whilst the 24eTi did present intense areas of red staining, the corresponding 24eTiHA showed much denser areas of red staining. This suggests that the residual CaP (HA) coating present during the culture period enhanced the expression of ALP and the subsequent mineralisation of cells present on this HA coated substrate. By comparison, the CaP (SrHA) coated substrates elicited a much lower cell response than those on both the CaP (HA) coated and uncoated substrates. As indicated previously, fluorescent images for the DAPI stained nuclei and SEM images for adhered cells on these surfaces showed very low numbers of flattened and rounded cells, as well as sparse spreading of cells across the surface. The supporting alizarin red staining for the SrHA coated substrates further supports this analysis, with the staining present on these surfaces lower than that of the HA coated samples, and similar to that of the uncoated substrates, with no red staining observed for 24eTiSrHA after 28-days in culture. This much lower cell response could be due, in part, to the higher solubility of the SrHA, as observed in Chapter 5, wherein the SrHA coated samples were found to exhibit the lowest CaP content after 1 and 7-days immersion in aqueous solution. This high solubility and release of ions into the surrounding environment can have an adverse on the attendant cellular response.

In summary, the results obtained here indicated a general trend for cellular adhesion and proliferation as follows: Uncoated Substrates > HA Coated Substrates > SrHA Coated Substrates. Moreover, a general order of bioactivity for the various surfaces studied (as per the cell response measured herein) follows a general trend of: HA Coated Substrates > Uncoated Substrates > SrHA Coated Substrates. Hence, within the limitations of the various data sets attained here, the 24eTi substrates were found to elicit the most positive results in respect to U-2 OS response, due to the nature of the surface roughness created[110,177,184,260]. The *in vitro* results presented in this thesis suggest that the ‘honeycomb’ pitted features present on the 24eTi surface promote enhanced cell interaction when compared to that of the Ti and PolyTi250 surfaces.

Chapter 7: Thesis Conclusions and Recommendations for Future Work

7.1 Conclusions

The main aim of this thesis was to evaluate the ability of a chemically etched titanium surface to control the dissolution of as-deposited sputtering CaP coatings (HA or SrHA) in a manner that delivers a residual bioactive response thereon. This was achieved through the delivery of several objectives, as described in Chapter 1.2. It has been found that chemical etching of titanium sheet coupons by exposure to piranha solution (H_2SO_4/H_2O_2) for 24 hrs provides a roughened surface with a 'honeycomb' pitted morphology (24eTi). Chemical characterisation confirmed that these substrates exhibited a similar chemistry to that of the pristine titanium (Ti). As expected, annealing of both the pristine and sputtered titanium was found to reduce the carbon present on the surface whilst increasing the titanium and oxygen content due to the increase in the surface oxide thickness. This increase in the surface oxide led to 'smoothing' of the morphology present on the surface. It was therefore determined that the extra processing step of thermal annealing was not warranted and that only the unannealed pristine titanium would act as a control for this thesis. A number of titanium substrate topographies that have been previously studied in respect to controlling CaP coating dissolution were considered as comparators for eTi. Specifically, radio frequency (RF) magnetron sputter deposited polycrystalline titanium (PolyTi) substrates and titania nanotubes created by electrochemical anodisation (TiNT) which have both shown previously to have surface properties that can work effectively with CaP thin films[29,31,45,115]. Sputter deposited substrates created with a titanium target power of 250 W (PolyTi250) were found to exhibit similar surface chemistry to that of the chemically etched titanium (24eTi), as well as the pristine titanium control (Ti). The sample to sample repeatability of titania nanotubes was difficult to maintain due to the loss of fluorine in the electrolyte[188]. Therefore, the PolyTi250 substrate were selected as the comparator surface.

Due to its capability to allow for sputtering of both conducting and insulting materials, RF magnetron sputtering was also used to deposit CaP thin films from hydroxyapatite (HA), and strontium substituted hydroxyapatite (SrHA) powder targets onto the various substrates of interest to this thesis. The relevant published literature has described how RF magnetron sputtering gives very good adherence between the substrate and the target material, leading to a homogenous and continuous thin film that conforms well to the underlying substrate topography[29,115,160,200]. By comparison, plasma sprayed

coatings that are used commercially to coat orthopaedic implants tend to be thicker and take on their own morphology rather than mimicking that of the substrate[261–263].

Previous work carried out at Ulster University has detailed the ability of these CaP thin films to direct cell response *in vitro*[29,115,160]. Typically, these sputter deposited CaP thin films are thermally annealed to enhance their crystalline structure and thus reduce dissolution that occurs when in aqueous solution. However, for this work the thin film CaP coatings (HA and SrHA) were left in the as-deposited amorphous state so as to achieve a partially soluble thin film that will deliberately release ions into the surrounding biological environment that have the potential to invoke an osteoinductive response, while still retaining remnants of CaP on the substrate surface topography that are capable of engendering an osteoconductive bioactive response[122,129,264].

Extensive characterisation of the titanium substrate surfaces with and without CaP coatings (HA or SrHA) has been carried out. XPS analysis indicated that all titanium substrates had a similar surface chemistry where carbon, oxygen and titanium were detected with no other unexpected signals. It is also confirmed that the sputter deposited CaP coatings (HA and SrHA) formed a continuous thin film on each substrate, with no underlying titanium detected in any of the positive ion spectra graphs. However, trace amounts of titanium were found to be present in the positive ion maps for SrHA samples. This general lack of titanium signals suggests that these thin films are continuous across the surfaces but may be thinner in places due to the underlying surface roughness. The XPS spectra for the CaP (SrHA) coatings also confirmed the presence of strontium (Sr 3p), albeit at a lower concentration than that of the powder target material. The corresponding ToFSIMS analysis of the substrates indicated high calcium and calcium phases present on the surface and also confirmed the absence of any signals from titanium in spectral data from the CaP coatings (HA and SrHA) on these surfaces, whilst again confirming the presence of strontium ions in the spectrum for the SrHA coated samples. It was notable from the XPS and ToFSIMS analysis that SrHA coated substrates exhibited the lowest calcium content. Strontium substitutes for calcium in the hydroxyapatite lattice, therefore reducing the calcium content[202,265]. This implies that the SrHA coating will be more soluble in aqueous solution due to the higher atomic radius of the strontium ion (Sr^{2+}) when compared to that of the calcium ion (Ca^{2+}), i.e. this increase in ion size distorts the ionic lattice and thus suggests the lattice may be more suspectable to break down when placed in solution[32,33,264]. X-ray diffractograms for the CaP coated (HA and SrHA) substrates confirmed that as expected, these as-deposited thin films were in the amorphous state, with no peaks for HA or SrHA detected. The peaks that are present

represent Miller Indices corresponding to the ICDD file 00-44-1294[205,227] for semi-crystalline titanium. The microstructure of the various sample surfaces was visualised here using SEM. The images obtained confirmed that all the titanium substrates had the lines and grooves on the surface attributed to processing. In addition, the chemically etched samples (24eTi) exhibited a roughened 'honeycomb' pitted morphology across the surface. The SEM images for as-deposited CaP coatings (HA and SrHA) indicated that they do indeed conform to the underlying morphology of the chemically etched (24eTi), control (Ti) and comparator (PolyTi250) substrate surfaces. The distinctive 'honeycomb' pitted morphology of the 24eTi substrate was visible on both the 24eTiHA and 24eTiSrHA samples along with the lines and grooves, attributed to the processing of the titanium coupons. At high magnification, both the 24eTiHA and 24eTiSrHA images suggested that individual particles of the CaP material nucleate and grow on the surface features in a way that produces ridges of CaP (HA and SrHA) in these areas. These individual material particles were not observed on the related TiHA, TiSrHA, PolyTi250HA and PolyTi250SrHA samples, which did show the underlying (line and groves) core features.

It is well known that as-deposited sputtered CaP coatings (HA) on smooth flat surface (e.g. glass) will dissolve almost instantly when placed in aqueous solution[29,160]. Therefore, it was hypothesised here that these as-deposited amorphous CaP coatings (HA or SrHA) would be mostly resorbed into the surrounding environment after 7-days in aqueous solution. It was further hypothesised that the topography of the 24eTi substrates would have the capability to retain an appreciable amount of the CaP material (HA or SrHA) after 7-days immersion in solution, due to the higher surface area and the physical keying of thin film materials into these features. To test this, dissolution studies of the CaP coated (HA and SrHA) substrates in cell culture medium at 37 °C with 5 % CO_2 were carried out over a 7-day study. As expected, a significant proportion of the CaP coatings (HA and SrHA) were indeed found to dissolve after 1-day immersion in aqueous solution as indicated by XPS data which showed an associated decrease in calcium, phosphorus and oxygen content present on the surfaces. However, after 7-days in cell culture media there was a degree of reprecipitation of calcium and phosphorus onto some of the surfaces, as evaluated with ToFSIMS positive ion mapping, with the highest amount found on the 24eTiHA surface. Conversely, the SrHA coated substrates showed the highest loss of calcium and phosphorus concentration on the surface, and thereby had the lowest retention of CaP of all the substrates studies. This latter observation reflects the higher solubility of SrHA compared to HA. However, interestingly there were no

titanium signals detected on any of the CaP coated (HA or SrHA) substrates after 7-days exposure to aqueous cell media, which suggests that in all cases, there is still a form of homogenous, continuous thin film CaP present across the substrate surfaces. As discussed previously in Chapter 2.7.1, it is believed that formation of a salt electric bilayer has formed between days 1 and 7 of dissolution. This bilayer protects the remaining CaP (HA or SrHA) thin film from further dissolution, as well as encouraging the reprecipitation of calcium and phosphorous ions. The increase of carbon content seen across all samples after 7-days was thought to be attributable to protein adhesion to the sample surfaces during the submersion in aqueous cell media. When comparing the three SrHA coated substrates with each other, both the 24eTiSrHA and PolyTi250SrHA showed similar coating retention whilst the TiSrHA showed the lowest overall CaP (SrHA) material at 7-days exposure to media. These data indicate the topography of the etched titanium is indeed capable in retaining the more soluble SrHA at a level that is at least as good as that on the sputtered polycrystalline morphology.

The influence that the etched surface morphology and residual Cap coating chemistry has on a bone cell model *in vitro* has been investigated with particular emphasis on the ability of an offset orientated surface roughness to provide for a higher cell response due to the availability of the bioactive CaP contribution. An initial *in vitro* evaluation of U-2 OS cells on the uncoated titanium substrates over a 7-day study exhibited positive results for all sample types, with again the highest values obtained for the 24eTi surface, as reflected in the both the MTT and PicoGreen™ assays. SEM imaging of adhered cells on the various substrates indicated that those on the 24eTi surface exhibited a mostly flattened cell morphology whilst those on both the Ti and PolyTi250 exhibited both flat and rounded cell bodies on the surface. These data suggest that U-2 OS cells on the etched morphology are more actively engaged with the surface features. A subsequent investigation of U-2 OS cellular response to the CaP coated (HA and SrHA) substrates at day 3 found that there was a higher cell attachment and proliferation on the HA coated surfaces, with the 24eTiHA surface showing evidence of elevated activity. The SrHA coated samples exhibited values that were similar to those recorded for the equivalent HA coated samples, but likewise were generally lower in value that that of the uncoated counterparts at the same time point. However, when comparing the DAPI images obtained for the HA coated substrates and their uncoated counterparts, the HA coated substrates, particularly the 24eTiHA, show an increase in cells/cm^2 than that of the uncoated counterparts. Notwithstanding, the corresponding DAPI images for the SrHA coated surfaces indicate a low cell number and low cell coverage on these surface

when compared to both the HA coated and uncoated counterparts, with the PolyTi250SrHA exhibiting the lowest cell coverage per cm^2. The SEM images of adhered cells on the 24eTiHA surface showed mostly flattened cells, with a higher number of cells on the surface. The corresponding TiHA and PolyTi250HA surfaces exhibited cells with both flat and rounded cell bodies, similar to those seen on the uncoated counterparts, but again indicated a higher cell number than on the uncoated counterparts. Contrary to these HA surfaces, the SrHA surfaces exhibited few, sparsely spread cells across all SrHA coated substrates, with the 24eTiSrHA and PolyTi250SrHA exhibiting the lowest cell presence. The lack of cells on all SrHA coated samples, as compared to those seen on the uncoated substrates, suggests that this surface is so unstable during the culture period that cells are unable to attach and proliferate in numbers representative of the underlying substrate.

A 28-day culture study of U-2 OS cells on the CaP coated (HA and SrHA) surfaces was investigated, with the expression of alkaline phosphatase (ALP) and total whole protein biocinchonic (BCA) at days 7, 14, 21, and 27 used to assess the potential bioactivity of the surfaces and their ability to promote differentiation. All of the CaP coated substrates exhibited a positive ALP trend from days 7 – 21, which reflects stimulation of the U-2 OS cells, whilst the BCA increased across all of the time points out to 28-days.

Alizarin red staining was applied to the U-2 OS cells on the uncoated and CaP coated (HA and SrHA) samples after 28-days in culture as a means of determining if they have excreted calcium, as expected during differentiation. All of the substrates, with the exception of the 24eTiSrHA, exhibited areas of positive red staining across the surface. The 24eTiHA exhibited the densest areas of red staining, whilst the 24eTi also displayed spread out dense areas of red staining across the surface. The lack of appreciable staining of cells on the SrHA coated samples supports the proposition that these surfaces are inherently unstable such that they prevent cell attachment.

Overall, the data obtained from the experimental studies carried out here suggest there is a general trend of cellular attachment of U-2 OS cells to the substrate types as follows: HA coated substrates > uncoated substrates > SrHA coated substrates. The uncoated 24eTi had high levels of attachment, whilst the 24eTiHA showed the highest coverage and calcium excretion. When comparing the 24eTi and 24eTiHA surfaces, the clear difference in cell numbers present and their surface coverage are notable, with the 24eTiHA exhibiting higher cell coverage and the most ‘bone-like’ cell morphology[49,266]. Therefore, is it concluded that the trend in bioactivity of the various surface types is as

follows: HA coated substrates > uncoated substrates > SrHA coated substrates.

To the best of the authors knowledge, this is the first time that the bioactivity of chemically etched (24 hrs in piranha solution) titanium substrates with an as-deposited amorphous CaP coating (HA and SrHA) has been investigated in respect of their ability to promote bone cell maturation. The pitted 'honeycomb' morphology created on the titanium can clearly retain enough of the HA thin film to elicit an enhanced effect *in vitro*. Even though a sputter deposited SrHA coated can also be created on this surface and is significantly retained for up to 7-days in aqueous solution, its inherent solubility creates an environment that dramatically reduces cell adhesion and proliferation. However, although there is clear evidence provided here that chemically etched titanium can provide many of the surface feature attributed attained via more complex, expensive and time-consuming process, further investigation is needed here to assess the possible *in vivo* capabilities of these surfaces in the context of orthopaedic implant therapies and devices.

7.2 Recommendations for Future Work

Based on the conclusions from the work presented here, a number of areas for future studies are suggested, as follows;

- A long-term dissolution evaluation of the 24eTiHA in cell culture media to understand when the thin film is completely dissipated from the surface
- A 28-day U-2 OS culture study with a PCR evaluation of osteocalcin (OCN) and osteopontin (OPN) to establish their early stage response to 24eTiHA surfaces
- A 28-day U-2 OS culture study with a PCR evaluation of osteocalcin (OCN) and osteopontin (OPN) to establish their early stage response to uncoated 24eTi surfaces and allow comparison to values obtained for 24eTiHA surfaces
- A 28-day ALP/BCA study and PCR evaluation of osteocalcin (OCN) and osteopontin (OPN) on 24eTi and 24eTiHA seeded with mesenchymal stem cells, cultured in normal media and osteogenic media, to provide an insight into how these cells respond to the topography presented by the etched surfaces in long term culture and if the supplemented media is necessary
- Mirror finish polishing to the titanium surface to remove lines and grooves before chemically etching to investigate if the acquired surface chemistry and morphology is similar to those of the current 24eTi and what differences are notable

- Subsequent *in vitro* evaluation of mirror polished chemically etched titanium surfaces to evaluate and compare cellular response to these particular surfaces in regard to the response from the 24eTi and 24eTiHA
- Investigation into low annealing temperatures of CaP coatings (HA and SrHA) in combination with the chemically etched 24eTi surfaces to slow the rapid dissolution in aqueous media, particularly to control the unstable SrHA coatings
- Evaluation of other substituted HA materials, such as zinc or magnesium, or co-substituted HA materials to be sputtered onto the chemically etched surfaces and their subsequent response in aqueous media before further evaluation in culture
- Investigation of chemically etched titanium alloy surfaces and how the subsequent surface chemistry and morphology compares to that of the chemically etched pure titanium (24eTi)

References

1. Biswal T, Badjena S., Pradham D. Sustainable biomaterials and their applications: A short review. Mater Today Proc. 2020;

2. Gao X, Usas A, Tang Y, Lu A, Tan J, Schneppendahl J, et al. Biomaterials A comparison of bone regeneration with human mesenchymal stem cells and muscle-derived stem cells and the critical role of BMP. Biomaterials 2014;35(25):6859–70.

3. Roach P, Eglin D, Rohde K, Perry CC. Modern biomaterials : a review - bulk properties and implications of surface modifications. 2007;1263–77.

4. Gallagher NE, Bruce-Brand R, Bennett D, O'Brien S, Beverland DE. No difference in gait kinematics or kinetics between limbs in bilateral total hip replacement patients at long-term follow-up. Clin Biomech. 2019;

5. Malahias M-A, Kostretzis L, Greenberg A, Nikolaou VS, Atrey A, Sculco PK. Highly Porous Titanium Acetabular Components in Primary and Revision Total Hip Arthroplasty: A Systematic Review. J Arthroplasty. 2020;

6. Karachalios T, Komnos G, Amprazis V, Antoniou I, Athanaselis S. A 9-Year Outcome Study Comparing Cancellous Titanium-Coated Cementless to Cemented Tibial Components of a Single Knee Arthroplasty Design. J Arthroplasty. 2018;

7. Dehl M, Bulaïd Y, Chelli M, Belhaouane R, Gabrion A, Havet E, et al. Total knee arthroplasty with the Medial-Pivot knee system: Clinical and radiological outcomes at 9.5 years' mean follow-up. Orthop Traumatol Surg Res. 2018;

8. Harwin SF, Patel NK, Chughtai M, Khlopas A, Ramkumar PN, Roche M, et al. Outcomes of Newer Generation Cementless Total Knee Arthroplasty: Beaded Periapatite-Coated vs Highly Porous Titanium-Coated Implants. J Arthroplasty. 2017;

9. Hatamleh MM, Wu X, Alnazzawi A, Watson J, Watts D. Surface characteristics and biocompatibility of cranioplasty titanium implants following different surface treatments. Dent Mater. 2018;

10. Taylor D. Observations on the role of fracture mechanics in biology and medicine. Engineering Fracture Mechanics. 2018.

11. Niinomi M. Recent research and development in titanium alloys for biomedical

applications and healthcare goods. Science and Technology of Advanced Materials. 2003.

12. Schwartz Z, Raz P, Boyan BD. Effect of Micrometer-Scale Roughness of the Surface of Ti6Al4V Pedicle Screws in Vitro and in Vivo. J Bone Joint Surg Am. 2008;90(11):2485–98.

13. Stenport VF, Johansson CB. Evaluations of Bone Tissue Integration to Pure and Alloyed Titanium Implants. Clin Implant Dent Relatted Reasearch. 2008;

14. Rajaee SS, Bae H., Kanim LE., Delamarter R. Spinal Fusion in the UNited States: Analysis of Trends from 1998 to 2008. Spine (Phila Pa 1976). 2012;37(1):67–76.

15. Chong E, Pelletier MH, Mobbs RJ, Walsh WR. The design evolution of interbody cages in anterior cervical discectomy and fusion: a systematic review. BMC Musculoskelet Disord. 2015;

16. Rao PJ, Pelletier MH, Walsh WR, Mobbs RJ. Spine Interbody Implants: Material Selection and Modification, Functionalization and Bioactivation of Surfaces to Improve Osseointegration. Orthop Surg. 2014;

17. Xie Y, Zuo J, Zhou B, Ma L, Yu ZM, Wei Q, et al. Sandblast-free double-etched titanium for dental implants application. 2016;176:74–7.

18. He W, Yin X, Xie L, Liu Z, Li J, Zou S, et al. Enhancing osseointegration of titanium implants through large-grit sandblasting combined with micro-arc oxidation surface modi fi cation. J Mater Sci Mater Med. 2019;

19. Liu Z, Tsai IL, Thompson GE, Liu H, Donatus U. Chemical etching behaviour of titanium in bromine-methanol electrolyte. Mater Chem Phys. 2015;

20. Wei D, Zhou Y, Wang Y, Jia D. Chemical etching of micro-plasma oxidized titania film on titanium alloy and apatite deposited on the surface of modified titania film in vitro. Thin Solid Films. 2008;

21. Mohan L, Anandan C, Rajendran N. Electrochemical behaviour and bioactivity of self-organized TiO2 nanotube arrays on Ti-6Al-4V in Hanks' solution for biomedical applications. Electrochim Acta. 2015;

22. Andrukhov O, Huber R, Shi B, Berner S, Rausch-fan X, Moritz A, et al. Influence of surface topography on osteoblast response to fibronectin coated calcium

phosphate thin films. Colloids Surfaces B Biointerfaces. 2010;65(4):944–9.

23. Qadir M, Li Y, Wen C. Ion-substituted calcium phosphate coatings by physical vapor deposition magnetron sputtering for biomedical applications: A review. Acta Biomaterialia. 2019.

24. Radziejewska J, Sarzyński A, Strzelec M, Diduszko R, Hoffman J. Evaluation of residual stress and adhesion of Ti and TiN PVD films by laser spallation technique. Opt Laser Technol. 2018;

25. Ren J, Zhao D, Qi F, Liu W, Chen Y. Heat and hydrothermal treatments on the microstructure evolution and mechanical properties of plasma sprayed hydroxyapatite coatings reinforced with graphene nanoplatelets. J Mech Behav Biomed Mater. 2020;

26. Liu X, Chu PK, Ding C. Surface modification of titanium, titanium alloys, and related materials for biomedical applications. Mater Sci Eng R Reports. 2004;47(3–4):49–121.

27. Dalby MJ, Gadegaard N, Tare R, Andar A, Riehle MO, Herzyk P, et al. The control of human mesenchymal cell differentiation using nanoscale symmetry and disorder. Nat Mater. 2007;6.

28. Mccafferty MM, Burke GA, Meenan BJ. Mesenchymal stem cell response to conformal sputter deposited calcium phosphate thin films on nanostructured titanium surfaces. 2013;3585–97.

29. McLister R. hMSC response to augmented CaP nanotopography. 2016.

30. O'Kane C, Duffy H, Meenan BJ, Boyd AR. The influence of target stoichiometry on the surface properties of sputter deposited calcium phosphate thin films. Surf Coatings Technol. 2008;

31. Mutreja I, Kumar D, Boyd AR, Meenan BJ. Titania nanotube porosity controls dissolution rate of sputtered deposited calcium phosphate (CaP) thin film coatings. RSC Adv. 2013;3(28):11263–73.

32. Dorozhkin S V. Calcium orthophosphate-based bioceramics. Materials (Basel). 2013;6(9):3840–942.

33. Technologies C, Eliaz N, Metoki N. Calcium Phosphate Bioceramics : A Review

of Their. 2017;

34. Bai Y, Chi B xiang, Ma W, Liu C wen. Suspension plasma-sprayed fluoridated hydroxyapatite coatings: Effects of spraying power on microstructure, chemical stability and antibacterial activity. Surf Coatings Technol. 2019;

35. Sun L, Berndt C, Gross K, Kucuk A. Material Fundamentals and Clinical Performance of Plasma-Sprayed Hydroxyapatite Coatings: A Review. J Biomed Mater Res. 2001;58(5):570–92.

36. Guo Y, Liu B, Hu B, Xiao G, Wu Y, Sun P, et al. Antibacterial activity and increased osteoblast cell functions of zinc calcium phosphate chemical conversion on titanium. Surf Coat Technol. 2016;294:131–8.

37. Capuccini C, Torricelli P, Boanini E, Gazzano M, Giardino R, Bigi A. Interaction of Sr-doped hydroxyapatite nanocrystals with osteoclast and osteoblast-like cells. 2008;

38. Fu Y, Chen D, Zhang J. In Vitro Study on the Cytotoxicity of Strontium Substituted Hydroxyapatite. Shanghai J Stomatol. 2002;11(3).

39. Von Recum AF. Handbook of Biomaterials Evaluation: Scientific, Technical and Clinical Testing of Implant Materials. 1999.

40. McNamara LE, McMurray RJ, Biggs MJP, Kantawong F, Oreffo ROC, Dalby MJ. Nanotopographical Control of Stem Cell Differentiation. J Tissue Eng 2010;1(1):120623–120623.

41. Im KH, Lee SB, Kim KM, Lee YK. Improvement of bonding strength to titanium surface by sol-gel derived hybrid coating of hydroxyapatite and titania by sol-gel process. Surf Coatings Technol. 2007;

42. Fedotkin AY, Bolbasov EN, Kozelskaya AI, Dubinenko G, Shesterikov E V., Ashrafov A, et al. Calcium phosphate coating deposition by radio frequency magnetron sputtering in the various inert gases: The pilot study. Mater Chem Phys. 2019;

43. Ahmadi S, Mohammadi I, Sadrnezhaad SK. Surface & Coatings Technology Hydroxyapatite based and anodic Titania nanotube biocomposite coatings : Fabrication , characterization and electrochemical behavior. Surf Coat Technol 2016;287:67–75.

44. Block M, Finger I, Fontenot M, Kent J. Loaded hydroxylapatite-coated and grit-blasted titanium implants in dogs. Int J Oral Maxillofac Implant. 1989;4(3):219–25.

45. Boyd AR, Duffy H, McCann R, Meenan BJ. Sputter deposition of calcium phosphate/titanium dioxide hybrid thin films. Mater Sci Eng C. 2008;

46. Pereira M, Dulce G, Soares DA, Dentzer J, Anselme K, Ágata L, et al. Synthesis of magnesium- and manganese-doped hydroxyapatite structures assisted by the simultaneous incorporation of strontium. Mater Sci Eng C 2016;61:736–43.

47. Robinson L, Salma-Ancane K, Stipniece L, Meenan BJ, Boyd AR. The deposition of strontium and zinc Co-substituted hydroxyapatite coatings. J Mater Sci Mater Med 2017;28(3):51.

48. Onder S, Kok FN, Kazmanli K, Urgen M. Magnesium substituted hydroxyapatite formation on (Ti,Mg)N coatings produced by cathodic arc PVD technique. Mater Sci Eng C. 2013;

49. Florencio-silva R, Rodrigues G, Sasso-cerri E, Simões MJ, Cerri PS, Cells B. Biology of Bone Tissue : Structure , Function , and Factors That Influence Bone Cells. 2015;2015.

50. Stylios G, Wan T, Giannoudis P. Present status and future potential of enhancing bone healing using nanotechnology. Injury. 2007;38(SUPPL. 1).

51. Buckwalter J., Glimcher M., Cooper R., Recker R. Bone biology I: structure, blood supply,cells, matrix, and mineralisation. Instr Course Lect. 1996;45:371–86.

52. Downey PA, Siegel MI. Bone Biology and the Clinical Implications for Osteoporosis. 2006;86(1):77–91.

53. Prideaux M, Findlay DM, Atkins GJ. Osteocytes: The master cells in bone remodelling. Current Opinion in Pharmacology. 2016.

54. Johnell O, Kanis JA. An estimate of the worldwide prevalence and disability associated with osteoporotic fractures. Osteoporos Int 2006;17(12):1726–33.

55. Wang D, Wu G, Lin X, Liu Y. Coatings for Osseointegration of Metallic Biomaterials. Surf Coat Modif Met Biomater. 2015;345–58.

56. Shrivats AR, Alvarez P, Schutte L, Hollinger JO. Bone Regeneration. In:

Principles of Tissue Engineering. 2014. p. 1201–20.

57. Schweikle M, Bjørnøy SH, van Helvoort ATJ, Haugen HJ, Sikorski P, Tiainen H. Stabilisation of amorphous calcium phosphate in polyethylene glycol hydrogels. Acta Biomater. 2019;

58. Golub EE, Boesze-battaglia K. The role of alkaline phosphatase in mineralization. 2007;444–8.

59. Sharma U, Pal D, Prasad R. Alkaline phosphatase: An overview. Indian J Clin Biochem. 2014;29(3):269–78.

60. Stein GS, Lian JB. Molecular Mechanisms Mediating Proliferation / Differentiation Interrelationships During Progressive Development of the Osteoblast Phenotype. 2017;14(4):424–42.

61. Christiansen C. Prevention and Treatment of Osteoporosis: A Review of Current Modalities. Bone. 1992;13:35–9.

62. Massachusetts F, Hospital G, Aires B, Gairdner SC, Lilly E, Brull PUL, et al. EFFECT OF PARATHYROID HORMONE (1-34) ON FRACTURES AND BONE MINERAL DENSITY IN POSTMENOPAUSAL WOMEN WITH OSTEOPOROSIS. 2001;344(19):1434–41.

63. Hernlund E, Svedbom A, Ivergård M, Compston J, Cooper C, Stenmark J, et al. Osteoporosis in the European Union: medical management, epidemiology and economic burden. Arch Osteoporos 2013;8(1):136.

64. Delannoy P, Bazot D, Marie PJ. Long-term treatment with strontium ranelate increases vertebral bone mass without deleterious effect in mice. Metabolism 2002 Jul ;51(7):906–11.

65. Williams D. The Williams Dictionary of Biomaterials. 1999.

66. Ghasemi-Mobarakeh L, Kolahreez D, Ramakrishna S, Williams D. Key terminology in biomaterials and biocompatibility. Current Opinion in Biomedical Engineering. 2019.

67. Chen Q, Thouas GA. Metallic implant biomaterials. Materials Science and Engineering R: Reports. 2015.

68. Kaur M, Singh K. Review on titanium and titanium based alloys as biomaterials

for orthopaedic applications. Materials Science and Engineering C. 2019.

69. Kumar S, Nehra M, Kedia D, Dilbaghi N, Tankeshwar K, Kim KH. Nanotechnology-based biomaterials for orthopaedic applications: Recent advances and future prospects. Materials Science and Engineering C. 2020.

70. Bergmann CP, Stumpf A. Dental Ceramics. 2013;9–14. Available from: http://link.springer.com/10.1007/978-3-642-38224-6

71. Albrektsson T, Johansson C. Osteoinduction, osteoconduction and osseointegration. Eur Spine J [Internet]. 2001 Oct 30;10(Suppl 2):S96–101. Available from: http://www.ncbi.nlm.nih.gov/pmc/articles/PMC3611551/

72. Goriainov V, Hulsart-billstrom G, Sjostrom T, Dunlop DG, Su B. Harnessing Nanotopography to Enhance Osseointegration of Clinical Orthopedic Titanium Implants — An in Vitro and in Vivo Analysis. 2018;6(April):1–14.

73. Davison NL, Barrére-de Groot F, Grijpma DW. Chapter 6 - Degradation of Biomaterials. In: Tissue Engineering (Sencond Edition). 2014. p. 177–215.

74. Anitua E, Piñas L, Murias A, Prado R, Tejero R. Effects of calcium ions on titanium surfaces for bone regeneration. Colloids Surfaces B Biointerfaces. 2015;

75. Favero R, Botticelli D, Antunes AA, Martinez Sanchez R, Caroprese M, Salata LA. Sequential Healing at Calcium versus Calcium Phosphate Modified Titanium Implant Surfaces: An Experimental Study in Dogs. Clin Implant Dent Relat Reasearch. 2015;18(2).

76. Nakamura S, Matsumoto T, Sasaki J, Egusa H, Lee K., Nakano T, et al. Effect of calcium ion concentrations on osteogenic differentiation and hematopoietic stem cell niche-related protein expression in osteoblasts. Tissue Eng - Part A. 2010;16(8).

77. Goulet JA, Senunas LE, Desilva GL, Lou M, Greenfield KH. Autogenous Iliac Crest Bone Graft Complications and Functional Assessment. 1997;(339):76–81.

78. Greenwald AS, Oxon DP, Boden SD, Goldberg VM, Khan Y. Bone Graft Substitutes: Facts, Fictions and Applications. J Bone Jt Surg. 2003;83:98–103.

79. Lementowski P, Lucas P, Taddonio R. Acute and Chronic Complications of Intracortical Iliac Crest Bone Grafting Versus the Traditional Corticocancellous

Technique for Spinal Fusion Surgery. Orthopedics. 2010;33(4).

80. Branemark P-I. Osseointegration and its experimental background. J Prosthet Dent 1983 Sep;50(3):399–410.

81. Albrektsson T, Johansson C. Osteoinduction, osteoconduction and osseointegration. Eur Spine J. 2001;10:96–101.

82. Veronesi F, Giavaresi G, Fini M, Longo G, Alexandra C, Scotto A, et al. Osseointegration is improved by coating titanium implants with a nanostructured thin fi lm with titanium carbide and titanium oxides clustered around graphitic carbon. Mater Sci Eng C [Internet]. 2017;70:264–71. Available from: http://dx.doi.org/10.1016/j.msec.2016.08.076

83. Silverwood RK, Fairhurst PG, Sjöström T, Welsh F, Sun Y, Li G, et al. Analysis of Osteoclastogenesis / Osteoblastogenesis on Nanotopographical Titania Surfaces. 2016;(May):947–55.

84. Roach P, Farrar D, Perry CC. Surface Tailoring for Controlled Protein Adsorption : Effect of Topography at the Nanometer Scale and Chemistry. 2006;17(7):617–21.

85. Carradò A, Perrin-Schmitt F, Le Q V., Giraudel M, Fischer C, Koenig G, et al. Nanoporous hydroxyapatite/sodium titanate bilayer on titanium implants for improved osteointegration. Dent Mater. 2017;

86. Shaheen BS, Bakir M, Jain S. Corneal nerves in health and disease. Surv Ophthalmol 2014;59(3):263–85.

87. Pautke C, Schieker M, Tischer T, Kolk A, Neth P, Mutschler W, et al. Characterization of Osteosarcoma Cell Lines MG-63 , Saos-2 and U-2 OS in Comparison to Human Osteoblasts. 2004;3748:3743–8.

88. ATCC. U--2 OS (ATCC ® HTB-96 ™) Product Sheet.

89. Rodan SB, Imai Y, Thiede MA, Wesolowski G, Thompson D, Bar-shavit Z, et al. Characterization of a Human Osteosarcoma Cell Line (Saos-2) with Osteoblastic Properties. 1987;4961–6.

90. Childs PG, Boyle CA, Pemberton GD, Nikukar H, Curtis ASG, Henriquez FL, et al. Acta Biomaterialia Use of nanoscale mechanical stimulation for control and manipulation of cell behaviour q. Acta Biomater [Internet]. 2016;34:159–68.

Available from: http://dx.doi.org/10.1016/j.actbio.2015.11.045

91. Guadarrama D, Fouillen A, Badia A, Nanci A. Acta Biomaterialia A nanoporous titanium surface promotes the maturation of focal adhesions and formation of filopodia with distinctive nanoscale protrusions by osteogenic cells. Acta Biomater 2017;60:339–49.

92. Salmasi S, Kalaskar DM, Yoon W, Blunn GW, Seifalian AM, Salmasi S, et al. Role of nanotopography in the development of tissue engineered 3D organs and tissues using mesenchymal stem cells. 2015;7(2):266–80.

93. Kim D, Provenzano PP, Smith CL, Levchenko A. Matrix nanotopography as a regulator of cell function. 2012;197(3):351–60.

94. McNamara LE, McMurray RJ, Biggs MJP, Kantawong F, Oreffo ROC, Dalby MJ. Nanotopographical Control of Stem Cell Differentiation. J Tissue Eng. 2010;1(1):120623–120623.

95. George J, Kuboki Y, Miyata T. Differentiation of Mesenchymal Stem Cells Into Osteoblasts on Honeycomb Collagen Scaffolds.

96. Wang Y, Yu Z, Guo X, Hu J. Surface morphology of modified titanium alloy affects proliferation stability of bone marrow mesenchymal stem cells. Surf Coatings Technol. 2019;

97. Human S, Chen W, Villa-diaz LG, Sun Y, Weng S, Kim JK, et al. Nanotopography Influences Adhesion, Spreading and Self Renewal of Human Embryonic Stem Cells. 2012;4094–103.

98. Mei YU, Junlan YI, Jianhua LIU, Songmei LI, Guolong WU, Liang WU. Effect of Electropolishing on Electrochemical Behaviours of Titanium Alloy Ti-10V-2Fe-3Al. 2011;(June):469–77.

99. Hotchkiss KM, Reddy GB, Hyzy SL, Schwartz Z, Boyan BD, Olivares-navarrete R. Acta Biomaterialia Titanium surface characteristics , including topography and wettability , alter macrophage activation. Acta Biomater2016;31:425–34.

100. Yuan Z, Su B. Titanium oxide nanotubes , nanofibers and nanowires. 2004;241:173–83.

101. Ferraris S, Vitale A, Bertone E, Guastella S, Cassinelli C, Pan J, et al.

Multifunctional commercially pure titanium for the improvement of bone integration : Multiscale topography , wettability , corrosion resistance and biological functionalization. Mater Sci Eng C 2016;60:384–93.

102. Gadegaard N, Dalby MJ, Riehle MO, Wilkinson CDW, Gadegaard N, Dalby MJ, et al. Optimizing substrate disorder for bone tissue engineering of mesenchymal stem cells Optimizing substrate disorder for bone tissue engineering of mesenchymal stem cells. 2016;2554(2008).

103. Article O, Bauer S, Park J, Pittrof A, Mark K Von Der, Schmuki P, et al. TiO 2 nanotubes : Self-organized electrochemical formation , properties and applications. YGHIR 2012;24(6):2904–39.

104. Bauer S, Park J, Pittrof A, Mark K Von Der, Schmuki P. Synergistic control of mesenchymal stem cell differentiation by nanotopography and immobilized BMP-2 on TiO 2 nanotubes. 2012;57(1):4015.

105. Brunette DM, Hamilton DW, Chehroudi B, Waterfield JD. Update on improving the bio-implant interface by controlling cell behaviour using surface topography. 2005;1284:229–38.

106. Kulangara K, Yang Y, Yang J, Leong KW. Biomaterials Nanotopography as modulator of human mesenchymal stem cell function. Biomaterials 2012;33(20):4998–5003.

107. Abdel E, Yuehai M, Junfeng K, Ahmed J. Stem cells applications in bone and tooth repair and regeneration : New insights , tools , and hopes. 2017;(March):1825–35.

108. Castro-raucci LMS, Francischini MS, Teixeira LN, Ferraz EP, Lopes HB, Oliveira PT De, et al. Titanium With Nanotopography Induces Osteoblast Differentiation by Regulating Endogenous Bone Morphogenetic Protein Expression and Signaling Pathway. 2016;1726(December 2015):1718–26.

109. Boyan BD, Cheng A, Schwartz Z. Implant Surface Design Regulates Mesenchymal Stem Cell Differentiation and Maturation. 2016;10–7.

110. Gittens RA, Mclachlan T, Olivares-navarrete R, Cai Y, Berner S, Tannenbaum R, et al. Biomaterials The effects of combined micron- / submicron-scale surface roughness and nanoscale features on cell proliferation and differentiation. Biomaterials 2011;32(13):3395–403.

111. Civantos A, Domínguez C, Juliana R, Setti G, José J, Martínez-campos E, et al. Surface & Coatings Technology Designing bioactive porous titanium interfaces to balance mechanical properties and in vitro cells behavior towards increased osseointegration. Surf Coat Technol 2019;368(March):162–74.

112. Rodriguez-contreras A, Guadarrama D, Nanci A. Applied Surface Science Surface nanoporosity has a greater influence on osteogenic and bacterial cell adhesion than crystallinity and wettability. Appl Surf Sci 2018;445:255–61.

113. Minagar S, Wang J, Berndt CC, Ivanova EP, Wen C. Review Article Cell response of anodized nanotubes on titanium and titanium alloys. 2013;110101974:2726–39.

114. Roy P, Berger S, Schmuki P. TiO 2 Nanotubes : Synthesis and Applications Angewandte. 2011;2904–39.

115. Mutreja I. Controlled dissolution of CaP thin films via surface engineering. 2012.

116. Alivov Y, Fan ZY, Johnstone D, Alivov Y, Fan ZY, Johnstone D. Titanium nanotubes grown by titanium anodization Titanium nanotubes grown by titanium anodization. 2017;034314(2009):1–6.

117. Khudhair D, Bhatti A, Li Y, Hamedani HA, Garmestani H, Hodgson P, et al. Anodization parameters in fl uencing the morphology and electrical properties of TiO 2 nanotubes for living cell interfacing and investigations. 2016;59:1125–42.

118. Oh S, Daraio C, Chen L, Pisanic T, Fiñones R, Jin S. Significantly accelerated osteoblast cell growth on aligned TiO2 nanotubes. J Biomed Mater Res A. 2006;78:97–103.

119. Skoog SA, Kumar G, Narayan RJ, Goering PL. Biological responses to immobilized microscale and nanoscale surface topographies. Pharmacology and Therapeutics. 2018.

120. Park J, Han S, Hanawa T. Effects of Surface Nanotopography and Calcium Chemistry of Titanium Bone Implants on Early Blood Platelet and Macrophage Cell Function. 2018;2018.

121. Dorozhkin S V. Amorphous Calcium Orthophosphates : Nature , Chemistry and Biomedical Applications. 2012;2(1):19–46.

122. Tao J, Pan H, Zeng Y, Xu X, Tang R. Roles of Amorphous Calcium Phosphate

and Biological Additives in the Assembly of Hydroxyapatite Nanoparticles. 2007;13410–8.

123. Vecstaudza J, Gasik M, Locs J. Amorphous calcium phosphate materials: Formation, structure and thermal behaviour. J Eur Ceram Soc. 2019;

124. Kilpadi K, Chang P, Bellis S. Hydroxylapatite binds more serum proteins, purified integrins, and osteoblast precursor cells than titanium or steel. J Biomed Mater Res. 2001;57(2):258–67.

125. Okuda T, Ioku K, Yonezawa I, Minagi H, Gonda Y, Kawachi G, et al. The slow resorption with replacement by bone of a hydrothermally synthesized pure calcium-deficient hydroxyapatite. Biomaterials. 2008;

126. Stastny P, Vacek P, Trunec M. Characterization of microstructure and phase distribution of sintered multiphasic calcium phosphate bioceramics. Ceram Int. 2020;

127. Stastny P, Sedlacek R, Suchy T, Lukasova V, Rampichova M, Trunec M. Structure degradation and strength changes of sintered calcium phosphate bone scaffolds with different phase structures during simulated biodegradation in vitro. Mater Sci Eng C. 2019;

128. Diez-Escudero A, Espanol M, Beats S, Ginebra MP. In vitro degradation of calcium phosphates: Effect of multiscale porosity, textural properties and composition. Acta Biomater. 2017;

129. Yokota S, Nishiwaki N, Ueda K, Narushima T, Kawamura H, Takahashi T. Evaluation of thin amorphous calcium phosphate coatings on titanium dental implants deposited using magnetron sputtering. Implant Dent. 2014;23(3):343–50.

130. Hamdi M, Ide-Ektessabi A. Dissolution behavior of simultaneous vapor deposited calcium phosphate coatings in vitro. Mater Sci Eng C. 2007;

131. Schaefer S, Detsch R, Uhl F, Deisinger U, Ziegler G. How Degradation of Calcium Phosphate Bone Substitute Materials is influenced by Phase Composition and Porosity. Adv Eng Mater. 2011;

132. Yamashita K, Matsuda M, Arashi T, Umegaki T. Crystallization , fluoridation and some properties of apatite thin films prepared through rf-sputtering from CaO — P 2 O 5 glasses. 1998;19:1239–44.

133. López EO, Mello A, Farina M, Rossi AM, Rossi AL. Surface & Coatings Technology Nanoscale analysis of calcium phosphate fi lms obtained by RF magnetron sputtering during the initial stages of deposition. Surf Coat Technol 2015;279:16–24.

134. Li L, Kim H, Lee S, Kong Y, Kim H. Biocompatability of titanium implants modified by microarc oxidation and hydroxyapatite coating. J Biomed Mater Res A. 2005;73(1):48–54.

135. Hare PO, Meenan BJ, Burke GA, Byrne G, Dowling D, Hunt JA. Biomaterials Biological responses to hydroxyapatite surfaces deposited via a co-incident microblasting technique. Biomaterials 2010;31(3):515–22.

136. Ohgushi H, Goldberg VM, Caplan AI. Hetertopic osteogenesis in porous ceramics induced by marrow cells. J Biomed Mater Res. 1989;7(4):568–78.

137. Ohgushi H, Okumura M, Yoshikawa T, Inoue K, Senpuku N, Tamai S, et al. Bone formation process in porous calcium carbonate and hydroxyapatite. J Biomed Mater Res. 1992;26(7):885–95.

138. Handschin RG, Stern WB. X-Ray Diffraction Studies on the Lattice Perfection of Human Bone Apatite (Crista Iliaca). 1995;16(4).

139. Mucalo M. Hydroxyapatite (HAp) for Biomedical Applications. 1st editio. Woodhead Publishing; 2015.

140. Wopenka B, Pasteris JD. A mineralogical perspective on the apatite in bone. Mater Sci Eng C 2005;25(2):131–43.

141. Yilmaz B, Alshemary AZ, Evis Z. Co-doped hydroxyapatites as potential materials for biomedical applications. Microchem J 2019;144(October 2018):443–53.

142. Boanini E, Gazzano M, Bigi A. Acta Biomaterialia Ionic substitutions in calcium phosphates synthesized at low temperature. 2010;6:1882–94.

143. Bohner M. Silicon-substituted calcium phosphates – A critical view. Biomaterials 2009 Nov;30(32):6403–6.

144. Bigi A, Foresti E, Gregorini R, Ripamonti A, Roveri N, Shah JS. The role of magnesium on the structure of biological apatites. Calcif Tissue Int 1992;50(5):439–44.

145. Landi E, Logroscino G, Proietti L, Tampieri A, Sandri M, Sprio S. Biomimetic Mg-substituted hydroxyapatite: from synthesis to in vivo behaviour. J Mater Sci Mater Med 2008;19(1):239–47.

146. Bolland M, Grey A. Ten years too long: strontium ranelate, cardiac events, and the European Medicines Agency. BMJ. 2016;354.

147. Ozbek YY, Bastan FE, Ustel F. Synthesis and characterization of strontium-doped hydroxyapatite for biomedical applications. 2016;745–50.

148. Frasnelli M, Cristofaro F, Sglavo VM, Dirè S, Callone E, Ceccato R, et al. Synthesis and characterization of strontium-substituted hydroxyapatite nanoparticles for bone regeneration. Mater Sci Eng C 2017;71:653–62.

149. Zhang W, Shen Y, Pan H, Lin K, Liu X, Darvell BW, et al. Acta Biomaterialia Effects of strontium in modified biomaterials. Acta Biomater 2011;7(2):800–8.

150. Mouriño V, Cattalini JP, Boccaccini AR. Metallic ions as therapeutic agents in tissue engineering scaffolds: an overview of their biological applications and strategies for new developments. J R Soc Interface 2012 Jan 24;9(68):401 LP – 419.

151. Tamm T, Peld M. Computational study of cation substitutions in apatites. 2006;179:1581–7.

152. Yilmaz B, Alshemary AZ, Evis Z. Co-doped hydroxyapatites as potential materials for biomedical applications. Microchem J. 2019;144(October 2018):443–53.

153. Veiderma M, To K, Knubovets R, Peld M. Impact of anionic substitutions on apatite structure and properties. 2005;690:2638–43.

154. Kim S, Bang H, Song J, Park S. Effect of fluoride additive on the mechanical properties of hydroxyapatite / alumina composites. 2009;35:1647–50.

155. Rivas M, del Valle LJ, Turon P, Puiggalí J, Alemán C. Influence of the atmosphere conditions in the structure, properties and solubility of fluorine-substituted hydroxyapatites. Mater Chem Phys. 2019;

156. Ebrahimi-Kahrizsangi R, Nasiri-Tabrizi B, Chami A. Synthesis and characterization of fluorapatite-titania (FAp-TiO 2) nanocomposite via mechanochemical process. Solid State Sci. 2010;

157. Kim HW, Kim HE, Knowles JC. Fluor-hydroxyapatite sol-gel coating on titanium substrate for hard tissue implants. Biomaterials. 2004;

158. Lowry N, Han Y, Meenan BJ, Boyd AR. Strontium and zinc co-substituted nanophase hydroxyapatite. Ceram Int 2017;43(15):12070–8.

159. Lowry N, Brolly M, Han Y, Mckillop S, Meenan BJ, Boyd AR. Synthesis and characterisation of nanophase hydroxyapatite co-substituted with strontium and zinc. Ceram Int 2018;44(7):7761–70.

160. McCafferty M. Mesenchymal stem cell response to sputter deposited thin film surfaces. 2012.

161. Mingar S, Wang J, Berndt C, Ivanova E, Wen C. Cell response of anodized nanotubes on titanium and titanium alloys - A review. J Bioimed Mater Res Part A. 2013;101(A):2726–39.

162. Dalby MJ, Gadegaard N, Oreffo ROC. interactions to influence stem cell fate. Nat Publ Gr 2014;13(6):558–69.

163. Mcnamara LE, Sjöström T, Burgess KE V, Kim JJW, Liu E, Gordonov S, et al. Biomaterials Skeletal stem cell physiology on functionally distinct titania nanotopographies. 2011;32.

164. Anderson HJ, Sahoo JK, Ulijn R V, Dalby MJ, Anderson HJ. Mesenchymal Stem Cell Fate : Applying Biomaterials for Control of Stem Cell Behavior. 2016;4(May):1–14.

165. Drab M, Kralj-Iglič V. Electric double layer of electrons: Attraction between two like-charged surfaces induced by Fermi–Dirac statistics. Phys Lett Sect A Gen At Solid State Phys. 2019;383(4):358–65.

166. Su H, Lian C, Gallegos A, Deng S, Shang Y, Liu H, et al. Microscopic insights into the Faradaic reaction effects on the electric double layers. Chem Eng Sci 2020;215:115452.

167. Liu X, Lim JY, Donahue HJ, Dhurjati R, Mastro AM, Vogler EA. Influence of Substratum Surface Chemistry/Energy and Topogrpahy on the Human Fetal Osteoblastic Cell Line hFOB 1.19: Phenotypic and Genotypic Responses Observed in vitro. Biomaterials. 2007;28(31):4535–50.

168. Xu LC, Bauer JW, Siedlecki CA. Proteins, platelets, and blood coagulation at biomaterial interfaces. Colloids Surfaces B Biointerfaces 2014;124:49–68.

169. Mavropoulos E, Costa AM, Costa LT, Achete CA, Mello A, Granjeiro JM, et al. Adsorption and bioactivity studies of albumin onto hydroxyapatite surface. Colloids Surfaces B Biointerfaces 2011;83(1):1–9.

170. Vogler EA. Protein adsorption in three dimensions. Biomaterials 2012;33(5):1201–37.

171. Rabe M, Verdes D, Seeger S. Understanding protein adsorption phenomena at solid surfaces. Adv Colloid Interface Sci 2011;162(1–2):87–106.

172. Anselme K. Biomaterials and interface with bone. Osteoporos Int. 2011;22.

173. Prowse ABJ, Chong F, Gray PP, Munro TP. Stem cell integrins : Implications for ex-vivo culture and cellular therapies. Stem Cell Res 2011;6(1):1–12.

174. de Ruijter J., ter Brugge P., Dieudonne S., van Vliet S., Torensma R, Jansen J. Analysis of Integrin Expression in U2OS Cells Cultured on Various Calcium Phosphate Ceramic Substrates. Tissue Eng. 2001;7(3):279–89.

175. Choe HC. Photofunctionalization of EB-PVD HA-coated nano-pore surface of Ti-30Nb-xZr alloy for dental implants. Surf Coatings Technol. 2013;

176. Unabia RB, Bonebeau S, Candidato RT, Jouin J, Noguera O, Pawłowski L. Investigation on the structural and microstructural properties of copper-doped hydroxyapatite coatings deposited using solution precursor plasma spraying. J Eur Ceram Soc. 2019;

177. Fiorucci MP, López AJ, Ramil A. Multi-scale characterization of topographic modifications on metallic biomaterials induced by nanosecond Nd:YVO4 laser structuring. Precis Eng. 2018;

178. Oyane A, Kakehata M, Sakamaki I, Pyatenko A, Yashiro H, Ito A, et al. Biomimetic apatite coating on yttria-stabilized tetragonal zirconia utilizing femtosecond laser surface processing. Surf Coatings Technol. 2016;

179. Carvalho A, Grenho L, Fernandes MH, Daskalova A, Trifonov A, Buchvarov I, et al. Femtosecond laser microstructuring of alumina toughened zirconia for surface functionalization of dental implants. Ceram Int. 2019;

180. Yang Y, Lai Y, Zhang Q, Wu K, Zhang L, Lin C, et al. A novel electrochemical strategy for improving blood compatibility of titanium-based biomaterials. Colloids Surfaces B Biointerfaces. 2010;

181. Furiya-Sato S, Fukushima A, Mayanagi G, Sasaki K, Takahashi N. Electrochemical evaluation of the hydrogen peroxide- and fluoride-induced corrosive property and its recovery on the titanium surface. J Prosthodont Res. 2019;

182. Boyd AR, Rutledge L, Randolph LD, Meenan BJ. Strontium-substituted hydroxyapatite coatings deposited via a co-deposition sputter technique. Mater Sci Eng C. 2015;

183. Christopher Jeremy Tredwin. Sol-Gel Derived Hydroxyapatite, Fluorhydroxyapatite and Fluorapatite Coatings for Titanium Implants. University College London; 2009.

184. Granato R, Bonfante EA, Castellano A, Khan R, Jimbo R, Marin C, et al. Osteointegrative and microgeometric comparison between micro-blasted and alumina blasting/acid etching on grade II and V titanium alloys (Ti-6Al-4V). J Mech Behav Biomed Mater. 2019;

185. Vishnu J, Manivasagam VK, Gopal V, Garcia CB, Hameed P, Manivasagam G, et al. Hydrothermal treatment of etched titanium : A potential surface nano-modification technique for enhanced biocompatibility ,. Nanomedicine Nanotechnology, Biol Med 2019;20:102016.

186. Xie Y, Zuo J, Zhou B, Ma L, Yu ZM, Wei Q, et al. Sandblast-free double-etched titanium for dental implants application. Mater Lett. 2016;

187. Janson O, Gururaj S, Pujari-palmer S, Karlsson M, Strømme M, Engqvist H, et al. Materials Science & Engineering C Titanium surface modi fi cation to enhance antibacterial and bioactive properties while retaining biocompatibility. Mater Sci Eng C 2019;96(November 2018):272–9.

188. Schneiker T, Forsberg K. Process Chemistry and Acid Management in Titanium Pickling Processes. Conf Titan Eur. 2014;

189. Freitas GP, Lopes HB, Almeida A De, Oliveira PT De. Effect of Surface Nanotopography on Bone Response to Titanium Implant. 2015;(June 2016).

190. Prosolov KA, Popova KS, Belyavskaya OA, Rau J V., Gross KA, Ubelis A, et al. RF magnetron-sputtered coatings deposited from biphasic calcium phosphate targets for biomedical implant applications. Bioact Mater. 2017;

191. Ong JL, Yang Y, Oh S, Appleford M, Chen W, Liu Y, et al. Calcium Phosphate Coating Produced by a Sputter Deposition Process. In: Thin Calcium Phosphate Coatings for Medical Implants. 2008.

192. Kailath BJ, DasGupta A, DasGupta N. Optimisation of ac anodisation parameters for the improvement of electrical properties of thermally grown ultrathin gate oxide. Solid State Electron. 2007;

193. Pinto R, Carmezim MJ, Ferreira MGS, Montemor MF. A two-step surface treatment, combining anodisation and silanisation, for improved corrosion protection of the Mg alloy WE54. In: Progress in Organic Coatings. 2010.

194. Forero López AD, Lehr IL, Saidman SB. Anodisation of AZ91D magnesium alloy in molybdate solution for corrosion protection. J Alloys Compd. 2017;

195. Jurczyk K, Jurczyk M. Nanostructured Surfaces. In: Narayan R, editor. Nanobiomaterials, Nanostructured materials for biomedical applications. 2018. p. 179–95.

196. Awad NK, Edwards SL, Morsi YS. A review of TiO 2 NTs on Ti metal : Electrochemical synthesis , functionalization and potential use as bone implants. Mater Sci Eng C 2017;76:1401–12.

197. Zhang L, Liao X, Fok A, Ning C, Ng P, Wang Y. Materials Science & Engineering C E ff ect of crystalline phase changes in titania (TiO 2) nanotube coatings on platelet adhesion and activation. 2018;82(March 2017):91–101.

198. Nasker P, Mukherjee M, Kant S, Tripathy S, Sinha A, Das M. Fluorine substituted nano hydroxyapatite: Synthesis, bio-activity and antibacterial response study. Ceram Int. 2018;

199. Fordyce FM. Fluorine: human health risks. Encylopedia Environ Heal. 2011;2.

200. Cairns ML, Meenan BJ, Burke GA, Boyd AR. Influence of surface topography on osteoblast response to fibronectin coated calcium phosphate thin films. Colloids Surfaces B Biointerfaces. 2010;

201. Surmeneva MA, Mukhametkaliyev TM, Khakbaz H, Surmenev RA, Bobby Kannan M. Ultrathin film coating of hydroxyapatite (HA) on a magnesium-calcium alloy using RF magnetron sputtering for bioimplant applications. Mater Lett. 2015;152.

202. Dorozhkin S V, Dorozhkin S V. Calcium orthophosphates Calcium orthophosphates a n d e s. 2017;2535(May).

203. Biesinger MC, Lau LWM, Gerson AR, St R, Smart C. Applied Surface Science Resolving surface chemical states in XPS analysis of first row transition metals , oxides and hydroxides : Sc , Ti , V , Cu and Zn. Appl Surf Sci 2010;257(3):887–98.

204. Miller DJ, Biesinger MC, Mcintyre NS. Interactions of CO 2 and CO at fractional atmosphere pressures with iron and iron oxide surfaces : one possible mechanism for surface contamination ? 2002;299–305.

205. (ICDD) IC for DD. Powder Diffraction File.

206. Garcia R, Perez R. Dynamic atomic force micrscopy methods. Surf Sci Rep. 2002;

207. Martinez NF, Garcia R. Measuring phase shifts and energy dissipation with amplitude modulation atomic force microscopy. Nanotechnology. 2006;

208. Trtik P, Kaufmann J, Volz U. On the use of peak-force tapping atomic force microscopy for quantification of the local elastic modulus in hardened cement paste. Cem Concr Res. 2012;

209. Giessibl FJ. Advances in atomic force microscopy. Rev Mod Phys. 2003;75.

210. San Paulo A, García R. High-resolution imaging of antibodies by tapping-mode atomic force microscopy: Attractive and repulsive tip-sample interaction regimes. Biophys J. 2000;

211. Yan XL, Duvenhage MM, Wang JY, Swart HC, Terblans JJ. Evaluation of sputtering induced surface roughness development of Ni/Cu multilayers thin films by Time-of-Flight Secondary Ion Mass Spectrometry depth profiling with different energies O2+ ion bombardment. Thin Solid Films. 2019;

212. Senoner M, Unger WES. SIMS imaging of the nanoworld: applications in science and technology. J Anal At Spectrom. 2012;

213. Jeynes C, Colaux JL. Thin film depth profiling by ion beam analysis. Analyst. 2016;141.

214. Niforou KN, Anagnostopoulos AK, Vougas K, Kittas C, Gorgoulis VG, Tsangaris GT. The Proteome Profile of the Human Osteosarcoma U2OS Cell Line. 2008;78:63–77.

215. Strober W. Trypan Blue Exclusion Test of Cell Viability. Curr Protoc Immunol. 2001;

216. Berridge M V., Herst PM, Tan AS. Tetrazolium dyes as tools in cell biology: New insights into their cellular reduction. Biotechnol Annu Rev. 2005;11(SUPPL.):127–52.

217. Boncler M, Rózalski M, Krajewska U, Podswdek A, Watala C. Comparison of PrestoBlue and MTT assays of cellular viability in the assessment of anti-proliferative effects of plant extracts on human endothelial cells. J Pharmacol Toxicol Methods. 2014;

218. Dragan AI, Casas-Finet JR, Bishop ES, Strouse RJ, Schenerman MA, Geddes CD. Characterization of PicoGreen interaction with dsDNA and the origin of its fluorescence enhancement upon binding. Biophys J. 2010;

219. Orimo H, Goseki-sone M, Hosoi T, Shimada T. Functional assay of the mutant tissue-nonspecific alkaline phosphatase gene using U 2 OS osteoblast-like cells. 2008;94:375–81.

220. Winning L, Robinson L, Boyd AR, Karim IA El, Lundy FT, Meenan BJ. Osteoblastic differentiation of periodontal ligament stem cells on non-stoichiometric calcium phosphate and titanium surfaces. 2017;1692–702.

221. Anaspec. Assay Kit * Colorimetric * Kit Components , Storage and Handling. :1–5.

222. Thermo Fisher Scientific. Pierce ™ BCA Protein Assay Kit. 2000.

223. Jonášová L, Müller FA, Helebrant A, Strnad J, Greil P. Biomimetic apatite formation on chemically treated titanium. Biomaterials. 2004;25(7–8):1187–94.

224. Duffy H. Microstructural Evolution in Calcium Phosphate Thin Films. 2011.

225. Lowry N, Han Y, Meenan BJ, Boyd AR. Strontium and zinc co-substituted

nanophase hydroxyapatite. Ceram Int. 2017;43(15):12070–8.

226. Lowry N, Brolly M, Han Y, Mckillop S, Meenan BJ, Boyd AR. Synthesis and characterisation of nanophase hydroxyapatite co-substituted with strontium and zinc. Ceram Int. 2018;44(7):7761–70.

227. Elliott J, Wilson R, Douker S. Apatite Structures - ICDD. Adv X-ray Anal. 2002;45:176.

228. Bigi A, Boanini E, Gazzano M. Ion Substitution in Biological and Synthetic Apatites. In: Biomineralization and Biomaterials. 2016. p. 235–66.

229. Frasnelli M, Cristofaro F, Sglavo VM, Dirè S, Callone E, Ceccato R, et al. Synthesis and characterization of strontium-substituted hydroxyapatite nanoparticles for bone regeneration. Mater Sci Eng C. 2017;71:653–62.

230. Kaygili O, Keser S, Kom M, Eroksuz Y, Dorozhkin S V, Ates T, et al. Strontium substituted hydroxyapatites : Synthesis and determination of their structural properties , in vitro and in vivo performance. Mater Sci Eng C 2015;55:538–46.

231. Mattox DM. Chapter 7 - Physical Sputtering and Sputter Deposition (Sputtering). In: Handbook of Physical Vapor Deposition (PVD) processing (Second Edition). 2010. p. 237–86.

232. Jürgensen A, Raschke H, Hergenröder R. Surface-electron-gas interaction: Inelastic scattering of photoelectrons. J Electron Spectros Relat Phenomena. 2019;

233. Chantler CT, Bourke JD. Low-energy electron properties: Electron inelastic mean free path, energy loss function and the dielectric function. Recent measurements, applications, and the plasmon-coupling theory. Ultramicroscopy. 2019;

234. Boyd A, Akay M, Meenan BJ. Influence of target surface degradation on the properties of r . f . magnetron-sputtered calcium phosphate coatings. 2003;188–98.

235. Boyd AR, Meenan BJ, Leyland NS. Surface characterisation of the evolving nature of radio frequency (RF) magnetron sputter deposited calcium phosphate thin films after exposure to physiological solution. Surf Coatings Technol. 2006;

236. Morozowich NL, Lerach JO, Modzelewski T, Jackson L, Winograd N, Allcock HR. Characterization of hydroxyapatite deposition on biomimetic polyphosphazenes by time-of-flight secondary ion mass spectrometry (ToF-

SIMS). RSC Adv. 2014;4(38):19680–9.

237. Eriksson C, Börner K, Nygren H, Ohlson K, Bexell U, Billerdahl N, et al. Studies by imaging TOF-SIMS of bone mineralization on porous titanium implants after 1 week in bone. Appl Surf Sci. 2006;

238. Palmquist A, Emanuelsson L, Sjövall P. Chemical and structural analysis of the bone-implant interface by TOF-SIMS, SEM, FIB and TEM: Experimental study in animal. Appl Surf Sci. 2012;

239. Boyd AR, Duffy H, McCann R, Meenan BJ. Sputter deposition of calcium phosphate/titanium dioxide hybrid thin films. Mater Sci Eng C. 2008;

240. Donnell MDO, Fredholm Y, Rouffignac A De, Hill RG. Structural analysis of a series of strontium-substituted apatites. 2008;4:1455–64.

241. Aldrich S. McCoys 5A Medium - product number M9309.

242. Hong W, Zhang Q, Jin H, Song L, Tan Y, Luo L, et al. Materials Science & Engineering C Roles of strontium and hierarchy structure on the in vitro biological response and drug release mechanism of the strontium-substituted bioactive glass microspheres. Mater Sci Eng C. 2020;107(October 2019):110336.

243. Liu C, Zhang Y, Wang L, Zhang X, Chen Q, Wu B. A strontium-modified titanium surface produced by a new method and its biocompatibility in vitro. PLoS One. 2015;10(11).

244. Querido W, Rossi AL, Farina M. The effects of strontium on bone mineral : A review on current knowledge and microanalytical approaches. 2016;80:122–34.

245. Pascua-Maestro R, Corraliza-Gomez M, Diez-Hermano S, Perez-Segurado C, Ganfornina MD, Sanchez D. The MTT-formazan assay: Complementary technical approaches and in vivo validation in Drosophila larvae. Acta Histochem. 2018;

246. Mosmann T. Rapid colorimetric assay for cellular growth and survival: Application to proliferation and cytotoxicity assays. J Immunol Methods. 1983;65.

247. Ikeda Y, Iwakiri S, Yoshimori T. Development and characterization of a novel host cell DNA assay using ultra-sensitive fluorescent nucleic acid stain “PicoGreen.” J Pharm Biomed Anal. 2009;

248. Ashley N, Harris D, Poulton J. Detection of mitochondrial DNA depletion in living

human cells using PicoGreen staining. Exp Cell Res. 2005;

249. Surmenev RA, Surmeneva MA, Ivanova AA. Significance of calcium phosphate coatings for the enhancement of new bone osteogenesis - A review. Acta Biomaterialia. 2014.

250. Long EG, Buluk M, Gallagher MB, Schneider JM, Brown JL. Bioactive Materials Human mesenchymal stem cell morphology , migration , and di ff erentiation on micro and nano-textured titanium. Bioact Mater. 2019;4(August):249–55.

251. Huang GNZYG, Lu WLWW. The effect of strontium incorporation in hydroxyapatite on osteoblasts in vitro. 2011;961–7.

252. Boanini E, Torricelli P, Fini M, Bigi A. Osteopenic bone cell response to strontium-substituted hydroxyapatite. 2011;2079–88.

253. Zhao L, Liu L, Wu Z, Zhang Y, Chu PK. Effects of micropitted/nanotubular titania topographies on bone mesenchymal stem cell osteogenic differentiation. Biomaterials. 2012;

254. Su Jin S, Jeon O, Yang HS, Han DK, Kim B-S. Effects of Culture Conditions on Osteogenic Differentiation in Human Mesenchymal Stem Cells. J Microbiol Biotechnol . 2007;17(7):1113–9.

255. Aldrich S. Alizarin-Red staining solution. 2020.

256. Yang JX, He Y Bin, Lai LN, Li JB, Song XL. Electrochemical sensors using gold submicron particles modified electrodes based on calcium complexes formed with alizarin red S for determination of Ca2+ in isolated rat heart mitochondria. Biosens Bioelectron. 2015;

257. Brugge PJ, Dieudonne S, Jansen JA. Initial interaction of U2OS cells with noncoated and calcium phosphate coated titanium substrates. 2001;

258. Orimo H, Shimada T. Effects of phosphates on the expression of tissue-nonspecific alkaline phosphatase gene and phosphate-regulating genes in short-term cultures of human osteosarcoma cell lines. 2006;101–8.

259. Deligianni DD, Katsala N, Ladas S, Sotiropoulou D, Amedee J, Missirlis YF. Effect of surface roughness of the titanium alloy Ti-6Al-4V on human bone marrow cell response and on protein adsorption. Biomaterials. 2001;

260. Guehennec L Le, Enkel B, Weiss P, Amouriq Y, Layrolle P. Osteoblastic cell behaviour on different titanium implant surfaces. 2008;4:535–43.

261. Gross KA, Walsh W, Swarts E. Analysis of retrieved hydroxyapatite-coated hip prostheses. J Therm Spray Technol. 2004;13.

262. Li H, Ma Y, Zhao Z, Tian Y. Fatigue behavior of plasma sprayed structural-grade hydroxyapatite coating under simulated body fluids. Surf Coatings Technol. 2019;

263. Nilsson KG, Cajander S, Karrholm J. Early failure of hydroxyapatite-coating in total knee arthroplasty: A case report. Acta Orthop Scand. 1994;65(2).

264. Wu VM, Uskoković V. Is there a relationship between solubility and resorbability of different calcium phosphate phases in vitro? Biochim Biophys Acta - Gen Subj. 2016;

265. Bussola Tovani C, Gloter A, Azaïs T, Selmane M, Ramos AP, Nassif N. Formation of stable strontium-rich amorphous calcium phosphate: Possible effects on bone mineral. Acta Biomater. 2019;

266. Long E, Buluk M, Gallagher M, Schneider J, Brown J. Human mesenchymal stem cell morphology, migration and differentiation on micro and nano-textured titanium. Bioact Mater. 2019;